Magnetic Domain Effects in High Sensitive, 2-2 Composite Magnetoelectric Sensors

Dissertation

zur Erlangung des akademischen Grades

Doktor der Ingenieurwissenschaften (Dr.-Ing)

Technische Fakultät

Christian-Albrechts Universität zu Kiel

Necdet Onur Urs

September, 2017

1. Gutachter	Prof. Dr.-Ing. Jeffrey McCord
2. Gutachter	Prof. Dr.-Ing. Eckhard Quandt

Datum der mündlichen Prüfung	19.12.2017

Erklärung

Hiermit versichere ich, dass die vorliegende Arbeit - abgesehen von der Beratung durch die Betreuer - nach Inhalt und Form die eigene Arbeit ist. Ich versichere weiterhin, dass ich die Inanspruchnahme aller fremder Hilfen aufgeführt habe sowie, dass ich die wörtlich oder inhaltlich aus anderen Quellen übernommenen Stellen als Solche gekennzeichnet habe.

Zudem ist die Arbeit unter Einhaltung der Regeln guter wissenschaftlicher Praxis der Deutschen Forschungsgemeinschaft entstanden.

Ich erkläre auserdem, dass die Arbeit bisher keiner anderen Prüfungsbehörde vorgelegt wurde und nicht als ganzes veröffentlicht worden ist bzw. zur Veröffentlichung eingereicht wurde.

_____ _____

Ort, Datum Unterschrift

Abstract

High permeability magnetic materials possess diverse physical properties and are frequently integrated to many technological applications as magnetic field sensors. Composed of a magnetostrictive and a piezoelectric phase, the 2-2 thin film magnetoelectric (ME) sensors in cantilever design emerged as a new promising candidate for magnetic field sensing in recent years. In order to optimize the sensor response, it is useful to accumulate knowledge on the response in each constituent phase. In this thesis, by complementary employment of magneto-optical imaging, inductive magnetization and electrical device response measurements, the magnetization as well as magnetic domain response in soft magnetic, magnetostrictive materials are investigated and are linked to the ME response.

The first results section of the thesis deals with revealing the origin of the hysteretic hard axis magnetization response of FeCoSiB. Two distinct magnetic domain configurations leading to two magnetic field history dependent magnetization branches are identified. The occurring blocked and modulated magnetic domain states are discussed in terms of the transpiring domain wall type, their magnetic susceptibilities and spatially varying effective magnetic anisotropy. Later, the influence of film topology in differently layered FeCoSiB films deposited on Si/ SiO_2 and AlN substrates is investigated revealing an inverted film behavior for FeCoSiB films on rough AlN surfaces.

The second part connects the magnetic domain effects discussed in the first part with the real ME sensor response by *in situ* domain observations. A prompt transference of the magnetization response to the device response is exposed. Moreover, two magneto-optical approaches to obtain local magnetostriction maps and curves are demonstrated, granting the opportunity for separating and linking the magnetostrictive response and the ME response.

The last part focuses on the hard axis magnetic domain response of differently layered and structured CoFeB films with the objective to control the magnetic domain state. The emphasis is put on the developing hysteretic hard axis magnetization response in micrometer in-plane dimensions due to dominant domain wall transformations and movement. For exchange biased specimens the increasing in-

plane demagnetizing field with higher CoFeB thicknesses results in formation of magnetic domain walls. Finally, it is demonstrated that the antiparallel biasing of adjacent CoFeB films leads to preservation of the single domain state and retainment of a reversible, linear magnetization response.

Zusammenfassung

Hochpermeable magnetische Werkstoffe besitzen vielfältige physikalische Eigenschaften und sind häufig als Bestandteil der Magnetfeldsensoren zu finden. Aus einer magnetostriktiven und einer piezoelektrischen Phase bestehende 2-2 Dünnfilm magnetoelektrische Sensoren im Biegebalken-Design haben sich in den letzten Jahren als neuer, vielversprechender Kandidat für die Magnetfeldsensorik heraus gestellt. Um die Sensorantwort zu optimieren, ist es sinnvoll Verständnis über die Antwort jeder konstituierenden Phase zu erlangen. In dieser Arbeit werden durch komplementäre Verwendung von magnetooptischer Bildgebung, induktiver Magnetisierungsmessung und direkter Messung der elektrischen Antwort, sowohl die Magnetisierung als auch die magnetische Domänenantwort in weichmagnetischen, magnetostriktiven Materialien untersucht und mit der ME-Antwort verknüpft.

Der erste Abschnitt des Ergebnisteils dieser Arbeit beschäftigt sich mit der Erforschung des Ursprungs der Magnetisierungsantwort von FeCoSiB an der hysteretischen harten Achse. Zwei unterschiedliche magnetische Domänenkonfigurationen werden identifiziert, die zu zwei magnetfeldabhängigen Magnetisierungszweigen führen. Die auftretenden blockierten und modulierten magnetischen Domänenzustände werden in Bezug auf die vorkommenden Domänenwandtypen, ihre magnetischen Suszeptibilitäten und die räumlich variierende effektive magnetische Anisotropie diskutiert. Später wird der Einfluss der Filmtopologie auf unterschiedlich geschichtete FeCoSiB-Filme, die auf Si/ SiO_2 und AlN-Substraten abgeschieden wurden, untersucht. Hierbei konnte ein invertiertes Filmverhalten für FeCoSiB-Filme auf rauer AlN-Oberfläche gezeigt werden.

Der zweite Teil verbindet die im ersten Teil diskutierten magnetischen Domäneneffekte mit der realen ME-Sensorantwort durch *in situ* Domänenbeobachtungen. Eine direkte Übertragung des Magnetisierungssignals auf die Geräteantwort wird offen gelegt. Darüber hinaus werden zwei magnetooptische Ansätze zur Erzielung ortsaufgelöster Magnetostriktionskarten und -kurven demonstriert, wodurch die Möglichkeit besteht, die magnetostriktive Antwort und die ME-Antwort zu trennen und zu verknüpfen.

Der letzte Teil konzentriert sich auf die magnetische Domänenantwort entlang

der harten Achse unterschiedlich geschichteter und strukturierter CoFeB-Filme mit dem Ziel, den magnetischen Domänenzustand zu kontrollieren. Der Schwerpunkt liegt auf dem Auftreten der hysteretischen Hartachsenmagnetisierungsantwort in Filmen mit Filmebene dimensionen im Mikrometerbereich aufgrund dominanter Domänenwandtransformationen und -bewegungen. Bei Proben mit *exchange bias* ergibt sich das zunehmende Entmagnetisierungsfeld in der Filmebene mit steigender CoFeB-Dicke zur Bildung von magnetischen Domänenwänden. Es wird gezeigt, dass die antiparallele Anordnung des *exchange bias* benachbarter CoFeB-Filme zur Erhaltung des Eindomänenzustands und einer reversiblen, linearen Magnetisierungsantwort führt.

Contents

Abbreviation list

Some abbreviations used frequently in the thesis are defined.

ME	Magnetoelectric
AMR	Anisotropic magnetoresistance
MO	Magneto-optical
MO sens	Magneto-optical sensitivity
MOKE	Magneto-optical Kerr effect
MOVE	Magneto-optical Voigt effect
LoD	Limit of Detection
SNR	Signal-to-noise ratio
ABW	Asymmetric Block wall
ANW	Asymmetric Néel wall
FeCoSiB	$(Fe_{90}Co_{10})_{78}Si_{12}B_{10}$
CoFeB	$Co_{40}Fe_{40}B_{20}$
$\boldsymbol{H_{ext}}$	External magnetic field
$\boldsymbol{H_{mea}}$	Measuring magnetic field
$\boldsymbol{H_{wp}}$	Working point (magnetic field)
$\boldsymbol{H_{eb}}$	Induced exchange bias field
$\boldsymbol{H_{k}}$	Magnetic anisotropy field
$\mathbf{K_u}$	Uniaxial magnetic anisotropy
$\mathbf{K_{eb}}$	Induced exchange bias anisotropy
$\mathbf{K_{eff}}$	Effective magnetic anisotropy
$\mathbf{M_s}$	Saturation magnetization
$\boldsymbol{\lambda}$	Magnetostriction
$\boldsymbol{H_{d}}$	Demagnetizing field
$\boldsymbol{\alpha_{ME}}$	Magnetoelectric voltage coefficient
$\mathbf{f_{res}}$	Resonance frequency

1 State of magnetic field sensors

Since the invention of compasses, applied magnetism has remained to be of great technological relevance and in the last decades has played an indispensable role in everyday life. Magnetic field sensing has found functional usage, for instance, inside computers for data storage [1], in mobile phones as an integral component to global positioning systems (GPS) [2] and in medicine for detecting biomagnetic signals [3, 4].

A figure of merit for all magnetic field sensing applications is the limit of detection (LoD), which states the lowest (or the highest) measurable magnetic field amplitude by the sensor before the noise floor is reached (or the sensor is saturated). Additionally, most sensors are limited by a frequency range/ point, where the measured sensor response is the highest. Therefore, there are various sensor designs available for sensing low magnetic fields with numerous advantages and disadvantages.

Superconducting quantum interference devices (SQUIDs), based on measuring tunneling currents between two superconducting metals [5], are established devices due to their high signal-to-noise ratio (SNR) and ability to measure low amplitude magnetic field signals. Commercially available SQUID sensors are able to reach LoDs of 3.6 $\mathrm{fT/Hz^{1/2}}$ and even below at 1 Hz [6]. Therefore, SQUIDs are widely accepted to be the gold standard in low frequency magnetometry and widely find application in medicine for measuring biomagnetic signals. However, liquid Nitrogen or Helium requirement for low temperature cooling to obtain superconductivity and generally requiring a magnetically shielded environment due to SQUID's low magnetic field saturation are main drawbacks for its applicability. Hence, in order to find a possible substitute for SQUIDs, other old and new magnetic field sensing concepts are extensively researched. Here, some magnetic field sensor concepts with magnetic materials as sensing layers are covered.

Although measurement concepts can be quite different from one another, for magnetic field sensors employing magnetic layers as the sensing element, the common material parameter is the magnetic permeability $\boldsymbol{\mu}$. The fluxgate sensors involve a magnetic core and pick-up coil(s) to measure $\boldsymbol{\mu}$ variations in the magnetic core under external magnetic field. In a ring shaped magnetic core with two orthogo-

nally aligned pick-up coils, vectorial information about the magnetic fields can be obtained [7]. Recently, LoDs as low as 12 pT/Hz$^{1/2}$ at 8 Hz have been reported for space based applications [8].

Another concept is to use the so-called magnetoresistance (MR) effect inherent to all magnetic materials. The simplest case is the anisotropic magnetoresistance (AMR) effect. Only a singlelayer of magnetic material is required to obtain AMR response. Originating from the spin-orbit coupling in magnetic materials, the measured resistance $\boldsymbol{R}$ in a magnetic material is a function of the angle $\boldsymbol{\theta_{AMR}}$ between the applied current and the magnetization direction in the magnetic material. AMR is quadratic in magnetization, i.e. the response is equal for collinear magnetization directions. $\boldsymbol{R}$ becomes a minimum with magnetization perpendicular to the current direction and vice versa. Traditionally, the figure of merit for an AMR sensor is the field dependency of the relative MR resistivity change $\boldsymbol{\Delta R/R_{\perp}}$ with $\boldsymbol{R_{\perp}}$ being the measured AMR with magnetization perpendicular to the current direction [1, 9]. Compared to other MR effects, AMR displays relatively low resistance changes (2%-3%). However, LoD = 40 pT/Hz$^{1/2}$ at 1 Hz have been realized [10].

Giant magnetoresistance (GMR) involves, in the most simple case, a bilayer layer system with two ferromagnetic materials separated by a thin non-ferromagnetic, conducting material. Upon application of an electric current through the bilayer structure, relative parallel or anti-parallel magnetization alignment in the ferromagnetic layers leads to respective low and high resistance values [11,12]. GMR elements have been widely used as read-heads in hard disk drives [13]. Lately, they have also found application in sensing biomagnetic fields. GMR sensors with magnetic field sensitivities as low as 250 fT/Hz$^{1/2}$ and 700 fT/Hz$^{1/2}$ at 1 Hz at respective temperatures of 4.2 K and 77 K have been fabricated [14]. Lately, biomagnetic signals from the heart have also been measured with GMR sensor arrays with a magnetic field resolution of 3 pT/Hz$^{1/2}$ at 1 Hz [15].

Instead of using a conducting spacer layer, an insulating spacer layer can also be employed. The resulting structure is a magnetic tunnel junction. For very thin spacer layer thicknesses, an electron tunneling probability develops between the ferromagnetic layers and similar to the GMR effect the parallel and anti-parallel alignment of magnetization in the neighboring layers leads to measurement of low and high resistance values, respectively. The effect is named the tunneling magnetoresistance (TMR) effect. Until 2000s, amorphous Al_2O_3 was used as the insulating layer, but has since been replaced with crystalline MgO for higher tunneling resistance, where TMR values up to 600% and above can be obtained at room temperature for CoFeB/ MgO/ CoFeB stacks [16]. Due to their high signal such MR elements are used for magnetic field sensing. In a magnetic tunnel junction with a TMR stack as the sensing element, LoD around 70 pT/Hz$^{1/2}$ at 1 Hz have been reported at room

temperature (with 15 mV bias at the junction) [17].

Another approach for magnetic field sensing is the utilization of the giant magnetoimpedance (GMI) effect. Originating from the skin effect most prominently encountered in conductors, a magnetic conductor driven by a high frequency current (AC) $\boldsymbol{I_{dri}}$ experiences a substantial variation in its AC impedance [18, 19]. In order to obtain a significant impedance change, the magnetic material is preferred to be a soft ferromagnetic material (high relative magnetic permeability $\boldsymbol{\mu_r}$) e.g. amorphous Co rich alloys [19–21] or $Ni_{81}Fe_{19}$ [22]. $\boldsymbol{I_{dri}}$ generates a magnetic field $\boldsymbol{H_{ind}}$ inside the material. Consequently, $\boldsymbol{H_{ind}}$ induces a current $\boldsymbol{I_{ind}}$, which opposes $\boldsymbol{I_{dri}}$ and the current flow gets restricted towards the surface (skin) of the conductor and the extent of this restriction is defined as the skin depth. The skin depth is indirectly proportional to the $\boldsymbol{I_{dri}}$ frequency. The presence of an external magnetic field along the $\boldsymbol{I_{dri}}$ direction (thus $\boldsymbol{I_{ind}}$ and $\boldsymbol{H_{ind}}$) results in the expansion of the skin depth region and the impedance is decreased. Relative GMI variations as high as 600 %/Oe and above have been reported [20]. Moreover, several papers published in recent years show that the effect is applicable to high sensitive AC magnetic field detection. Magnetic field amplitudes in the low picotesla regime have been shown to be detectable [20, 21].

A relatively new approach for sensing low amplitude magnetic fields is by utilizing the magnetoelectric (ME) effect. The ME effect for magnetic field sensing is based on changing the magnetization of a sensor structure and due to induced magnetostrictive strain, a piezoelectric voltage is measured (In detail explanation of the ME effect is given later in Section 2.3). It was first observed in multiferroic materials, in which both magnetic and dielectric properties are present simultaneously. However, typically for single-phase multiferroic materials, the obtainable ME responses are rather low. Therefore, composite sensor structures has been lately gathering much attention. In this work emphasis is given on 2-2 thin film ME sensors in cantilever design [23–28]. The cantilever design allows for signal enhancement at mechanical resonance. Moreover, individual magnetic and piezoelectric properties can be separately altered and optimized. As a result ME-coefficients not yet available to single-phase multiferroic materials can be reached.

An overview of some discussed magetic field sensor concepts and exemplary LoD values from scientific literature are displayed in Table 1.1.

Table 1.1: A list of magnetic field sensors with magnetic sensing layers and examples for achieved limit of detections (LoD) are displayed. The SQUID sensor is shown for comparison.

Sensor type	LoD at 1 Hz ($pT/Hz^{1/2}$)	Additional Information	Reference
SQUID	3.6 x 10^{-3}	at 4.2K	[6]
Fluxgate	12	at 288K	[8]
AMR	40		[10]
GMR	3		[15]
	0.25 - 0.7	4.2 K - 77 K	[14]
TMR	70		[17]
GMI	10 - 80		[20, 21]
ME	300	exchange biased sensor	[27]

1.1 Magnetic noise

As has been briefly touched upon in the previous section, the noise level defines the LoD of a sensor. It is the point, where the ratio of the sensor signal to the effective noise contribution, i.e. SNR, becomes unity. Therefore, for easy detection of the desired signals, the SNR is to be maximized. The challenge can be tackled by maximizing the ultimate sensor signal (e.g. $\Delta R/R_{\perp}$ for the MR sensors) and/or by minimizing the effective noise sources. Therefore, vast amount of research is conducted both in the industry and universities for understanding the underlying mechanisms and factors leading to noisy signals and thus minimize them.

From electronics to acoustics, there are many possible noise sources in such devices. However, in this section emphasis is given on noise sources originating from magnetic layers. Scientific reviews dating as early as 1969 can be found covering this problem [29].

The magnetic properties of a magnetic material depend closely on temperature. Therefore, many devices are designed to work under conditions, where little temperature variations occur. Thus, making the temperature related device response deviations negligible. However, for magnetic field sensors working in harsh environments, such as in space [30], high variations in temperature might cause degradation in sensor response and needs to be addressed [10]. Nonetheless, this temperature dependency has been lately utilized to garnet films in a magneto-optical detection scheme in order to sense temperature variations. A temporal resolution of 1 ms and

temperature resolution of 0.01 $K/Hz^{1/2}$ has been demonstrated [31, 32].

Furthermore, for high frequency applications, the induced eddy currents in the magnetic material can substantially decrease the material's $\boldsymbol{\mu}$. The effect scales with the thickness of the magnetic material and for effective mitigation, the sensing layer can be laminated with non-magnetic, insulating spacer layers [33]. By preference, the ferromagnetic sensing layer can be exchanged with an appropriate ferrimagnetic material, which are known to possess high electrical resistance.

However, for thin magnetic films submitted to negligibly small temperature variations, the major noise source stems from magnetic domain activity inside the material [34, 35], which is characterized by the sudden magnetization changes (jumps) in the magnetization loop measurements. This magnetic behavior is defined as the magnetic noise (Barkhausen noise) and from magnetism point of view, points out towards the existence of magnetic domains [36]. Such sudden magnetization changes are linked directly to the magnetic field history dependent annihilation and nucleation of magnetic domain and domain wall structures, as well as domain wall motion. They are largely irreversible, meaning the magnetic state does not revert back to its original state after the magnetization jump has occurred. As a result, the magnetization response deviates from linearity and magnetic hysteresis is observed. For sensor applications with magnetic sensing layers, it is common to observe a transfer of the magnetic hysteresis to the sensor response [9, 37].

The key to deal with this issue is to suppress the magnetic domain activity by obtaining a single domain state in the sensing material. As will be covered in the following sections, the compensation of the demagnetizing field is the key to prevent magnetic domain formation. This can be achieved, for example, by incorporating magnetic materials with sufficiently high magnetic anisotropy. Moreover, the shape anisotropy can be varied. For example, a continuous magnetization state has been acquired in fluxgate sensors by employing materials in ring core shape. Thus, demagnetizing effects leading to magnetic domain formation are largely avoided. Additionally, such a configuration allows for two dimensional vector magnetometry [7, 30].

The linearization of the magnetization response can be obtained e.g. by applying a constant external magnetic bias field $\boldsymbol{H_{bias}}$ through a conductor strip or be supplied by external coils (also called shunt biasing) (Figure 1.1a). As a result, the magnetic domain and domain wall formation can be largely prevented [9, 37]. However, implementing external magnetic field sources into sensor design can be both energy inefficient and for sensor arrays might lead to cross-talk of the sensors and contribute to the overall noise. Therefore, different magnetic layering schemes can be utilized to internally bias the magnetic sensing element.

One way is the use of soft adjacent layer (SAL) saturation, where another soft

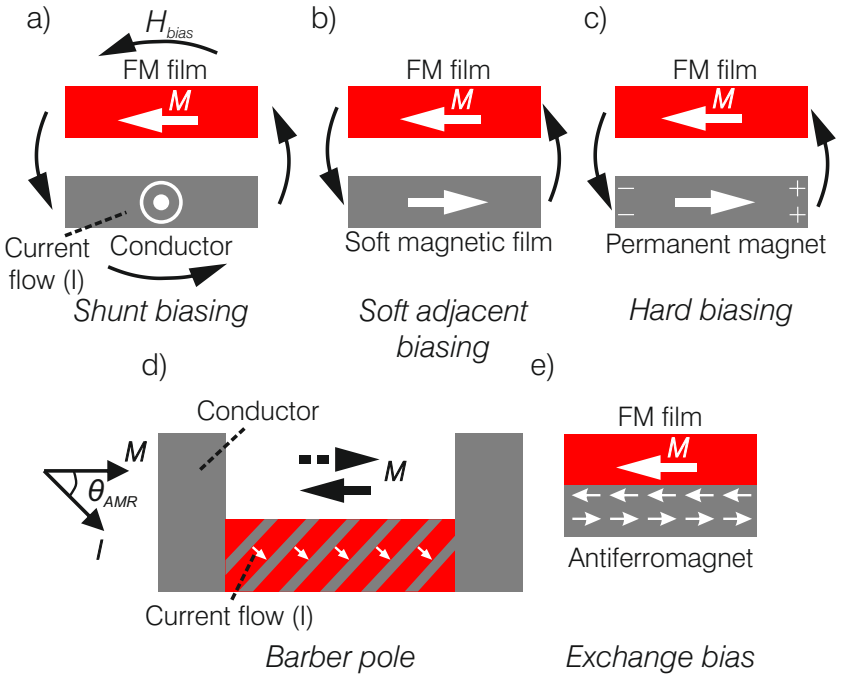

Figure 1.1: Different biasing schemes for reduced magnetic domain activity in the ferromagnetic (FM) sense layer (red rectangles) are depicted. (Adapted from [37])

magnetic film is brought in proximity of the magnetic film [37, 38]. The magnetic flux closure is obtained through the magnetostatic interactions between the films (Figure 1.1b). Also designs involving implementation of permanent magnets are available. The permanent magnet serves, similar to shunt biasing, as a source of constant external bias field (Figure 1.1c).

In AMR sensors, the commonly observed $\boldsymbol{H_{ext}}$ hysteresis have been addressed with the so-called barber pole configuration (Figure 1.1d) [37, 39]. The AMR curve is linear, when the relative angle $\boldsymbol{\theta_{AMR}}$ between the current $\boldsymbol{I}$ and the magnetization $\boldsymbol{M}$ equals to $\pm 45°$. Considering a sensor structure, where the ferromagnetic layer is shaped as a rectangular prism, the magnetic domain effects start to take effect with varied $\boldsymbol{M}$ alignment and magnetic domain wall movements degrade the dynamic sensor response. Through photolithographic processes, the relative angle between the current and the magnetization direction is varied preferably to $\pm 45°$. I.e. for the discussed case (Figure 1.1d), $\boldsymbol{M}$ at $\boldsymbol{H_{ext}} = 0$ Oe is kept along the long axis of the rectangular structure and the conducting terminals are aligned $\pm 45°$ with respect to $\boldsymbol{M}$. As a result, the linear part of the static AMR curve is shifted towards $\boldsymbol{H_{ext}} = 0$ Oe [39, 40] and in addition to the limited magnetic domain activity, the dynamic AMR response becomes non-zero at $\boldsymbol{H_{ext}} = 0$ Oe ($\boldsymbol{d(\Delta R/R_{\perp})/dH_{mea}} \neq 0$).

Furthermore, different interlayer exchange coupling mechanisms between ferromagnetic/ ferromagnetic, ferromagnetic/ antiferromagnetic materials are utilized to suppress the magnetic domain activity [41, 42]. One such example is shown in Figure 1.1e. Exchange bias stems from the interfacial coupling between a ferromagnetic

and an antiferromagnetic material in direct contact (also see Section 2.1.3.4). For high enough effective magnetic anisotropy, the ferromagnetic material stays in single domain state.

All the aforementioned biasing schemes have been successfully applied to limit magnetic domain activity in a soft magnetic film. Consequently, a linearized sensor response has been obtained.

2 Fundamentals

This chapter introduces basics on magnetic domain formation, magnetoelectric effect and later investigated ME sensors.

2.1 Energy terms influencing magnetic domain formation

In this section, various energy parameters influencing magnetic domain formation in magnetic materials are introduced. With energy densities for exchange $\boldsymbol{e_{ex}}$, external magnetic field $\boldsymbol{e_{ext}}$, magnetic anisotropy $\boldsymbol{e_K}$ and magnetostatic field (stray field) $\boldsymbol{e_{ms}}$, the total magnetic energy density $\boldsymbol{e_{total}}$ can be defined. By forming magnetic domains, a magnetic material minimizes its $\boldsymbol{e_{total}}$ (2.1) [43–46].

$$e_{total} = e_{ex} + e_{ext} + e_K + e_{ms} \tag{2.1}$$

The driving force for magnetic domain formation is $\boldsymbol{e_{ms}}$. The parameters covered in the sections below, directly determine the occurring magnetic domain configurations and thus the magnetization distribution inside magnetic materials. From the magnetic domain density and shape to the developing magnetic domain wall types, a material's magnetic permeability $\boldsymbol{\mu}$ and susceptibility $\boldsymbol{\chi}$ are influenced. A magnetic material's quality factor $\mathbf{Q}$ is accepted as one of the figure of merits, characterizing the magnetic softness of a material. $\mathbf{Q}$ is the ratio of the effective magnetic anisotropy $\mathbf{K_{eff}}$ (Section 2.1.3) to the maximum magnetostatic energy density $\mathbf{K_d}$ (Section 2.1.3.5) (2.2). For $\mathbf{Q} < 1$ and $\mathbf{Q} > 1$, soft and hard magnetic materials are obtained, respectively.

$$Q = \frac{K_{\mathrm{eff}}}{K_{\mathrm{d}}} \tag{2.2}$$

Intrinsic and extrinsic parameters effecting magnetic properties can be shortly listed as:

- Crystallinity
- Temperature (T)
- Stress (σ)
- Magnetic field and history (H_{ext})
- Layering
- Patterning
- Magnetic anisotropy (K)
- Stray field (K_d)

2.1.1 Exchange energy

Exchange interaction is an isotropic effect, which originates from spin-spin interaction and defines the relative spin alignment inside a magnetic material, where parallel orientation of the spins is a requirement for ferromagnetism. Accordingly, a ferromagnetic material is spontaneously magnetized. This interaction is not only important for an individual ferromagnet but also very relevant for layered films coupled by exchange interactions. The strength and type of the spin-spin interaction is represented by the exchange integral $\mathbf{J_{ex}}$. The exchange energy $\boldsymbol{E_{ex}}$ can be expressed as in (2.3).

$$E_{ex} = -2J_{ex}\boldsymbol{S_1} \cdot \boldsymbol{S_2} = -2J_{ex}S^2 \cos\phi \tag{2.3}$$

$\boldsymbol{S_1}$ and $\boldsymbol{S_2}$ represent the spins in the neighboring atoms of interest and ϕ is the relative angle between them. Possessing parallel and anti-parallel spin alignment results in an energy minimum for ferromagnetic ($\mathbf{J_{ex}} > 0$, solid line in Figure 2.1) and antiferromagnetic materials ($\mathbf{J_{ex}} < 0$, dashed line in Figure 2.1), respectively.

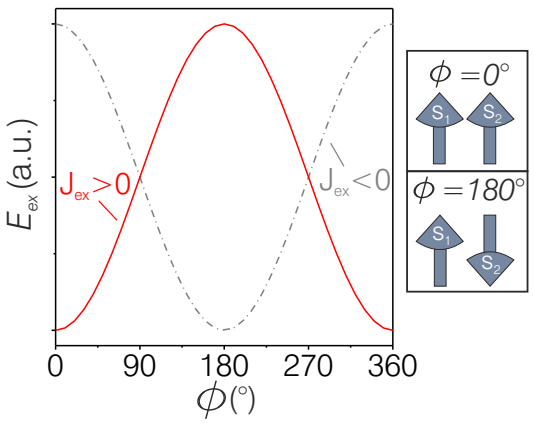

Figure 2.1: Exchange energy E_{ex} in arbitrary units is plotted against the relative angle between two coupled spins with exchange integrals $\mathbf{J_{ex}} > 0$ and $\mathbf{J_{ex}} < 0$. The energetically favorable spin alignment in a material is determined by the energy minima. Exemplary spin alignments are sketched for $\phi = 0°$ and 180°.

The Bethe-Slater curve is the figure of merit for various elements in the periodic table, displaying $\boldsymbol{J_{ex}}$ vs. $\boldsymbol{r_a/r_{3d}}$, where $\boldsymbol{r_a}$ and $\boldsymbol{r_{3d}}$ are defined as the atomic radius and 3d shell radius (e.g. Fe, Co and Ni possess $\mathbf{J_{ext}} > 0$, whereas Mn and Cr are elements with $\mathbf{J_{ex}} < 0$). $\mathbf{J_{ex}}$ is temperature dependent. Only few elements

in the periodic table are ferromagnetic at room temperature. The exchange forces decrease with increasing temperature and vanish over a critical temperature. As a result, a ferromagnetic material becomes paramagnetic and loses its spontaneous magnetization. For ferromagnetic materials, this temperature is defined as the Curie temperature $\mathbf{T_C}$ and for antiferromagnetic materials is named as the Néel temperature $\mathbf{T_N}$.

2.1.2 External magnetic field energy

The external magnetic field (Zeeman) energy describes the magnetization $\boldsymbol{M}$ response of a material under external magnetic field $\boldsymbol{H_{ext}}$. With $\boldsymbol{\gamma}$ the angle between $\boldsymbol{M}$ and $\boldsymbol{H_{ext}}$, the external magnetic field energy density $\boldsymbol{e_{ext}}$ is given in equation (2.4).

$$e_{ext} = -\mu_0 \boldsymbol{H_{ext}} \cdot \boldsymbol{M} = -\mu_0 H_{ext} M \cos\gamma \tag{2.4}$$

2.1.3 Magnetic anisotropy energy

There are various types of magnetic anisotropies with different origins. A magnetic specimen can simultaneously possess more than one type of magnetic anisotropy. Without any external magnetic field present, the spontaneous magnetization is aligned along the effective magnetic anisotropy axis $\boldsymbol{K_{eff}}$ (or direction), which is defined as the easy axis (or direction). As a result, in order to align the magnetization perpendicular (or antiparallel) to it, the magnetic anisotropy energy has to be overcome.

2.1.3.1 Magnetocrystalline anisotropy

For crystalline magnetic materials, the magnetic anisotropy axis (or axes) are dependent on the crystal structure. The electron orbits are effectively quenched in a crystal lattice due to strong lattice-orbit coupling. The spins and orbits are also coupled, however, much weakly. Therefore, when an external magnetic field is applied, the spins can align themselves along the field and the magnetization changes. Depending on the crystal structure, for the magnetization vector(s), a certain crystal axis (or axes) is energetically favorable. In the case of crystalline magnetic materials with cubic crystal symmetry, the energy density $\boldsymbol{e_{cubic}}$ is defined by (2.5), where $\mathbf{K_0}$, $\mathbf{K_1}$ and $\mathbf{K_2}$ are temperature dependent anisotropy constants and $\boldsymbol{m_1}$, $\boldsymbol{m_2}$ and $\boldsymbol{m_3}$ are direction cosines of magnetization [44].

$$e_{cubic} = \mathrm{K}_0 + \mathrm{K}_1(\boldsymbol{m}_1^2\boldsymbol{m}_2^2 + \boldsymbol{m}_1^2\boldsymbol{m}_3^2 + \boldsymbol{m}_2^2\boldsymbol{m}_3^2) + \mathrm{K}_2(\boldsymbol{m}_1^2\boldsymbol{m}_2^2\boldsymbol{m}_3^2) \tag{2.5}$$

The anisotropy constants are dependent on the crystal structure. As a conse-

quence, i.e. for bcc-Fe and fcc-Ni, the easy axes lies along <100> and <111> crystallographic directions, respectively. For hexagonal and tetragonal crystals, the crystal anisotropy is uniaxial. I.e. for Co the easy axis is aligned along the c-axis of its hexagonal crystal structure. With $\boldsymbol{\theta_u}$ as the angle between magnetization and the anisotropy axis, the energy density of a crystal with uniaxial anisotropy can be expressed by (2.6).

$$e_u = \mathrm{K}_0 + \mathrm{K}_1 \sin^2 \theta_u + \mathrm{K}_2 \sin^4 \theta_u + ... \tag{2.6}$$

2.1.3.2 Magnetization induced anisotropy

Crystal structure is not a prerequisite for magnetic anisotropy. Short range spin ordering can be obtained in amorphous and polycrystalline magnetic materials. The attained magnetic anisotropy $\mathbf{K_u}$ is uniaxial. A well-defined $\mathbf{K_u}$ can be aligned during material deposition or by heating the magnetic film up to a temperature $\mathbf{T}$, where atomic diffusion can take place, resulting in next ion pair ordering inside the magnetic material. Spontaneous magnetization is a requirement ($\mathbf{T}<\mathbf{T_C}$). An external magnetic field is applied, which saturates the magnetic material. The direction of the applied magnetic field defines the $\mathbf{K_u}$ axis.

Similar to (2.6), the uniaxial magnetic anisotropy energy density $\boldsymbol{e_{uni}}$ is expressed by (2.7), where higher order terms can be omitted. $\boldsymbol{\theta_u}$ is the angle between the magnetization direction and $\mathbf{K_u}$ axis.

$$e_{uni} = \mathrm{K}_0 + \mathrm{K}_\mathrm{u} \sin^2 \theta_u \tag{2.7}$$

$\boldsymbol{e_{uni}}$ possesses two energy minimums (at 0° and 180° in Figure 2.2), both collinear magnetization states lying along the magnetic anisotropy axis are equal in energy and favorable without application of an external magnetic field $\boldsymbol{H_{ext}}$ (compare sketches and the plot in Figure 2.2).

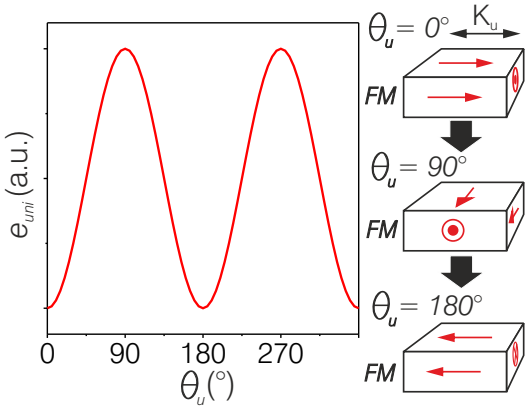

Figure 2.2: For a material with $\mathbf{K_u} > 0$, its energy density $\mathbf{e_{uni}}$ in arbitrary units is plotted against the relative angle $\boldsymbol{\theta_u}$ between the magnetization $\boldsymbol{M}$ and $\mathbf{K_u}$ axis. Possible magnetization alignments relative to $\mathbf{K_u}$ axis are sketched.

$\mathbf{K_u}$ is the energy density that is required to be overcome in order to rotate the

magnetization by 90° and can be calculated with $\mathbf{M_s}$ as the saturation magnetization and $\mathbf{H_k}$ the magnetic anisotropy field strength (2.8).

$$K_u = \frac{1}{2} M_s H_k \tag{2.8}$$

As an example, the inductively measured magnetization $\boldsymbol{M}$ response to $\boldsymbol{H_{ext}}$ for an amorphous $Co_{40}Fe_{40}B_{20}$ film possessing magnetization induced magnetic anisotropy is displayed in Figure 2.3. Important points during the magnetic reversal process are marked and possible magnetization states are sketched.

In Figure 2.3a, $\boldsymbol{H_{ext}}$ is applied along $\mathbf{K_u}$, which depicts the easy axis magnetization loop. Decreasing $\boldsymbol{H_{ext}}$ from positive saturation $\mathbf{+H_{sat}}$, at $\mathbf{H_{ext}} = 0$ Oe the remanent magnetization state $\mathbf{M_R}$ is reached. Increasing $\boldsymbol{H_{ext}}$ in minus direction, a sudden magnetization change occurs. At $\mathbf{H_{c,\ left}}$ (and also $\mathbf{H_{c,\ right}}$), the magnetic material is effectively in the demagnetized state. The net magnetization is zero. Further $\boldsymbol{H_{ext}}$ increase in $\mathbf{-}\boldsymbol{H_{ext}}$ direction leads to magnetic saturation $\mathbf{-H_{sat}}$. Along easy axis, magnetic domain wall movement is the dominant magnetization reversal process.

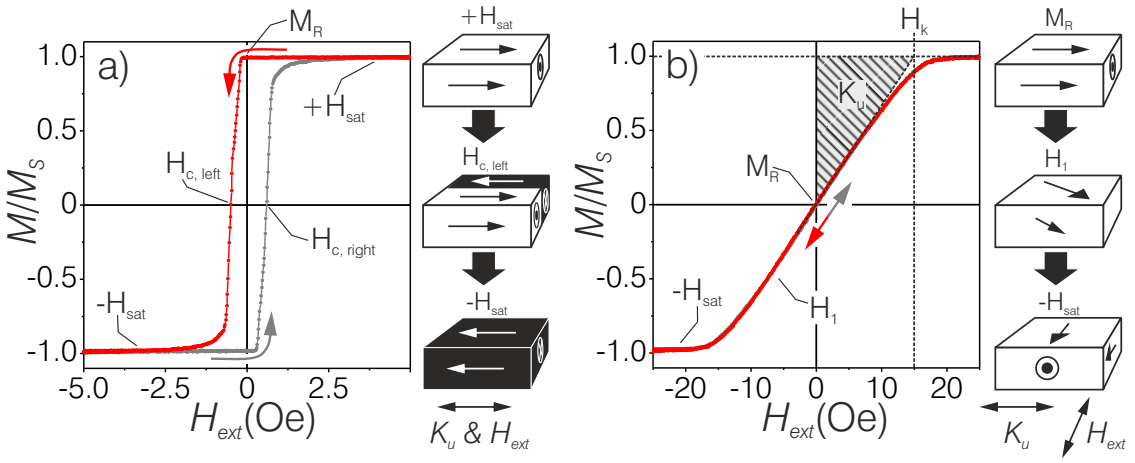

Figure 2.3: Inductively measured magnetization loop along (a) and perpendicular (b) to K_u are displayed. Possible magnetization states during magnetization reversal are sketched to the right of every curve. The shaded area depicts the K_u that is required to be overcome to align the magnetization perpendicular to K_u (as measured). (in plane dimensions: 1 cm x 2 cm) (Sample: [Si/ SiO_2] 300 μm/ Ta 3 nm/ CoFeB 160 nm/ TaN 5 nm)

Figure 2.3b displays the hard axis magnetization loop for the same sample. $\boldsymbol{H_{ext}}$ is applied perpendicular to the $\mathbf{K_u}$ axis. Unlike the easy axis loop (Figure 2.3a), the hard axis loop exhibits a linear $\boldsymbol{M}$ change with $\boldsymbol{H_{ext}}$. $\boldsymbol{M}$ rotates away from the $\mathbf{K_u}$ axis as $\boldsymbol{H_{ext}}$ is increased (see sketch in Figure 2.3b). This reversal process is called the coherent rotation of magnetization. Further increment of $\boldsymbol{H_{ext}}$ leads to $\mathbf{H_{sat}}$ along $\boldsymbol{H_{ext}}$ direction. It is the point, where $\mathbf{K_u}$ is effectively compensated by $\boldsymbol{H_{ext}}$ ($\boldsymbol{H_{ext}} = \mathbf{H_k}$).

2.1.3.3 Stress induced anisotropy

Magnetostriction $\boldsymbol{\lambda}$ is a material property inherent to all magnetic materials. Originating from spin-orbit coupling in magnetic materials [47], the effect leads to magnetization induced changes in a magnetic material's dimensions and is characterized by the investigated material's saturation magnetostriction constant $\boldsymbol{\lambda_s}$, which defines the extent of material response to variations in magnetization direction $\boldsymbol{m}$, as well as to internal and external stresses $\boldsymbol{\sigma}$ [44]. The minimization of magnetoelastic energy is the driving force for the resulting response.

Generally, treating stress induced magnetic effects is rather demanding for crystalline materials. $\boldsymbol{\lambda}$ is a function of the crystallographic directions, i.e. $\boldsymbol{\lambda_{100}}$ and $\boldsymbol{\lambda_{111}}$ defined along [100] and [111], respectively [44, 47, 48]. However, an isotropic, invariant material parameter $\boldsymbol{\lambda}_\mathrm{s}$ can be defined for amorphous and polycrystalline films. In this case, the effect becomes relatively simpler to handle. Only one $\boldsymbol{\lambda_s}$ value is sufficient to define the strain response along any measurement direction. $\boldsymbol{\lambda_s}$ can be positive or negative in sign and is both composition and temperature dependent. However, even at constant temperature it is a function of stress state $\boldsymbol{\sigma}$ (2.9) [49, 50].

$$\lambda_s(\sigma) = \lambda_s(0) + \frac{d\lambda_s}{d\sigma}\sigma \tag{2.9}$$

The deviation from $\boldsymbol{\lambda_s}(0)$ is generally quite low, but is very relevant for near zero $\boldsymbol{\lambda_s}$ films under high film stress. E.g. for amorphous $(\mathrm{CoMnFeMo})_{76}(\mathrm{SiB})_{24}$ films with $\boldsymbol{\lambda_s}(0) = +5.5{\cdot}10^{-8}$ and $\mathrm{d}\boldsymbol{\lambda}_\mathrm{s}/\mathrm{d}\boldsymbol{\sigma} = -3.4{\cdot}10^{-10}$ MPa^{-1}, a flip in $\boldsymbol{\lambda_s}$ sign occurs at 260 MPa [50].

Due to magnetostriction, a magnetic material undergoes a change in its dimensions depending on $\boldsymbol{m}$ and $\boldsymbol{\lambda_s}$. The resulting length change can be expressed phenomenologically as (2.10), where $\boldsymbol{l_f}$ and $\boldsymbol{l_i}$ are the respective final and initial lengths along a measurement direction $\boldsymbol{a}$, $\mathbf{l_{max}}$ is the maximum length change and $\boldsymbol{\theta}$ is the relative angle between $\boldsymbol{m}$ and $\boldsymbol{a}$.

$$l_f = l_i \pm l_{max}(\boldsymbol{m}\cdot\boldsymbol{a})^2 = l_i \pm l_{max}\cos^2\theta \tag{2.10}$$

Here, $\boldsymbol{l_i}$ is measured along $\boldsymbol{a}$ with $\boldsymbol{m}$ pointing perpendicular to it ($\boldsymbol{l_i}$, when $\boldsymbol{m}\perp\boldsymbol{a}$). Moreover, having + or − signs in the equation depends on the sign of $\boldsymbol{\lambda_s}$ (+ for positive $\boldsymbol{\lambda_s}$ materials and vice versa). $\mathbf{l_{max}}$ scales with $\boldsymbol{\lambda_s}$ but they are not equal in magnitude.

Furthermore, apparent from (2.10), the change in length is quadratic in $\boldsymbol{m}$, which means $\boldsymbol{l_f}$ is the same for collinear $\boldsymbol{m}$ directions and the maximum length changes occur in perpendicular $\boldsymbol{m}$ variations.

With $\boldsymbol{\Delta l}= \boldsymbol{l_f}-\boldsymbol{l_i}$, $\boldsymbol{\lambda}$ is expressed as (2.11).

$$\lambda = \frac{\Delta l}{l_i} = \frac{3}{2}\lambda_\mathrm{s}\left((\boldsymbol{m}\cdot\boldsymbol{a})^2 - \frac{1}{3}\right) = \frac{3}{2}\lambda_\mathrm{s}\left(\cos^2\theta - \frac{1}{3}\right) \tag{2.11}$$

Along $\boldsymbol{m}$, the material contracts for $\boldsymbol{\lambda_\mathrm{s}} < 0$ or expands for $\boldsymbol{\lambda_\mathrm{s}} > 0$. Furthermore, $\boldsymbol{\lambda}$ is quadratic in $\boldsymbol{m}$ ($\boldsymbol{\lambda} \propto \boldsymbol{m^2}$). The resulting $\boldsymbol{\lambda}$ is identical for antiparallelly aligned $\boldsymbol{m}$ and the maximum $\boldsymbol{\lambda}$ response is obtained for orthogonal magnetization directions.

As $\boldsymbol{m}$ alignment changes the dimensions of a magnetic material, application of $\boldsymbol{\sigma}$ introduces stress induced magnetic anisotropy $\boldsymbol{K_\sigma}$ to the magnetic material, the magnitude and alignment of which is dictated by $\boldsymbol{\lambda_\mathrm{s}}$ and the effective stress state $\boldsymbol{\sigma_e}$. As a result $\boldsymbol{m}$ can be realigned. The induced $\boldsymbol{K_\sigma}$ is expressed in (2.12).

$$K_\sigma = \frac{3}{2}\lambda_\mathrm{s}\sigma_\mathrm{e} \tag{2.12}$$

The induced $\boldsymbol{K_\sigma}$ is uniaxial and with $\boldsymbol{\theta_\sigma}$ as the angle between $\boldsymbol{m}$ and $\boldsymbol{K_\sigma}$, the energy density $\boldsymbol{e_\sigma}$ can be written as (2.13).

$$e_\sigma = K_\sigma \sin^2\theta_\sigma \tag{2.13}$$

Moreover, for a uniformly magnetized film that is linearly elastic and isotropic, the $\boldsymbol{m}$ independent, total internal energy density $\boldsymbol{e_{tot}}$ along with elastic $\boldsymbol{e_{el}}$ and magnetoelastic $\boldsymbol{e_{ma}}$ contributions can be expressed as (2.14), where $\mathbf{E}$ is the Young's modulus and $\boldsymbol{\nu}$ the Poisson's ratio ($\boldsymbol{e_{tot}}=\boldsymbol{e_{el}}+\boldsymbol{e_{ma}}$) [48].

$$e_{el} = \frac{3}{4}\frac{\lambda_s^2 E}{(1+\nu)}, \quad e_{ma} = -\frac{3}{2}\frac{\lambda_s^2 E}{(1+\nu)}, \quad e_{tot} = -\frac{3}{4}\frac{\lambda_s^2 E}{(1+\nu)} \tag{2.14}$$

Equation (2.14) expresses a spatially invariant energy density that becomes crucial in magnetic materials with low $\mathbf{K_{eff}}$ and as a result the magnetoelastic effects dictate the magnetic domain formation [51].

2.1.3.4 Unidirectional anisotropy

The unidirectional magnetic anisotropy in a ferromagnetic material (FM) originates from the exchange coupling at an interface to another FM or an antiferromagnetic material (AFM) and is characterized by a loop shift in the biased film's magnetization curves measured along the established unidirectional magnetic anisotropy axis. An indirect coupling between two separate FM layers can be obtained through a non-magnetic (NM) spacer, e.g. Cr or Ru [11,12]. The coupling strength and sign depends on the NM layer thickness and can be explained by the *Ruderman-Kittel-Kasuya-Yosida* (RKKY) model [46]. Moreover, exchange-spring magnets consisting of a hard FM in direct contact with a soft FM layer result in a unidirectional

magnetic anisotropy in the soft FM through direct exchange coupling between the layers [52].

Here, the emphasis is given on the exchange bias effect, which is the result of a strong exchange coupling at the interface between a FM in direct contact with an AFM [53–57]. A homogeneous, well defined exchange bias direction can be obtained by depositing an AFM on a magnetically saturated FM [58, 59] or the already deposited layered structure can, later, be heated and cooled down with the FM in a magnetically saturated state (field cooling process) [56,60]. For both cases, magnetization is required in the FM ($\mathbf{T} < \mathbf{T_c}$). Traditionally, an external magnetic field $\boldsymbol{H_{set}}$ is applied to saturate the FM. The introduction of the exchange bias is a magnetization induced process.

Additionally, to set the exchange bias, the AFM needs to retain its antiferromagnetic properties ($\mathbf{J_{ex}^{AFM}} < 0$). Therefore, the exchange coupling at the AFM/ FM interface is initialized under $\mathbf{T_N}$ [54, 55, 57]. The setting of the exchange bias direction is preferably performed above the AFM's blocking temperature $\mathbf{T_B}$. In this temperature range ($\mathbf{T_B} < \mathbf{T} < \mathbf{T_N}$), the thermal energy stored in the AFM $\mathbf{E_T^{AFM}}$ is higher than its magnetocrystalline anisotropy energy $\mathbf{E_K^{AFM}}$ in volume $\mathbf{V}$. With $\mathbf{k}$ as the Boltzmann constant, $\mathbf{M_s^{AFM}}$ and $\mathbf{H_k^{AFM}}$ as the saturation magnetization and the magnetocrystalline anisotropy field in AFM, respectively, the relationship between $\mathbf{E_T^{AFM}}$ and $\mathbf{E_K^{AFM}}$ at $\mathbf{T_B}$ can be crudely approximated as (2.15).

$$\underbrace{\frac{3}{2}\mathrm{k}\mathrm{T}_\mathrm{B}}_{\mathbf{E_T^{AFM}}} > \underbrace{\frac{1}{2}\mathrm{M}_\mathrm{s}^\mathrm{AFM}\mathrm{H}_\mathrm{k}^\mathrm{AFM}\mathrm{V}}_{\mathbf{E_K^{AFM}}} \tag{2.15}$$

Therefore, the AFM spins at the AFM/ FM interface can, in principle, freely align themselves with FM spins (at $\mathbf{T_B}$, there is yet no loop shift in the magnetization curve) [56, 57]. The characteristic loop shift occurs as the essential exchange bias layer structure is cooled down under the $\mathbf{T_B}$ [57]. For strong enough AFM magnetocrystalline anisotropy, the AFM spin sublattices are frozen along the FM magnetization direction during cooling process and due to the established exchange coupling at the AFM/ FM interface, the FM magnetization is now pinned along $\boldsymbol{H_{set}}$ and the magnetization loops measured along the exchange bias direction exhibit a loop shift along $-\boldsymbol{H_{ext}}$, which is also defined as negative exchange bias. However, positive exchange bias has been reported to be obtainable for some bilayer systems like FeF_2/ Fe depending on deposition conditions [61].

An uncompensated AFM spin alignment at the AFM/FM interface is a requirement to obtain the desired loop shift. As a rule of thumb, the parameters that contribute to unidirectional magnetic anisotropy energy are the applied field $\boldsymbol{H_{set}}$, AFM's magnetocrystalline anisotropy strength and the coupling constant at the

AFM/ FM interface $\mathbf{J_{eb}}$ [36,45,54]. However, this model alone can not fully explain the effect, extended models such as formation of magnetic domain walls inside the AFM at the AFM/ FM interface [62], interface roughness [63] and grain size and boundaries [64,65] are also known to effect the resulting loop shift.

On the other hand, when exchange biasing amorphous FM layers, possible crystallization processes such as filament formation can occur at elevated temperatures [66], which might degrade the FM layer's soft magnetic properties. Furthermore, oxidation in the FM layer can lead to additional unintentional exchange bias contributions [67].

For better illustration of the resulting magnetization response, easy and hard axis loops of an exchange biased amorphous $Co_{40}Fe_{40}B_{20}$ (CoFeB) layer is displayed in Figure 2.4. A thin $Ni_{81}Fe_{19}$ film is used to establish the exchange bias during material deposition. Note that the CoFeB also possesses magnetization induced uniaxial magnetic anisotropy $\mathbf{K_u}$ ($\mathbf{K_u} \| \mathbf{K_{eb}}$).

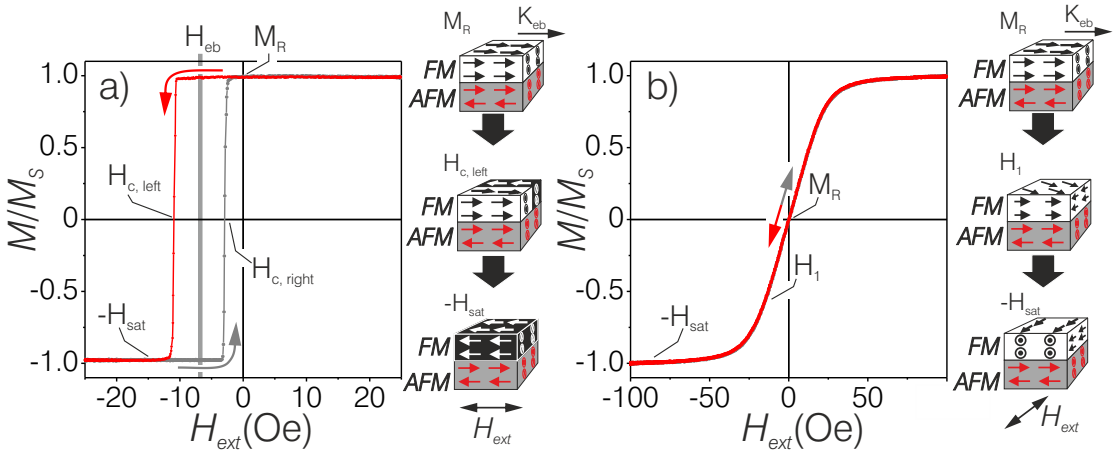

Figure 2.4: Magnetization loops of an exchange biased CoFeB layer measured inductively parallel (a) and perpendicular (b) to the unidirectional magnetic anisotropy. To the right of each curve, possible magnetization states during magnetization reversal are sketched. (in plane dimensions: 1 cm x 2 cm) (Sample: [Si/ SiO_2] 300 μm/ Ta 3 nm/ NiFe 2.5 nm/ IrMn 7 nm/ CoFeB 80 nm/ TaN 5 nm)

Traditionally, the loop shift is expressed as the exchange bias field $\boldsymbol{H_{eb}}$ and is calculated as the mean average of left and right coercive field strengths, $\boldsymbol{H_{c,\,left}}$ and $\boldsymbol{H_{c,\,right}}$, respectively (Figure 2.4a). $\boldsymbol{H_{eb}}$ is the unidirectional magnetic anisotropy field strength inside the FM that causes the loops shift. The obtained $\boldsymbol{H_{eb}}$ is indirectly proportional to the FM thickness $\mathbf{t_{FM}}$ ($\boldsymbol{H_{eb}} \sim \frac{1}{t_{FM}}$). With $\boldsymbol{J_{eb}}$ as the coupling constant at the AFM/ FM interface and the saturation magnetization $\mathbf{M_s}$ of the FM, $\boldsymbol{H_{eb}}$ can be approximated as (2.16).

$$H_{eb} = -\frac{\mathrm{J_{eb}}}{\mu_0 \cdot \mathrm{M_s} \cdot t_{FM}} = -\frac{\mathrm{K_{eb}}}{\mu_0 \cdot \mathrm{M_s}} \tag{2.16}$$

The magnetization curves measured perpendicular to the exchange bias direction approaches asymptotically to magnetic saturation (Figure 2.4b).

The ratio of $\mathbf{J_{eb}}$ to $\mathbf{t_{FM}}$ expresses the induced exchange bias anisotropy $\mathbf{K_{eb}}$ inside the FM and phenomenologically the exchange bias anisotropy energy density $\boldsymbol{e_{eb}}$ can be expressed as (2.17) [44]. $\boldsymbol{\theta_{eb}}$ is the relative angle between the magnetization direction and $\mathbf{K_{eb}}$ direction.

$$e_{\mathrm{eb}} = -\mathrm{K_{eb}} \cos \theta_{eb} \tag{2.17}$$

As a result, without any external magnetic field present only one magnetization direction is energetically favorable, which lies along the exchange bias direction (Figure 2.5).

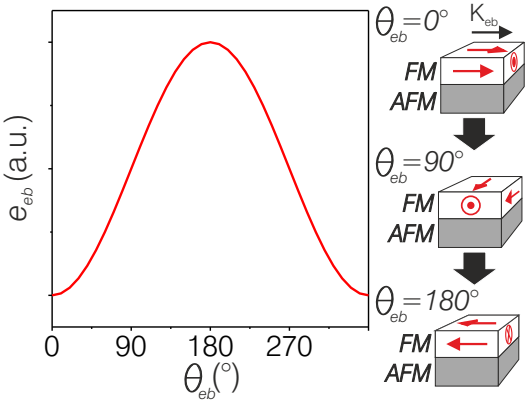

Figure 2.5: Exchange bias energy density $\boldsymbol{e_{eb}}$ in arbitrary units is plotted against the relative angle between the magnetization $\boldsymbol{M}$ and unidirectional anisotropy $\boldsymbol{K_{eb}}$ direction. Relative magnetization alignments are sketched.

2.1.3.5 Shape anisotropy

The shape anisotropy is an induced magnetic anisotropy term and is a consequence of magnetostatic interactions in a magnetic material. Based on the Maxwell's equations, for a closed surface the magnetic flux $\boldsymbol{B}$ diverges to zero ($\mathrm{div}\boldsymbol{B} = 0$). Consequently, $\boldsymbol{B}$-field always forms closed loops and magnetic poles appear in pairs of opposite polarity. As a result, $\boldsymbol{H}$-field both outside (stray field $\boldsymbol{H_s}$) and inside (demagnetizing field $\boldsymbol{H_d}$) the magnetic material are generated [44].

$\boldsymbol{H_s}$ and $\boldsymbol{H_d}$ are practically the same since they originate from magnetostatic interactions between magnetic poles and therefore possess equivalent energies E_{ms} (2.18).

$$E_{ms} = \frac{1}{2}\mu_0 \int\limits_{all\ space} \boldsymbol{H}_s^2 dV = -\frac{1}{2}\mu_0 \int\limits_{sample} \boldsymbol{H}_d \boldsymbol{M} dV \tag{2.18}$$

Due to structure shape, $\boldsymbol{H_d}$ differs from one axis to another, unless the shape is a sphere. $\boldsymbol{H_d}$ scales with $\mathbf{M_s}$ and the direction, along which the magnetization vector is aligned. The directional scaling factor is the demagnetizing factor $\widetilde{\boldsymbol{N}}_{\boldsymbol{i}}$, which is a

symmetrical tensor. $\boldsymbol{N_i}$ varies with the aspect ratio of the magnetic structure. The sum of demagnetizing factors in cartesian coordinates, $\mathbf{N_x}$, $\mathbf{N_y}$ and $\mathbf{N_z}$ equals to unity.

For all shapes with corners, $\boldsymbol{N_i}$ varies locally and is a function of position in the material. It is not homogeneous in any directions. $\boldsymbol{H_d}$ from the inside of the material "leaks" out of the structure due to it's geometry [1, 46]. $\boldsymbol{H_d}$= +∞ at the corners and decreases towards the middle [68–70] (for calculation of demagnetizing factors for a rectangular prism see Appendix). In order obtain a homogeneous $\boldsymbol{H_d}$ along one axis, the sides of the rectangle is curved towards the inside until every corner is eliminated. The resulting shape is an ellipsoid. When magnetized along one of its principle axes, $\boldsymbol{H_d}$ is homogeneous inside an ellipsoid. $\boldsymbol{H_d}$ along one of the principle axes of a magnetic material in ellipsoid shape can be written as (2.19).

$$H_d^i = -N_i \mathrm{M_s} \tag{2.19}$$

Only for a sphere (aspect ratio 1), $\mathbf{N_i}$ and the resulting $\boldsymbol{H_d}$ is identical in all space ($\mathbf{N_x}$=$\mathbf{N_y}$=$\mathbf{N_z}$=1/3 and $\boldsymbol{H_d^x}$=$\boldsymbol{H_d^y}$=$\boldsymbol{H_d^z}$= -1/3 $\mathrm{M_s}$).

One of the most important magnetic material parameters is $\mathbf{K_d}$, which is a shape invariant property. $\mathbf{K_d}$ is defined as the maximum stray field energy density in a magnetic material. For any extended magnetic film that is magnetized along the thickness of the film $\mathbf{t}$, $\mathbf{N_t}$=1 and $\mathbf{K_d}$ becomes (2.20).

$$\mathrm{K_d} = \frac{1}{2}\mu_0 N_t \mathrm{M_s^2} = \frac{1}{2}\mu_0 \mathrm{M_s^2} \tag{2.20}$$

The magnetostatic energy inside a magnetic material varies axially, resulting in an energy density dictated by the magnetic material's shape. For a magnetic material in spheroid shape with demagnetizing factors $\mathbf{N_a}$ and $\mathbf{N_c}$ along it's principle axes and $\boldsymbol{\theta_s}$ as the angle between the magnetization vector $\boldsymbol{M}$ and shape anisotropy axis with anisotropy coefficient $\mathbf{K_s}$, the shape anisotropy energy density $\boldsymbol{e_s}$ is calculated by (2.21).

$$e_s = \underbrace{\overbrace{\frac{1}{2}\mu_0 M^2}^{\mathbf{K_d}}\,\mathrm{N_a}}_{\mathbf{K_0}} + \underbrace{\overbrace{\frac{1}{2}\mu_0 M^2}^{\mathbf{K_d}}\,(\mathrm{N_c}\text{-}\mathrm{N_a})}_{\mathbf{K_s}} \sin^2\theta_s \tag{2.21}$$

2.2 Magnetic domain walls

Since the prediction of existence of domain walls in magnetic materials [71], a vast amount of research has been conducted to uncover their mysterious nature both experimentally [72–74] and most importantly theoretically [44, 75–78], since most of

the imaging techniques are insensitive to the inner wall structures. Magnetic domain walls are extremely important for many device applications [79,80] and are a mirror reflecting the magnetic properties [44]. Magnetic domain walls form, when the film is in a multi-domain state and they separate domains with different magnetization directions. Since an abrupt reversal of magnetization from one domain to another is energetically unfavorable (Figure 2.1) in order to reduce the exchange energy density $\boldsymbol{e_{ex}}$, a continuous change of magnetization takes place inside a domain wall separating two magnetic domains [43].

In this section, magnetic domain walls encountered in ferromagnetic thin films are discussed. Emphasis is given on domain wall formation in soft magnetic ($\mathbf{Q}\ll 1$) films. There are several possible types of domain walls that can be encountered in a soft magnetic thin film. Commonly, domain walls are subdivided into two general types depending on whether the magnetization inside the wall rotates in or out of the wall plane, namely Bloch and Néel walls, respectively. Domain wall energy and width are dependent on material's exchange stiffness constant $\mathbf{A}$ and the effective magnetic anisotropy energy density $\mathbf{K_{eff}}$ inside the material [44, 81]. The magnetic energy stored in a Bloch wall can be expressed as (2.22).

$$e_{wall} \propto \sqrt{A\, K_{eff}} \tag{2.22}$$

Width of a Bloch wall is proportional to the square root of $\mathbf{A}$ to $\mathbf{K_{eff}}$ ratio. The exchange interactions widens the wall, where as magnetic anisotropy shrinks it (2.23).

$$l_{wall} \propto \sqrt{\frac{A}{K_{eff}}} \tag{2.23}$$

The domain wall type is not fixed for a particular material. The observed domain wall type varies with ferromagnetic layer thickness. Minimization of the stray field energy is the driving force for a charge free magnetization change from one domain to another. Furthermore, the domain wall type is also a function of the wall angle separating the domains. E.g. 90° closure domains at $\boldsymbol{H_{ext}} = 0$ Oe or application of $\boldsymbol{H_{ext}}$ perpendicular to a 180° wall leads to a transformation in the domain wall structure.

Additionally, in ultra-thin, soft magnetic materials (e.g. for $Ni_{19}Fe_{81}$ typically $\boldsymbol{t_{film}}< 50$ nm) a third domain wall type, cross-tie walls, is defined. They are high angle domain walls and are typically observed separating antiparallelly magnetized domains. Here, we are interested in film thicknesses exceeding the cross-tie wall regime, namely Bloch and Néel walls (see phase diagram for domain walls in soft magnetic films in [44, 75, 78]).

Further classification of the wall structure is established by analyzing the magnetization symmetry along the wall plane ($\boldsymbol{m_z}$ component in Figure 2.6). Contour lines with $\boldsymbol{m_z} = 0$ illustrate the extent of wall symmetry. In symmetric Bloch, as well as Néel walls, $\boldsymbol{m_z} = 0$ is a straight line aligned perpendicular to the film plane. Symmetric Bloch walls are only observed for high film thicknesses and $\mathbf{K_{eff}} \gg \mathbf{K_s}$, whereas symmetric Néel walls are preferred at ultra-low film thicknesses and for very low wall angles.

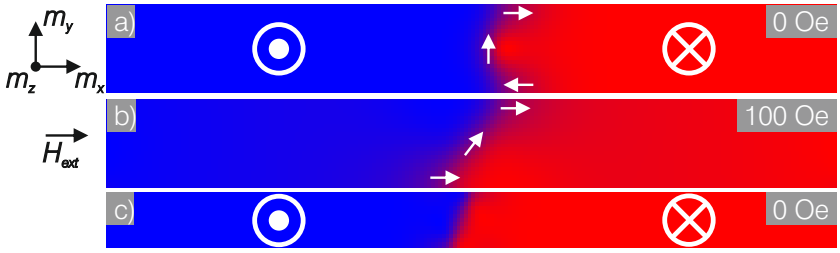

Figure 2.6: Exemplary calculated $\boldsymbol{m_z}$ magnetization components of magnetic domain wall configurations for Permalloy are shown. (a) is an asymmetric Bloch wall. (b-c) are asymmetric Néel walls with (b) and without (c) $\boldsymbol{H_{ext}}$. The simulations are performed with object oriented micromagnetic framework OOMMF [82]. The calculation parameters are $\mathbf{M_s} = 8 \cdot 10^5$ A/m, $\mathbf{K_u} = 100$ J/m^3, $\mathbf{A} = 10^{-11}$ J/m [78]. Cell size for all calculations are $5 \cdot 10^{-9}$m. The structure dimensions are 1 μm x 120 nm for (a-b) and 1 μm x 75 nm for (c).

For soft magnetic thin films, around $\boldsymbol{H_{ext}} = 0$ Oe asymmetric Bloch walls (ABW) are preferred. Due to high local $\boldsymbol{H_d}$, the symmetric $\boldsymbol{m_z} = 0$ line gets curved towards the film surface, the $\boldsymbol{m_z} = 0$ contour line possesses a **C** shape (Figure 2.6a). The magnetization at the wall edges lies in film plane. Such walls are also rather stable at relatively high domain wall angles. Application of a $\boldsymbol{H_{ext}}$ perpendicular to an ABW leads to a structural change inside the wall. As a result, asymmetric Néel walls (ANW) are formed (Figure 2.6b). The $\boldsymbol{m_z}= 0$ contour line of an ANW is **S** shaped. Such domain wall structures are also encountered in relatively small film thicknesses (Figure 2.6c). An interesting and important property of ANWs is the tails associated with them, which extend into the material possibly reaching lengths up to 100 μm [75, 76]. At short distances (high domain wall density), ANW tails interact with each other, causing drastic changes in the effective magnetic susceptibility [51].

2.3 Magnetoelectric effect

Ferroic ordering defines material properties, such as spontaneous magnetization $\boldsymbol{M}$ for ferro- and ferrimagnetic materials, spontaneous electric polarization $\boldsymbol{P}$ in ferroelectric materials and spontaneous deformation for ferroelastic materials. Some

materials embody simultaneously more than one ferroic property, making them multiferroic. Magnetoelectric (ME) effect arises from the concurrent coexistence of ferroelectricity and ferromagnetism. With application of an external magnetic field $\boldsymbol{H_{ext}}$, a change in $\boldsymbol{P}$ is observed [83]. The effect can be expressed as in (2.24). $\boldsymbol{\alpha}$ denotes the ME susceptibility tensor, which shows the extent of $\boldsymbol{P}$ response of the material to $\boldsymbol{H_{ext}}$.

$$dP = \alpha \, dH_{ext} \tag{2.24}$$

$\boldsymbol{\alpha}$ is defined in terms of ME voltage coefficient $\boldsymbol{\alpha_{ME}}$ and relative permittivity $\boldsymbol{\epsilon_r}$ of the material (2.25). $\boldsymbol{\epsilon_0}$ is the vacuum permittivity.

$$\alpha = \epsilon_r \, \epsilon_0 \, \alpha_{ME} \tag{2.25}$$

where α_{ME} is,

$$\alpha_{ME} = \frac{\partial E}{\partial H_{ext}} \tag{2.26}$$

$\boldsymbol{\alpha_{ME}}$ ($\mathrm{Vcm^{-1}Oe^{-1}}$) is a measure of $\boldsymbol{E}$-field response of the magnetoelectric material to $\boldsymbol{H_{ext}}$.

Generally, for single-phase multiferroic materials, the obtained $\boldsymbol{\alpha_{ME}}$ is quite low due to conflicting origins of ferroelectricty and ferromagnetism [84, 85]. For ferroelectricity, non-centrosymmetric crystal structure is required and the stabilization of the ferroelectric phase is dictated by repulsive short range ionic interactions, whereas at high temperatures short-range electron cloud interactions become dominant, which tend to hinder ferroelectricity. As a rule of thumb, the cations responsible for polarization in ferroelectric materials have d^0 electron configuration. However, non-occupancy of d-shells contradicts with ferromagnetism. When the d-shells get partially occupied, the short-range electron cloud interactions inside the crystal start to become predominant and the crystal distortion is eliminated. For this reason, there are few materials, which are magnetoelectric (i.e. $BiFeO_3$ [86]), and the contradicting nature of ferroelectricity and ferromagnetism doesn't allow for high ME voltage coefficients in single phase ME materials [84, 85]. However the effect, which is interesting from both physics and application point of view, can still be utilized by using composite materials, which stand at the heart of this work (Section 2.3.1).

2.3.1 Magnetoelectric effect for magnetic field sensing

Here, the working principle of the investigated 2-2 thin film composite ME sensors in cantilever design and the figure of merits of such devices are covered. In recent

years, they have gathered much attention due to their high signals, MEMS compatibility and possibility to operate at room temperature [87,88]. With different sensor concepts, AC magnetic fields $\boldsymbol{H_{mea}}$ in low pT to fT range have been demonstrated to be detectable [25, 27, 28, 60, 89]. Such magnetic field sensing devices consist of separate magnetostrictive and piezoelectric phases (Figure 2.7a) that are coupled mechanically through stress $\boldsymbol{\sigma}$. By using a composite device, individual film properties can be fine tuned almost independent of each other (i.e. selecting materials with high $\boldsymbol{\lambda}_{\mathrm{s}}$ and $\boldsymbol{\chi}$ for the magnetostrictive phase and high piezoelectric voltage coefficient ($\frac{\boldsymbol{d_{31}}}{\boldsymbol{\epsilon_{r,33}}}$) for the piezoelectric phase). Thus ME responses yet unavailable to single-phase multiferroics can be achieved. Due to the device's composite nature, the ME voltage coefficient $\boldsymbol{\alpha_{ME}}$ derived in (2.26) becomes a product property of the constituent phases (2.27) [25, 90].

$$\alpha_{ME} = \frac{\partial E}{\partial H_{mea}} = \frac{\partial E}{\partial \sigma}\frac{\partial \sigma}{\partial \lambda}\frac{\partial \lambda}{\partial H_{mea}} \tag{2.27}$$

Frequently, $\boldsymbol{\partial E/\partial \sigma}$, $\boldsymbol{\partial \sigma/\partial \lambda}$ and $\boldsymbol{\partial \lambda/\partial H_{mea}}$ are defined as the piezoelectric coefficient $\boldsymbol{e}$ of the piezoelectric phase, the coupling factor $\boldsymbol{k_c}$ between the films and piezomagnetic coefficient $\boldsymbol{e^m}$ of the magnetostrictive phase, respectively. $\boldsymbol{H_{mea}}$ induces a change in magnetostrictive phase's magnetization state and as a result the material's dimensions change by magnetostriction. $\boldsymbol{\lambda}$ is transferred through $\boldsymbol{\sigma}$ mediation to the piezoelectric phase, where an electric polarization is generated and ME voltage $\boldsymbol{U_{ME}}$ is measured. In order to obtain the sensor specific parameter $\boldsymbol{\alpha_{ME}}$, $\boldsymbol{U_{ME}}$ is divided by the amplification factor $\mathbf{G}$, if a charge amplifier is present, the piezoelectric phase thickness $\mathbf{d_{PE}}$ and $\boldsymbol{H_{mea}}$ amplitude (2.28).

$$\alpha_{ME} = \frac{U_{ME}}{G \cdot d_{PE} \cdot H_{mea}} \tag{2.28}$$

Generally, ME sensors work with simultaneous application of a DC $\boldsymbol{H_{ext}}$, which serves as a bias field and $\boldsymbol{H_{mea}}$ (Direct measurement). As a result, the sensor response is ramped to the point with maximum $\boldsymbol{\partial \lambda(H_{ext})/\partial H_{mea}}$. Such a sensor design typically works with $\boldsymbol{H_{ext}}$ applied perpendicular to $\mathbf{K_u}$, where $\boldsymbol{\lambda}$-response is the highest (Figure 2.7a).

Moreover, in cantilever design, where the sensing element is fixed at one end (Figure 2.7a), $\boldsymbol{\alpha_{ME}}$ is a function of $\boldsymbol{H_{mea}}$ frequency [23, 24]. The point, where the ME response is maximum, is the mechanical resonance frequency of the cantilever $\mathbf{f_{res}}$. $\boldsymbol{\alpha_{ME}}$ is amplified by several orders of magnitude at $\mathbf{f_{res}}$. Therefore the sensors are generally operated at $\mathbf{f_{res}}$. $\mathbf{f_{res}}$ is dependent on the dimensions of the sensing element.

Exemplary measurements demonstrating $\boldsymbol{H_{mea}}$ frequency and $\boldsymbol{H_{ext}}$ dependencies and limit of detection (LoD) of such a sensor are shown in Figure 2.7b-d. The

essential layer structure is AlN 2 μm/ (Si/SiO_2) 300 μm/ FeCoSiB 1 μm. The measurements were performed together with Volker Röbisch and Sebastian Salzer at the ME measurement setup in *microwave engineering group* in *Kiel University*.

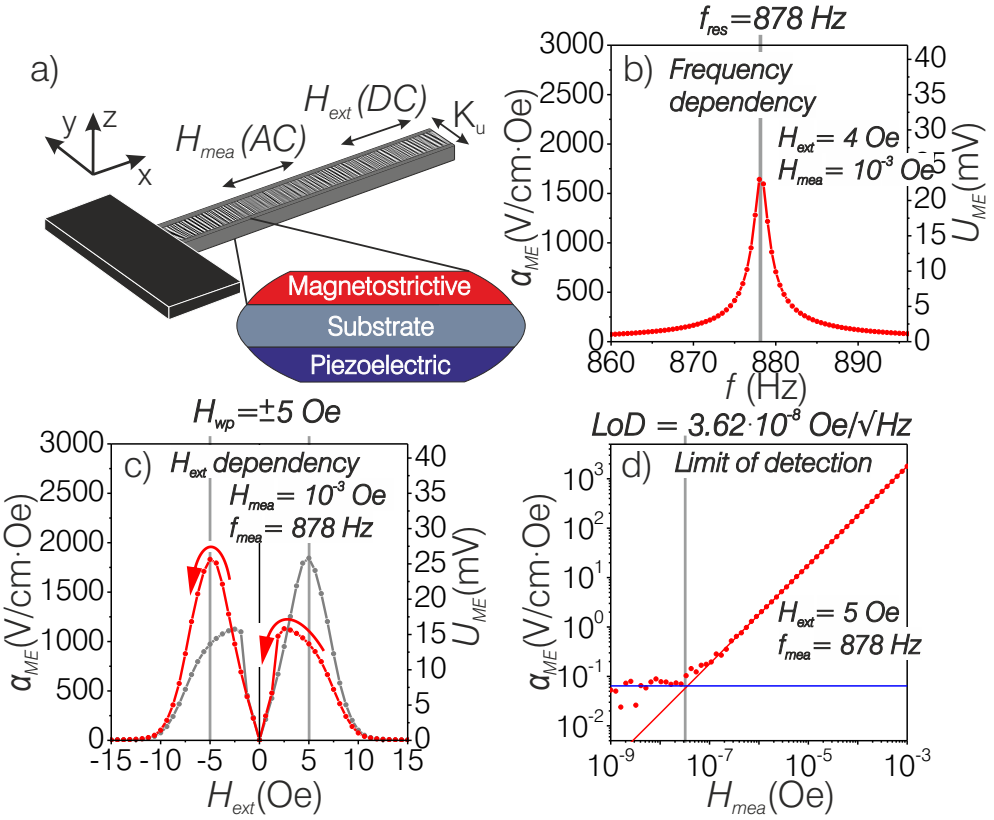

Figure 2.7: Sketch of a 2-2 composite ME sensor in cantilever design is shown in (a). Exemplary $\boldsymbol{H_{mea}}$ frequency dependency (b), $\boldsymbol{H_{ext}}$ dependency of the ME response (c) and limit of detection (d) measurements are shown. $\boldsymbol{H_{ext}}$ and $\boldsymbol{H_{mea}}$ are both applied along x-axis ($\boldsymbol{H_{ext}}$, $\boldsymbol{H_{mea}} \perp \mathbf{K_u}$) (see coordinate system in (a)). (Sample: AlN 2 μm/ [Si/ SiO_2] 300 μm/ FeCoSiB 1 μm)

Figure 2.7b shows the $\boldsymbol{\alpha_{ME}}$ and $\boldsymbol{U_{ME}}$ response measured at varying $\boldsymbol{H_{mea}}$ frequencies. $\boldsymbol{H_{ext}}$ = +4 Oe and $\boldsymbol{H_{mea}}$ = 10^{-3} Oe are set during the measurement. At $\mathbf{f_{res}}$ = 878 Hz, $\boldsymbol{U_{ME}}$ and thus $\boldsymbol{\alpha_{ME}}$ is a maximum due to strain amplification at the mechanical resonance frequency.

With $\mathbf{f_{res}}$ obtained, now the $\boldsymbol{H_{ext}}$ dependency of $\boldsymbol{\alpha_{ME}}$ can be measured (Figure 2.7c). $\boldsymbol{H_{mea}}$ and $\mathbf{f_{mea}}$ are set at 10^{-3} Oe and $\mathbf{f_{res}}$ = 878 Hz, respectively. The idea is to find out the sensor's working point $\mathbf{H_{wp}}$, which is defined as the $\mathbf{H_{ext}}$ value, where $\boldsymbol{\alpha_{ME}}$ is the highest. $\boldsymbol{\alpha_{ME}}$ is measured as $\boldsymbol{H_{ext}}$ is changed between two $\boldsymbol{\alpha_{ME}}$ saturation states. For the investigated sensor (Figure 2.7c), $\mathbf{H_{wp}}$ is determined to be at ±5 Oe.

Traditionally, the limit of detection (LoD) of a ME sensor is measured at the $\mathbf{H_{wp}}$ and $\mathbf{f_{mea}}$ = $\mathbf{f_{res}}$. For the displayed LoD in Figure 2.7d, $\mathbf{H_{ext}}$ and $\mathbf{f_{mea}}$ were set to +5 Oe and 878 Hz, respectively. $\boldsymbol{\alpha_{ME}}$ is plotted against the applied $\boldsymbol{H_{mea}}$

amplitude. Both axes are in logarithmic scale. Starting from 10^{-3} Oe, $\boldsymbol{H_{mea}}$ amplitude is decreased stepwise. The measured $\boldsymbol{\alpha_{ME}}$ decreases linearly with decreasing $\boldsymbol{H_{mea}}$ amplitude. The point, where the curve diverges from linearity, the sensor's noise floor is reached (SNR = 1). It defines the LoD of the sensor. For the investigated sensor, linear fits were performed in the regions with linear $\boldsymbol{\alpha_{ME}}$ change (red line) and at the noise floor (blue line), the intersection of both lines indicates the LoD = $3.62{\cdot}10^{-8}$ Oe/ $\sqrt{}$Hz for the investigated ME sensor.

From magnetism point of view, $\boldsymbol{\alpha_{ME}}$ at $\boldsymbol{H_{ext}}$ can be approximated as the first order derivative of $\boldsymbol{\lambda}(\boldsymbol{H_{ext}})$ with respect to $\boldsymbol{H_{mea}}$ and can, therefore, be assessed as a measure of the magnetic materials's magnetostrictive susceptibility. $\boldsymbol{\lambda}$ is quadratic in magnetization direction (2.11). With $\boldsymbol{M_y}$ as the component of magnetization perpendicular to $\mathbf{K_u}$ (see Figure 2.7a), the $\boldsymbol{\alpha_{ME}}$ becomes (2.29) [51].

$$\alpha_{ME}(H_{ext}) \approx \frac{d\lambda(H_{ext})}{dH_{mea}} \approx \frac{1}{M_s^2}\frac{dM_y^2}{dH_{mea}} \tag{2.29}$$

(2.29) states that the ME response scales with the rate of $\boldsymbol{\lambda} \propto \boldsymbol{M_y^2}$ change. A detailed expression can be derived from first-order derivation of (2.11). Thus, $\boldsymbol{\alpha_{ME}}$ as well as $\boldsymbol{d\lambda/dH_{mea}}$ are correlated to $\boldsymbol{\lambda_s}$ and magnetic susceptibility $\boldsymbol{\chi} = \boldsymbol{dM_y/dH_{mea}}$ (2.30) (see Appendix for detailed derivation).

$$\alpha_{ME}(H_{ext}) \approx \frac{d\lambda(H_{ext})}{dH_{mea}} = \frac{3\lambda_s\chi}{M_s^2}M_y \tag{2.30}$$

(2.30) expresses that $\boldsymbol{\alpha_{ME}}$ at an arbitrary $\boldsymbol{H_{ext}}$ scales with $\boldsymbol{\lambda_s}$ and $\boldsymbol{\chi}$ of the material. Moreover, it possesses a linear relationship with $\boldsymbol{M_y}$, which leads to a $\boldsymbol{\alpha_{ME}}$ sign change for negative $\boldsymbol{H_{ext}}$, thus predicts a zero crossing for $\boldsymbol{\alpha_{ME}}$. The zero crossing occurs at $\boldsymbol{H_{ext}}$, when $\boldsymbol{\lambda}$ response for $\pm\boldsymbol{H_{mea}}$ are the same. In the discussed case ($\boldsymbol{H_{ext}} \| \boldsymbol{H_{mea}} \perp \mathbf{K_u}$), the zero-crossing occurs at $\boldsymbol{H_{ext}} = 0$ Oe. Furthermore, $\boldsymbol{\alpha_{ME}}$ becomes a maximum exactly at $\boldsymbol{H_{ext}} = \mathbf{H_k}$ ($|\boldsymbol{M_y}| = \mathbf{M_s}$), whereas for $\boldsymbol{H_{ext}} > \mathbf{H_k}$, $\boldsymbol{\alpha_{ME}}$ is zero since $\boldsymbol{\chi} = 0$.

Up until now, the measurements performed directly at $\mathbf{f_{res}}$ has been discussed. However, as is apparent from Figure 2.7b, the $\boldsymbol{\alpha_{ME}}$ drops drastically for out-of-resonance measurements (i.e. when $\mathbf{f_{mea}} \neq \mathbf{f_{res}}$) and generally, $\boldsymbol{\alpha_{ME}}$ decrease leads to measurement of LoDs that are inferior to direct measurements at $\mathbf{f_{res}}$, i.e. SNR = 1 is reached at higher $\boldsymbol{H_{mea}}$ values [26, 27]. To overcome this problem, instead of operating the ME sensor directly at $\mathbf{H_{wp}}$, an AC magnetic field $\boldsymbol{H_{mod}}$ is applied. $\boldsymbol{H_{mod}}$ amplitude is generally several orders of magnitude higher than $\boldsymbol{H_{mea}}$ amplitude and sweeps the linear region of the magnetostriction curve. It serves as a frequency modulation field, which along with $\boldsymbol{H_{mea}}$ brings the ME sensors in cantilever design to the mechanical resonance frequency ($\mathbf{f_{mod}} \pm \mathbf{f_{mea}} = \mathbf{f_{res}}$, where $\mathbf{f_{mod}}$ is the frequency of $\boldsymbol{H_{mod}}$) [26].

3 Experimental methods

In this chapter, the experimental devices and setups applied for the investigation of magnetic films and sensors along with their working principles are introduced. Starting with the employed inductive magnetization measurement setup (BH-looper) (Section 3.1), the magneto-optical (MO) microscope setup (Section 3.2) is shown. Due to extensive use of different MO effects in the following chapters, in detail descriptions of different MO effects are presented (Section 3.2.2). Lastly, the setup for measuring ME sensor response integrated into the MO microscope is introduced (Section 3.3).

3.1 BH-loop tracer

A BH-loop tracer (BH looper) is an integral measurement setup for measuring the magnetization $\boldsymbol{M}$ response of a magnetic material. The inductively measured magnetization curves displayed in this work are obtained by a BH looper *model 108* from *Shb instruments* [91]. The device consist of two coils in Helmholtz configuration to introduce an homogeneous, time-changing (10 Hz) $\boldsymbol{H_{ext}}$ to the investigated sample, which is situated in the middle and is surrounded by a pick-up coil (Figure 3.1). Samples up to 2 cm in diameter can easily be mounted and rotated in-plane by 360°, allowing for any desired in-plane measurement angles.

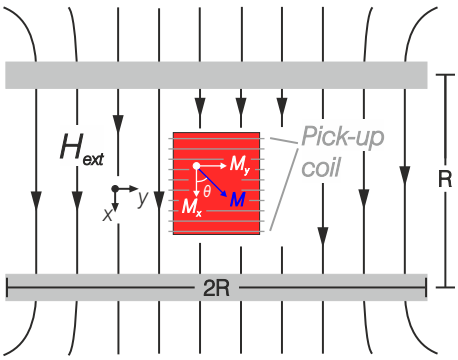

Figure 3.1: Sketch depicting the working principle of a BH-loop tracer. General coil setup fulfilling Helmholtz configuration is shown. Sample's magnetization $\boldsymbol{M}$, as well as, it's components $\boldsymbol{M_x}$ and $\boldsymbol{M_y}$ are shown. θ is the angle between $\boldsymbol{M_x}$ and $\boldsymbol{M}$. $\boldsymbol{H_{ext}}$ is the external field supplied by the Helmholtz coils.

$\boldsymbol{H_{ext}}$ changes the $\boldsymbol{M}$ alignment in the sample and accordingly its magnetic flux $\boldsymbol{B_{sample}}$. The time-changing $\boldsymbol{B}$ induces a voltage ($\boldsymbol{V_{sense}}$) that can be sensed at the

terminals of the pick-up coil ($\boldsymbol{V_{sense}} = \boldsymbol{dB/dt}$). The integral of which provides the $\boldsymbol{B}$. However, the pick-up coil collects $\boldsymbol{B}$-fields from the investigated sample $\boldsymbol{B_{sample}}$ and also the Helmholtz coils $\boldsymbol{B_{ext}}$ ($\boldsymbol{B_{total}} = \boldsymbol{B_{ext}} + \boldsymbol{B_{sample}}$). Therefore, a balance coil, sufficiently far away from the sample and additional electronics (both not shown in Figure 3.1) are present to deduct $\boldsymbol{B_{ext}}$ from $\boldsymbol{B_{total}}$ to obtain the desired $\boldsymbol{B_{sample}}$ [91]. The BH-loops can be acquired in real time and final loops can be averaged over any desired amount of loops.

Although $\boldsymbol{B}$-field is measured in the described setup, for soft magnetic materials ($\boldsymbol{\chi} \gg 1$), the permeability $\boldsymbol{\mu}$ is almost equal to the magnetization susceptibility $\boldsymbol{\chi}$ (i.e. $\boldsymbol{\mu} = 1 + \boldsymbol{\chi}$ and $\boldsymbol{\mu} \approx \boldsymbol{\chi}$). Thus, $\boldsymbol{M}$ is approximately equal to the measured $\boldsymbol{B}$-field. Such a detection setup results in measurement of $\boldsymbol{M_x}$ component of $\boldsymbol{M}$ ($\boldsymbol{M_x} = \boldsymbol{M}\cos\theta$) (Figure 3.1).

3.2 Magnetic domain observation

There are many microscopy techniques available, which offer the possibility to image magnetic domains in different length and time scales. First magnetic domain observations can be dated back to the Bitter technique, which relies on using small magnetic particles in a liquid solution, where the particles settle at highest local magnetic field gradient [73]. Also electron microscopy techniques have been applied for magnetic domain imaging. Scanning electron microscopy with spin analysis relies on the spin polarization of the secondary electrons emitted from a magnetic material [92]. In a transmission electron microscope, Lorentz and electron holography allow for magnetic domain imaging [93, 94]. Using a polarization microscope, light in the visible spectrum can also be applied to gather information on magnetic domains. Traditionally, the magneto-optical microscopy depends on the detection of the occurring circular birefringence and dichroism of incident linearly polarized light upon interacting with a magnetized body. Though rarely employed, methods using linear birefringence and dichroism are also available.

Every imaging technique brings invaluable information on the magnetic domain configurations in various device and material systems. Most importantly, they reveal the underlying magnetization reversal processes, which are unavailable to most integral measurement techniques.

3.2.1 Magneto-optical microscopy

Depending on the optical properties of the investigated magnetic sample, two different microscope setups can be used. For transparent films (e.g. garnets), a transmission type polarization microscope; for opaque materials (e.g. metals), re-

flection type polarization microscope should be used. In this section, emphasis is made on MO microscopy in reflection. MO microscopy in reflection is highly surface sensitive. The information depth is only about 30 nm, which is approximately the penetration depth of light in metals.

In principle, for general microscopy purposes homogeneous illumination of the specimen is required. MO microscopy is no exception to this rule. A schematic of a MO microscope with Köhler illumination geometry in reflection is shown in Figure 3.2. Additionally, two light polarizing elements, one before (polarizer) and another one after the sample (analyzer), is a requirement. Furthermore, an optical phase shifting element (compensator) can be installed between the polarizers to compensate for the occurring light ellipticity from the magnetic sample and/or the optical elements in the microscope. However, for detection of high-order MO effects, the phase shifting element is a necessity, since high-order MO effects generally depend on linear birefringence and dichroism [32, 95].

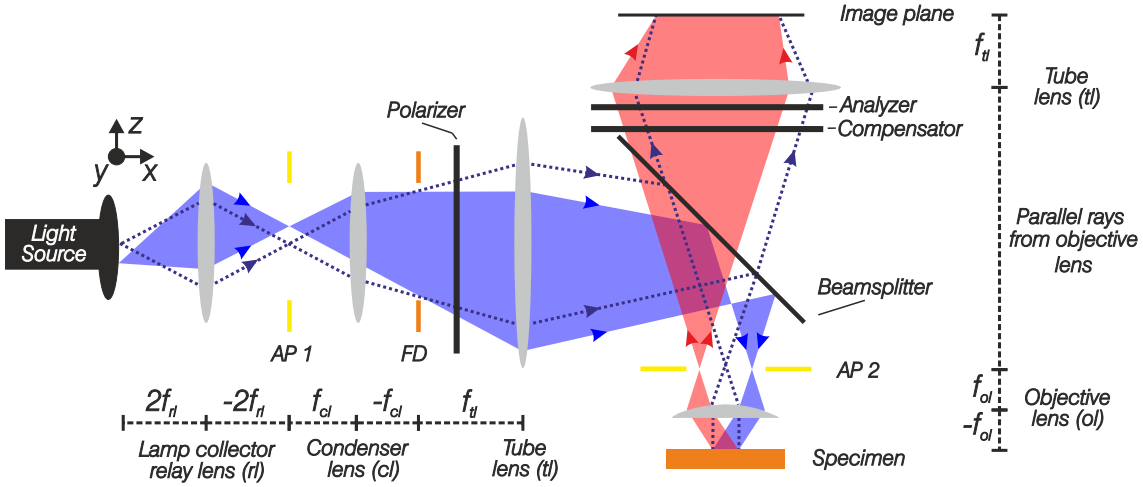

Figure 3.2: Sketch of a polarization microscope with Köhler illumination geometry used for magnetooptical imaging. Blue and red areas indicate the incident and reflected ray paths. Aperture planes (AP) and the field diaphragm (FD) are marked. (Adapted from [32, 95] and [96])

For the illustrated illumination scheme, the light source (e.g. LED or Laser) is situated at double the focal length ($2f_{rl}$) of the lamp collector relay lens (rl). As a result, an image of the light source forms at $-2f_{rl}$, which defines the first aperture plane AP1 of the microscope. After passing through a condenser lens, the rays diverge at the field diaphragm (FD). FD is homogeneously illuminated. The incident light passes through the polarizer and gets linearly polarized. The tube lens (tl) is positioned so that its front focal point coincides with the focal point of the condenser lens and the incident beam is focused at AP2 after getting reflected at the beamsplitter. AP2 coincides with the backfocal plane of the objective lens. The incident light rays that pass through the objective lens, shine almost

parallel to specimen's surface, homogeneously illuminating it. The reflected beam, which interacted with the specimen and now carries magnetic information, transmits through the beamsplitter and passes through the compensator and analyzer. Finally, a magnified image of the specimen is focused on the image plane, which can then be acquired with a camera or be seen through an ocular.

As will be discussed in the next sections, for all MO effects, the proper adjustment of the angle of incidence $\boldsymbol{\theta_{inc}}$ is one of the deciding parameters leading to maximization of the MO contrast. For this purpose, a conoscopic image is required. Therefore, in most MO microscope setups a Bertrand lens is inserted between the image plane and the beamsplitter (not shown in Figure 3.2), which focuses the image of the light source at the backfocal plane of the objective lens f_{ol} (AP2) to the image plane [95]. Now, $\boldsymbol{\theta_{inc}}$ can be aligned by installing an aperture slit at AP1. Alternatively, the light can be fed into the microscope through a glass fiber, whose position at $2f_{rl}$ can be aligned in y-z plane (Figure 3.2), resulting in a change of $\boldsymbol{\theta_{inc}}$ at the specimen.

One of the disadvantages of the displayed polarization microscope setup for MO microscopy is that the objective lens is used for both illumination and observation purposes (Figure 3.2). The achievable maximum $\boldsymbol{\theta_{inc}}$ is limited by the numerical aperture (NA) of the objective lens. From Snell's law [95], with $\mathbf{n_{inc}}$ as the refractive index of the incident medium, the maximum $\boldsymbol{\theta_{inc}}$ can be calculated as (3.1).

$$\theta_{inc} = \arcsin\left(\frac{NA}{n_{inc}}\right) \tag{3.1}$$

Therefore for objective lenses with low NA, the maximum achievable MO contrast is low for longitudinal and transverse MOKE effects (Section 3.2.2.1). However, by separating the illumination and observation paths, the maximum attainable $\boldsymbol{\theta_{inc}}$ can be made independent of the objective lens's NA. [32, 95].

Independent of the applied MO effect, the MO microscopy allows for imaging magnetic domains of a few hundred nanometers to centimeters in size [95]. Additionally, by triggering the light sources and/or camera, magnetization processes in a board range of temporal resolution can be imaged [32, 97, 98].

Here, the microscope setup used for performing MO imaging is a modified version of *Axio Imager.Z2 Vario* from *Zeiss* [99]. The microscope is mounted on a passively damped table. Two high power light emitting diodes (LEDs) from *Prizmatix* with wavelengths of 460 nm (*UHP-LED 460*) and 640 nm (*UHP-LED 640*) are integrated as light sources (Figure 3.3a) [100]. The light from the LEDs are fed into the microscope through fiber optic cables. Each fiber end is fixed to an x-y translation mount, providing free adjustment of the angle incidence, which is necessary for MO imaging. Both fiber ends are situated at one focal length away (f_{cl} from the

collimator lens (Figure 3.3a). A dichroic filter/ mirror, fixed at 45° in the x-z plane (see the coordinate system in Figure 3.3a), is used to guide both light beams into the microscope. Furthermore, the collimator lens is affixed on a mount that is movable along the x-axis (Figure 3.3a) to compensate for small differences in the focal length of different objective lenses.

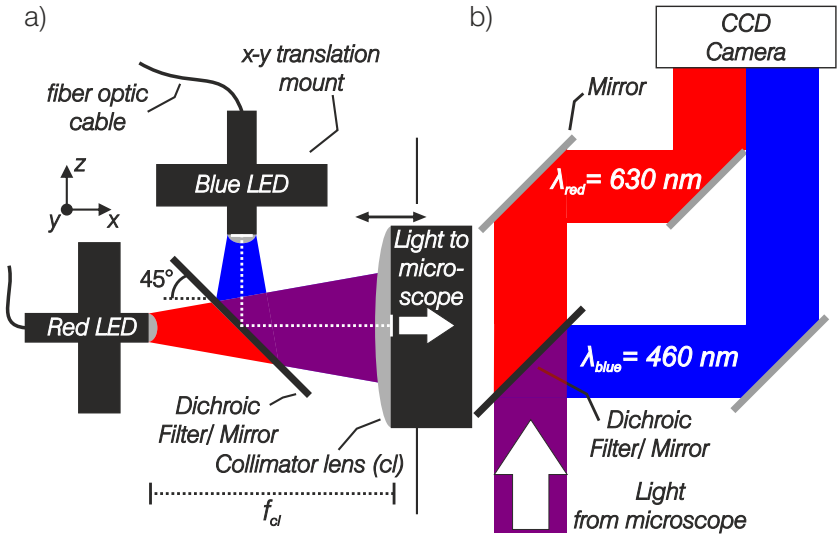

Figure 3.3: (a) Sketch depicting simultaneous supply of red and blue lights is shown. (b) Interior sketch of *Optosplit II* [101], a beam splitter used for simultaneous, dual-wavelength imaging.

Similar to the microscope sketch in Figure 3.2, two linear light polarizers and a quarter wave plate are installed into the setup for obtaining different kinds of MO effects (i.e. MOKE, MOVE and MOGE). Final images are acquired through *Hamamatsu C10600-10B-H* digital CCD camera [102]. The dynamic range of the camera in normal scan mode is 70 dB (18000 full-well electron capacity, read-out noise 6 electrons r.m.s.). Additionally, later shown data in the following chapters contain several complementary magnetic domain images with different MOKE sensitivities and/ or different MO effects. They are obtained through *Optosplit II* (*Cairn research*) [101], a microscope extension mounted before the camera. The separation of light beams with different wavelengths is achieved using a dichroic filter. Subsequently, the separated beams are guided via additional mirrors to the camera (Figure 3.3b). With correct adjustment of the device, the final images are acquired from the same region on the sample and for every recorded image, half of the image is illuminated by the red LED and the rest by the blue LED. The extension grants the opportunity to perform dynamic or static measurements using two different MO effects and/ or sensitivities simultaneously without triggering the light sources or the camera. However, with the drawback of field of view in the images getting halved.

For in-situ observation of magnetic domains with $\boldsymbol{H_{ext}}$, two types of electromagnets are available both are purchased from the company *evico magnetics*. The first

one is a one axis electromagnet setup, which is composed of two independent coils on either side. The second electromagnet setup consist of four separate electromagnets with identical turning numbers. They are aligned in a quadropole arrangement, allowing for application of $\boldsymbol{H_{ext}}$ in any desired in-plane angle.

3.2.2 Magneto-optical effects

Magneto-optical (MO) effects rely on the interaction of light in visible spectrum with magnetization. The polarization states of light before and after interacting with a magnetized body is different. For randomly polarized (unpolarized) light, this effect is indistinguishable. Therefore, polarized light is employed to measure the change in the polarization state of the incident light after interacting with a magnetized body. The MO effects can be divided into two subgroups depending on their relationship with magnetization, namely first- and second-order MO effects. Both effects occur due to presence of spin-orbit coupling and exchange interaction in a magnetic material [103]. A linearly polarized light is shone on a magnetized surface. The components (circular or linear) of the linearly polarized light possess different absorption/refraction coefficients for minority and majority spins. As a consequence, a rotation in the plane of polarization and/or ellipticity occurs. Phenomenologically, the most general form for the resulting effect can be expressed in terms of electric displacement $\boldsymbol{D}$ in incident light's electric vector $\boldsymbol{E}$ (3.2) [44, 95]. $\boldsymbol{\epsilon}$ stand for the permittivity of the medium.

$$D = \epsilon E + \epsilon_{total} \times E \tag{3.2}$$

The first and second terms on the right hand side of the equation signifies the electric displacement in the dielectric medium and the occurring MO effects for magnetized bodies, respectively.

All MO effects scale with magnetization. Both first- (linear) and second-order (quadratic) MO effects can be represented in the total dielectric permittivity tensor $\boldsymbol{\epsilon_{total}}$ (3.3), where $\boldsymbol{m_x}$, $\boldsymbol{m_y}$ and $\boldsymbol{m_z}$ stand for the direction cosines of magnetization. $\mathbf{Q_V}$ and $\mathbf{B_i}$ are linear and quadratic MO constants, respectively. Furthermore, experimental indications of MO constants scaling with the material's saturation magnetization $\mathbf{M_s}$ are present [104, 105] and some authors have suggested a linear relationship $\mathbf{Q_V} \propto \mathbf{M_s}$ [106].

$$\boldsymbol{\epsilon_{total}} = \epsilon \begin{pmatrix} 1 & -i\mathrm{Q_V}\boldsymbol{m_z} & i\mathrm{Q_V}\boldsymbol{m_y} \\ i\mathrm{Q_V}\boldsymbol{m_z} & 1 & -i\mathrm{Q_V}\boldsymbol{m_x} \\ -i\mathrm{Q_V}\boldsymbol{m_y} & i\mathrm{Q_V}\boldsymbol{m_x} & 1 \end{pmatrix} \Rightarrow \textbf{Linear MO effects}$$

$$+ \tag{3.3}$$

$$\textbf{Quadratic MO effects} \Leftarrow \begin{pmatrix} \mathrm{B_1}\boldsymbol{m_x^2} & \mathrm{B_2}\boldsymbol{m_x m_y} & \mathrm{B_2}\boldsymbol{m_x m_z} \\ \mathrm{B_2}\boldsymbol{m_x m_y} & \mathrm{B_1}\boldsymbol{m_y^2} & \mathrm{B_2}\boldsymbol{m_y m_z} \\ \mathrm{B_2}\boldsymbol{m_x m_z} & \mathrm{B_2}\boldsymbol{m_y m_z} & \mathrm{B_1}\boldsymbol{m_z^2} \end{pmatrix}$$

Both first- and second-order terms add to the measured MO signal to a certain extent, the degree of which is defined by the relative alignment of the incident light's polarization plane with respect to the magnetization direction and the angle of light incidence. In the sections below, the illumination geometries, which lead to maximization of the mentioned effects are discussed. Additionally, the MO gradient effect is discussed that emerges strongly at certain illumination geometries as an additional MO effect.

3.2.2.1 First-order magneto-optical effects

Represented in the linear term of the total dielectric permittivity tensor, first-order MO effects mainly rely on the occuring circular birefringence of the incident light's polarization state upon interacting with a magnetized body. The measured first-order MO intensity scales linearly with the magnetization component along a measurement axis (e.g. $\boldsymbol{m_x}$) and is analogous to the Hall effect.

In general, the optical properties of the investigated magnetic material define the utilized MO effect. For materials transparent to visible light, i.e. garnet films, MO Faraday effect (MOFE) in transmission and for non-transparent materials such as metals Kerr effect (MOKE) in reflection is applied. For MOKE, a linearly polarized light is shone on a reflective, magnetized surface. The linearly polarized incident light can be separated into two circular components of opposite sense of rotation ($\boldsymbol{E_1}$ and $\boldsymbol{E_2}$) (Figure 3.4a) and depending on the magnetization direction, the refractive index of the magnetized medium varies for $\boldsymbol{E_1}$ and $\boldsymbol{E_2}$. As a result, the occurring phase shift is different for either circularly polarized light components and the plane of polarization rotates by Kerr angle $\pm\boldsymbol{\theta_{Kerr}}$. For antiparallel magnetization directions, the occurring $\boldsymbol{\theta_{Kerr}}$ is of opposite sign (compare both sketches in Figure 3.4b). In addition to MO birefringent effects, dichroic effects also contribute to the signal due to absorption and higher order MO effects. Therefore, in addition to a rotation in the plane of polarization, light also becomes elliptically polarized (Figure 3.4b).

By installing a second polarizer (analyzer) after the sample, whose polarization

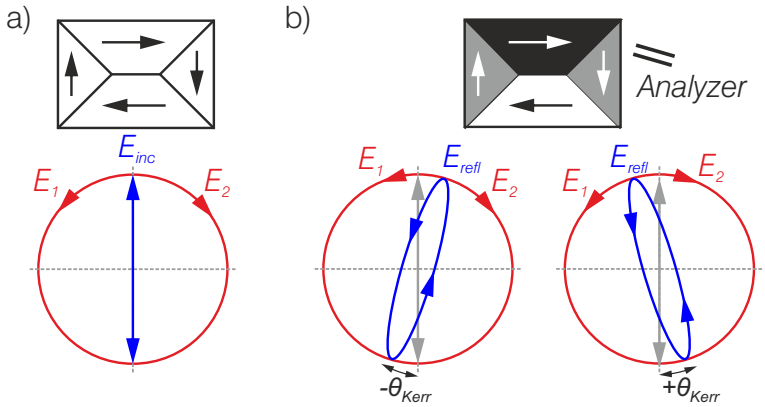

Figure 3.4: Polarization geometries of MOKE in (a) for before ($\boldsymbol{E_{inc}}$) and in (a) for after ($\boldsymbol{E_{refl}}$) the incident light reflects from a magnetized surface. Possible magnetization configurations are sketched. Gray arrows in (b) indicate $\boldsymbol{E_{inc}}$.

axis is aligned 90°$\pm\boldsymbol{\theta_{Kerr}}$ with respect to the first polarizer, information from one magnetization direction can be annihilated and thus dark contrast is observed. For the antiparallel magnetization direction, a small component of light passes through the analyzer, which depicts the bright contrast in magnetic domain images. Under such illumination and detection schemes, with the measured magnetization component $\boldsymbol{m_x}$ along the x-axis and the samples reflectivity constant $\mathbf{I_0}$, the detected MOKE intensity $\boldsymbol{I_K}$ can be expressed as in (3.4)) [107].

$$I_K = \mathrm{I}_0 + \mathrm{Q_V} m_x \tag{3.4}$$

Accordingly, depending on the polarizer settings, the maximum (bright contrast) and minimum (dark contrast) intensity is obtained for collinear magnetization directions, e.g. $\boldsymbol{-m_x}$ and $\boldsymbol{+m_x}$.

For imaging out of plane magnetic domains, with $\boldsymbol{k}$ as the wave vector, polar illumination is applied ($\boldsymbol{k} \| \boldsymbol{m}$). All linear light polarization states (s-, p-polarization and etc.) are identical in this case, since for out of plane magnetization and polar illumination, the polarization is perpendicular to the magnetization in all cases. For imaging in plane magnetic domains with MOKE, two different illumination geometries are present. Both require oblique angle of incidence. Longitudinal ($\boldsymbol{k} \| \boldsymbol{m}$) or transverse ($\boldsymbol{k} \perp \boldsymbol{m}$) sensitivities can be used for in-plane magnetic domain imaging. In longitudinal sensitivity, both s- and p-polarized light is employed and in transverse sensitivity, light polarization plane is 45° with respect to $\boldsymbol{m}$.

The term "MO sensitivity" stands for the magnetization axis (for MOKE and MOFE) or axes (for MO Voigt effect), along which the measurement is sensitive to. In order to demonstrate MO sensitivity of MOKE, two MO images of the same magnetic domain configuration are displayed in Figure 3.5. The polarizer and compensator settings are kept the same. Only $\boldsymbol{k}$ is different (see the backfocal plane

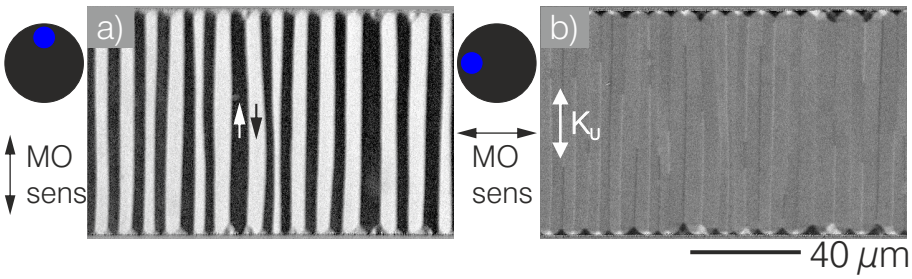

Figure 3.5: Complementary MO images of the same magnetic domain configuration are obtained at remanent magnetization with orthogonal MOKE sensitivities are displayed (a, b). $\mathbf{K_u}$ axis is depicted in (b). The position of the light source in the objective's backfocal plane and obtained MO sensitivities are shown to the left of each image. (Sample: [Si/ SiO_2] 300μm/ Ta 3 nm/ CoFeB 160nm/ TaN 5nm)

sketches). The dark and bright contrasts in Figures 3.5a and b indicate magnetic domains with anti-parallel magnetization directions. In Figure 3.5a, the plane of incidence is aligned parallel to the uniaxial magnetic anisotropy $\mathbf{K_u}$, which exposes the magnetic domains with collinear magnetization directions aligned along $\mathbf{K_u}$. The magnetic closure domains at the edges do not display any contrast. They all remain gray. Now by changing the plane of incidence by 90° (Figure 3.5b, compare backfocal plane sketches), the MO measurement is no longer sensitive to magnetic domains in the middle, they all display the same gray contrast. Now, the magnetic closure domains at the top and bottom of the image display dark and bright contrast. Additionally along this sensitivity, the asymmetric Bloch wall structures, separating the magnetic domains are exposed since their surface magnetization component is aligned along the current MO sensitivity axis (Figure 3.5b). MOKE is sensitive to a magnetization axis and with two perpendicular MOKE illumination geometries a complete understanding of the surface magnetic domain structure can be obtained for films with in-plane magnetization.

MOKE is not only used in imaging of magnetic microstructures and is actually more frequently applied to magnetometry. An exemplary measurement is shown in Figure 3.6.

With application of an external magnetic field $\boldsymbol{H_{ext}}$ the change in $\boldsymbol{I_K}$ can be recorded and local magnetization response of the material in terms of MO intensity can be obtained (Figure 3.6). MOKE magnetometry can be used as complementary measurement technique in combination with other integral methods. Furthermore, being able to acquire local magnetization response is quite beneficial for investigating many device applications, where local magnetization responses weigh differently in sensor response, such as magnetoresistive sensors and as will be later shown for magnetoelectric sensors. Additionally, for magnetic structure dimensions from nanometer to a few micrometers, where magnetic signals are too weak for inductive measurements, high-resolution MO microscopy techniques can be used with ease as

a MO magnetometry tool.

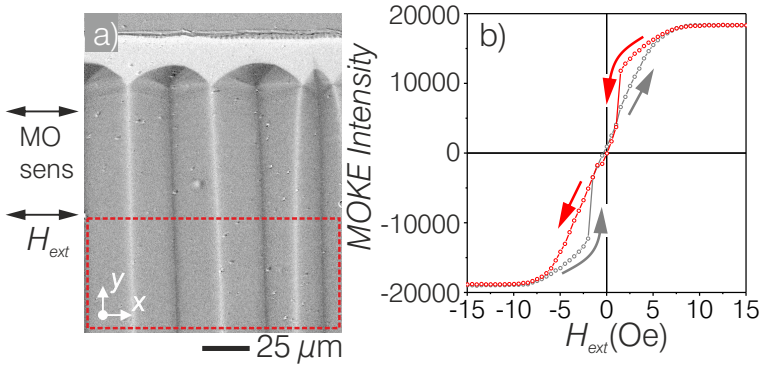

Figure 3.6: (a) exhibits the hard axis remanent magnetization state of investigated sample. The red dashed rectangle depicts the region, where the intensity of 121 images with different $\boldsymbol{H_{ext}}$ is analyzed. As a result the magnetization loop in (b) is obtained. The MOKE magnetization loop is shifted around 0 intensity. (Sample: AlN 2 μm/ [Si/ Si_2] 300 μm/ FeCoSiB 1 μm)

In this work, magnetic properties of metallic glasses are investigated. Mainly, MO effects in reflection is employed. However, even for opaque materials, MOFE can be applied. Using a magneto-optical indicator film (MOIF), the inner magnetic domain structure of the investigated sample can be revealed. A typical MOIF is composed of a garnet film and a substrate with a thin, reflective film, which acts as a mirror. When a MOIF is placed on top of a magnetic material, the stray field generated by the investigated material acts on the MOIF and changes its magnetic domain configuration. An image of the investigated sample's magnetic domain configuration gets imprinted in MOIF. Now, when a linearly polarized light is shone on the garnet film, it transmits through and gets reflected from the mirror. The observed rotation in the polarization plane is due to MOFE and generally, the magnetic domain contrast is several orders of magnitude higher than MOKE since the magnetic information is obtained from a much larger volume. This technique is advantageous for investigating the inner magnetic domain structure of bulk magnetic materials with out of plane magnetization components. Figure 3.7 displays the magnetic domain configuration at the same location of a single crystal $CoFe_2O_3$ (CFO) sample with <111> facets by using MOIF (a) and MOKE (b), which exhibit the magnetization distribution in the bulk and at the surface, respectively.

A Bismuth based garnet film with out of plane magnetic anisotropy is employed as the MOIF [108]. The magnetic domain configuration in MOIF is modified by the effective stray field from the internal CFO domains. The local average domain width is 25 μm. Black and white contrast in the image correspond to alternating out-of-plane magnetization components of the internal magnetic domains. The complementary MOKE image (Figure 3.7b) displays the surface magnetic domains at the same region. The patchy magnetic domain configuration on the surface most prob-

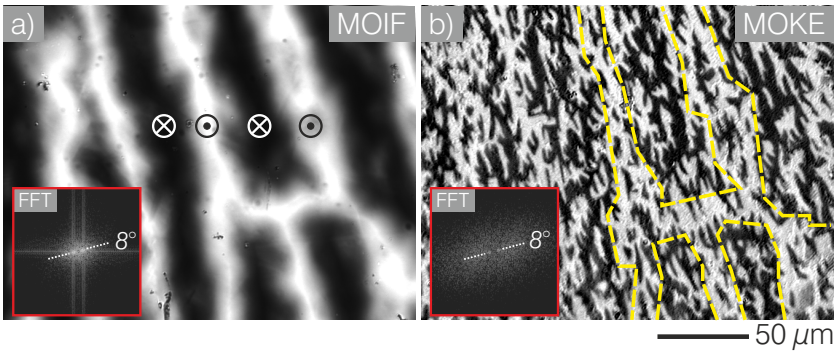

Figure 3.7: Complementary MO images at the same area on the CFO sample obtained with the MOIF (a) and MOKE (b) are displayed. In (b) some part of the imprinted magnetic domain structure in the MOIF is sketched with dashed lines to show the correlating magnetic domain configuration. The insets in (a) and (b) correspond to acquired Fast-fourier transformations from the corresponding images (Sample: single crystal $CoFe_2O_3$) (together with Dr. Bridget Murphy and Dr. Madjid Abes)

ably originates from closure domain formations caused by domain branching [44]. The Fast-Fourier transformation (FFT) of Figure 3.7a and b reveals the correlation between the surface and the internal magnetic domain structure. Both FFTs display diffraction peaks at 8°, indicating that the alignment of internal and surface magnetic domains are the same. CFO is a cubic crystal with <100> family of crystallographic directions as the easy axes. It has been reported that fir tree patterns with tilted magnetizations form at the surface, which are aligned along the effective easy axes [109]. However, in Figure 3.7b, a deviation from the fir pattern is observed. The reason probably lies in the local tilting of the effective magnetic anisotropy due to tensile stress and/ or polishing conditions. Together with MOKE, MOIF technique can give a much broader understanding of the overall magnetic domain structure particularly in bulk magnetic materials.

3.2.2.2 Second-order magneto-optical effects

Second-order MO effects are represented in the quadratic part of the total dielectric permittivity tensor and are quadratic in magnetization component $\boldsymbol{m_i}$ (3.3). In this section, emphasis is made on MO Voigt effect (MOVE) in reflection. MOVE is mainly based on the occurring linear birefringence in the incident light's polarization state upon interacting with a magnetized surface.

In comparison to MOKE, the MOVE signal is about two orders of magnitude smaller ($\mathbf{B} \ll \mathbf{Q_V}$) (see the total dielectric permittivity tensor in 3.3). MOVE is rarely used in imaging and mostly performed in MO magnetometry to extract the pure MOKE signal [110]. In order to obtain high MOVE signal, the plane of polarization of the incident light should be 45° with respect to the desired measurement

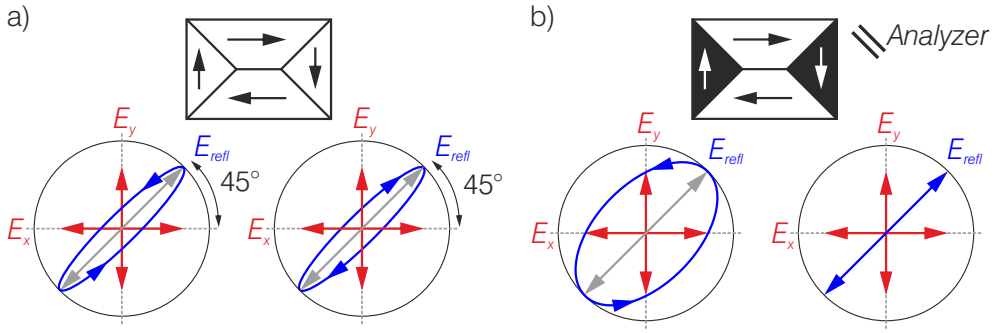

Figure 3.8: Polarization geometries $\boldsymbol{E_{ref}}$ of MOVE after the incident light reflects from a magnetized surface are given before (a) and after (b) the compensator. Possible magnetization configurations are sketched. Gray arrows indicate the polarization state of the incident light before reflecting from the surface.

axis. The linearly polarized incident light becomes elliptical, when the light reflects from a magnetized body. The incident light can be deconstructed into two orthogonal linear components ($\boldsymbol{E_x}$ and $\boldsymbol{E_y}$) (Figure 3.8a). As the light interacts with the magnetization, due to different refractance of each linear $\boldsymbol{E}$-component with respect to the magnetization direction, the arising phase shift is different for both light components. Thus, the reflected light becomes elliptically polarized. On one magnetization axis, the ellipticity has the same sense of rotation. For the orthogonal magnetization axis, the sense of rotation is opposite. In order to detect this effect, an optical phase shifting element has to be installed between the polarizers. With it, the phase shift occurring along one magnetization axis can be compensated and for the other axis, the ellipticity is enhanced (Figure 3.8b). Now with an analyzer that is aligned perpendicular to the first polarizer, the corrected reflected light is extincted and as a result, a small linear component of the elliptically polarized light is detected to obtain the MOVE contrast.

With the above mentioned illumination and detection schemes, the detected MOVE intensity, $\boldsymbol{I_V}$, can be expressed with $\boldsymbol{m_x}$ as the magnetization component along the measurement axis (x-axis) as (3.5) [107].

$$I_V = \mathrm{I}_0 + \mathrm{B}\, m_x^2 \tag{3.5}$$

From equation (3.5), collinear magnetization directions depict the same MOVE contrast ($+\boldsymbol{m_x}$ and $-\boldsymbol{m_x}$ in this case). However, orthogonal in-plane magnetization directions are different in contrast. By rotating the sample by 90°, the contrast is inverted.

Dissimilar to MOKE, where an oblique plane of incidence is required for imaging in plane magnetic domains, MOVE is maximized, when polar illumination geometry is employed and first-order MO effects vanish for in-plane magnetization directions. The obtained MO sensitivity is purely in-plane.

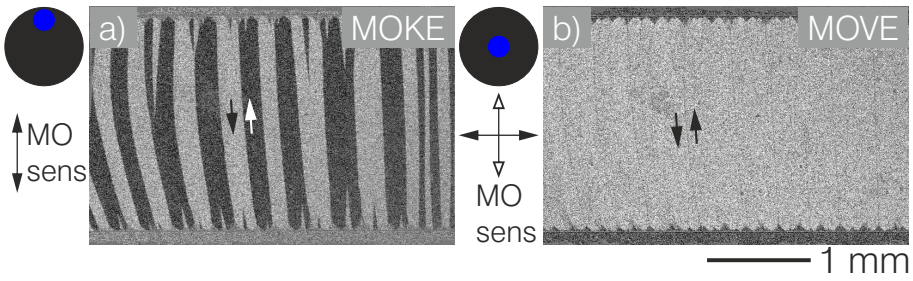

Figure 3.9: Remanent state magnetic domain configuration imaged with MOKE (a) and MOVE (b). Illumination geometry and the corresponding MO sensitivities are sketched next to each domain image. (Sample: AlN 2 μm/ [Si/ SiO_2] 300 μm/ FeCoSiB 1 μm)

Figure 3.9 displays the differences between MOKE (a) and MOVE (b). The imaging is performed with an objective of 0.06 NA, which corresponds to a maximum obtainable angle of incidence of 3.4°.

As mentioned, when discussing the first-order MO effects, the MOKE image (Figure 3.9a) exhibits MO sensitivity along an axis. The magnetic domains in the middle with anti-parallel magnetization directions show dark and bright contrast, however the closure domain structures at the very edges stay gray in contrast. On the other hand, in the acquired MOVE image all collinear magnetization directions display the same MO contrast, with perpendicularly magnetized domains exhibiting opposite contrast (Figure 3.9b).

In terms of obtained magnetization curves, unlike MOKE, the MOVE curves are quadratic in $\boldsymbol{m}$ (see equation (3.5)). Figure 3.10 is obtained from the same sample at the same location as in Figure 3.6. Features, such as magnetization jumps due to sudden magnetization changes can be reconstructed. However, the maximum obtainable MO intensity is much lower due to significantly less MO constant ($\mathbf{Q_V} \gg \mathbf{B}$).

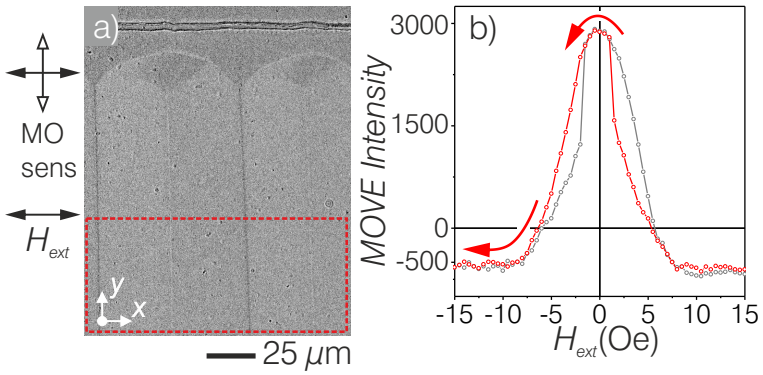

Figure 3.10: (a) shows the hard axis remanent magnetization state of investigated sample in MOVE illumination geometry. The red dashed rectangle depicts the region, where the intensity of 121 images with different $\boldsymbol{H_{ext}}$ is analyzed. As a result $\boldsymbol{m^2}$ loop in (b) is obtained. (Sample: AlN 2μm/ [Si/ SiO_2] 300μm/ FeCoSiB 1μm)

Although the detected signals are rather low for MOVE, MO imaging of in-plane magnetization response via MOVE can be, in certain instances, very advantageous. As has been discussed, the maximum obtainable angle of incidence is generally limited by the numerical aperture (NA) of the objective lens and are commonly small for low magnification objectives [95]. As a result such illumination conditions limit the maximum achievable MO intensity when performing imaging via first-order MO effects. However, polar illumination can be applied independent of the employed objective's NA. Therefore, by maximizing MOVE via applying polar illumination, magnetic domains with pure in-plane magnetization alignment can be imaged without any contributions from first-order MO effects.

3.2.2.3 Magneto-optical gradient effect

First-order MO effects vanish for in-plane magnetization under MOVE illumination conditions, due to application of polar illumination geometry. However, an additional MO effect emerges strongly at magnetic domain boundaries, which scales with first order MO effects. It originates from magnetization gradients at magnetic domain boundaries. With the relevant MO constant $\mathbf{P_{gr}}$, the effect can be expressed in the total dielectric tensor $\epsilon_{\mathbf{total}}$ (3.6) [95, 111].

$$\epsilon_{total} = \mathrm{P_{gr}} \begin{pmatrix} -\frac{\partial m_x}{\partial y} - \frac{\partial m_y}{\partial m_x} & \frac{\partial m_x}{\partial x} - \frac{\partial m_y}{\partial y} \\ \frac{\partial m_x}{\partial x} - \frac{\partial m_y}{\partial y} & \frac{\partial m_x}{\partial y} + \frac{\partial m_y}{\partial x} \end{pmatrix} \tag{3.6}$$

This additional MO effect is called MO gradient effect (MOGE), also named after its discoverers the Schäfer-Hubert effect. Differences of MOGE and MOKE is displayed in Figure 3.11.

The MOKE image shown in Figure 3.11a depicts closure domain structures with alternating bright and dark contrast. Additionally, asymmetric Bloch type walls are revealed, which are aligned along the uniaxial magnetic anisotropy axis of the material, where MOKE contrast appears due to in-plane magnetization component of the magnetic domain walls. In the region, where possible magnetization directions are sketched, the magnetic domain wall exhibits both bright and dark contrast, which indicates domain wall regions with antiparallel surface magnetization components separated by a Bloch line. In the complementary MOVE image, as was discussed in the previous section, magnetic domains with antiparallel magnetization directions show the same contrast. All closure domains and domains in the middle of the structure show bright and dark MO contrast, respectively. However, at the magnetic domain wall, where the Bloch line is present (Figure 3.11a), no change in contrast is observed in the MOVE geometry (Figure 3.11b). The MO contrast is homogeneously dark. Additionally, every adjacent magnetic domain boundary

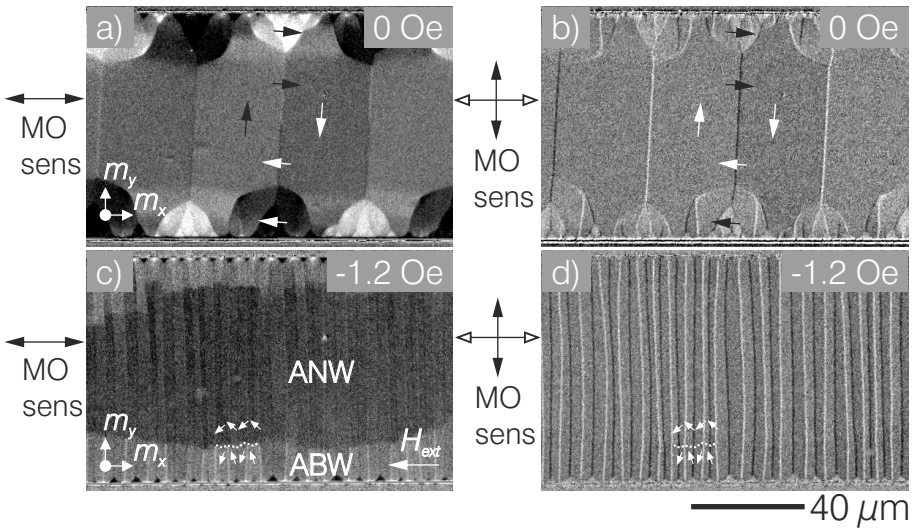

Figure 3.11: Complementary magnetic domain images obtained with MOKE (a) and MOVE (b) illumination geometries after the magnetic structure is demagnetized along its easy axis. (c) and (d) exhibit the acquired magnetic domain configuration at a small $\boldsymbol{H_{ext}}$ along the hard axis with MOKE and MOVE, respectively. (sample: Si 300 μm/ CoFeB 160 nm/ TaN 5 nm)

exhibit alternating MO contrast.

Now, with $\boldsymbol{H_{ext}}$ decreased from magnetic saturation along the hard axis, a magnetic domain configuration with high magnetic domain wall density ensues. At around $\boldsymbol{H_{ext}}$ = -1.2 Oe, the magnetization change transpires as sudden drops in $\boldsymbol{m_x}$ component of magnetization. This process starts from the edges of the magnetic structure, which is due to locally higher $\boldsymbol{H_d}$ with respect to the middle of the structure. The MO contrast in the middle region is still dark, which indicates that $\boldsymbol{m_x}$ component in the middle is higher than the edge regions. This transformation is accompanied by a magnetic domain wall transformation from asymmetric Néel wall (ANW) to asymmetric Bloch wall (ABW) (Figure 3.11c). At $\boldsymbol{H_{ext}}$ = -1.2 Oe, the domains at the edges are separated by ABWs, whereas low angle ANWs are still prevalent in the middle and two distinct domain wall types coexist along a single wall. Now, the same magnetic domain configuration imaged in MOVE geometry exhibits none of the domain wall transitions, all magnetic domain boundaries exhibit alternating bright and dark MO contrast (Figure 3.11d). MOGE is insensitive to magnetic domain wall transformations.

A concluding proof for the origin of MOGE contrast is obtained by imaging compensated domain wall structures during easy axis magnetization switching of an exchanged biased CoFeB bilayer structure with symmetric ferromagnetic film thicknesses ($\boldsymbol{t_{top}} = \boldsymbol{t_{bottom}}$ = 80 nm) (Figure 3.12). The displayed curve is obtained from the full film (in-plane dimensions: 1 cm x 2 cm) counterpart of the later shown structured sample, where imaging has been performed. The exchange bias in both

layers are aligned antiparallel with respect to each other. The inductively measured magnetization loop shows two distinct magnetic switching events. Due to antiparallel alignment of exchange bias for each CoFeB layer, half of the magnetization loop is shifted to $+\boldsymbol{H_{ext}}$ and the other half to $-\boldsymbol{H_{ext}}$, which correspond to magnetization switch in top and bottom layer, respectively.

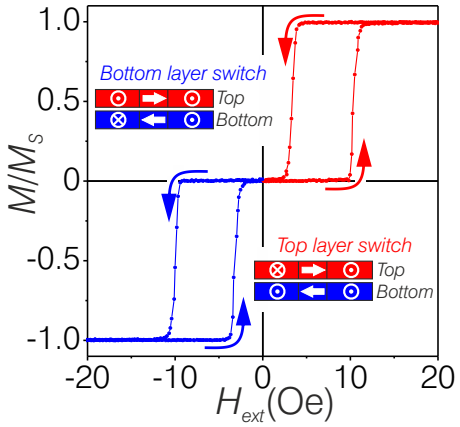

Figure 3.12: Inductively measured magnetization loop along the easy directions of an antiparallelly exchange biased bilayer structure. Possible magnetization configurations at the cross section during magnetization switch in each CoFeB layer for $\pm\boldsymbol{H_{ext}}$ are sketched. (Sample: [Si/ SiO_2] 300 μm/ Ta 3 nm/ NiFe 2.5 nm/ IrMn 7 nm/ CoFeB 80 nm/ Ta 3 nm/ NiFe 2.5 nm/ IrMn 7 nm/ CoFeB 80 nm/ TaN 5 nm)

The magnetic domain and wall structures in the top CoFeB layer of a structured sample in micrometer dimensions (80 μm x 320 μm) are imaged during magnetization switch in both top and bottom layers by two orthogonal MOKE and MOVE geometries (Figure 3.13). Dual-wavelength imaging has been employed (see Section 3.2.1). As has previously been mentioned, MO effects in reflection are very surface sensitive. Since the top magnetic layer thickness ($\boldsymbol{t_{top}}$ = 80nm) is far higher than the penetration depth of visible light in metals ($\boldsymbol{t_{pd}} \approx$ 30 nm), the magnetic information is only gathered from the topmost layer. Figure 3.13a displays the MO magnetization loop measured using MOKE. The MO sensitivity axis coincide with the presented magnetic domain images in Figure 3.13b and e. The magnetization switch at $+\boldsymbol{H_{ext}}$ correspond to the reversal in the top CoFeB layer. In the $-\boldsymbol{H_{ext}}$ range, the top layer is homogeneously magnetized along its unidirectional anisotropy direction. The MO curve contains no information about the reversal process in the bottom layer (Figure 3.13a, also compare with Figure 3.12).

Magnetic domain images in Figure 3.13b-g display the magnetic domain configurations at $\boldsymbol{H_{ext}}$ = +25 Oe (b-d) and $\boldsymbol{H_{ext}}$ = −25 Oe (e-g). For the MOVE images, the emphasis is made on the occurring MOGE. At $\boldsymbol{H_{ext}}$ = +25 Oe, the exchange bias in the top layer is compensated and consequently, a multi magnetic domain state is generated (Figure 3.13b). Along the horizontal MOKE sensitivity, the corresponding magnetic domain wall structures are imaged (Figure 3.13c). Domain walls consisting of wall segments of oppositely aligned surface magnetization components are revealed. At this field value, the bottom layer is homogeneously magnetized along the applied field direction. The same magnetic domain configuration imaged in MOVE sensitivity shows, similar to data shown in Figure 3.11, the same MO

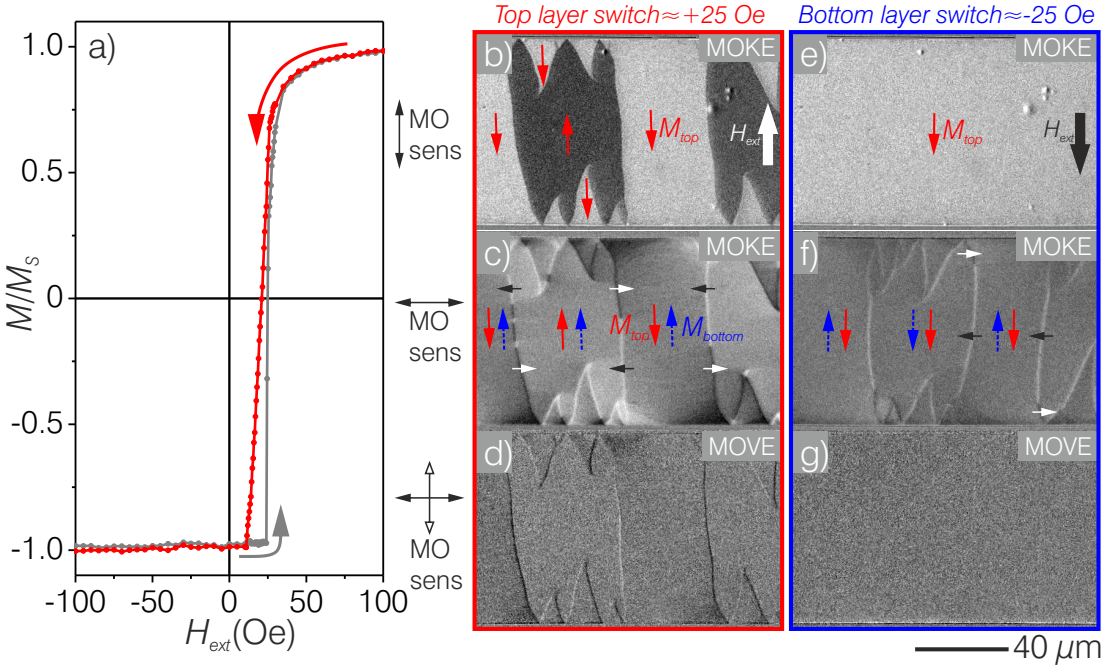

Figure 3.13: (a) Magneto-optically measured magnetization loop along the exchange bias direction of a bilayer thin film structure. (b-d) and (e-g) exhibit the magnetic domain configuration at +25Oe and −25Oe in the top and bottom CoFeB layers, respectively. The applied MO effect and the corresponding MO sensitivities are indicated for each row. Possible magnetization directions are sketched for both layers. (Sample: [Si/ SiO_2] 300 μm/ Ta 3 nm/ NiFe 2.5 nm/ IrMn 7 nm/ CoFeB 80 nm/ Ta 3 nm/ NiFe 2.5 nm/ IrMn 7 nm/ CoFeB 80 nm/ TaN 5 nm)

contrast for magnetic domains with antiparallel magnetization alignment. At the domain boundaries, an alternating MO contrast, originating from MOGE can be observed. Similar to Figure 3.11b and d, none of the domain wall transitions are visible. All boundaries display alternating, homogeneous dark or bright MO contrast (Figure 3.13d).

Now, by applying the $\boldsymbol{H_{ext}}$ in the opposite direction, at -25 Oe, the bottom CoFeB layer magnetization is switched (Figure 3.13e-g). With MOKE sensitivity aligned along the effective magnetic anisotropy axis, the top layer is homogeneously magnetized (Figure 3.13e). However, the orthogonal MOKE sensitivity reveals magnetic domain wall structures in the top layer. Comparing figure 3.13e and f, unveils that the walls in the top layer are 0° domain walls, where no change of magnetization occurs on either side of the wall. They originate from the bottom layer due to interlayer magnetostatic interactions. Antiparallelly magnetized compensating domain walls form in the neighboring CoFeB layers to reduce the domain wall energy (compare sketches in Figure 3.12 and magnetic domain images in Figure 3.13e-f). Thus, domain walls and magnetization gradients originating from the neighboring magnetic domains are untangled. Imaging the same magnetic domain configuration in MOVE illumination geometry, a homogeneous MO contrast is observed throughout to magnetic film and unlike the MOVE images in Figure 3.11b,d and Figure 3.13d, exhibits no MOGE contrast at the domain walls, which proves that MOGE originates purely from magnetization gradients, the effect is insensitive to magnetic domain walls and wall transitions.

3.3 Integrated magnetoelectric response measurement setup

The sensor response of investigated magnetoelectric (ME) sensors are obtained electrically by measuring the voltage difference induced at the piezoelectric film. As has been discussed under Section 2.3.1, the figure of merits for ME sensors include the frequency dependency of $\boldsymbol{\alpha_{ME}}$, the bias field $\boldsymbol{H_{bias}}$ dependency of the ME response $\boldsymbol{\alpha_{ME}}$ and the limit of detection curves. For measuring ultra low magnetic fields (pT to fT range), i.e. limit of detection curves of a sensor, it is essential to isolate the sensor from several ambient noise sources, which can stem from external magnetic and electric fields and acoustic vibrations. Details to achieve efficient isolation and mitigate such external noise sources have been reported in [25].

Here, the emphasis is given on the ME response measurement setup integrated to *Zeiss Axio Imager* microscope. The idea is to perform *in-situ* magnetic domain observations at ME sensor operation. Without application of a transverse magnetic

field $\boldsymbol{H_{bias}}$, the one axis magnet described in the previous section is employed to acquire the ME response. The inner coils are used for the low amplitude, alternating magnetic field $\boldsymbol{H_{mea}}$. The outer coils are employed for application of a DC offset $\boldsymbol{H_{ext}}$. The entire magnetization loop of the investigated sensors can be covered and the overall $\boldsymbol{H_{ext}}$ dependency of ME response can be obtained.

A schematic of the integrated ME response measurement setup is given in Figure 3.14. A lock-in amplifier *SR830 DSP* from *Stanford research systems* is employed for sending a sinusoidal voltage signal to the bipolar power supply (BPS) that is connected to the inner coils (BPS 1 in Figure 3.14). In this case, the lock-in amplifier is internally triggered, where the signal amplitude, as well as the frequency are manually selected. Voltage signal to operate the bipolar power supply (BPS 2 in Figure 3.14), which is connected to the outer coils, is sent from the computer. The ME sensor is connected to the single-ended signal input of the lock-in amplifier, where only the signals with the same frequency as has been set for BPS 1 at the lock-in amplifier is acquired. The measured data from the lock-in amplifier is accessed through the GPIB interface and saved at the computer.

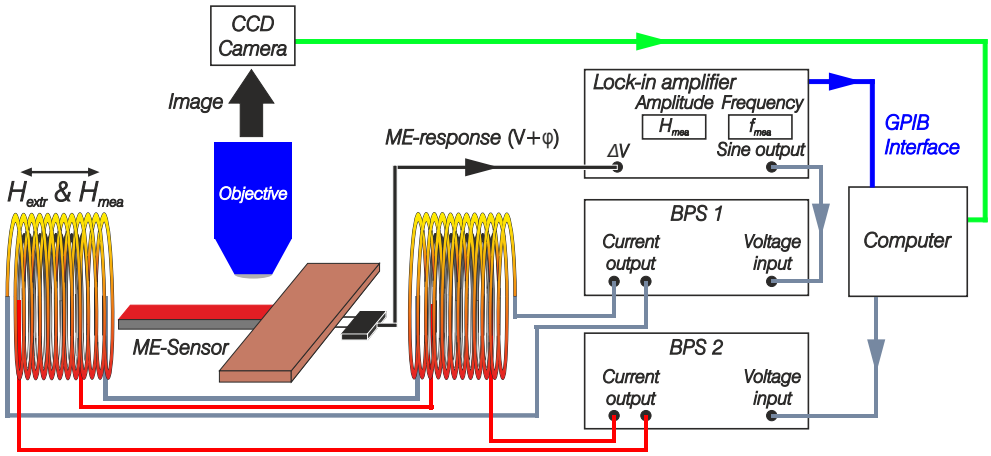

Figure 3.14: Schematic of ME response measurement setup with two pairs of electrically uncoupled electromagnets along one axis, integrated to the MO microscope for simultaneous acquisition of the sensor and magnetic domain response.

Another ME response measurement setup is used for measuring ME response in presence of a $\boldsymbol{H_{bias}}$ (Figure 3.15). For this purpose the two axis electromagnet setup is used (Figure 3.15). The electromagnets aligned along the long axis of the cantilever are utilized for simultaneous application of both $\boldsymbol{H_{ext}}$ and $\boldsymbol{H_{mea}}$ (BPS 2 in Figure 3.15). Both fields are controlled by the computer. $\boldsymbol{H_{mea}}$ frequency and amplitude are set prior to the measurement. Moreover the voltage signal sent to BPS 2 is, likewise, sent to the externally triggered lock-in amplifier as the reference signal. The electromagnets positioned perpendicular supply the $\boldsymbol{H_{bias}}$, which is controlled manually at BPS 1 (Figure 3.15).

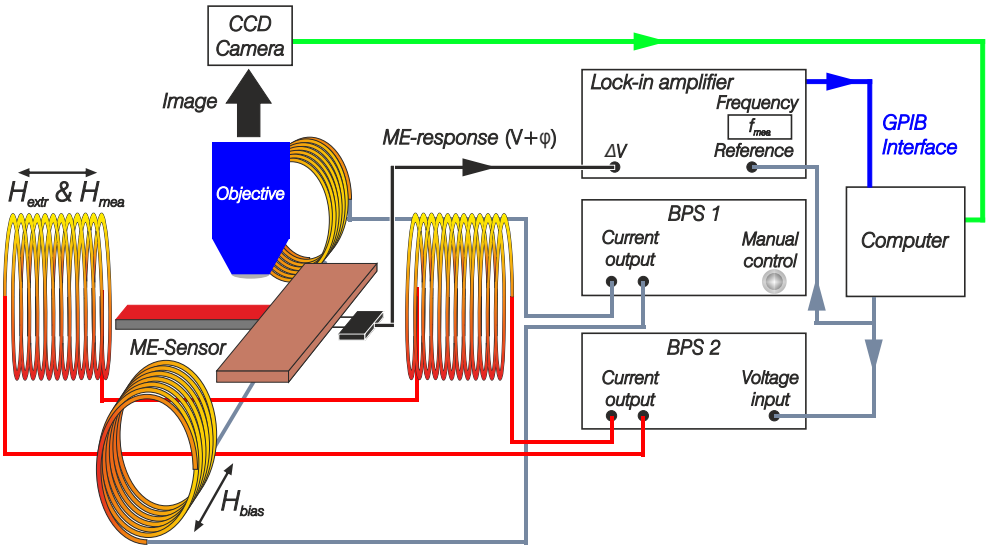

Figure 3.15: Schematic of ME-response measurement setup with a quadrupole electromagnet arrangement, integrated to the MO microscope for simultaneous acquisition of the sensor and magnetic domain response.

4 Influence of stress and topology on magnetic domain configuration

In this chapter, magnetic domain and domain wall effects in $(Fe_{90}Co_{10})_{78}Si_{12}B_{10}$ (FeCoSiB) films are reviewed. In its amorphous state, FeCoSiB possesses relatively high magnetostrictive properties ($\boldsymbol{\lambda_s} \approx 35{\cdot}10^{-6}$) [112] and is well known to be magnetically very soft. The magnetization induced magnetic anisotropy field $\mathbf{H_k}$ lies in the range of 5 Oe to 10 Oe. Therefore, its resulting $\boldsymbol{d\lambda_s/dH_{mea}}$ response is intrinsically high, which makes it one of the possible candidates to be used as the magnetic sensing layer in composite ME sensors.

The chapter begins by covering the cause of the commonly observed hysteresis in FeCoSiB films, as well as the influence of film stress on the local magnetic anisotropy distribution and the transpiring magnetic domain configurations (Section 4.1) [51]. Lastly, the effect of surface topology on magnetic domain formation and overall magnetization behavior is discussed (Section 4.2). All in all, the displayed results are relevant for other alloys with similar magnetic properties.

4.1 Magnetization hysteresis and the effect of stress anisotropy

Figure 4.1a and b display inductively measured hard axis ($\boldsymbol{H_{ext}} \perp \mathbf{K_u}$) magnetization loops and Barkhausen measurements of a 4 μm thick FeCoSiB film sputter deposited on a thermally oxidized Si wafer ([Si/ SiO_2] 300 μm). A well defined, in-plane magnetization induced magnetic anisotropy $\mathbf{K_u}$ is introduced along the short axis of the magnetic structure by post-deposition heat treatment at 250°C for 30 minutes in the presence of a magnetically saturating field $\mathbf{H_{sat}} \approx 2300$ Oe (see the sketch in Figure 4.1).

The investigated sample possess a magnetic anisotropy field $\mathbf{H_k} \approx 5$ Oe, corresponding to a $\mathbf{K_u}$ of 360 J/m^3 (FeCoSiB saturation magnetization $\mathbf{M_s} = 1.8$ T).

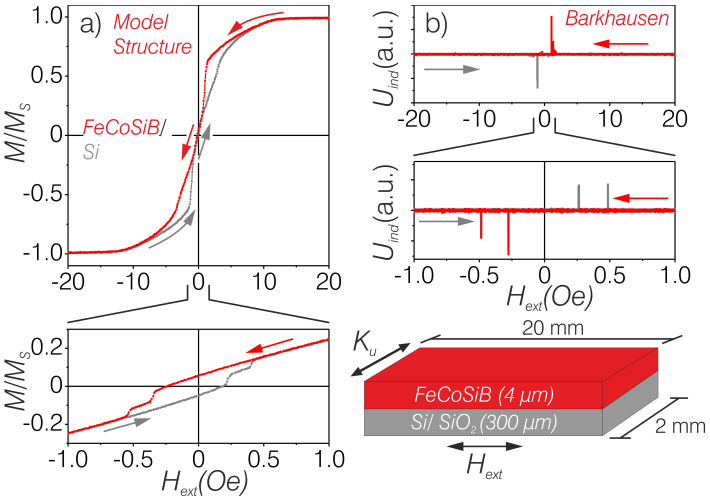

Figure 4.1: (a) and (b) display inductively measured magnetization and Barkhausen loops, respectively, for a FeCoSiB model structure. At the bottom of each graph, minor loops measured between ±1 Oe are displayed. Sample dimensions, $\mathbf{K_u}$ and $\boldsymbol{H_{ext}}$ are indicated. Barkhausen measurements performed are by Dr. Iulian Teliban. Sample courtesy of Dr. André Piorra. (Sample: [Si/ SiO_2] 300 μm/ FeCoSiB 4 μm)

The hard axis loop displays pronounced hysteresis at intermediate $\boldsymbol{H_{ext}}$ regime (Figure 4.1a). The magnetic response is highly $\boldsymbol{H_{ext}}$ history dependent. The magnetic susceptibility is different as $\boldsymbol{H_{ext}}$ is decreased from and increased to magnetic saturation. With decreasing $\boldsymbol{H_{ext}}$, at $\mathbf{H_{ext}} \approx 1.3$ Oe a sudden drop in magnetization occurs (Figure 4.1a), which can also be detected as sudden voltage spikes in the Barkhausen noise measurement measured in the same $\boldsymbol{H_{ext}}$ range (Figure 4.1b). Subsequently, magnetization follows $\boldsymbol{H_{ext}}$ almost linearly and with further $\boldsymbol{H_{ext}}$ increment, magnetic saturation is reached. Only a small portion in the low $\boldsymbol{H_{ext}}$ regime, the magnetization response seem to be almost hysteresis free. However, the minor magnetization and Barkhausen loops measured in $\boldsymbol{H_{ext}} = \pm 1$ Oe demonstrate two step magnetization change and voltage spikes (graphs at the bottom in Figure 4.1a and b). This magnetization response is reminiscent of an easy axis reversal behavior. Both full and minor loops indicate towards magnetic domain activity as the cause of the hysteretic magnetization response. However, no information on the magnetic domain configuration and/ or the dominant magnetization reversal mechanism can be acquired from the inductive measurements. In order to reveal the origin of the occurring magnetic hysteresis magnetic domain observations in low and high resolution are conducted.

The MO imaging in low magnification displays a highly $\boldsymbol{H_{ext}}$ history dependent magnetic domain response (Figure 4.2). The displayed magnetic domain images are obtained via a 2.5x magnification objective with 0.06 numerical aperture. At this magnification, the entire width of the structure (2 mm) is imaged. In the probed region, decreasing $\boldsymbol{H_{ext}}$ from magnetic saturation, a homogeneous magnetization response is observed until $\mathbf{H_{ext}} \approx 1$ Oe (Figure 4.2a). Subsequently, a sudden reorganization in the magnetic domain structure takes place (Figure 4.2b), which corresponds to the previously discussed magnetization drops and voltage spikes in

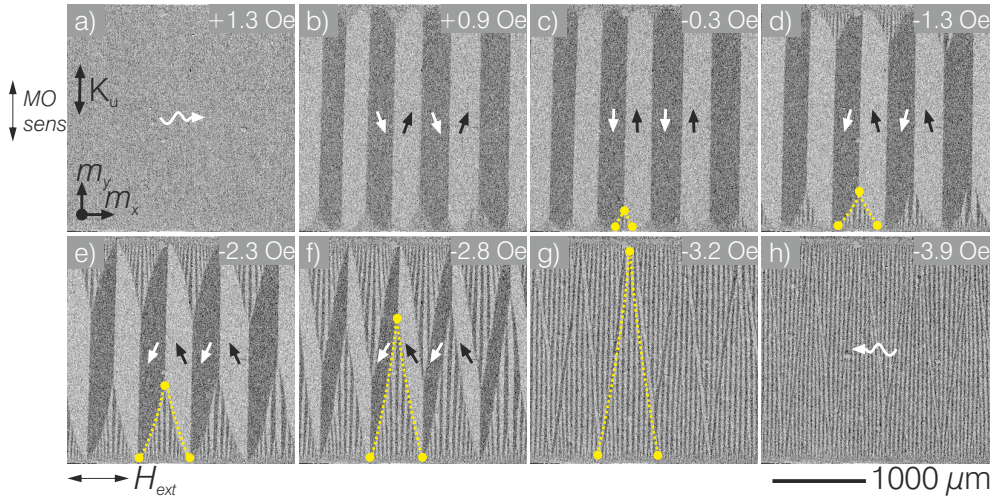

Figure 4.2: Some selected magnetic domain images demonstrating the magnetic domain configurations during magnetization reversal along the hard axis of magnetic anisotropy are shown. MO sensitivity and $\boldsymbol{H_{ext}}$ axes are indicated. For imaging, a 2.5x objective with 0.06 NA is used. (Sample: [Si/ SiO_2] 300 μm/ FeCoSiB 4μm)

Figure 4.1a and b, respectively. The resulting magnetic domain configuration consists of large magnetic domains in the middle with closure domains at the sides of the magnetic structure. Already in this magnification small domain modulations can be observed inside the closure domains. As $\boldsymbol{H_{ext}}$ is further reduced, closure domain structures with magnetization alignments antiparallel with respect to $\boldsymbol{H_{ext}}$ shrink and vice versa for closure domains with magnetization aligned parallel to $\boldsymbol{H_{ext}}$ (Figure 4.2c and d). In these regions, the magnetization response is governed by sudden almost maximum magnetization change from $\boldsymbol{m_y}$ to $\boldsymbol{m_x}$ through magnetic domain wall motion. Analyzing the middle of the magnetic structure, the magnetization seem to follow $\boldsymbol{H_{ext}}$ almost linearly through coherent rotation of magnetization. As $\boldsymbol{H_{ext}}$ is increased in the other direction, closure domains expand further into the middle of the structure (Figure 4.2e and f). The volume of the large domains shrink. The resulting magnetic domain configuration consists of high density magnetic domains and, consequently, domain walls (Figure 4.2h). Finally, increasing $\boldsymbol{H_{ext}}$ further leads to magnetic saturation along $\boldsymbol{H_{ext}}$ direction (not shown in the images).

Magnetic domain images at higher magnification expose certain features like the local magnetic domain density and modulations inside closure domains (Figure 4.3). For imaging, a 10x objective with 0.25 NA is used. Almost one-third of the structure width is imaged. The bottom of the images is the structure's long axis. With $\boldsymbol{H_{ext}}$ decreased from magnetic saturation, before the previously discussed magnetization jump, the magnetic domain configuration in the middle consists of periodic stripe-like domains with high domain wall density aligned along $\mathbf{K_u}$ (Figure 4.3a and b). At small distances asymmetric Néel walls interact with each other and the mag-

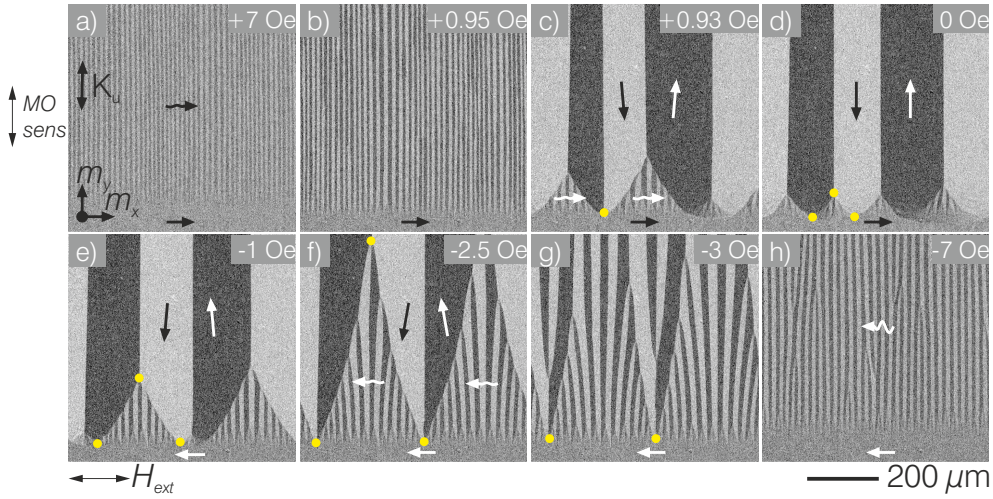

Figure 4.3: Some selected magnetic domain images demonstrating the magnetic domain configurations during magnetization reversal along the hard axis of magnetic anisotropy are shown. MO sensitivity and $\boldsymbol{H_{ext}}$ axes are indicated. For imaging a 10x objective with 0.25 NA is used. (Sample: [Si/ SiO_2] 300 μm/ FeCoSiB 4μm)

netization susceptibility drops significantly. This magnetic domain state is named the blocked domain state [37, 113–115]. However, micromagnetic simulations show ANW vortices interact repulsively in short distances, making this domain configuration a metastable state [77]. As $\boldsymbol{H_{ext}}$ is further decreased, the magnetization reversal proceeds almost locally uniform with limited magnetic domain reorganization. Nevertheless, small but irreversible modifications in the magnetic domain width can be observed (compare Figure 4.3a and b). Meanwhile, at the very edges of the film, the MO contrast remains to be uniformly gray, which indicates the edge region is yet homogeneously magnetized along $\boldsymbol{H_{ext}}$ direction. Subsequently after the sudden magnetization drop, magnetization modulations inside the closure domains are exposed more clearly (Figure 4.3c). Instead of homogeneously magnetized closure domain structures encountered in Landau patterns, the MO images display modulations displaying bright and dark MO contrast inside the closure domains, which indicate tilted magnetization alignment, away from closure domains' net magnetization direction. As $\boldsymbol{H_{ext}}$ is increased from the remanent state in the other direction and the modulated closure domains with net magnetization direction aligned along $\boldsymbol{H_{ext}}$ move into the material. Meanwhile, a sudden 180° magnetization reversal occurs at the very side region (Figure 4.3d to e). With $\boldsymbol{H_{ext}}$ applied along the long axis of the structure (also at remanence), the magnetization at the side is always aligned along the long axis. Moreover, the expanding closure domains never penetrate the very side regions (Figure 4.3g and h). Both observations confirm the 90° tilting of local $\mathbf{K_u}$ with respect to the intended axis (short axis of the structure). This observation also explains the hysteresis observed in inductive measurements performed at $\boldsymbol{H_{ext}} = \pm 1$ Oe (magnetization and Barkhausen measurements at the

bottom of Figure 4.1a and b). It stems from the easy axis magnetization reversal at sides of the cantilever and the two step magnetization jump for both increasing and decreasing $\boldsymbol{H_{ext}}$ originates from local $\mathbf{K_u}$ at either edge being different in strength ($|\mathbf{K_{u,\ left}}| \neq |\mathbf{K_{u,\ right}}|$).

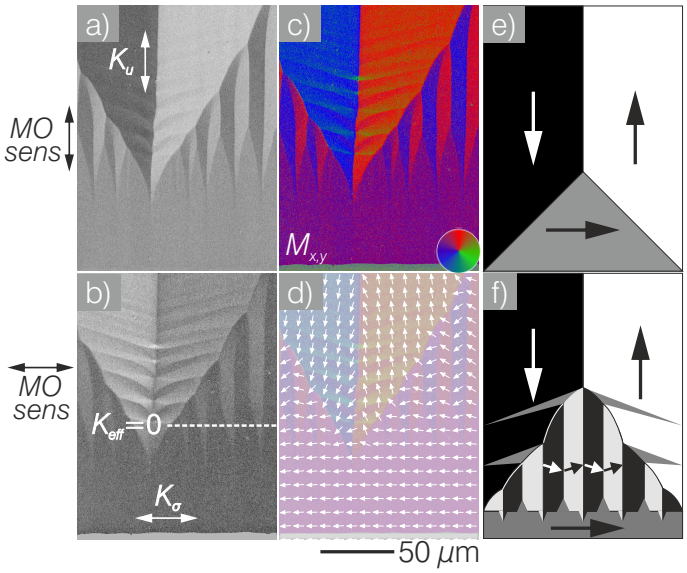

Figure 4.4: (a) and (b) displays the magnetic domain configuration at $\mathbf{H_{ext}}$= 2 Oe in two orthogonal MO sensitivities. (c) and (d) are the calculated quantitative color image and local magnetization distribution, respectively. Commonly observed Landau and the discussed modulated magnetic domain patterns are sketch in (e) and (f), respectively. MO sensitivities and the $\boldsymbol{H_{ext}}$ direction are indicated. $\mathbf{K_u}$ and $\mathbf{K}_\sigma$, as well as $\mathbf{K_{eff}} = 0$, are sketched. For imaging, a 50x objective with 0.5 NA is used. (Sample: [Si/ SiO_2] 300 μm/ FeCoSiB 4 μm)

In order to obtain information on the magnetization distribution inside and in the vicinity of the closure domains, quantitative magnetic domain imaging is performed. Figure 4.4a and b display two high resolution MO domain images, where quantitative magnetic domain imaging is applied. The MO sensitivity in the images are orthogonal with respect to each other. The obtained magnetization color (Figure 4.4c) and vectorial (Figure 4.4d) maps display internally folded closure domain structures. Furthermore, observable best in Figure 4.4b, the internal domain structure of the domains in the middle is likewise densely modulated. The modulated regions are separated by low angle ANWs and the magnetization inside them is tilted away from the net magnetization direction. Due to the domain modulation, the net magnetization inside the closure domains is reduced and a bended, non-perpendicular domain boundary is formed between the closure domains and the domains in the middle. Additionally, at the very edge, the magnetization is aligned uniformly perpendicular to the intrinsic magnetic anisotropy axis. Two additional sketches displayed in Figure 4.4e for a typical Landau pattern and Figure 4.4f for the investigated unconventional non-Landau pattern demonstrate the discussed dif-

ferences in a nutshell.

The overall magnetic domain formation at the edges is governed by minimization of magnetoelastic energy. Heat treatment procedure during introduction of a well-aligned $\mathbf{K_u}$ to the FeCoSiB film leads to stress relaxation at the edges of the film and a tensile stress gradient along the long axis of the magnetic structure. The induced tensile stress is highest at the very edge (bottom of the discussed images, e.g. Figure 4.4a and b) and diminishes further into the material. This results in a zero effective magnetic anisotropy $\mathbf{K_{eff}}$ line ($\mathbf{K_{eff}} = 0$ J/m^3) in the magnetic material (Figure 4.4b), where $\mathbf{K_u}$ is effectively compensated by the orthogonally aligned stress anisotropy $\mathbf{K_\sigma}$ ($\mathbf{K_u}$+$\mathbf{K_\sigma} = \mathbf{K_{eff}} = 0$ J/m^3). The effective stress difference $\boldsymbol{\Delta\sigma}$ required to compensate $\mathbf{K_u}$ is calculated from (4.1).

$$|\mathrm{K_u}| = |\mathrm{K_\sigma}| = \frac{3}{2} \cdot \lambda_s \cdot \Delta\sigma \tag{4.1}$$

With $\boldsymbol{\Delta\sigma} = 8$ MPa the initial $\mathbf{K_u}$ is canceled out and when $\boldsymbol{\Delta\sigma} > 8$ MPa (bottom of the $\mathbf{K_{eff}} = 0$ line in Figure 4.4b), the $\mathbf{K_{eff}}$ sign changes. Similar stress induced local $\mathbf{K_{eff}}$ variations have been reported for magnetostrictive Ni_xFe_{x-1} films [116].

The source of the resolved modulations can be clarified qualitatively by calculating the total magnetoelastic energy density inside FeCoSiB (2.14). With the Young's modulus $\mathbf{E} = 150$ GPa [117] and the Poisson ratio $\boldsymbol{\nu} = 0.38$ [118], $\mathbf{e_{total}}$ is approximated as 100 J/m^3, which corresponds to a magnetoelastic anisotropy field of $\mathbf{H_{k,\,me}} = 1.6$ Oe.

In regions with $\mathbf{K_{me}} > \mathbf{K_{eff}}$ the magnetic domain formation is governed by magnetoelastic effects. Magnetic domain modulations develop inside the closure domains as well as in the gusset of the central magnetic domains to minimize the self-stress energy (most clearly observed in Figure 4.4b).

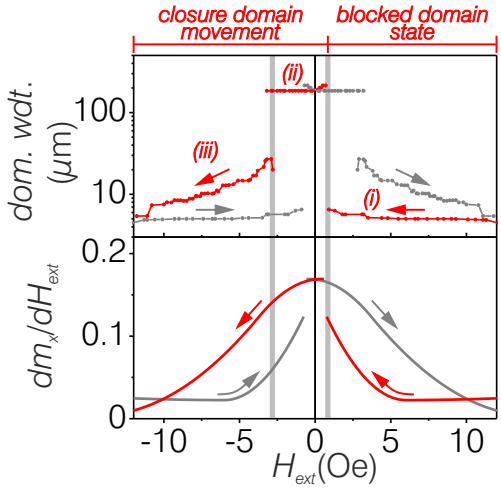

Figure 4.5: Average domain width (dom. wdt.) in logarithmic scale and magnetic susceptibility (dm_x/dH_{ext}) are plotted against the applied $\boldsymbol{H_{ext}}$. MO images in Figures 4.2 and 4.3 are used to measure/calculate the domain width and susceptibility curves. Distinct regimes are marked for clarity in domain width plot. (Sample: [Si/ SiO_2] 300 μm/ FeCoSiB 4 μm)

Up until now, the presence of two different magnetic domain configurations depending on $\boldsymbol{H_{ext}}$ history and their response to changing $\boldsymbol{H_{ext}}$ have been reviewed.

The average domain width and magnetic susceptibility with varying $\boldsymbol{H_{ext}}$ plotted in Figure 4.5 reveals the origin of the hysteretic magnetization response. The domain width plot is also a measure of domain wall density and are indirectly proportional to each other. At high $\boldsymbol{H_{ext}}$ regime ***(i)***, the average domain width is around 5 μm and possesses very limited magnetic susceptibility, both of which stay constant over a wide $\boldsymbol{H_{ext}}$ range until the sudden magnetization jump occurs. Subsequently, encompassed in region ***(ii)***, the average distance between two neighboring domain walls increases abruptly to 200 μm. At this time, the stable state magnetic domain configuration consisting of wide domains in the middle with modulated closure domain structures at the sides display a nearly twofold increase in magnetic susceptibility. As has been discussed previously, increasing $\boldsymbol{H_{ext}}$ leads to a magnetization response that is a combination of coherent rotation and closure domain motion (regions ***(ii)*** and ***(iii)***). Approximately at $\boldsymbol{H_{ext}} = \pm 3$ Oe, modulated closure domains approaching from both sides gradually decrease the domain width, thus increase the domain wall density and the magnetic responsiveness of the film drops. The discussed data exposes the influence of magnetic domain walls on magnetization susceptibility (Figure 4.5). Densely packed ANW tails interact with each other over long distances and decrease the magnetic susceptibility. Moreover, existence of different magnetic domain configurations with distinct domain wall densities generate the measured magnetization hysteresis.

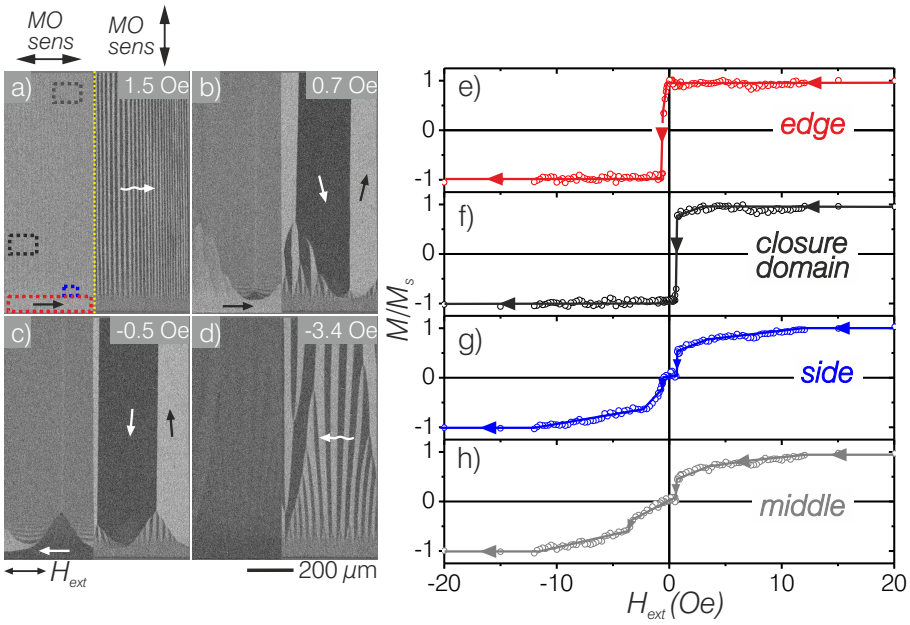

Figure 4.6: (a-d) some selected magnetic domain images during magnetization reversal along the hard axis acquired with two orthogonal MO sensitivities. The bottom of the images is the structure edge. (e-h) show the locally analyzed intensity change in selected regions. The evaluated areas are marked in (a). Possible magnetization directions are sketched. (Sample: [Si/ SiO_2] 300 μm/ FeCoSiB 4μm)

Magnetic thin film structures in millimeter in-plane dimensions are in general treated as extended films [44]. Magnetization loops measured along their hard axes show negligible hysteresis and the magnetization response is mostly through coherent rotation. Subtle domain wall motion related reversal processes might even be averaged out in integral measurements. The discussed, unorthodox reversal process occurring by a combination of magnetization rotation and domain wall motion has significant ramifications in terms of local magnetization response on the magnetic material to $\boldsymbol{H_{ext}}$ (Figure 4.6).

Some selected magnetic domain images at crucial points during magnetization reversal along the magnetic structure's hard axis are displayed in Figure 4.6(a-d). In order to obtain the images dual-wavelength imaging is used. The displayed magnetization curves (Figure 4.6e-h) are obtained by locally analyzing the intensity change at different regions in the same magnetic domain images. Only one $\boldsymbol{H_{ext}}$ sweep is shown. Decreasing $\boldsymbol{H_{ext}}$ from $+\mathbf{H_{sat}}$, at intermediate $\boldsymbol{H_{ext}}$ regime, where the blocked magnetic domain state is stable and the magnetization response is almost identical in all regions except at the very edge. The edge region is homogeneously magnetized along $+\boldsymbol{H_{ext}}$ direction (Figure 4.6a). At $\boldsymbol{H_{ext}} = +1$ Oe, the magnetic domain configuration in the middle reorganizes and the analyzed closure domain, side and middle regions experience the sudden magnetization drop (Figure 4.6f-h). The analyzed closure domain is antiparallelly magnetized with respect to the momentarily $\boldsymbol{H_{ext}}$ direction. As $\boldsymbol{H_{ext}}$ is reversed in the minus direction, the edge region undergoes a magnetization switch (also compare Figure 4.6b and c). Meanwhile, the closure domain expands into the middle towards the opposite side region (Figure 4.6c), causing a second magnetization drop for the region of interest. Yet, no closure domain has reached the analyzed region in the middle, where the magnetization still follows $\boldsymbol{H_{ext}}$ linearly. Increasing $\boldsymbol{H_{ext}}$ further, closure domains from both sides move through the middle region and causing the second sudden magnetization drop for the middle region (Figure 4.6h). Non-coherent magnetization reversal through domain wall motion results in locally varying magnetic response. Although inductive measurements (Figure 4.1) might average out such sudden local magnetization jumps induced by closure domain movement, MO imaging resolves local hysteretic magnetization processes.

Such stress induced magnetic effects are not unique to singlelayer FeCoSiB films but also influence the magnetic domain structure in laminated structures (Figure 4.7). Figure 4.7a displays the inductively measured hard axis magnetization loop of a laminated, unbiased FeCoSiB layer stack. The total FeCoSiB thickness is 2 μm. Similar to data shown for the singlelayer FeCoSiB films (Figure 4.1a), the hard axis magnetization loops for the laminated structure demonstrate a hysteretic magnetization response both in the full and minor loops (Figure 4.7a and

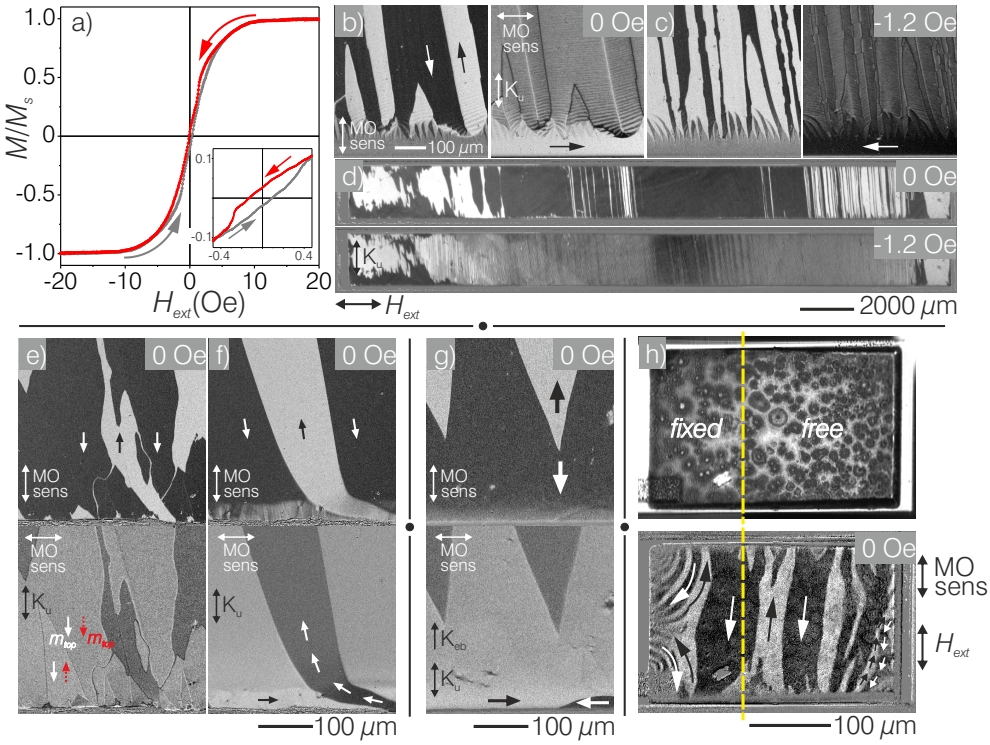

Figure 4.7: (a) Full and minor (inset) loops of a multilayered, unbiased FeCoSiB sample are shown. Complementary magnetic domain configurations in high magnification and two orthogonal MO sensitivities at remanence (b) and with a small $\boldsymbol{H_{ext}}$ (c) are shown. Magnetic domain configurations in low magnification at same $\boldsymbol{H_{ext}}$ values as in (b-c) are displayed in (d) (Sample: Substrate/ FeCoSiB 50 nm/ Ta 5 nm/ {FeCoSiB 100 nm/ Ta 5 nm}×19/ FeCoSiB 50 nm). (e-f) magnetic domain configurations in demagnetized state of FeCoSiB bilayers obtained with orthogonal MO sensitivities are shown (Samples: (e) Substrate/ FeCoSiB 75 nm/ Ta 5 nm/ FeCoSiB 75 nm; (f) Substrate/ FeCoSiB 200 nm/ Ta 5 nm/ FeCoSiB 200 nm). (g) Complementary magnetic domain images in demagnetized state of an exchange biased multilayer (Sample: Substrate/ {Ta 5 nm/ Cu 3 nm/ IrMn 7 nm/ FeCoSiB 200 nm}×5). (h) Optical and MO images of a ME sensor are shown (Sample: SiO_2 0.65 μm/ AlN 1 μm/ FeCoSiB 1.9 μm). Possible magnetization directions, H_{ext} and MO sensitivity axes are indicated.

its inset). Magnetic domain observations show that the $\mathbf{K_u}$ at the very edges are tilted away from the intended anisotropy axis (short axis of the structure) due to stress relaxation (Figure 4.7b and c). Furthermore, magnetic domain modulations can clearly be observed at the vicinity of the zero magnetic anisotropy line. Large view magnetic domain images also show a locally varying magnetization response to $\boldsymbol{H_{ext}}$. A complicated domain pattern emerges as the $\boldsymbol{H_{ext}}$ is applied along the hard axis (Figure 4.7d). Locally varying magnetic domain wall density leads to spatially changing magnetic response.

It should be kept in mind that the stress relaxation is a function of layer thickness. Magnetic domain images in Figure 4.7e and f display the thickness dependency of the stress relaxation at the edges. The shown complementary magnetic domain images with orthogonal MO sensitivities are obtained from FeCoSiB bilayer structures with symmetric FeCoSiB layers. Figure 4.7e and f possess 75 nm and 100 nm individual FeCoSiB layer thicknesses, respectively. Features such as 0° compensated wall structures and antiparallelly aligned magnetic domain structures are visible in the complementary domain images (Figure 4.7e). At the edge region, the $\mathbf{K_u}$ is aligned along the intended axis of the magnetic structure. However, the magnetic domain images of the bilayer with 100 nm individual FeCoSiB thickness show a change of $\mathbf{K_u}$ sign at the very edge region. Stress relaxation scales with the total layer thickness.

Similar edge relaxation effects are, likewise, observed in exchange biased magnetic layers. Figure 4.7g displays magnetic domain configuration after hard axis demagnetization of an exchange biased FeCoSiB layer stack. The individual FeCoSiB layer thickness is 200 nm. The intended $\mathbf{K_u}$ and $\mathbf{K_{eb}}$ axis is perpendicular to structure's edge (bottom of the images). $\mathbf{K_u}$ alignment and introduction of $\mathbf{K_{eb}}$ is initialized through post-deposition heat treatment in presence of a magnetically saturating $\boldsymbol{H_{ext}}$. Apparent from the domain images, the $\mathbf{K_{eb}}$ is not high enough to compensate for the demagnetizing field at the edges and spike domains form at the edges elongated towards the middle of the structure. Moreover, evidenced by the dark and bright contrast at the very edge region, $\mathbf{K_{eff}}$ in this area is tilted away from the intended direction and stays perpendicular to it.

The above discussed stress related local anisotropy variations becomes very relevant for magnetic structures with small in-plane dimensions. Figure 4.7h displays a ME sensor in cantilever design with in-plane dimensions of 200 μm x 300 μm. FeCoSiB thickness is 1.9 μm. The fixed and free parts are indicated at the top optical image. The domain wall alignments in the remanent magnetic domain state point out towards continuous tilting of magnetization and thus $\mathbf{K_u}$. The unintended rotation of $\mathbf{K_u}$ is most pronounced in the fixed portion of the cantilever with $\mathbf{K_u}$ tilted almost perpendicular to intended axis at the very edge. The high tensile

stress, the alignment of which also varies locally, rotates $\mathbf{K_{eff}}$ away from the intended anisotropy axis. For ME sensors, the fixed portion does not contribute to the sensor response. Nonetheless, such stress related anisotropy redistribution is also observed at the free edge region.

All in all, the origin of hysteretic hard axis magnetization response to $\boldsymbol{H_{ext}}$ has been exposed for ultra-soft FeCoSiB films with high magnetostrictive properties [51]. Two distinct $\boldsymbol{H_{ext}}$ history dependent magnetization branches linked to separate magnetic domain configurations with different magnetization susceptibilities are exposed. The relative difference in average domain wall density is almost 40 times. At short distances ANW tails interact attractively decreasing the magnetization responsiveness of the magnetic film in the blocked domain state. Furthermore, an unorthodox magnetic domain configuration consisting of regions with internally folded modulated structures are revealed. The heat treatment employed to introduce a well-defined $\mathbf{K_u}$ to the magnetic film leads to stress relaxation at the edges, which results in a tensile stress gradient along the long axis of the structures. At the very edges, the stress induced magnetic anisotropy is high enough to change the sign of the intended $\mathbf{K_u}$ axis. Moreover, the stress state is inhomogeneous, the tensile stress is highest at the very edges and diminishes further into the middle of the structure. A zero magnetic anisotropy line ($\mathbf{K_{eff}} = 0$ J/m^3) is formed, where magnetic domain modulations occur in its vicinity. A non-Landau, internally folded magnetic domain state forms.

4.2 Topological effects

For many applications benefiting from magnetic films as functional layers, the device architectures are generally rather complex and can consist of several layers of magnetic films laminated with non-magnetic layers. In the most simple case, e.g. AMR sensors, the magnetic thin films are deposited on relatively thick substrates. For instance, Permalloy films that have been accepted as one of the gold standards for soft magnetic films, have been subject to considerable amount of research. One important area, where a high level of attention has been paid, is the underlayer on which Permalloy films are deposited. Undesired stress anisotropy contributions might occur during the epitaxial growth of the magnetic films [119, 120]. Moreover, thin Permalloy films deposited on rough surfaces have been shown to display an undesired increase in $\mathbf{H_c}$, which leads to an inverted film behavior ($\mathbf{H_c} > \mathbf{H_k}$) and the measured magnetization loops cease to show the expected well-defined magnetization induced anisotropy [119, 121, 122].

Here, the influence of surface topology on magnetic properties of amorphous FeCoSiB films is investigated. Differently layered FeCoSiB films are sputter deposited

on AlN and Si/ SiO_2 underlayers. The samples have undergone post-deposition heat treatment at 200 °C in presence of an in-plane saturating magnetic field in order to introduce a well-defined $\mathbf{K_u}$. Magnetization loops and magnetic domain images are acquired via inductive BH-loop tracer and MOKE microscopy in longitudinal mode, respectively.

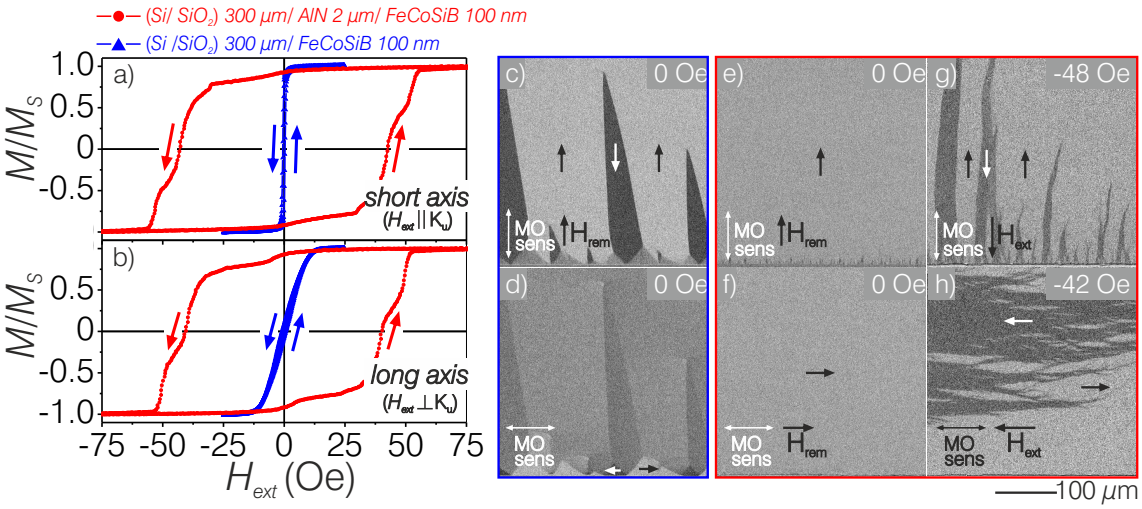

Figure 4.8: (a) inductively measured magnetization loops along the short (a) and long (b) axes of two FeCoSiB singlelayer films with different underlayers. Complementary remanent magnetic domain images of FeCoSiB deposited on SiO_2 after application of $\boldsymbol{H_{ext}}$ along $\mathbf{K_u}$ are displayed in (c) and (d). For FeCoSiB deposited on AlN, (e) and (f) are remanent magnetic domain states after application of $\boldsymbol{H_{ext}}$ along and perpendicular to $\mathbf{K_u}$. Furthermore (g) and (h) with $\boldsymbol{H_{ext}}$ applied along and perpendicular to $\mathbf{K_u}$, respectively. (Samples: (a-d) [Si/ SiO_2] 300 μm/ FeCoSiB 100 nm, (a,b, e-h) [Si/ SiO_2] 300 μm/ AlN 2 μm/ FeCoSiB 100 nm)

Figure 4.8a and b depicts the inductively measured magnetization response for the singlelayer, 100 nm thick FeCoSiB magnetic films sputtered on AlN (red curves) and Si/ SiO_2 (blue curves). Structure dimensions and FeCoSiB deposition parameters are identical for both samples. The short axis magnetization loops correspond to magnetic responses measured along the $\mathbf{K_u}$ for both films. FeCoSiB film deposited on Si/ SiO_2 exhibits very soft magnetic properties. $\mathbf{H_c} \approx 0.5$ Oe and $\mathbf{H_k} \approx 10$ Oe have been measured from the short and long axis magnetization loops, respectively. However, for the FeCoSiB film with the same thickness deposited on AlN, $\mathbf{H_c}$ increases almost 80 times to 40 Oe. Furthermore, the general magnetization behavior is rather isotropic and independent on the $\boldsymbol{H_{ext}}$ history the remanent magnetization state is along the applied $\boldsymbol{H_{ext}}$ direction, all of which indicate an inverted film behavior for the FeCoSiB film deposited on AlN (compare Figure 4.8a and b).

In addition to the inductive measurements, some selected magnetic domain images are displayed in Figure 4.8c-g. The remanent magnetization state $\boldsymbol{H_{rem}}$ for the FeCoSiB on Si/ SiO_2 displays the expected well-defined magnetic domain state

with spike domains and closure domains at the edges of the structure. The net magnetization is aligned along the intended $\mathbf{K_u}$ (Figure 4.8c, d).

Remanent magnetic domain configurations with different $\boldsymbol{H_{ext}}$ history for the FeCoSiB film on AlN are displayed in Figure 4.8e and f. Applying a saturating field along and perpendicular to the induced $\mathbf{K_u}$ and turning it off results in a remanent magnetic domain state that is largely single domain, where the net magnetization is aligned along the $\boldsymbol{H_{ext}}$ direction (Figure 4.8e, f). Applying $\boldsymbol{H_{ext}}$ around the $\mathbf{H_c}$, magnetic domains nucleate with their magnetization alignment parallel to the $\boldsymbol{H_{ext}}$ direction. 180° domain walls are, likewise, aligned along the field direction, largely independent of the relative angle between $\mathbf{K_u}$ and $\boldsymbol{H_{ext}}$. The magnetization reversal, as well as the magnetic domain state seem to be largely dominated by a possible stray field $\mathbf{K_s}$ contribution ($\mathbf{K_s} > \mathbf{K_u}$), which is in well-agreement with the measured surface roughness of AlN and Si/ SiO_2. AFM measurements[1] performed on AlN and SiO_2 show surface roughnesses of 6.4 - 12.9 nm and 0.98 nm, respectively, which in conjunction with the magnetic domain observations indicate that the inverted film behavior is induced by the rough film topography.

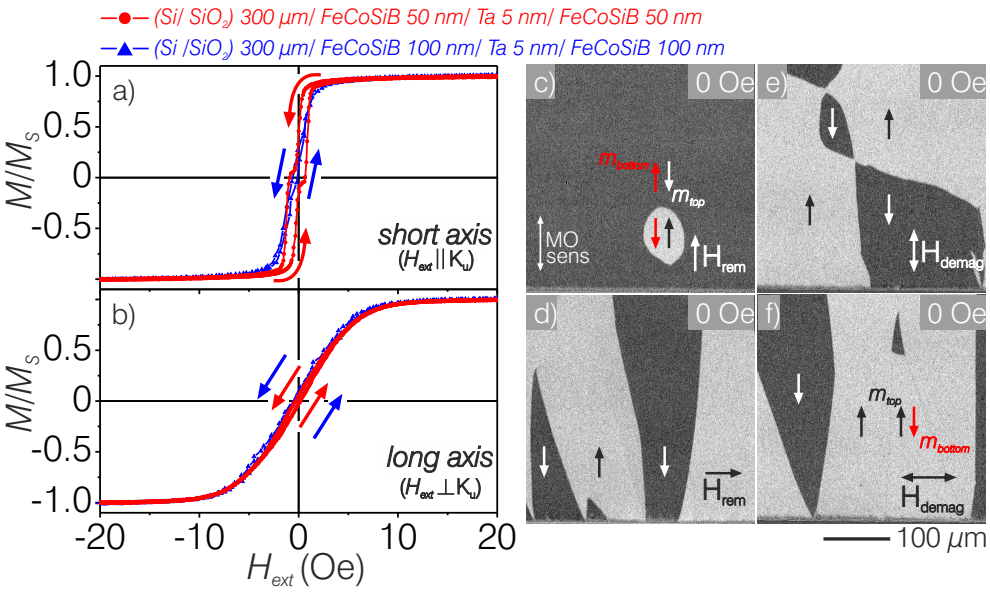

Figure 4.9: Inductively measured magnetization loops along the short and long axis of two different FeCoSiB bilayers sputtered on SiO_2 are shown in (a) and (b), respectively. (c-f) selected magnetic domain images at $\mathbf{H_{ext}} = 0$ Oe of the bilayer with 100 nm total FeCoSiB thickness are displayed (red curve in a and b). The difference between the shown images is the $\boldsymbol{H_{ext}}$ history. The applied MO sensitivity is same in all images (c). (Samples: (a-f) [Si/ SiO_2] 300 μm/ FeCoSiB 50 nm/ Ta 5 nm/ FeCoSiB 50 nm; (a-b) [Si/ SiO_2] 300 μm/ FeCoSiB 100 nm/ Ta 5 nm/ FeCoSiB 100 nm)

For laminated thin films, the underlayer surface topology is transferred further

[1]Private communication. AFM measurements are performed by Christine Kirchhof

to later deposited layers. Figure 4.9a and b show magnetization loops of two FeCoSiB bilayers laminated with a 5 nm Ta layer. Both multilayers are deposited on Si/ SiO_2. The red and blue curves possess 100 nm and 200 nm total FeCoSiB thicknesses, respectively. Both show similar magnetic properties with a well-defined $\mathbf{K_u}$ aligned along the short axis of the magnetic structures. For the bilayer with 50 nm individual FeCoSiB thickness, a pronounced loop shift to $\pm\boldsymbol{H_{ext}}$ occurs due to interlayer magnetostatic interactions. $\mathbf{H_k} \approx 7.5$ Oe is comparable to the singlelayer FeCoSiB film on Si/ SiO_2 substrate (compare Figure 4.8b and Figure 4.9b).

Some selected remanent magnetic domain images with different $\boldsymbol{H_{ext}}$ histories are shown in Figure 4.9c-f for the bilayer with 100 nm total FeCoSiB thickness. Magnetic domain configurations inherent to interacting magnetic layers such as head-to-head, tail-to-tail magnetic domain configurations through compensating domain walls (Figure 4.9c and e) and 0° walls (Figure 4.9f) can be identified. In all cases, the magnetization alignment at $\boldsymbol{H_{ext}} = 0$ Oe is preserved along the induced $\mathbf{K_u}$ axis.

Identically layered FeCoSiB bilayer films are deposited on AlN (Figure 4.10). Similar to its singlelayer counterpart, inductively measured magnetization loops for the 100 nm total FeCoSiB thickness displays a rather isotropic magnetization behavior with $\mathbf{H_c} \approx 40$ Oe for magnetization loops measured along and perpendicular to the $\mathbf{K_u}$ (red curves in Figure 4.10a, b). Doubling the total FeCoSiB layer thickness (blue curves in Figure 4.10a, b), lead to a significant decrease in overall $\mathbf{H_c}$ along both axes. Moreover, $\mathbf{K_u}$ axis induced along the short axis can be more clearly distinguished, which has a more square shape. The effect of topology on the magnetization reversal is weakened to a great extent.

Some selected magnetic domain images of the bilayer for 100 nm total FeCoSiB thickness with different $\boldsymbol{H_{ext}}$ histories are displayed in Figure 4.10c-f. As expected from the inductively measured magnetization loops, at magnetic remanence both FeCoSiB layers are almost fully saturated along the previously applied $\boldsymbol{H_{ext}}$ direction (Figure 4.10c). However, the magnetic domain configurations after demagnetization $\boldsymbol{H_{demag}}$ display overall patchy magnetic domain patterns (Figure 4.10d-f). At the very edge region (bottom of the images), a relatively wide domain configuration ensues, which becomes much finer further into the middle of the sample. The magnetization alignment inside the magnetic domains is along the demagnetization axis (Figure 4.10d, note the $\boldsymbol{H_{demag}}$ and MO sensitivity axes). Now keeping the MO sensitivity same but applying the $\boldsymbol{H_{demag}}$ perpendicular to the $\mathbf{K_u}$, the magnetization alignment inside the magnetic domains is rotated by 90° with respect to the previous case (Figure 4.10e). This is also confirmed by the complementary magnetic domain image with the MO sensitivity axis aligned parallel to the $\boldsymbol{H_{demag}}$ axis (Figure 4.10f). Similar to Figure 4.10c, the very edge region is almost homogeneously saturated and the magnetic domain configuration in the middle consists of a patchy

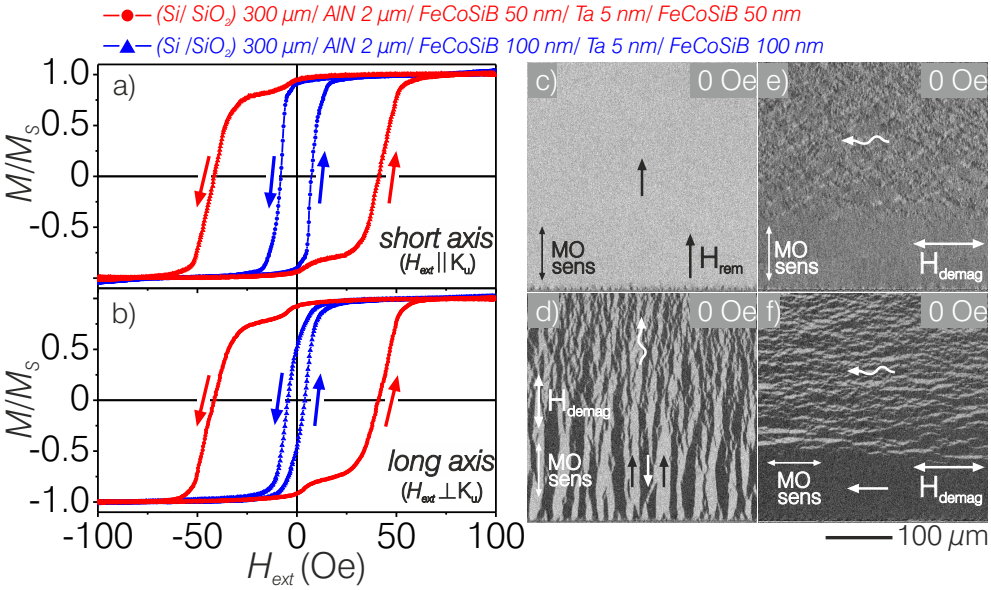

Figure 4.10: Inductively measured magnetization loops along the short (a) and long (b) axes of two different FeCoSiB bilayers deposited on AlN. (c-f) selected magnetic domain images at $\mathbf{H_{ext}} = 0$ Oe for bilayer with 50 nm individual FeCoSiB thickness (red curve in a). The difference between the shown images are the $\boldsymbol{H_{ext}}$ history and the applied MO sensitivities (see also text). (Samples: (a-f) [Si/ SiO_2] 300 μm/ AlN 2 μm/ FeCoSiB 50 nm/ Ta 5 nm/ FeCoSiB 50 nm; (a-b) [Si/ SiO_2] 300 μm/ AlN 2 μm/ FeCoSiB 100 nm/ Ta 5 nm/ FeCoSiB 100 nm)

magnetic domains. Collectively with the magnetization loops, the displayed magnetic domain images indicate that magnetic domain formation and magnetization reversal processes are dictated by the $\mathbf{K_s}$, whose effect is lessened with increasing FeCoSiB layer thickness.

It has been shown that magnetic film topography is very important for single-layer, as well as, laminated magnetic films. $\mathbf{K_s}$ dominance over the $\mathbf{K_u}$ result in inverted film behavior, which lead to a complex, $\boldsymbol{H_{ext}}$ dependent magnetic domain response and an overall isotropic magnetization response. A lot of research has been conducted in exchange coupled films, where undesired topographic coupling can dominate at high interface modulations [123]. On the other hand this dependency can be employed in a controlled manner to alter the magnetic properties of layered films [124]. The displayed data is also very relevant for magnetization behavior in ME sensors with the magnetostrictive material deposited directly on a rough surface, e.g. as discussed on AlN [23, 24].

5 Influence of magnetic domains on magnetoelectric sensor response

In this chapter, the extent of magnetic domain influence on the ME sensor response is covered. For detailed explanation of the observed magnetic domain configurations also see Section 4.1. The investigated sensor is in cantilever design with in-plane dimensions of 2 mm to 25 mm (the free part of the cantilever is 23 mm in length) and is composed of a 2 μm thick AlN layer and a 1 μm thick FeCoSiB layer as the piezoelectric and magnetostrictive layers, respectively. Post-deposition heat treatment at 250°C in presence of a magnetically saturating $\boldsymbol{H_{ext}}$ is applied to induce a well-defined $\mathbf{K_u}$ aligned along the cantilever's short axis.

For imaging, dual-wavelength MO domain imaging is adopted by triggering the camera and the red and blue LEDs at the same frequency. The signal width is half of the signal period. LED signals possess a constant phase shift of 180° with respect to each other to capture images from only one LED. By matching the phase of the camera signal with either LED alternatingly, images from both LEDs are obtained. LED outputs are aligned in orthogonal positions in the backfocal plane of the objective lens to obtain magnetization information in two orthogonal axes. The MO sensitivity axis aligned perpendicular to $\mathbf{K_u}$ is later employed for acquisition of the local hard axis magnetization loops. The displayed magnetization loops and magnetic domain images correspond to the local magnetization response only at a small region in the sample. Nevertheless, the imaged area is directly under the sensor electrode, where it is most relevant for the ME response [125]. Moreover, to obtain one-to-one correspondence with the acquired magnetic domain data, sensor response is recorded in-operando as described in Figure 3.14 at the sensor's mechanical resonance frequency $\mathbf{f_{res}} = 876$ Hz. The AC magnetic field $\boldsymbol{H_{mea}}$ is set to peak-to-peak amplitude of 0.1 Oe. The DC $\boldsymbol{H_{ext}}$ and AC $\boldsymbol{H_{mea}}$ are both applied along the long axis of the cantilever.

For most of the measurements, additional curves depicting the local average domain widths with changing $\boldsymbol{H_{ext}}$ are displayed. The domain widths displaying dark

and bright MO contrast are measured by performing line plots perpendicular to the domain walls at selected images. The exemplary measurement shown in Figure 5.1 for a magnetic domain image at $\boldsymbol{H_{ext}}$ = +4 Oe describes how the data is analyzed. The MO intensity plot, obtained from the measurement line $\boldsymbol{d}$ in Figure 5.1a displays spatially changing MO intensity (Figure 5.1b). Regions with maximum and minimum intensities correspond to bright and dark domains, respectively, which means the $\boldsymbol{m_y}$ components of magnetization for bright and dark domains are antiparallel with respect to each other (see Figure 5.1a). Additionally, in the later displayed curves the average domain widths are plotted, which is defined as half the domain period (Figure 5.1b). Also the extent of bright to dark domain change is depicted by plotting the bright domain to dark domain ratios (B/D). Not shown in the example given in Figure 5.1, where present, more than one domain period is measured and mean values are calculated to obtain the average bright and dark domain widths at distinct $\boldsymbol{H_{ext}}$ values.

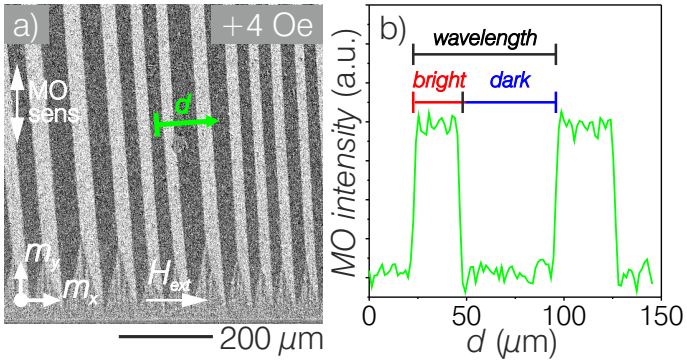

Figure 5.1: (a) displays the magnetic domain image, where the line plot displayed in (b) is measured, which depicts the spatial MO intensity change. The measurement distance $\boldsymbol{d}$ is indicated in (a) and bright, dark domain widths, as well as domain period are marked in (b). (Sample: AlN 2 μm/ [Si/ SiO_2] 300 μm/ FeCoSiB 1 μm)

Figure 5.2 displays the simultaneously measured ME sensor response (a) along with the local magnetization loop (b) and selected magnetic domain images (c-h and l-p). Additional, complementary magnetic domain images obtained by a large view microscope setup for the same sensor are displayed in Figure 5.2i-k. All shown data is obtained as $\boldsymbol{H_{ext}}$ is swept between ±15 Oe. For both loops, the red and gray colored curves indicate responses recorded as $\boldsymbol{H_{ext}}$ is swept from +15 Oe to −15 Oe and vice versa, respectively.

In the intermediate $\boldsymbol{H_{ext}}$ regime, different ME amplitudes are measured depending on $\boldsymbol{H_{ext}}$ history. The ME response is much lower for $\boldsymbol{H_{ext}}$ decreased from magnetic saturation than as $\boldsymbol{H_{ext}}$ is increased from the remanent state. E.g. at $\boldsymbol{H_{ext}}$ = −4.5 Oe, the relative ME response difference is almost as high as a factor of two depending on $\boldsymbol{H_{ext}}$ history (ΔME(−4.5 Oe) = 1 mV). Likewise, the local magnetization response demonstrates magnetic hysteresis in a similar $\boldsymbol{H_{ext}}$ regime, pointing out towards magnetic domain effects as the cause of ME hysteresis (Figure 5.2b).

Some selected magnetic domain images at important points during magnetization

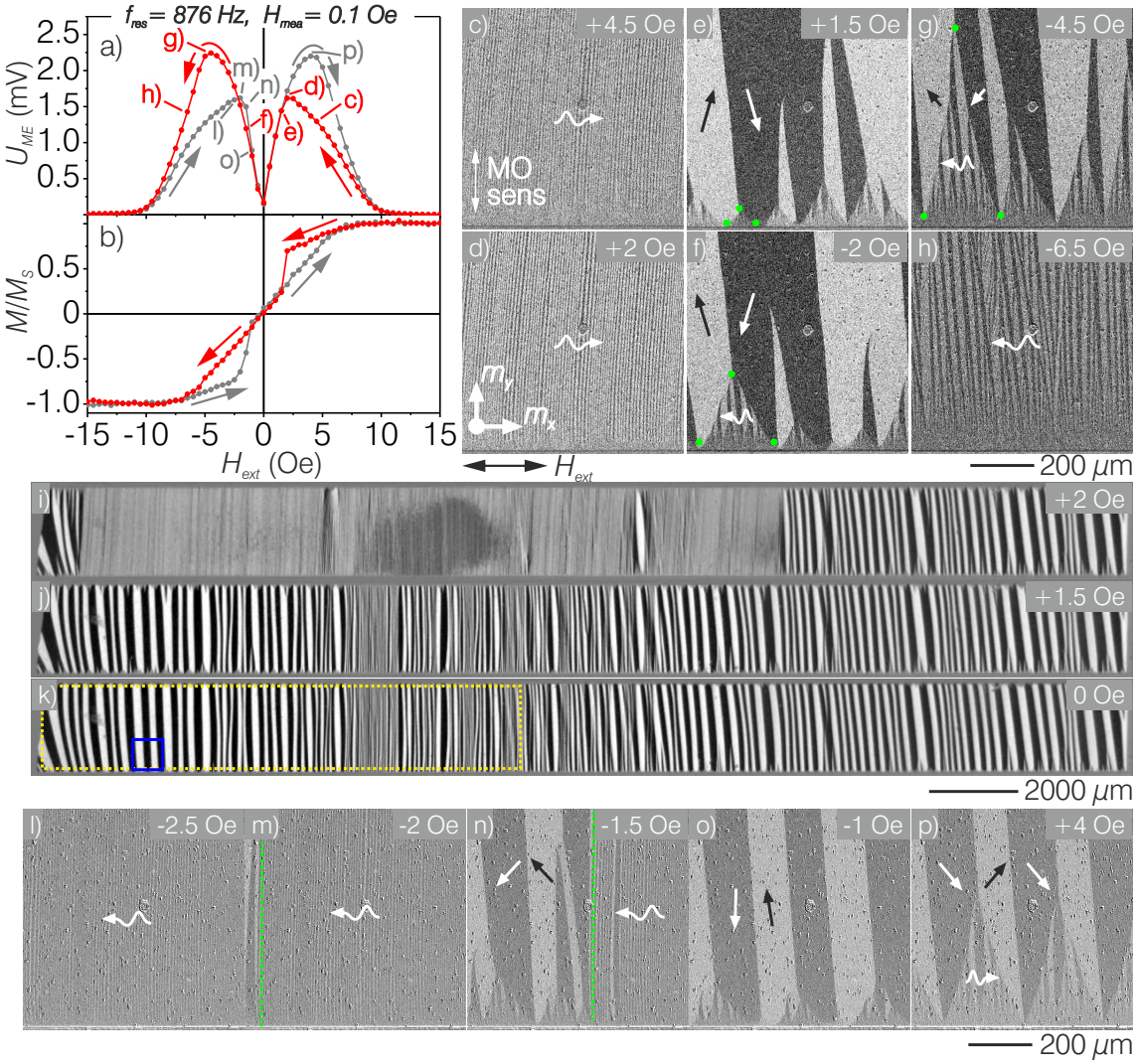

Figure 5.2: The ME sensor and magnetization responses measured between ±15 Oe is displayed in (a) and (b), respectively. Moreover, some selected magnetic domain images are shown in (c)-(h). Large view MO image displaying the magnetic domain configuration in the entirety of the sensor is shown in (i-k), where the area encapsulated by the dotted rectangle signifies the electrode position. (Sample: AlN 2 μm/ [Si/ SiO_2] 300 μm/ FeCoSiB 1 μm)

reversal are displayed in Figure 5.2c-h and l-p as $\boldsymbol{H_{ext}}$ is decreased from $+\mathbf{H_{sat}}$ (red curve) and $-\mathbf{H_{sat}}$ (gray curve), respectively, which are used to correlate the measured ME response with the magnetic domain response. The corresponding ME responses for the presented images are marked in Figure 5.2a. MO imaging reveals that the magnetic domain response is almost identical to the sample discussed in Section 4.1. A blocked domain state with an average domain width of 4.3 μm separated by low angle ANWs appears as $\boldsymbol{H_{ext}}$ is decreased from $\pm\mathbf{H_{sat}}$ and the corresponding ME response is rather low (compare Figure 5.2a and c, d). When $\boldsymbol{H_{ext}}$ is reduced from +2 Oe to +1.5 Oe, the blocked domain state transforms suddenly into a wide domain state with an average domain width of 276 μm (Figure 5.2e). This transformation is also characterized by the abrupt magnetization drop in Figure 5.2b. As has been discussed in Section 4.1, this change is irreversible, meaning increasing $\boldsymbol{H_{ext}}$ to +2 Oe does not revert the wide magnetic domain state back to the blocked domain configuration. $\boldsymbol{H_{ext}}$ has to be reduced from $\pm\boldsymbol{H_{sat}}$ to obtain the blocked domain state, which similarly holds true for the ME response. Therefore, since ME response is obtained through differential measurement of magnetostrictive response (ME $\approx \boldsymbol{d\lambda/dH_{mea}}$), this magnetic domain conversion is not necessarily sensed as a sudden change in ME response, but as a shift of the blocked domains' ME response to that of wide domain state's. In the case of the discussed data, the red curve converts to the gray curve after the transformation (compare d and e in Figure 5.2a and the corresponding domain images). Now in the wide domain state, the magnetization reversal processes through a combination of domain wall motion mostly by movement of modulated closure domains (the region enclosed by yellow dots) and coherent rotation inside the magnetic domains in the middle (compare Figure 5.2e and f). The domain wall alignment after the magnetic domain transformation suggests that $\mathbf{K_u}$ is tilted 5° with respect to the short axis of the cantilever (intended $\mathbf{K_u}$ axis), which plays an important role for the later displayed data. As has been discussed in Section 4.1, overall this domain configuration possesses higher magnetic susceptibility. After the magnetic domain transformation, reducing $\boldsymbol{H_{ext}}$ towards $\boldsymbol{H_{ext}} = 0$ Oe, the ME response decreases. With $\boldsymbol{H_{ext}}$ reversed to minus direction, at $\boldsymbol{H_{ext}} \approx -4.5$ Oe, the ME response is at maximum, corresponding to $\mathbf{H_{wp}} = -4.5$ Oe for the investigated ME sensor (Figure 5.2a and g). The effective (not necessarily the local) magnetic susceptibility is, likewise, the highest at this point. With further increment of $\boldsymbol{H_{ext}}$, the magnetic domain width is decreased (Figure 5.2h) and the measured ME response slowly approaches 0 mV. At this point, the sensor is magnetically saturated along $\boldsymbol{H_{ext}}$ direction and therefore $\boldsymbol{d\lambda/dH_{mea}} = 0$.

Now, with $\boldsymbol{H_{ext}}$ reduced from $-\mathbf{H_{sat}}$, the blocked domain state with net magnetization direction aligned along minus direction appears (Figure 5.2l and m). However to the very left of the magnetic domain image in Figure 5.2m the domain state has

transformed already to a wide domain state. The blocked and wide domain states are seperated by the dotted yellow line for easier recognition. With further decrease of $\boldsymbol{H_{ext}}$, at $\boldsymbol{H_{ext}} = -1.5$ Oe, the boundary separating blocked and wide domain states moves into the material and nearly half of the imaged area is comprised of blocked and wide domain states (Figure 5.2n). The stepwise magnetic domain transformation is also detected in the measured ME response. The blocked domain state's ME response converges to that of the wide domain states', only when the entire magnetic domain transformation is concluded (compare the ME responses f and n in Figure 5.2a and likewise the corresponding magnetic domain configurations in Figure 5.2f and n). With $\boldsymbol{H_{ext}}$ applied in plus direction, at $\boldsymbol{H_{ext}} = +4$ Oe the ME response reaches its peak value along $+\boldsymbol{H_{ext}}$. The discussed data consisting of simultaneous measurement of sensor response and observation of magnetic domain configurations reveals that the ME response is tightly linked to the magnetic domain response and the existence of two distinct $\boldsymbol{H_{ext}}$ dependent magnetic domain configurations (discussed throughly in Section 4.1) generate two different ME response branches. The magnetic susceptibility of the magnetic layer (both locally and globally) is sensed at the ME response.

Before proceeding with the measurements performed between different $\boldsymbol{H_{ext}}$ values, the degree of influence from non-uniform magnetic anisotropy distribution to ME response is displayed at a different ME sensor. In this context, the non-coherent transformation from the blocked domain state to the wide domain state is implied. Data shown in Figure 5.3 consist of complementary magnetization and ME loops, as well as some selected MO images. The ME sensor consists of a 4 μm thick FeCoSiB as the magnetostrictive layer and a 2 μm thick $Pb(Zr_{0.52}Ti_{0.48})O_3$ (PZT) layer as the piezoelectric layer (Figure 5.3d) [51]. The magnetization loops are measured inductively (Figure 5.3a and b) and the ME response at sensor's mechanical resonance frequency is acquired electrically at the chair of *microwave engineering* in *Kiel university* (Figure 5.3c).

The full and minor magnetization loops exhibit the common hysteretic behavior observed in FeCoSiB films (Figure 5.3a and b, also compare with Figure 4.1a and b in Section 4.1). The full loop hysteresis points out towards existence of blocked and wide domain states. Likewise, the magnetic hysteresis is transferred to the ME response (Figure 5.3c). Contradicting the observed, direct shift of the red loop to the gray loop for the previous ME sensor (Figure 5.2a), the low ME amplitude is retained at a much broader $\boldsymbol{H_{ext}}$ range (Figure 5.3c), i.e. the blue curve, when $\boldsymbol{H_{ext}}$ is decreased from $+\mathbf{H_{sat}}$, approaches the ME amplitudes recorded for the gray curve not directly but following a linear trend. Magnetic domain observations show that decreasing $\boldsymbol{H_{ext}}$ from magnetic saturation (Figure 5.3e), a blocked domain state with relatively low magnetic domain width emerges as expected (Figure 5.3f). Instead of

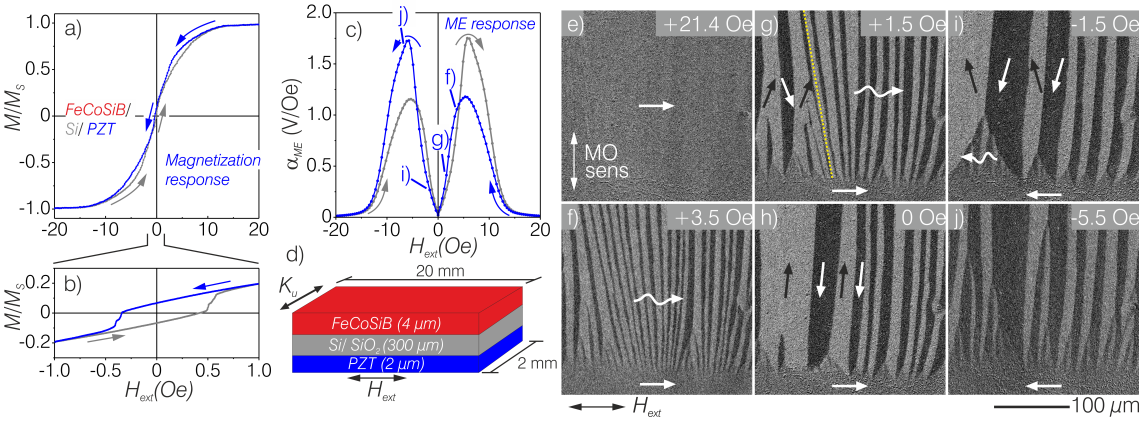

Figure 5.3: (a) and (b) display for an ME sensor in cantilever design, the inductively measured full and minor magnetization loops, respectively. (c) shows electrically measured ME response at the sensors mechanical resonance frequency. Sketch in (d) indicates the dimensions of the investigated sensor, $\mathbf{K_u}$ and $\boldsymbol{H_{ext}}$. (e-j) some selected magnetic domain images are demonstrated [51]. (Sample: PZT 2 μm/ [Si/ SiO_2] 300 μm/ FeCoSiB 4 μm)

a sudden magnetic domain transformation in the imaged area, the conversion occurs in small regional changes. For instance, in Figure 5.3g the dotted line separates two distinct regions, where the blocked domain and wide domain states coexist at the same $\boldsymbol{H_{ext}}$. At $\boldsymbol{H_{ext}}$ = +1.5 Oe, to the left of the line, the magnetic domain configuration is already in wide domain state, whereas at the right hand side blocked domain state ensues. With further $\boldsymbol{H_{ext}}$ reduction, all regions convert to wide domain state, which possesses high magnetization susceptibility, nevertheless the average magnetic domain width is different for both regions (Figure 5.3h). Reversing $\boldsymbol{H_{ext}}$ leads to magnetization reversal proceeding by a combination of domain wall motion and coherent rotation (Figure 5.3i and j). Possessing a non-homogeneous magnetic anisotropy distribution inside the magnetic material leads to spatially non-coherent transformation from blocked to wide domain state and the convergence of the ME response as $\boldsymbol{H_{ext}}$ is decreased from $\pm\mathbf{H_{sat}}$ is shifted to smaller $\boldsymbol{H_{ext}}$ values.

For in-depth understanding of the influence of magnetic domain effects on ME response, several measurements are performed in the same manner as data displayed in Figure 5.2 but between different $\boldsymbol{H_{ext}}$ ranges. Emphasis is made on magnetic anisotropy distribution and relative alignment between $\boldsymbol{H_{ext}}$ and $\mathbf{K_u}$. These measurements are further important for the commonly encountered increase in the noise level, when frequency conversion technique (Section 2.3.1) is employed for LoD measurements, where instead of a DC $\boldsymbol{H_{ext}}$, an AC $\boldsymbol{H_{ext}}$ is swept to amplify the ME response for measuring signals with frequencies other than mechanical resonance frequency [26]. MO imaging is performed at the same area as in Figure 5.2c-h. Prior to measurements the magnetostrictive phase is demagnetized along the long axis of the cantilever with an alternating $\boldsymbol{H_{ext}}$ field with decreasing amplitude and

in order to obtain a stable magnetic domain state $\boldsymbol{H_{ext}}$ is swept manually several times between the $\boldsymbol{H_{ext}}$ range to be measured.

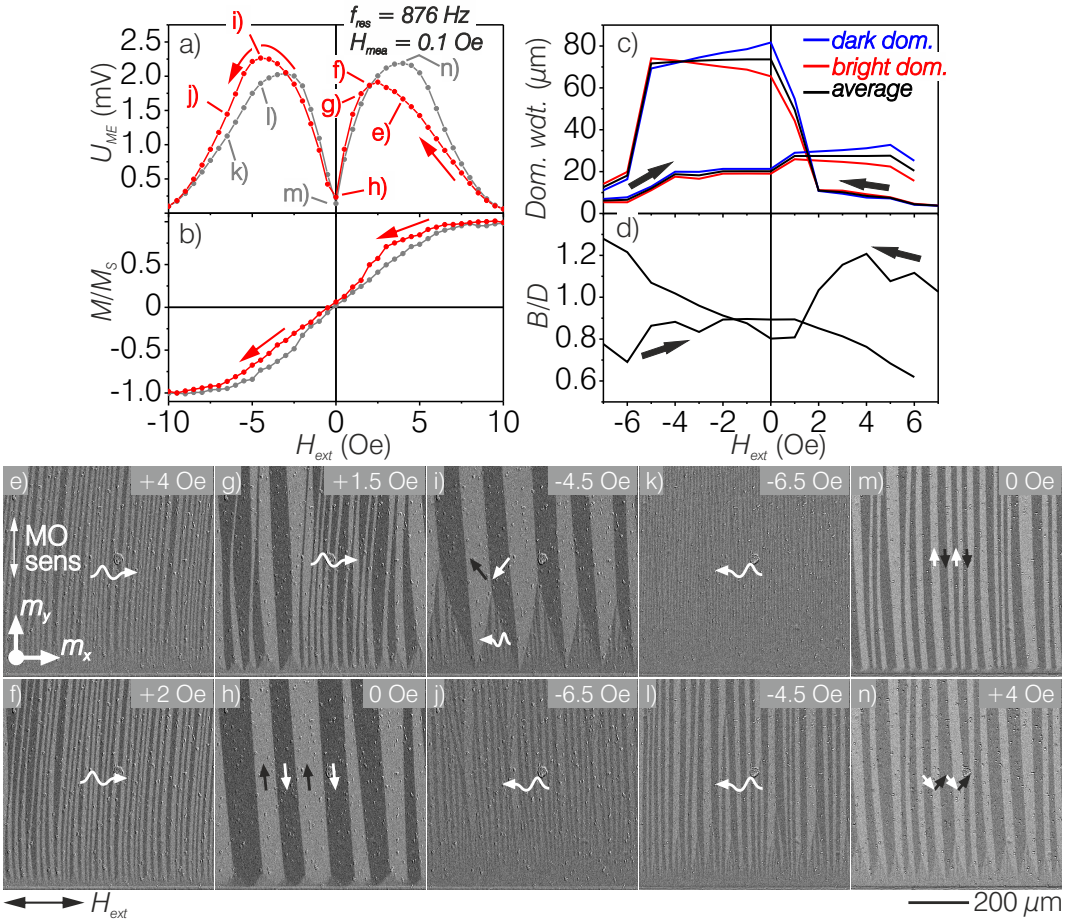

Figure 5.4: The ME and magnetization responses measured between ±10 Oe are displayed in (a) and (b), respectively. Moreover, dark and bright domain widths, as well as the average domain widths are plotted in (c). (d) displays the bright-to-dark domain ratio (B/D). Some selected magnetic domain images are shown in (e)-(n). All measurements are performed simultaneously. (Sample: AlN 2 μm/ [Si/ SiO_2] 300 μm/ FeCoSiB 1 μm)

Figure 5.4 demonstrates the measured ME response (a), local magnetization loop (b), domain width change (c), B/D plot (d) and some selected magnetic domain images (e-l). The corresponding ME responses for the displayed magnetic domain images are marked in Figure 5.4a. The measurements are performed between $\boldsymbol{H_{ext}}$ = ±10 Oe, at the onset of magnetic saturation. By not applying $\boldsymbol{H_{ext}}$ between $\pm\mathbf{H_{sat}}$, both the ME and local magnetization loops display reduced hysteresis along the measurement direction (Figure 5.4a and b, also compare with Figure 5.2a and b). Reducing $\boldsymbol{H_{ext}}$ from $\boldsymbol{H_{ext}}$ = +10 Oe, at $\boldsymbol{H_{ext}}$ = +4 Oe a blocked domain state appears (Figure 5.4e), however the bright (9.2 μm) and dark (7.6 μm) domain widths are dissimilar (Figure 5.4c and d). Due to interacting ANWs, the magnetic susceptibility and the corresponding ME responses are quite low (Figure 5.4a and b).

With further decrease of $\boldsymbol{H_{ext}}$, the bright and dark domain widths as well as the average domain width increase (Figure 5.4c). Although at $\boldsymbol{H_{ext}} = 0$ Oe (Figure 5.4h), the dark domains possess a magnetization alignment with $\boldsymbol{m_y}$ along the currently applied $+\boldsymbol{H_{ext}}$ direction (Induced $\mathbf{K_u}$ is tilted approximately by −4° away from the intended axis), for $\boldsymbol{H_{ext}} > +4$ Oe as $\boldsymbol{H_{ext}}$ is decreased from $+\boldsymbol{H_{sat}}$, the overall bright domain width is higher than the dark domain width (Figure 5.4d). This discrepancy stems from the $\boldsymbol{H_{ext}}$ history dependent domain wall alignment and could orıgınate from a small external bias field $\boldsymbol{H_{bias}}$. At $\boldsymbol{H_{ext}} > +4$ Oe, the domain walls are aligned almost +5° away from the short axis and correspodingly +9° away from the induced $\boldsymbol{K_u}$ axis (Figure 5.4e and f). This magnetization alignment leads to preferencial widening of the bright domains through domain wall motion in this $\boldsymbol{H_{ext}}$ regime.

Further decrease of $\boldsymbol{H_{ext}}$ results in gradual rearrangement of the magnetic domain configuration to the wide domain state (Figure 5.4g). Now, the domain walls slowly realign along the $\boldsymbol{K_u}$ and the relative dark domain width increases and exceeds the bright domain width (Figure 5.4d). In low $\boldsymbol{H_{ext}}$ regime, the local average domain width stays almost constant around 72 μm. Applying $\boldsymbol{H_{ext}}$ along minus direction, the dark domain volume shrinks through domain wall motion by the expanding bright domains (Figure 5.4c). The reason lies in the current domain wall alignment with respect to the $\boldsymbol{H_{ext}}$, where bright domains possess the $\boldsymbol{m_y}$ component of magnetization along $-\boldsymbol{H_{ext}}$. Increasing $\boldsymbol{H_{ext}}$ further in the minus direction, the bright domain width rises and B/D = 1 is reached at $\boldsymbol{H_{ext}} = -3.8$ Oe. The measured ME signal increases, reaching its peak value of $\boldsymbol{U_{ME}} \approx 2.25$ mV at $\boldsymbol{H_{ext}} = -4.5$ Oe (Figure 5.4a and h). Increasing $\boldsymbol{H_{ext}}$ further towards $\boldsymbol{H_{ext}} = -10$ Oe leads to an increase in domain wall density and accordingly the ME response decreases (Figure 5.4c and i).

In the reverse direction (gray curves in Figure 5.4a and b), the average domain width is far narrower (compare Figure 5.4j and k), at $\boldsymbol{H_{ext}} = -7$ Oe, the average bright and dark domain widths are 5.4 μm and 7 μm, respectively. Decreasing $\boldsymbol{H_{ext}}$ towards remanence, the average domain width goes up steadily (Figure 5.4c). Moreover, similar to the case as $\boldsymbol{H_{ext}}$ is decreased from +10 Oe, the domain walls are not aligned along the induced $\boldsymbol{K_u}$ axis with $\boldsymbol{H_{ext}}$ reduced from −10 Oe (see Figure 5.4j and k). They are tilted by +1°, almost in line with the short axis of the cantilever, which further agrees with a possible, small $\boldsymbol{H_{bias}}$ presence during the measurements. With varying $\boldsymbol{H_{ext}}$, the domain wall angle stays almost constant (Figure 5.4k). Now, with $+\boldsymbol{H_{ext}}$ the wall angle slightly rotates towards the $\boldsymbol{K_u}$ axis (Figure 5.4l) and the dark domains possess an $\boldsymbol{m_y}$ component that is aligned along $+\boldsymbol{H_{ext}}$ direction. As a result, the average bright domain width decreases gradually through domain wall motion at the expense of dark domains (Figure 5.4c from −10 Oe until +5 Oe, also Figure 5.4d). Hence, the overall domain width, which has

been constant at a wide $\boldsymbol{H_{ext}}$ regime, starts to diminish. The magnetic susceptibility and accordingly, the ME response decrease. It is clear from the discussed data in Figures 5.2 and 5.4 that the non-linear magnetization response stemming from magnetic domain activity contribute to ME hysteresis. Therefore, especially relevant for frequency conversion techniques, the ME response needs to be operated in $\boldsymbol{H_{ext}}$ regimes, where the magnetization response is linearized. Moreover, $\boldsymbol{H_{ext}}$ dependent domain wall alignment lead to locally hysteretic magnetization response. Domains with magnetization components aligned along the $\boldsymbol{H_{ext}}$ expand at the expense of the others.

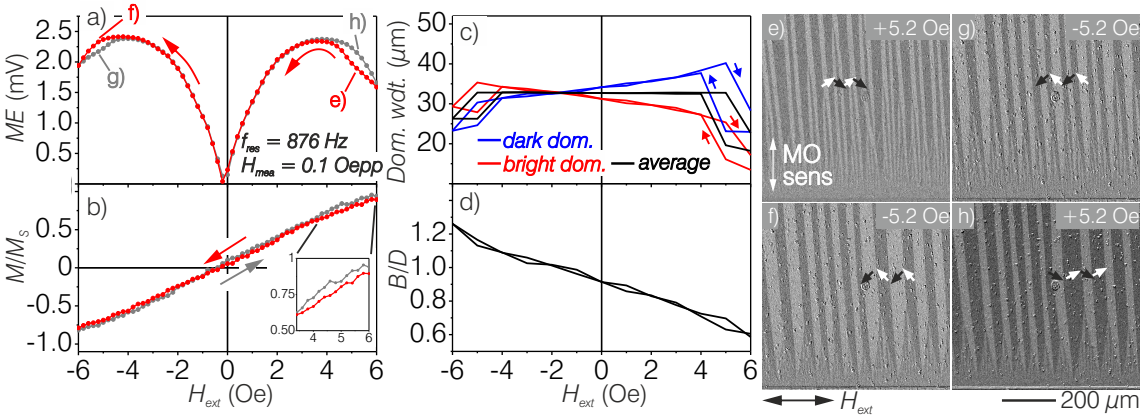

Figure 5.5: The ME sensor and magnetization responses measured between ±6 Oe is displayed in (a) and (b), respectively. Moreover, dark and bright domain widths, as well as the average domain widths are plotted in (c). (d) displays the bright-to-dark domain ratio. Some selected magnetic domain images are shown in (e)-(h). All measurements are performed simultaneously. (Sample: AlN 2 μm/ [Si/ SiO_2] 300 μm/ FeCoSiB 1 μm)

Figure 5.5 displays the data measured in $\boldsymbol{H_{ext}}$ = ±6 Oe range. The ME hysteresis is reduced to a large extent, only around the measurement limits ±6 Oe some hysteretic sensor response remains. The ME hysteresis at $+\boldsymbol{H_{ext}}$ is noticeably larger than at $-\boldsymbol{H_{ext}}$ (Figure 5.5a). The local magnetization loop, on the other hand, displays a very linear response (Figure 5.5b). Only noteworthy divergence from linearity is at +3 Oe < $\boldsymbol{H_{ext}}$ < +6 Oe (see inset in Figure 5.5b). Unlike the previously displayed data for $\boldsymbol{H}$ = ±10 Oe, the domain width variation is mostly reversible with some hysteresis near the measurement limits (Figure 5.5c). However, some selected magnetic domain images, where the ME response difference is the highest, display notable magnetic domain activity via domain wall motion, which are not detected in the magnetization curve (Figure 5.5e-h and compare with a and b).

Starting with an average domain width of 18 μm, the bright (13 μm) and dark (23 μm) domain widths are dissimilar at $\boldsymbol{H_{ext}}$ = +6 Oe (Figure 5.5c). With decreasing $\boldsymbol{H_{ext}}$, the overall bright and dark domain widths, as well as the average domain width increase due to a small angle between the $\boldsymbol{H_{ext}}$ and $\boldsymbol{K_u}$. Around

$\boldsymbol{H_{ext}}$ = +4 Oe, the average domain width reaches its stable value of 32 μm, which stays constant over a wide $\boldsymbol{H_{ext}}$ range. However, examining the width change for bright and dark domains individually reveals that they do not stay constant. Although the B/D plot in Figure 5.5d displays a rather linear change, it also indicates sudden local magnetization changes by magnetic domain wall motion characterized by domain width modifications, which are not necessarily detected in the magnetization response. The MO measurements depict the local magnetization response, only a small region is probed and as has been discussed for the magnetic domain images obtained by a large view microscope (Figure 5.2i-k), the $\boldsymbol{K_u}$ distribution is inhomogeneous, therefore the magnetization loop does not correlate one-to-one with the ME hysteresis. More importantly, for the displayed magnetization loop the MO measurement is sensitive to $\boldsymbol{m_x}$ component of magnetization and sudden $\boldsymbol{m_y}$ variations are not sensed. At this $\boldsymbol{H_{ext}}$ range the magnetic domain wall related changes are mostly reversible and no sudden transformation in magnetic domain configuration occurs. The measured ME response correlates well with the observed domain width hysteresis. At $-\boldsymbol{H_{ext}}$ values, where the domain width hysteresis is smaller, likewise the extent of hysteretic ME region is limited.

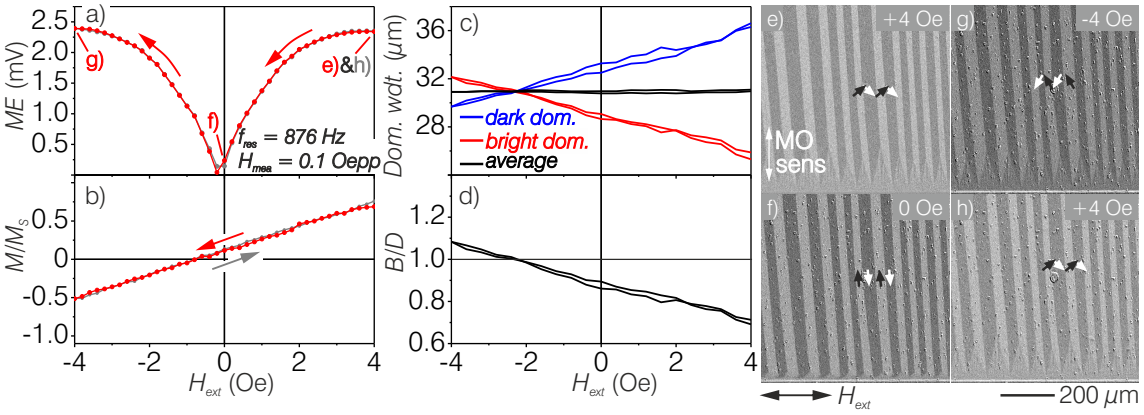

Figure 5.6: The ME sensor and magnetization responses measured between ±4 Oe is displayed in (a) and (b), respectively. Moreover, dark and bright domain widths, as well as the average domain widths are plotted in (c). (d) displays the bright-to-dark domain ratio. Some selected magnetic domain images are shown in (e)-(h). All measurements are performed simultaneously. (Sample: AlN 2 μm/ [Si/ SiO_2] 300 μm/ FeCoSiB 1 μm)

Now working at a $\boldsymbol{H_{ext}}$ regime ($\boldsymbol{H_{ext}}$ = ±4 Oe) far below the blocked domain formation and limited closure domain motion, the ME hysteresis vanishes (Figure 5.6). The sensor response changes linearly with the applied $\boldsymbol{H_{ext}}$ (Figure 5.6a). The magnetization response likewise displays no hysteresis (Figure 5.6b). One important feature in both the ME and magnetization responses is that they do not cross zero at $\boldsymbol{H_{ext}}$ = 0 Oe (e.g. $\mathbf{ME(0\ Oe)} \neq 0$ mV and $\mathbf{M/M_s(0\ Oe)} \neq 0$), which has also been measured in the previously discussed data (Figures 5.2, 5.4 and 5.5) but is

most clearly observed in Figure 5.6a and b. The curves are shifted to $-\boldsymbol{H_{ext}}$. Their non-zero crossing points out towards non-homogeneous $\boldsymbol{K_u}$ distribution overall in the sample. The MO domain observations supports this (Figure 5.6e-h). Although the average domain width does not change in this $\boldsymbol{H_{ext}}$ regime (Figure 5.6c), individually analyzed bright and dark domain display, similar to the low $\boldsymbol{H_{ext}}$ response in the previously discussed data, a linear variation with $\boldsymbol{H_{ext}}$ (Figure 5.6c and d). Although the domain width hysteresis observed at higher $\boldsymbol{H_{ext}}$ has vanished (Figure 5.4 and 5.5) and both domain widths change linearly with $\boldsymbol{H_{ext}}$, the domain wall motion causes sudden local magnetization changes, which are not detected in the magnetization loop (Figure 5.6b) and can lead to noise originating from magnetostrictive phase.

The data reviewed in this section revealed the tight relationship between the magnetic domains and ME response. The occurring magnetization reversal processes and magnetic domain configurations influence the ME response both in terms of magnitude and curve shape. The presented magnetic domain width variations through magnetic domain wall motion is likewise significant for other sensor concepts with magnetic sensing layers. For ME sensors, the results are very crucial for frequency conversion technique used for LoD measurements [26, 27], where linear magnetization and magnetic domain response is critical for achieving reduced noise floor, which in return makes measuring low magnetic field signals possible. The discussed data reveals that despite working at $\boldsymbol{H_{ext}}$ regimes, where the magnetization and ME responses are almost linear (Figure 5.5) and hysteresis free (Figure 5.6), magnetic domain wall motion related magnetization changes take effect. Non-uniform $\boldsymbol{K_u}$ distribution leads to non-homogeneous magnetic domain response, applying $\boldsymbol{H_{ext}}$ at an angle other than 90° to the magnetic domain walls induces a torque on them. Domains with $\boldsymbol{m_y}$ component along the applied $\boldsymbol{H_{ext}}$ expand at expense of rest, leading to hysteretic magnetic domain width variations. Such subtle changes could lead to an increase in noise floor related to magnetic domain effects. Therefore, it is very important to hinder magnetic domain wall formation in such magnetic field sensing concepts, which can be accomplished through different biasing schemes (i.e. see Figure 1.1).

5.1 Probing effects quadratic in magnetization

In this chapter, the influence of magnetic domains on the magnetostrictive ($\boldsymbol{\lambda}$) response in ME sensors is covered. Many techniques are present for $\boldsymbol{\lambda}$ measurements such as using strain-gauge for volumetric response [126]. Local $\boldsymbol{\lambda}$ responses have been obtainable by atomic force microscopy [127] or capacitive measurements [128]. Optical methods include laser deflection [129]. For non-magnetic materials opti-

cal methods such as photoelastic imaging have been demonstrated to be capable of approximating the local strain variations inside a slide glass [130]. Measuring $\boldsymbol{\lambda}$ response at regions relevant for integrated sensing applications can be rather demanding. Furthermore no direct magnetic domain information can be obtained through most of the methods. Therefore, in this chapter acquisition of local, quasi magnetostrictive response maps in an all magneto-optical manner are displayed and moreover the ME responses are reconstructed.

It is extremely important to understand the magnetization response for devices with magnetic sensing layers and direct imaging of the occurring magnetic domain configurations in a material brings invaluable information on the magnetization response. As was previously discussed, in MO imaging mostly first-order effects such as MOKE is applied, which has a linear relationship with magnetization. However, in many cases the measured device response possesses a quadratic relationship with magnetization direction ($\boldsymbol{m^2}$), e.g. AMR and $\boldsymbol{\lambda}$ in ME sensors.

In the following sections, two approaches are demonstrated to acquire $\boldsymbol{m^2}$ maps, namely through first-order (MOKE) (Section 5.1.1) and second-order (MOVE) (Section 5.1.2) MO effects. $\boldsymbol{m^2}$ response of magnetic materials are locally visualized. Furthermore, intensity in different images are analyzed to obtain $\boldsymbol{m^2}$ loops. Special emphasis is given on $\boldsymbol{\lambda}$ response in ME sensors. However, the displayed $\boldsymbol{m^2}$ response extraction is applicable to other magnetic effects sharing the same magnetization symmetry.

5.1.1 Through first-order magneto-optical effects

Here, MOKE in longitudinal mode is employed for $\boldsymbol{\lambda}$(x, y) map acquisition. Other first-order MO effects such as the transverse MOKE is as well applicable, as both MOKE modes share the same, linear magnetization symmetry.

In Figure 5.7a-b, magnetic domain configurations at $\boldsymbol{H_{ext}}$ = +1.5 Oe and +0.9 Oe of a millimeter sized ME sensor are displayed. $\boldsymbol{H_{ext}}$ has been applied along the long axis of the cantilever and decreased from +3 Oe to the mentioned values. Magnetic domains across the entire cantilever is probed. The MO measurement is sensitive to the $\boldsymbol{m_y}$ component. Moreover, the data displayed in Figure 5.7 has been obtained with an electromagnet setup in Helmholtz configuration, therefore the $\boldsymbol{H_{ext}}$ is homogeneous.

At high $\boldsymbol{H_{ext}}$ regime (Figure 5.7a), where a blocked domain state is present almost across the whole sample, several regions with different MO contrast emerges (i.e. region encircled by the white dashed line). The non-homogeneous MO contrast indicates spatially varying $\mathbf{K_{eff}}$ alignment. Furthermore, local differences in domain wall alignment (illustrated with yellow lines) support this. As $\boldsymbol{H_{ext}}$ is decreased

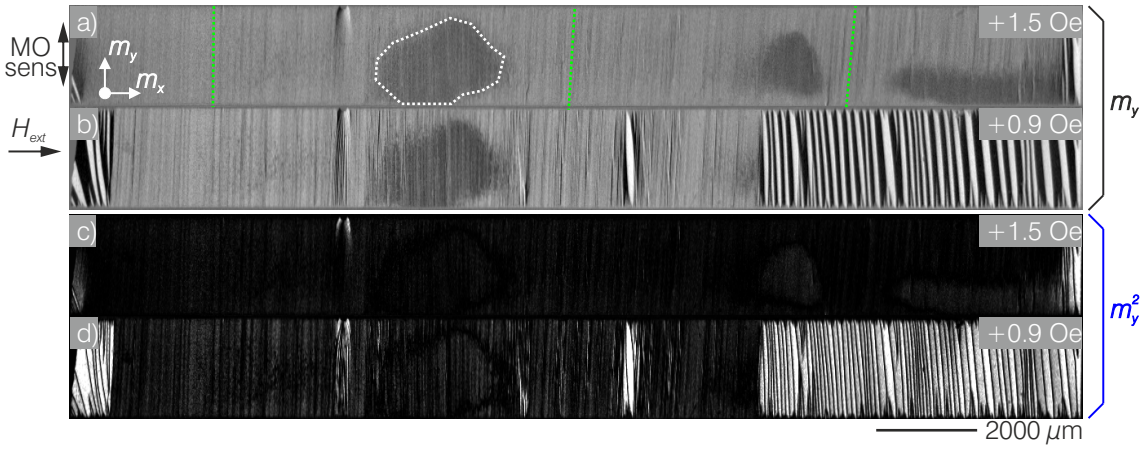

Figure 5.7: Images exhibiting the magnetic domain configuration at the entirety of a millimeter sized ME sensor are shown in (a) at +1.5 Oe and (b) at +0.9 Oe. MO sensitivity is aligned to acquire the magnetization response $\boldsymbol{m_y}$. Respective, calculated $\boldsymbol{m_y^2}$ maps, analogous to local $\boldsymbol{\lambda}$(x, y) response are depicted in (c) and (d). MO sensitivity axis and applied $\boldsymbol{H_{ext}}$ direction are indicated. (Sample: AlN 2 μm / [Si/SiO_2] 300 μm/ FeCoSiB 1 μm)

the blocked domain state is converted to a domain configuration with substantial reduction in domain wall density (Figure 5.7b). Due to naturally higher demagnetizing field at the edges, the reorganization of the domain configuration is also non-uniform as it first starts from the edges. Along with the inhomogeneous demagnetizing field distribution, local deviations from the intended $\mathbf{K_u}$ axis leads to spatially non-uniform magnetic domain transformation.

Images displayed in Figure 5.7c and d are $\boldsymbol{m_y^2}$ maps of the magnetization configurations in Figure 5.7a and b, respectively. They are analogous to the magnetic layer's $\boldsymbol{\lambda}$ response at given $\boldsymbol{H_{ext}}$ values. In order to acquire $\boldsymbol{\lambda}$(x, y) maps, the gray intensity value ($\mathbf{(I(black)+I(white))/2}$), depicting the MO intensity offset, should be extracted from the raw first-order MO images. Afterwards, by simple squaring of the MO image, $\boldsymbol{\lambda}$(x, y) maps are acquired. The dark and bright contrast in $\boldsymbol{\lambda}$(x, y) maps (Figure 5.7c and d) correspond to an expansion and contraction of the magnetic film along the long axis of the cantilever, respectively. Moreover, $\boldsymbol{\lambda}$ reponse of magnetic domains with antiparallel magnetization alignment are almost identical. However, some MO contrast difference is seen between anti-parallelly magnetized domains (e.g. right of the image in Figure 5.7d) and along with the dark contrast at the domain boundaries points out towards a possible residual $\boldsymbol{m_x}$ sensitivity in the first-order MO images. Despite all that the local deviations from a uniform $\boldsymbol{\lambda}$ response due to inhomogeneous magnetization distribution are revealed in the $\boldsymbol{\lambda}$ maps (i.e. compare Figure 5.7a, b and the $\boldsymbol{m^2}$ maps in Figure 5.7c, d).

Such $\boldsymbol{\lambda}$ maps can further be employed to acquire regional ME response maps $\boldsymbol{ME}$(x, y), which corresponds to local $\boldsymbol{\lambda}$ susceptibility maps. Starting from (2.29),

with $\boldsymbol{H_{mea}}$ as the measuring AC magnetic field, two $\boldsymbol{\lambda}$ maps at $\boldsymbol{H_{ext}} \pm 1/2\boldsymbol{H_{mea}}$ are subtracted and thus the $\boldsymbol{ME}$(x, y) at $\boldsymbol{H_{ext}}$ is reconstructed (5.1) [51].

$$\begin{aligned} ME(x,y)(H_{ext}) &\approx \frac{d\lambda(x,y)(H_{ext})}{dH_{mea}} \approx \frac{\Delta\lambda(x,y)(H_{ext})}{\Delta H_{mea}} \\ &\approx m_y^2(H_{ext} + \frac{1}{2}H_{mea}) - m_y^2(H_{ext} - \frac{1}{2}H_{mea}) \end{aligned} \tag{5.1}$$

Exemplary images are displayed in Figure 5.8a-e, demonstrating the reconstruction of $\boldsymbol{ME}$(x, y) at $\boldsymbol{H_{ext}}$ = +1 Oe (Figure 5.8e). The displayed data are obtained from the same sample, which has been discussed in Section 4.1. In order to observe a reasonable contrast in the $\boldsymbol{ME}$(x, y) maps, the peak-to-peak amplitude of $\boldsymbol{H_{mea}}$ is chosen to be 1 Oe. Before every image acquisition, $\boldsymbol{H_{mea}}$ is swept several times to obtain a stable magnetic domain configuration. After calculation of $\boldsymbol{\lambda}$(x, y) maps at $\boldsymbol{H_{ext}}$±0.5 Oe (Figure 5.8c and d). $\boldsymbol{ME}$(x, y)($\boldsymbol{H_{ext}}$) = $\boldsymbol{\Delta\lambda}$(x, y) is calculated by simple image subtraction of Figure 5.8c from Figure 5.8d. Gray contrast in $\boldsymbol{ME}$(x, y) maps correspond to zero ME response, whereas dark and bright contrasts in the images correlate to maximum ME response, however with different signs.

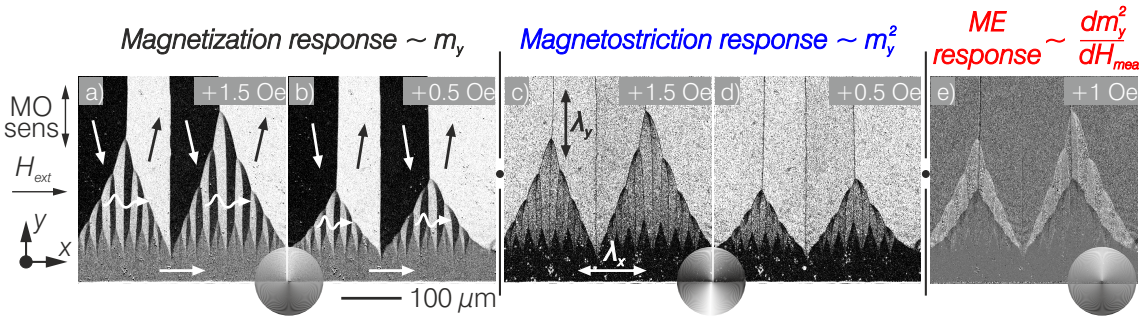

Figure 5.8: Local magnetization response $\boldsymbol{m_y}$ at +1.5 Oe (a) and +0.5 Oe (b) are shown. Respective, reconstructed $\boldsymbol{m_y^2}$ maps, analogous to local $\boldsymbol{\lambda}$ response are displayed in (c) and (d). In (e) local ME response at +1 Oe is displayed. MO sensitivity axis and applied $\boldsymbol{H_{ext}}$ direction are indicated. (Sample: [Si/ SiO_2] 300 μm/ FeCoSiB 4 μm) [51]

In Figure 5.9, $\boldsymbol{ME}$(x, y) maps at decreasing $\boldsymbol{H_{ext}}$ from $+\boldsymbol{H_{sat}}$ (a-d) and increasing $\boldsymbol{H_{ext}}$ towards $-\boldsymbol{H_{sat}}$ (e-h) are displayed. $\boldsymbol{\Delta H_{mea}}$ is also 1 Oe (peak-to-peak). $\boldsymbol{ME}$(x, y) maps visualize the local ME response of the magnetic layer. At $\boldsymbol{H_{ext}}$ = +4 Oe (Figure 5.9a), the edge region, where the $\mathbf{K_{eff}}$ is aligned along the long axis of the sample, is homogeneously gray meaning $\boldsymbol{ME}$(x, y) = 0. Because with $\boldsymbol{H_{ext}}$ and $\boldsymbol{H_{mea}}$ applied along x-axis the magnetostrictive response is the same for antiparallel magnetization alignments. The middle region displays some ME contrast, however the difference is rather limited due to the blocked domain state with low magnetic susceptibility. Nevertheless, the ME contrast is uniform, which

is an indication that the obtained ME response is generated dominantly through rotation of magnetization in this region. Now decreasing $\boldsymbol{H_{ext}}$ further (Figure 5.9b), the boundary separating the edge and the middle regions is shifted slightly towards the edge. After the sudden reorganization in the magnetic domain configuration, application of $\boldsymbol{H_{mea}}$ leads to ME response dominantly through movement of closure domains. The bright contrast in $\boldsymbol{ME}$(x, y) maps mean the ME response is almost maximum at this region. $\boldsymbol{\lambda}$ varies nearly from $\boldsymbol{\lambda_x}$ to $\boldsymbol{\lambda_y}$. At $\boldsymbol{H_{ext}} = 0$ Oe (Figure 5.9d), the dark contrast (encapsulated by yellow dots) originates from nucleation and expansion of the closure domains with the magnetization alignment along $-\boldsymbol{H_{ext}}$ direction, the sign of the obtained ME response has reversed in this region, however the absolute intensity is almost the same as the bright regions and thus the ME response of bright and dark regions are in principle identical. The unequal volume encompassed by the bright and dark areas reveal the occuring magnetic hysteresis, which is further transferred to $\boldsymbol{\lambda}$ response and can be resolved in $\boldsymbol{ME}$(x, y) map (i.e. non-zero crossing of the ME response.).

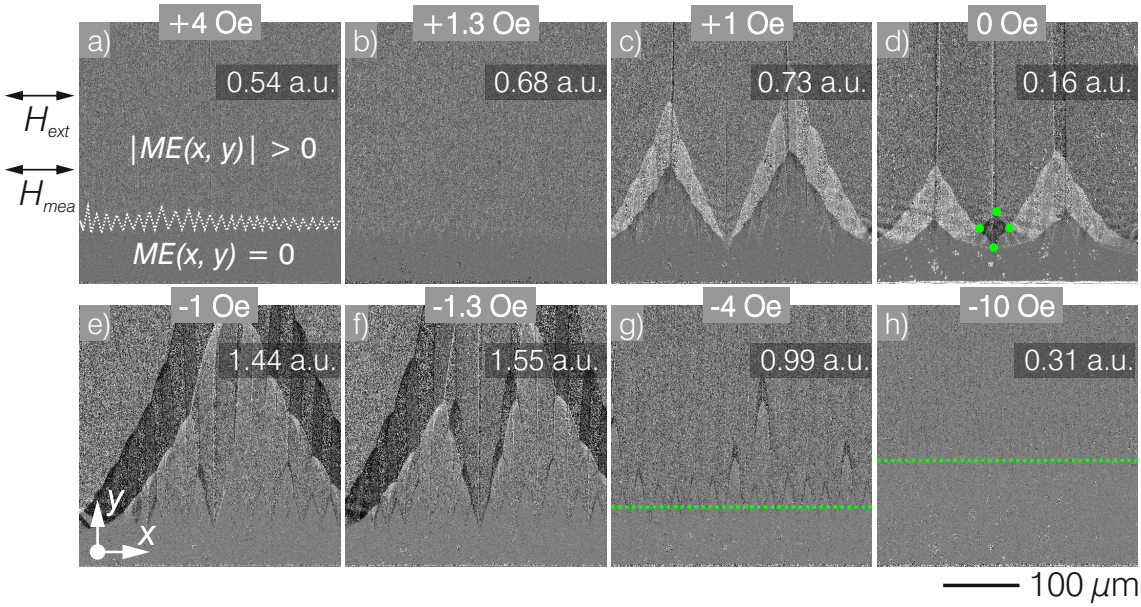

Figure 5.9: Selected, local $\boldsymbol{ME}$(x,y) maps at different $\boldsymbol{H_{ext}}$ values are displayed. $\boldsymbol{H_{mea}}$ is 1 Oe peak-to-peak. The structure's long axis is at the bottom of the images. The reconstructed ME response are specified in the maps. (Sample: [Si/ SiO_2] 300 μm/ FeCoSiB 4 μm) [51]

Now, increasing $\boldsymbol{H_{ext}}$ towards $-\boldsymbol{H_{sat}}$, the closure domains with magnetization alignment along $\boldsymbol{H_{ext}}$ expand, the ME response is nearly maximum, where the movement occurs (Figure 5.9e). Inside the closure domains the ME response is limited. Comparing $\boldsymbol{ME}$(x, y) maps at +1.3 Oe (Figure 5.9b) and at −1.3 Oe (Figure 5.9f), blocked domain state in Figure 5.9b generates a rather limited but homogeneous ME response, whereas the closure domain movement leads to sudden almost maximum

ME variations (Figure 5.9f). With increasing $\boldsymbol{H_{ext}}$, magnetic domain refinement results in uniform ME response (Figure 5.9g). However, some regions displaying dark contrast pinpoint local ME jumps due to spike domain nucleation and movement into the material. As $\boldsymbol{H_{ext}}$ is increased further towards saturation (Figure 5.9h), the very edge region with $\boldsymbol{ME}$(x, y)= 0 expands further into the material (compare Figure 5.9g and h). This region is now magnetically saturated and does not contribute to ME response. Further $\boldsymbol{H_{ext}}$ increase leads to magnetic saturation of the whole film and the ME response becomes zero (not shown).

Calculation of $\boldsymbol{\lambda}$(x, y) and $\boldsymbol{ME}$(x, y) maps not only allows for direct visualization of the mentioned effects. The intensity change in the images can be analyzed locally and corresponding $\boldsymbol{\lambda}(\boldsymbol{H_{ext}})$ and $\boldsymbol{ME}(\boldsymbol{H_{ext}})$ curves are reconstructed (Figure 5.10). The scatter points in Figure 5.10a correspond to reconstructed $\boldsymbol{\lambda}(\boldsymbol{H_{ext}})$ data, which has been interpolated and fitted (full lines) to derive the corresponding $\boldsymbol{ME}(\boldsymbol{H_{ext}})$ curve (Figure 5.10b). The measurements are performed from $+\boldsymbol{H_{ext}}$ to $-\boldsymbol{H_{ext}}$. The response from $-\boldsymbol{H_{ext}}$ to $+\boldsymbol{H_{ext}}$ is obtained by mirroring the measured curve due to symmetric response.

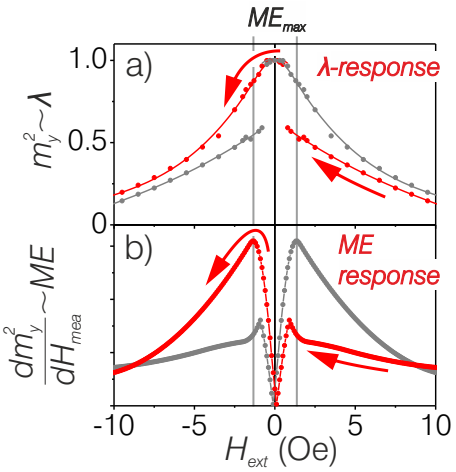

Figure 5.10: Reconstructed, local $\boldsymbol{m_y^2} \approx \boldsymbol{\lambda}$ (a) and $\boldsymbol{dm_y^2/dH_{mea}} \approx \boldsymbol{ME}$ (b) curves are displayed. The absolute $\boldsymbol{ME}$ values are plotted. For the $\boldsymbol{ME}$ reconstruction, $\boldsymbol{H_{mea}}$ is chosen to be 0.2 Oe. (Sample: [Si/ SiO_2] 300 μm/ FeCoSiB 4 μm)

Supporting the observations made for the $\boldsymbol{ME}$(x, y) maps, as $\boldsymbol{H_{ext}}$ is decreased from $\boldsymbol{H_{sat}}$, $\boldsymbol{\lambda}$ response is very limited (Figure 5.10a). With the sudden change in magnetic domain configuration around +1 Oe, $\boldsymbol{\lambda}$ abruptly changes to the $\boldsymbol{\lambda}$ response of the wide domain state. Subsequent $\boldsymbol{H_{ext}}$ increase in minus direction leads to an asymptotic change until $\boldsymbol{H_{sat}}$ is reached.

The reconstructed ME curve exhibits the influence of the hysteretic $\boldsymbol{\lambda}$ response on ME (Figure 5.10b). ME curve is obtained by first-order derivation of the fitted $\boldsymbol{\lambda}$ curve ($\boldsymbol{ME} \sim \boldsymbol{dm_y^2/dH_{mea}}$). $\boldsymbol{H_{mea}}$ is now 0.2 Oe. At high $\boldsymbol{H_{ext}}$ regime, ME response is low due to limited magnetization susceptibility and switches to a high susceptibility regime after the domain reorganization, as a result the ME response increases. The ME hysteresis commonly observed in ME sensors can be reconstructed to a large degree [51]. For the discussed data, a ME response difference

up to a factor of 2 at the maximum ME response ($\boldsymbol{ME_{max}}$) can be reconstructed (Figure 5.10b).

All in all, the local $\boldsymbol{\lambda}$(x, y) maps can be reconstructed through MOKE imaging. Such $\boldsymbol{\lambda}$(x, y) maps establish a prompt link between the magnetic domain response to $\boldsymbol{\lambda}$ response. Furthermore, ME response can be visualized by deriving the $\boldsymbol{ME}$(x, y) maps. The local ME response is directly approximated. The dominant, as well as minor magnetic domain effects and their local contributions to ME response are exposed in an all MO manner [51]. The magnetization and $\boldsymbol{\lambda}$ responses can be separated directly from the device response.

5.1.2 Through second-order magneto-optical effects

Here, similar to Section 5.1.1, local $\boldsymbol{m^2}$(x, y) $\approx$ $\boldsymbol{\lambda}$(x, y) maps are acquired and $\boldsymbol{\lambda}(\boldsymbol{H_{ext}})$ curves are reconstructed in an all MO manner. Instead of obtaining $\boldsymbol{m^2}$ maps/ loops from first-order MO images, magneto-optical Voigt effect (MOVE) (see Section 3.2.2.2 for theory) is applied for imaging. As has been discussed in Section 3.2.2.1, an oblique angle of incidence is a requirement for imaging in-plane magnetic domains via MOKE and in a MO microscope setup, where the illumination and observation are performed concurrently through the objective lens (i.e. see Figure 3.2), the maximum obtainable angle of incidence is mainly dependent on the NA of the objective lens [95]. Therefore, for low NA objectives the attainable MO signal is rather low. On the other hand, to maximize MOVE, perpendicular illumination geometry is a necessity. This property makes application of MOVE convenient for imaging magnetization distributions restricted solely to film plane with low NA objectives. Moreover, due to shared magnetization symmetry, the obtained $\boldsymbol{m^2}$(x, y) maps and loops via MOVE are reminiscent of $\boldsymbol{\lambda}$ response. Through MOVE imaging, $\boldsymbol{\lambda}$(x, y) maps of the transpiring magnetic domain configurations are visualized directly and the reconstructed $\boldsymbol{\lambda}(\boldsymbol{H_{ext}})$ depict the quasi-magnetostriction response of the material with changing $\boldsymbol{H_{ext}}$.

Figure 5.11 shows MO data obtained at the magnetic film of an unbiased ME sensor with the layer structure of Au 100 nm/ Cr 5 nm/ AlN 2 μm/ Pt 150 nm/ Ta 24 nm/ [Si/SiO_2] 300 μm/ FeCoSiB 1 μm. A dual-wavelength imaging scheme (see Figure 3.3a and b) is adopted for imaging. The same, local magnetic domain response is simultaneously probed with MOKE and MOVE, revealing the differences in acquired MO sensitivities and the information that can be gathered from both MO effects (Figure 5.11a-h). The images, furthermore, allow local $\boldsymbol{m}(\boldsymbol{H_{ext}})$ (Figure 5.11i, j) and $\boldsymbol{m}^2(\boldsymbol{H_{ext}})$ (Figure 5.11k, l) curve reconstruction by analyzing intensity change at different regions in the recorded images (indicated in Figure 5.11b).

At $\boldsymbol{H_{ext}}$ = +15 Oe, the $\boldsymbol{m}$(x, y) map displays uniform bright MO contrast, the

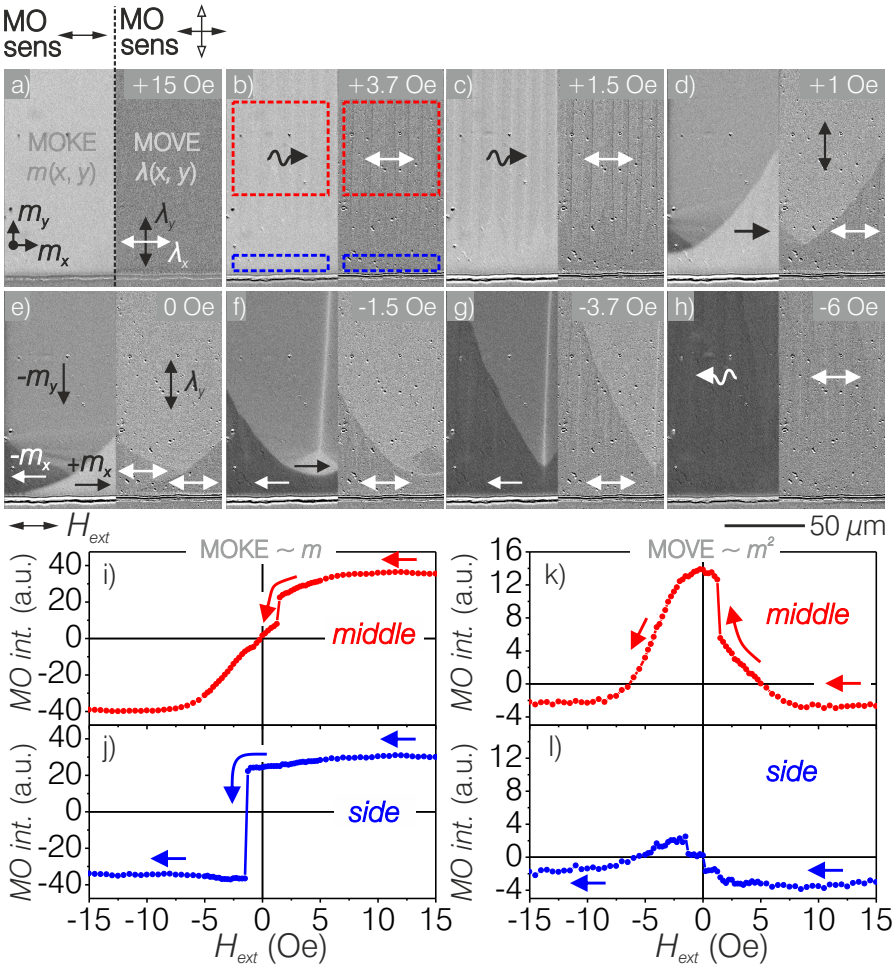

Figure 5.11: Some selected multi MO effect images obtained through dual-wavelength imaging are displayed (a-h). Left and right parts of the images are obtained by MOKE and MOVE, respectively. MO sensitivities and $\boldsymbol{H_{ext}}$ axes are indicated. The bottom of the images are the sample's long edge. As indicated, the displayed curves (i, k) and (j, l) are obtained by analyzing the MO intensity change locally in the middle and at the side of the structure, respectively. (Sample: AlN 2 μm/ [Si/SiO_2] 300 μm/ FeCoSiB 1 μm)

magnetic structure is homogeneously magnetized along $+\boldsymbol{m}_{\mathbf{x}}$. The corresponding $\boldsymbol{\lambda}$(x, y) map exhibits as expected homogeneously dark contrast over the whole imaged area, resulting in $\boldsymbol{\lambda}_{\mathbf{x}}$. Now decreasing $\boldsymbol{H}_{ext}$, the blocked domain state is formed in the middle of the sample (Figure 5.11b), which possesses limited magnetic and consequently $\boldsymbol{\lambda}$ susceptibility (compare Figure 5.11b and c). Moreover, at the sides of the magnetic structure, there seems to be no change in both magnetization and $\boldsymbol{\lambda}$ responses. After the magnetic domain transformation (Figure 5.11d), the closure domains near the edge exhibit bright ($+\boldsymbol{m}_{\mathbf{x}}$) and dark ($-\boldsymbol{m}_{\mathbf{x}}$) MOKE contrast. The middle region, which is magnetized uniformly along $-\boldsymbol{m}_{\mathbf{y}}$ is as expected homogeneously gray. In the MOVE portion of the image, the closure domains display the same dark contrast, indicating identical $\boldsymbol{\lambda}_{\mathbf{x}}$ response generated by them. The MO contrast for the magnetic domain in the middle is reversed to bright contrast resulting in $\boldsymbol{\lambda}_{\mathrm{y}}$ response (Figure 5.11e). Now, increasing $\boldsymbol{H}_{ext}$ towards −15 Oe the closure domains with dark MOKE contrast expand at the expense of ones with bright MOKE contrast. Additionally, at the sides of the magnetic film (region encapsulated by the blue rectangle in Figure 5.11b), a 180° magnetization reversal occurs indicated by the sudden change of MOKE contrast from bright to dark (compare Figure 5.11d and f). Examining the corresponding MOVE response, $\boldsymbol{\lambda}$ remains to be the same inside both closure domains due to quadratic nature of both effects (Figure 5.11f). With increasing $\boldsymbol{H}_{ext}$, the closure domains with dark MOKE contrast expand, accompanied by an almost maximum change from $\boldsymbol{\lambda}_{\mathbf{y}}$ to $\boldsymbol{\lambda}_{\mathbf{x}}$ (Figure 5.11g and h).

The next step involves local intensity analysis of middle (Figure 5.11i, k, red curves) and side (Figure 5.11j, l, blue curves) regions in the recorded images. Data from only with $\boldsymbol{H}_{ext}$ swept from +15 Oe to −15 Oe are shown. First thing to notice in the displayed curves is that the MOKE curves depict distinct MO intensity values at reversed magnetic saturation states (Figure 5.11i, j), whereas for the MOVE curves the measured MO intensities at both plus and minus magnetic saturation are identical (Figure 5.11k, l). Moreover, the sudden magnetization change at $\boldsymbol{H}_{ext} = +1.5$ Oe is sensed in the MOVE curve. Depicting an irreversible $\boldsymbol{\lambda}$ change linked to the discussed magnetic domain transformation (compare Figure 5.11i, k; also c and d). Furthermore, the $\boldsymbol{m}$ curve at the side region clearly reveal the easy axis magnetization reversal process (Figure 5.11j) and as anticipated, the corresponding MOVE curve shows that $\boldsymbol{\lambda}$ response of this easy axis magnetization switch is very limited (Figure 5.11l).

MOVE imaging has been performed in low magnification on the previously discussed unbiased ME sensor (Figure 5.11) and an exchange biased ME sensor consisting of a laminated FeCoSiB stack with a layer sequence of Au 100 nm/ Cr 5 nm/ AlN 2 μm/ Pt 150 nm/ Ta 24 nm/ [Si/ SiO_2] 300 μm/ [Ta 5 nm/ Cu 3 nm/

IrMn 8 nm/ FeCoSiB 100 nm] x10. A 2.5x objective with a NA 0.06 and blue LED (wavelength: 460 nm) are employed for imaging. For both ME sensors, the imaging has been carried out close to the fixed portion of the cantilevers and directly under the sensor electrodes, where the obtained ME response is most relevant [125]. In the images, the MOVE response across the whole width of the magnetic structure is acquired. Furthermore, during MOVE imaging, in-operando sensor response is measured with the setup shown in Figure 3.14 at the sensors' respective mechanical resonance frequencies $\mathbf{f_{res}}$ of 872 Hz for the unbiased and 839 Hz for the biased ME sensors to correlate with the reconstructed ME loops.

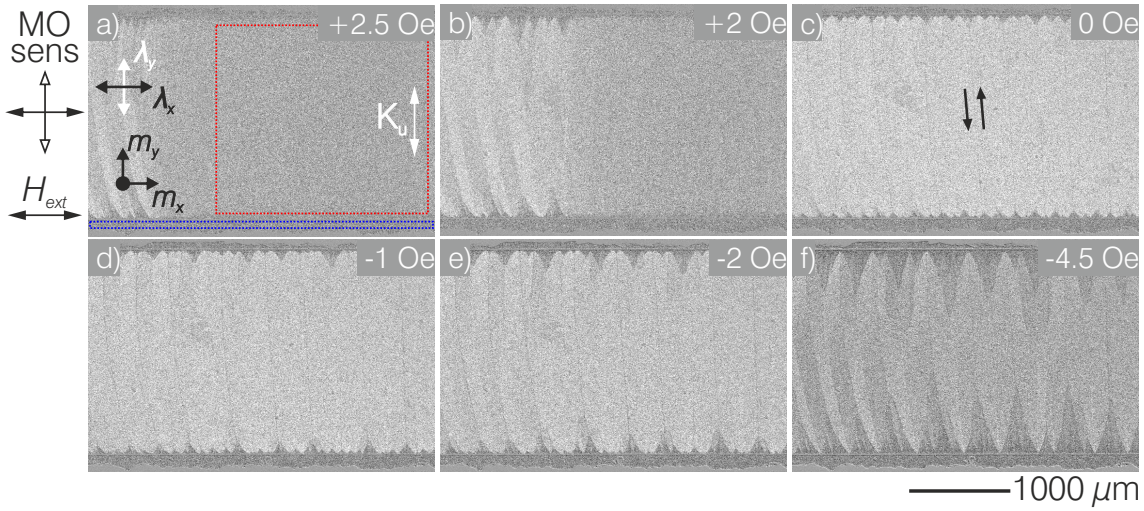

Figure 5.12: Selected MOVE images during magnetization reversal along the structure's long axis of a ME sensor with singlelayer of FeCoSiB as the magnetostrictive film are displayed (a-f). MO sensitivity and $\boldsymbol{H_{ext}}$ axes are indicated. Red and blue areas encompass respectively the analyzed magnetic and non-magnetic regions, which are utilized to obtain $\boldsymbol{m^2}$ loops. (Sample: AlN 2 μm/ [Si/SiO_2] 300 μm/ FeCoSiB 1 μm)

Some selected MOVE images at important points during magnetization reversal are displayed in Figure 5.12(a-f). The presented $\boldsymbol{\lambda}$(x, y) map at $\boldsymbol{H_{ext}}$= +2.5 Oe displays spatially uniform MOVE contrast corresponding to $\boldsymbol{\lambda_y}$ response (Figure 5.12a). As $\boldsymbol{H_{ext}}$ is decreased, at $\boldsymbol{H_{ext}}$= +2 Oe two regions exhibiting different MOVE contrast emerge (Figure 5.12b). The left and right hand side of the image display respectively bright and dark MOVE contrasts, which stems from coexisting blocked and wide domain configurations at the same $\boldsymbol{H_{ext}}$ (see also Figure 5.2n and its discussion). This suggest that the $\boldsymbol{\lambda}$ response imposed by these distinct magnetic domain configurations are almost of opposite sign (i.e. for bright region $\sim \boldsymbol{\lambda_y}$ and dark region $\sim \boldsymbol{\lambda_y}$) (Figure 5.12b). With decreasing $\boldsymbol{H_{ext}}$, a total conversion of the magnetic domain state occurs and the resulting magnetization state depicts a homogeneous $\boldsymbol{\lambda}_y$ response in the middle of the magnetic structure (Figure 5.12c). Now, with increasing $\boldsymbol{H_{ext}}$ along the minus direction the movement of the closure domains

at the sides lead to sudden $\boldsymbol{\lambda}$ variations almost from $\boldsymbol{\lambda}_\mathbf{y}$ to $\boldsymbol{\lambda}_\mathbf{x}$, whereas in the middle of the structure the $\boldsymbol{\lambda}$ response varies almost linearly towards $\boldsymbol{\lambda}_\mathbf{x}$ (Figure 5.12d-f). Overall, the $\boldsymbol{\lambda}$(x, y) maps display to the right of the images a relatively uniform $\boldsymbol{\lambda}$ response due to well-aligned $\mathbf{K_u}$ in this region. However, to the left of the images, where the cantilever is fixed, local deviations from the intended $\mathbf{K_u}$ axis leads to discrepancies in local $\boldsymbol{\lambda}$ response possibly originating from stress-induced magnetic anisotropy contributions.

Now, similar to the procedure in Figure 5.11, the $\boldsymbol{\lambda}$ curves are obtained by analyzing the intensity in each $\boldsymbol{\lambda}$(x, y) map and $\boldsymbol{\lambda}$ response is plotted against $\boldsymbol{H_{ext}}$. As has been mentioned in Section 3.2.2.2, MOVE, even when it is maximized, is a relatively weak effect leading to very low detectable signals. Therefore it is important to minimize possible external noise sources and/or extract them from the measured data. Relevant noise sources for the displayed MO measurements resulting in a decrease of SNR are as follows [95]:

1. **Fluctuations in light intensity**: Undesired contributions to the detected signal might stem from light intensity variations of the employed illumination source.

2. **Imaged object moving out of focus**: As is the case for the investigated ME sensors in cantilever design, when imaging volatile devices in operation, the object moves in and out of objective's focus. This will lead to variations in overall detected intensity. Moreover, in instances with inhomogeneous illumination for objects drifting in focal plane the measured signal will vary with position.

3. **Contributions from Faraday rotation**: The applied $\boldsymbol{H_{ext}}$ leads to Faraday rotation to the incident and reflected light at the objective lens as well as in the imaging medium. Possessing mostly a linear $\boldsymbol{H_{ext}}$ relationship, the Faraday rotation is especially noticeable at high $\boldsymbol{H_{ext}}$, which is usually characterized by a change of intensity even after magnetic saturation is reached [131].

4. **Camera**: The read noise is defined by the dynamic range of the camera. Additionally, electronic noise stemming from analog-to-digital conversion at pixel read-out is introduced to the final image.

The way to extract such undesired signals from the measured signal is displayed in Figure 5.13. The discussed method is used for all presented $\boldsymbol{\lambda}(\boldsymbol{H_{ext}})$ loops. This technique is likewise viable for other MO effects and will in most cases greatly enhance $\boldsymbol{m}(\boldsymbol{H_{ext}})$ and $\boldsymbol{m^2}(\boldsymbol{H_{ext}})$ curve quality in MO measurements.

For all displayed data, the intensity change is obtained from the differential MO images. In Figure 5.13a the intensity change at FeCoSiB film is plotted against the

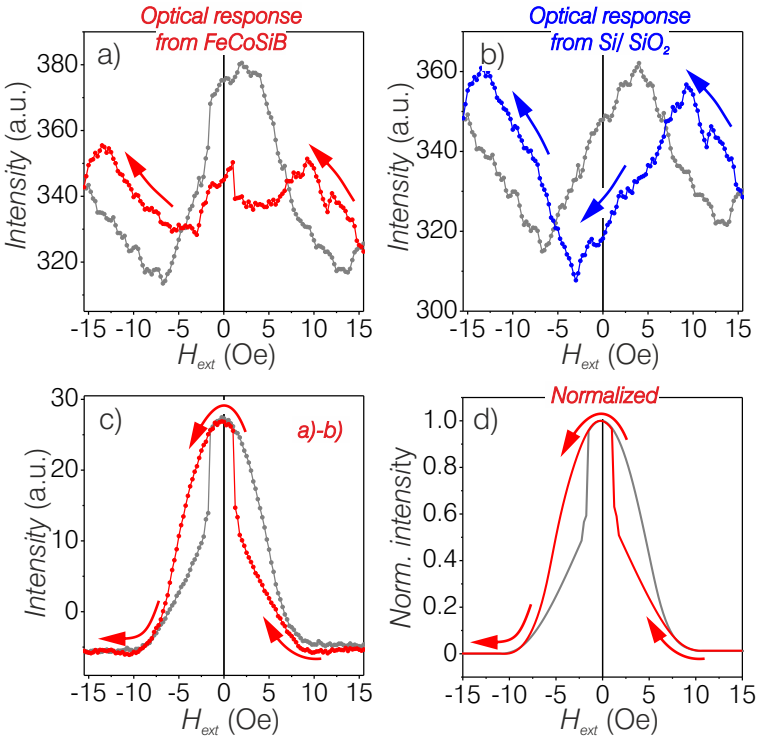

Figure 5.13: In (a) and (b), the measured intensity with varying $\boldsymbol{H_{ext}}$ at unbiased FeCoSiB film and at the SiO_2 substrate are displayed. (c) is the $\boldsymbol{m^2}$ loop acquired by subtracting the (b) from (a). (d) displays the normalized fit of (c), which is later used for local ME response calculation. The regions analyzed for acquisition of the loops in (a) and (b) are indicated in Figure 5.12a. (Sample: AlN 2 μm/ [Si/SiO_2] 300 μm/ FeCoSiB 1 μm)

applied $\boldsymbol{H_{ext}}$. The analyzed region is indicated with red rectangle in Figure 5.12a. The resulting curve carries along with the desired $\boldsymbol{m^2}$ response the above mentioned noise sources (Figure 5.13a). In order to extract the pure MOVE signal, the intensity change at a non-magnetic part on the sample is analyzed. For the investigated sensors, dicing is used after lithography processes in order to obtain the cantilever shape. The dicing results in regions with only Si/ SiO_2 at the edges of the cantilever, which is indicated by the region enclosed by the blue rectangle in Figure 5.12a. The evaluated signal contains the noisy part of the optical response in Figure 5.13a. The plotted signal follows an almost sinusoidal trend and is reminiscent of the movement of the cantilever with changing $\boldsymbol{H_{ext}}$ (Figure 5.13b).

Now by simple point-to-point subtraction of the data points in Figure 5.13a and b, a nearly noise free MOVE curve is obtained (Figure 5.13c). In the final curve, the intensity reaches below zero. This is an offset caused by the difference in reflectivity of the analyzed FeCoSiB and Si/ SiO_2 surfaces (compare measured intensities in Figure 5.13a and b). Nevertheless, the greatly enhanced curve quality allows for resolution of essential features such as sudden hysteretic variations in $\boldsymbol{\lambda}$ response and hysteresis caused by non-linear magnetization changes. The curve is later fitted by applying exponential functions at different regions and the final curve is normalized (Figure 5.13d) in order to reconstruct $\boldsymbol{dm^2/dH_{ext}} \approx$ ME curve. Normalization is performed in order to compensate for the differences in reflectivity between the unbiased and biased ME sensors, hence to compare the reconstructed ME amplitudes with the measurements carried out for the biased sensor.

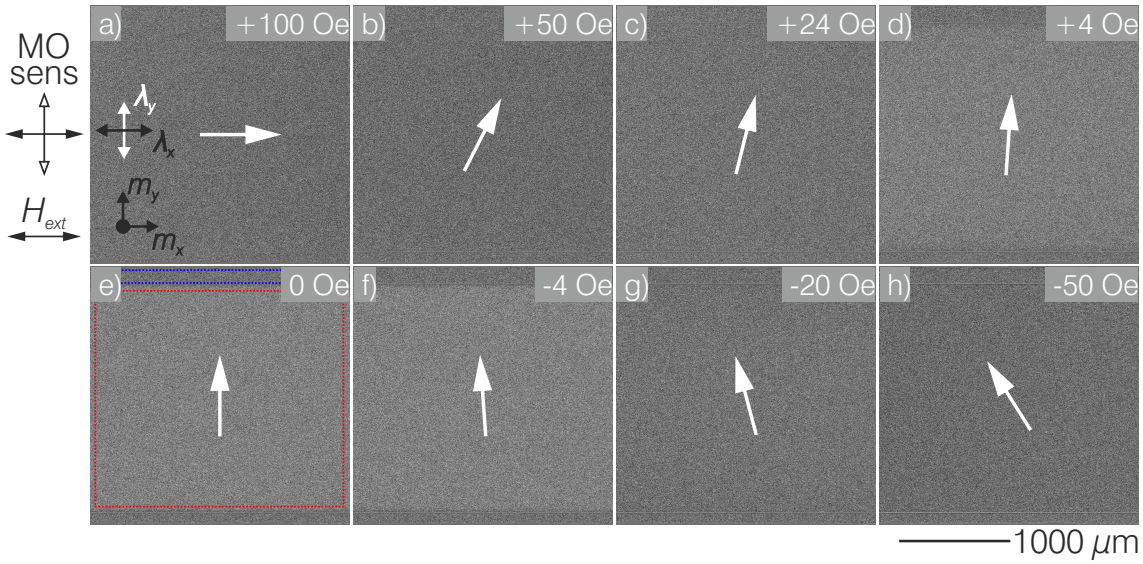

Figure 5.14: Selected MOVE images during magnetization reversal along the structure's long axis of a ME sensor with biased FeCoSiB as the magnetostrictive film are displayed (a-f). Magneto-optical sensitivity and $\boldsymbol{H_{ext}}$ axes are indicated. Red and blue areas in (e) encompass respectively the analyzed magnetic and non-magnetic regions, which are utilized to obtain $\boldsymbol{m^2}$ loops. (Sample: AlN 2 μm/ [Si/SiO_2] 300 μm/ [Ta 5 nm/ Cu 3 nm/ IrMn 8 nm/ FeCoSiB 100 nm]x 10)

The MOVE images of the biased ME sensor are displayed in Figure 5.14. For the investigated laminated sensor, the topmost FeCoSiB layer (100 nm) is thicker than the penetration depth of visible light ($\boldsymbol{t_{pd}} \approx$ 30 nm). Therefore, the following MO measurements are only sensitive to the top FeCoSiB layer.

Overall, the MOVE images display no sign of magnetic domain formation in the topmost FeCoSiB layer (Figure 5.14). With $\boldsymbol{H_{ext}}$ applied along the cantilevers long axis (i.e. perpendicular to exchange bias direction), the $\boldsymbol{\lambda}$ response is homogeneous. As $\boldsymbol{H_{ext}}$ is reduced towards remanence (Figure 5.14a to e), a uniform $\boldsymbol{\lambda}$ variation occurs from $\boldsymbol{\lambda_x}$ to $\boldsymbol{\lambda_y}$ and the magnetostrictive film contracts with respect to Figure 5.14a. Likewise, when the direction of $\boldsymbol{H_{ext}}$ is reversed and with increasing $\boldsymbol{H_{ext}}$ a coherent change of $\boldsymbol{\lambda}$ takes place back to $\boldsymbol{\lambda x}$ (Figure 5.14e to h). The observed linear $\boldsymbol{\lambda}$ response is directly linked with the single domain state in the imaged layer. Avoiding domain wall formation leads to coherent rotation of magnetization.

Similar to the data shown for the unbiased sensor (Figure 5.13), by analyzing the optical intensity at FeCoSiB (Figure 5.15a) and Si/ SiO_2 (Figure 5.15b) (red and blue rectangles in Figure 5.14e, respectively), and with subsequent subtraction of the curves, local $\boldsymbol{\lambda}$ response is obtained for the biased sensor (Figure 5.15c). The intensity plot from FeCoSiB follows a very noisy trend, subtraction of possible noise sources contained in the optical response from Si/ SiO_2 leads to a nearly noise free $\boldsymbol{m^2}$ loop (Figure 5.15c). Just like for the unbiased ME sensor, the offset originates from the difference in reflectivity between FeCoSiB and Si/ SiO_2 surfaces.

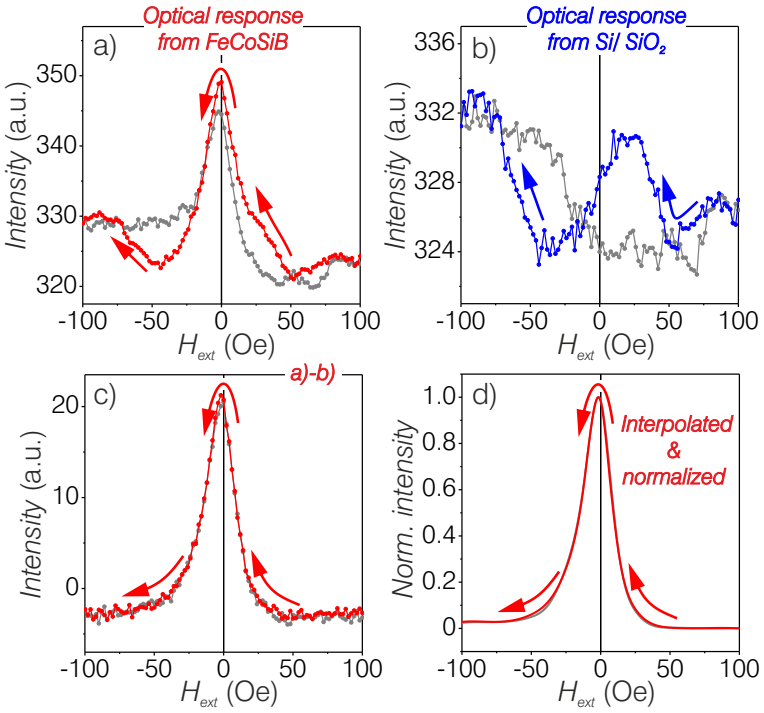

Figure 5.15: In (a) and (b), the measured intensity with varying $\boldsymbol{H_{ext}}$ at biased FeCoSiB film and at the SiO_2 substrate are displayed. (c) is the $\boldsymbol{m^2}$ loop acquired by subtracting the (b) from (a). (d) displays the normalized fit of (c), which is later used for local ME response calculation. The regions analyzed for acquisition of the loops in (a) and (b) are indicated in figure 5.14e. (Sample: AlN 2 μm/ [Si/SiO_2] 300 μm/ [Ta 5 nm/ Cu 3 nm/ IrMn 8 nm/ FeCoSiB 100 nm]x 10)

In accordance with the discussed $\boldsymbol{\lambda}$(x, y) maps, little to no hysteresis is observed in the overall $\boldsymbol{\lambda}$ response to $\boldsymbol{H_{ext}}$. Moreover, the resolved asymmetric approach to plus and minus $\mathbf{H_{sat}}$ is likely due to a small angle between the induced $\mathbf{K_{eff}}$ and the applied $\boldsymbol{H_{ext}}$. As a last step, Figure 5.15c is interpolated and smoothened. The fitted curve possesses 0.25 Oe step width between $\boldsymbol{H_{ext}}$ (same as Figure 5.13d). Finally, the curve is normalized to later reconstruct the local ME response.

As has been mentioned previously, the ME responses of the investigated sensors have been measured simultaneously with MOVE imaging. Figure 5.16 displays the ME response $\boldsymbol{U_{ME}}$ at the sensors' respective mechanical resonance frequency $\mathbf{f_{res}}$, the calculated local $\boldsymbol{dm^2/dH_{mea}} \approx$ ME, inductively and magneto-optically (MO) measured magnetization loops for the sensors with unbiased (a-d) and biased (e-h) FeCoSiB layers. The MO loops have been measured at the same region as in Figure 5.12 and Figure 5.14.

In Figure 5.16a, the measured $\boldsymbol{U_{ME}}$ for the unbiased sensor displays a rather hysteretic behavior. $\boldsymbol{U_{ME}}$ reaches its maximum value of 5.32 mV at $\boldsymbol{H_{ext}}$= -5 Oe (red curve). At the same $\boldsymbol{H_{ext}}$, but with different $\boldsymbol{H_{ext}}$ history the ME response is 2.06 mV (gray curve), corresponding to a ME response ratio $\boldsymbol{U_{ME,\,red}}$(-5 Oe)/ $\boldsymbol{U_{ME,\,gray}}$(- 5 Oe) = 2.58 (see Table 5.1). The reconstructed local ME response $\boldsymbol{dm^2/dH_{mea}}$ is obtained by first-order derivation of the normalized $\boldsymbol{m^2}$ loop (Figure 5.13d). $\boldsymbol{H_{mea}}$ is 0.25 Oe (Figure 5.16b). Abrupt $\boldsymbol{\lambda}$ changes such as the jump starting from +1.75 Oe to +1 Oe are excluded from the derivations (Figure 5.13c and d). They correspond to irreversible magnetic domain configuration

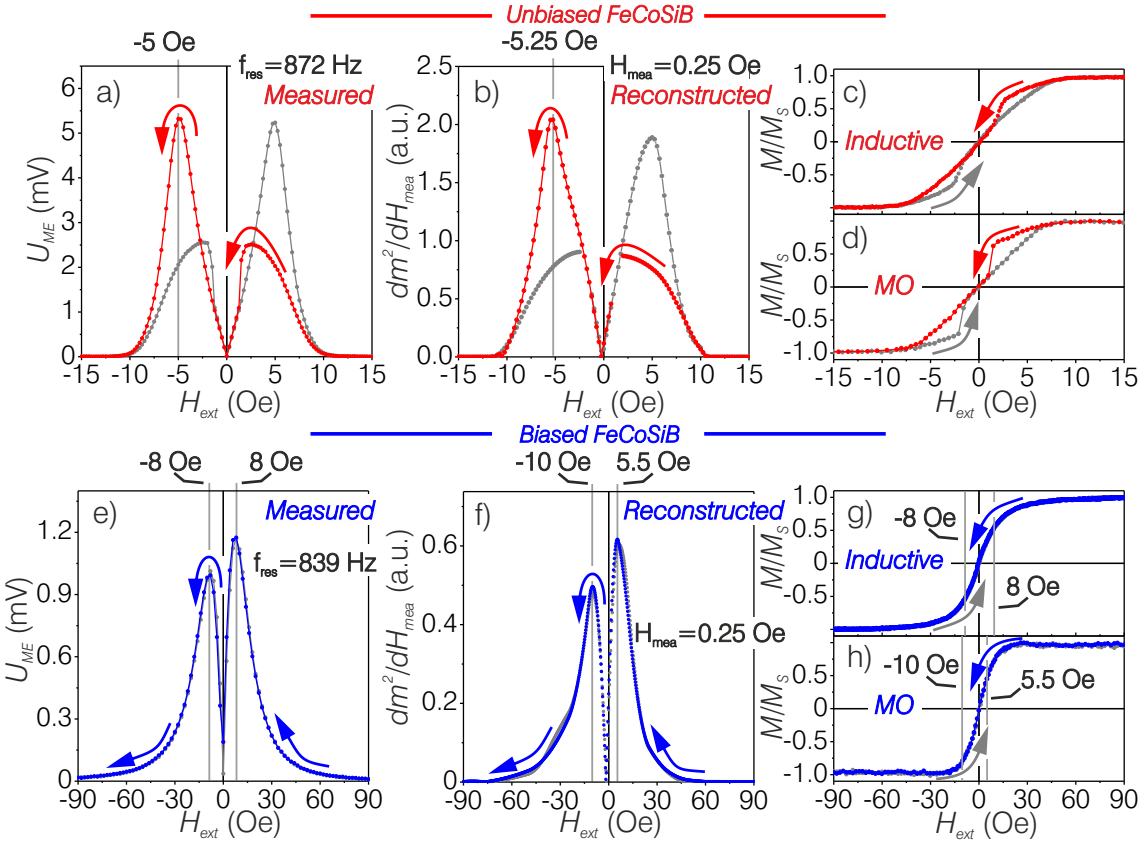

Figure 5.16: Measured (a, e) and reconstructed (b, f) ME data are shown along with inductively (c, g) and magneto-optically (MO) (d, h) measured magnetization loops of ME sensors with unbiased (a-d) and exchange biased (e-h) FeCoSiB layers. (Samples: (a-d) AlN 2 μm/ [Si/ SiO_2] 300 μm/ FeCoSiB 1 μm and (e-h) AlN 2 μm/ [Si/ SiO_2] 300 μm/ [Ta 5 nm/ Cu 3 nm/ IrMn 8 nm/ FeCoSiB 100 nm]x 10)

changes and in differential measurements do not add to the measured ME response.

Table 5.1: Selected measured and reconstructed ME responses for the unbiased sensor at their respective maximums (red curve) and the hysteretic response as $\boldsymbol{H_{ext}}$ is decreased from −15 Oe (gray curve) along with their ratios are shown. Values are obtained from Figure 5.16

	$\boldsymbol{H_{ext}}$ **decreased from +15 Oe**	$\boldsymbol{H_{ext}}$ **decreased from −15 Oe**	**ratio**
measured (−5 Oe)	5.32 mV	2.06 mV	2.58
reconstructed (−5.25 Oe)	2.04 a.u.	0.78 a.u.	2.62

The ME hysteresis is reconstructed to a great degree. At $\boldsymbol{H_{ext}}$= −5.25 Oe, the curve exhibits the highest ME response $\boldsymbol{dm^2/dH_{mea}}$= 2.04 a.u. as $\boldsymbol{H_{ext}}$ is increased from remanence. At the same $\boldsymbol{H_{ext}}$, but for $\boldsymbol{H_{ext}}$ decreased from $-\boldsymbol{H_{sat}}$, $\boldsymbol{dm^2/dH_{mea}}$ is only 0.78. The calculated ratio of 2.62 is comparable with the measured case (see Table 5.1). The curve asymmetry in $+\boldsymbol{H_{ext}}$ and $-\boldsymbol{H_{ext}}$ can be attributed to possible residual MOKE contrast present during MOVE imaging. Moreover, inductively (Figure 5.16c) and magneto-optically (MO) (Figure 5.16d) acquired magnetization responses measured along the long axis are displayed. Despite exhibiting similar $\mathbf{H_k} \approx 5$ Oe, the hysteresis is much pronounced in MO measurement. This indicates that the magnetic anisotropy distribution is not the same across the FeCoSiB film, which might lead to small differences between the measured and the reconstructed ME curves (see also large view MOKE images from the same ME sensor in Figure 5.2k).

Similar to the sensor with unbiased FeCoSiB film, data consisting of measured and reconstructed ME responses and magnetization measurements for the biased sensor are displayed (Figure 5.16e-h). $\boldsymbol{U_{ME}}$ response exhibits a hysteresis free behavior, which is linked to prevention of magnetic domain formation (Figure 5.16e). Through biasing a single domain state is maintained and the magnetic domain effects are avoided (see MOVE images in Figure 5.14). However, the additional magnetic anisotropy contribution from the exchange bias to linearize the magnetization response leads to noticeably higher saturation fields than the unbiased ME sensor (compare $\boldsymbol{H_{ext}}$ values Figure 5.16a and e). As a result, $\boldsymbol{H_{wp}}$ is shifted up to $\boldsymbol{H_{ext}}$ = +8 Oe. In addition to that $\boldsymbol{U_{ME}}$ response is asymmetric at $\boldsymbol{H_{ext}} = \pm 8$ Oe, which corresponds to a ratio of $\boldsymbol{U_{ME}}$(+8 Oe)/ $\boldsymbol{U_{ME}}$(−8 Oe) = 1.16 ($\boldsymbol{U_{ME}}$(+8 Oe) = 1.17 mV and $\boldsymbol{U_{ME}}$(−8 Oe) = 1.01 mV).

Table 5.2: Selected measured and reconstructed ME responses for the biased sensor at their local maximums along $\pm \boldsymbol{H_{ext}}$ and their ratios are shown. Values are obtained from Figure 5.16

	local maximum at +$\boldsymbol{H_{ext}}$	**local maximum at -$\boldsymbol{H_{ext}}$**	**ratio**
measured	1.17 mV (+8 Oe)	1.01 mV (-8 Oe)	1.16
reconstructed	0.78 a.u. (+5.5 Oe)	0.62 a.u. (-10 Oe)	1.27

As for the reconstructed ME response, features like almost hysteresis free ME response and the mentioned curve asymmetry are reconstructed (Figure 5.16f). However, the calculated maximum ME responses are shifted away from the measured case to $\boldsymbol{dm^2}$(-10 Oe)/$\boldsymbol{dH_{mea}}$= 0.49 a.u. and $\boldsymbol{dm^2}$(+5.5 Oe)/$\boldsymbol{dH_{mea}}$= 0.62 a.u. (compare Figure 5.16e and f), corresponding to a ratio of 1.27. Indications to the origin of subtle differences such as the shift in peak positions are obtained from inductive and MO magnetization measurements (Figure 5.16g and h). Firstly, as has been discussed for the unbiased sensor, both the reconstructed ME (Figure 5.16f) as well as the MO magnetization (Figure 5.16h) curves depict corresponding local responses. Moreover, for sufficiently thick individual layer thicknesses in laminated structures, the MO measurements and subsequent reconstructions are only sensitive to the topmost magnetic layer. Therefore, no direct information about magnetization processes in optically invisible, underlying FeCoSiB layers can be obtained from the displayed MO measurements/ reconstructions. Although, particularly for samples in millimeter dimensions, the magnetization signals in the inductive measurements are weighed different spatially, they detect the volumetric response. Figure 5.16g and h indicate that the magnetization response at the top magnetic layer differs from the volumetric response, which might be the reason in the shift observed in reconstructed curve.

Considering that both sensors possess the same amount of FeCoSiB and AlN, and moreover that irreversible processes linked to magnetic domain processes are omitted from the $\boldsymbol{dm^2/dH_{mea}}$ curves, the measured and reconstructed response for both unbiased and biased sensors should be comparable, where the magnetization responses are linear. For the measured loops, the $\boldsymbol{U_{ME}}$ ratio at the large peaks for both sensors ($\boldsymbol{U_{ME}^{SL}/U_{ME}^{EB}}$) is 4.55, whereas for the reconstructed case the ratio becomes 3.29. This difference of nearly 30% is probably due to MO measurements being insensitive to the underlying FeCoSiB layers in the case of the biased sensor and moreover, for both sensors the measured area does not cover the whole sensor area. Additional, possible hysteretic polarization mechanisms in AlN differing from one sensor to another can also explain the mentioned discrepancies.

The magnetization symmetry of MOVE allows the MO effect to be applicable to other magnetic effects that are quadratic in magnetization. Similar to $\boldsymbol{\lambda}$, AMR is an effect that possesses a quadratic relationship with magnetization direction $\boldsymbol{m}$ and $\boldsymbol{\Delta R}/\boldsymbol{R}_{\perp}$ is one of the figure-of-merits of such sensors. Phenomenologically, the angular $\boldsymbol{\theta}$ dependence of AMR effect can be expressed as (5.2), where $\boldsymbol{R}_{\perp}$ is the resistance of the magnetic material with $\boldsymbol{m}$ perpendicular to the measurement direction (current direction) $\boldsymbol{a}$ and $\boldsymbol{\Delta R}$ is the resistance difference between $\boldsymbol{R}_{\parallel}$ and $\boldsymbol{R}_{\perp}$ [1].

$$R(\theta) = R_{\perp} + \Delta R(m \cdot a)^2 = R_{\perp} + \Delta R \cos^2(\theta); \qquad \Delta R = R_{\parallel} - R_{\perp} \tag{5.2}$$

In order to demonstrate MOVE's applicability for AMR response reconstruction, a hybrid magnetic film is used [132–134]. The film is composed of Ta 3 nm/ $Ni_{81}F_{19}$ 50 nm/ $Ir_{23}Mn_{77}$ 7 nm/ TaN 5 nm stack deposited on a thermally oxidized [Si/ SiO_2] 300 μm substrate. The initial exchange bias direction is aligned during film deposition by application of a magnetically saturating $\boldsymbol{H_{ext}}$. A further photolithography step composed of a periodic stripe patterned mask (20 μm stripe width) is adopted to partially cover the film before ion-irradiation, which allows to locally vary the exchange bias direction in the uncovered part of the film. For the investigated sample, a periodic variation of exchange bias alignment by 90° between alternating stripes is obtained. Furthermore, for extraction of possible noise sources from the later shown MOVE curves, 30 nm thick Ta structures are deposited on IrMn layer (Hybrid film courtesy of Julia Trützschler. See [133] for details on film preparation. Ta layer deposition is performed by Volker Röbisch in Kiel cleanroom facilities).

Through MOVE imaging, regions with different AMR responses are separated, which is not available to electrically measured AMR responses and even to most magnetometric measurements, where one can at most approximate what is happening inside the magnetic volume.

An optical image of the investigated sample area is shown in Figure 5.17a. On top, the irradiated and as-prepared parts are marked respectively with red and blue rectangles. The low reflectance in the irradiated stripes stems due to ion-irradiation. The later deposited Ta layer is indicated by the black rectangle at the bottom of Figure 5.17a. The displayed experimental data correspond to $\boldsymbol{H_{ext}}$ applied along the stripe length. From the optical image, individual stripe widths are measured. Individual stripe widths for the irradiated and as-deposited parts are different due to photolithography procedures. Considering negligible thickness variations due to ion-irradiation and periodic, same amount of stripes for each stripe type, the volume encapsulated by the irradiated and as-prepared regions are measured to be $0.55 \cdot V_{\mathrm{total}}$

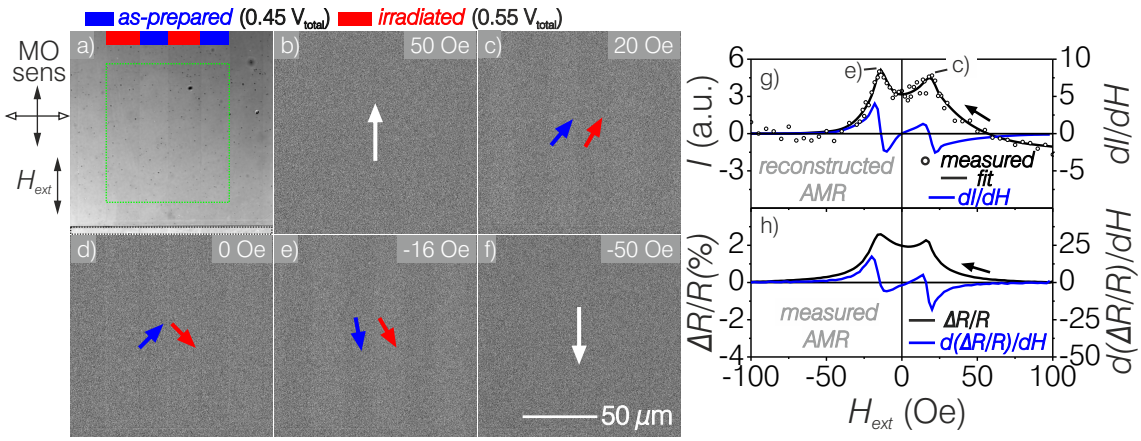

Figure 5.17: Optical image (a) as well as MOVE images at selected points during magnetization reversal with $\boldsymbol{H_{ext}}$ applied parallel to the stripes (b-f) are displayed for a partially ion irradiated magnetic material. Magneto-optical sensitivity (MO sens) and $\boldsymbol{H_{ext}}$ axis are indicated. At the bottom of the images, a 30 nm Ta film is deposited to later extract the pure MO signal (see bottom of (a)). The reconstructed local and measured AMR responses, along with their corresponding sensitivity curves are displayed in (g) and (h), respectively. (Sample: [Si/SiO_2] 300 nm/ Ta 3 nm/ $Ni_{81}Fe_{19}$ 50 nm/ $Ir_{23}Mn_{77}$ 7 nm/ TaN 5 nm)

and $0.45 \cdot V_{total}$, respectively, which also determines their amount of contribution to the total AMR signal.

Some selected MOVE images are shown in Figure 5.17b-f. Starting from $\mathbf{H_{sat}}$, the MOVE contrast is uniformly dark. All stripes are saturated in the $\boldsymbol{H_{ext}}$ direction (Figure 5.17b). Around $\boldsymbol{H_{ext}}$ = 20 Oe, as-prepared regions display bright MO contrast. In remanent magnetization state both stripes show approximately the same MO contrast (Figure 5.17d), pointing out towards both stripes having the same angle with respect to the applied MO sensitivity. Increasing $\boldsymbol{H_{ext}}$ in minus direction, at $\mathbf{H_{ext}}$ = −16 Oe, the magnetization switch in the irradiated region occurs (Figure 5.17e). Further $\boldsymbol{H_{ext}}$ increase leads to magnetic saturation of both stripes and the MO contrast is homogeneously dark (Figure 5.17f). Compared to the previous measurements conducted on FeCoSiB based ME sensors, the discussed MO images for the NiFe structures display rather low MO contrast, which is an indication that the essential 2nd order MO coefficient (see equation (3.3)) is lower for NiFe than FeCoSiB. This implies relatively little ellipticity upon reflection. Moreover, unlike FeCoSiB, the MO measurements have been performed through the top IrMn layer that leads to a possible decrease to the acquired MO signal.

Now by analyzing the intensity change in the acquired $\boldsymbol{m^2}$ images, the local AMR response can be magneto-optically reconstructed (Figure 5.17g). For this purpose, intensity change in two pairs of irradiated/ as-deposited stripes is measured as indicated by the yellow rectangle in Figure 5.17a. For comparison the AMR response with $\boldsymbol{H_{ext}}$ applied along the same axis is also displayed (Figure 5.17h). Only

one $\boldsymbol{H_{ext}}$ direction is displayed in Figure 5.17g and h ($\boldsymbol{H_{ext}}$ is swept from +100 Oe to −100 Oe). Additionally, calculated AMR sensitivity curves are presented, which exhibits the rate of AMR change at distinct $\boldsymbol{H_{ext}}$ values (blue curves in Figure 5.17g and h). They are obtained by first order derivation of their respective AMR curves with respect to $\boldsymbol{H_{mea}}$ = 1 Oe.

Through MO reconstruction of the AMR response, the general AMR behavior is approximated with very good precision. The relative local highest peak ratios in $\pm\boldsymbol{H_{ext}}$ for both reconstructed and measured responses correspond to 0.9 (AMR_{recon}(+18 Oe)= 4.5 a.u., AMR_{recon}(−14 Oe) = 5.1 a.u. and AMR_{mea}(+16 Oe) = 2.3 %, AMR_{mea}(−14 Oe) = 2.6 %). Furthermore, the derived AMR sensitivity curves ($\boldsymbol{dI/dH}$ and $\boldsymbol{d(\Delta R/R)/dH}$) are in very good agreement and both exhibit the AMR sensor's most $\boldsymbol{H_{mea}}$ sensitive point at $\boldsymbol{H_{ext}}$ = −18 Oe.

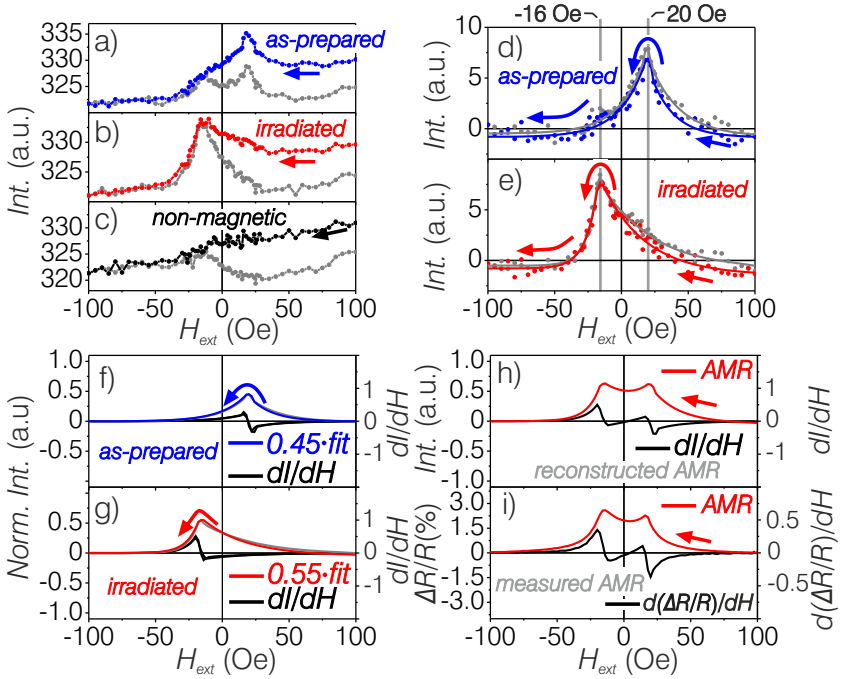

Figure 5.18: The analyzed regions from the measurement in Figure 5.17 are displayed in (a-c). (d) and (e) correspond to the non-magnetic region extracted for the corresponding magnetic regions along with the curve fits. The signals calculated accordingly from normalized fits of (d) and (e) are displayed in (f) and (g), respectively. (h) and (i) are reconstructed and measured AMR responses along with the calculated sensitivity curves. $\boldsymbol{H_{ext}}$ is in all cases applied as shown in Figure 5.17a parallel to the stripes. (Sample: [Si/ SiO_2] 300 nm/ Ta 3 nm/ $Ni_{81}Fe_{19}$ 50 nm/ $Ir_{23}Mn_{77}$ 7 nm/ TaN 5 nm)

For all akin hybrid magnetic films, the individual magnetization and AMR responses are weighed in the total signal according to the respective volumes encompassed by the magnetic structures. Therefore, individual contributions to the overall response can at best be approximated from integral measurements. AMR response reconstruction exclusive to each type of stripe is demonstrated in Figure 5.18.

The intensity change in each stripe is analyzed separately (Figure 5.18a, b), subsequently non-magnetic contributions to the signals (Figure 5.18c) are extracted to acquire $\boldsymbol{m}^2(\boldsymbol{H_{ext}})$ behaviors of both as-deposited and irradiated stripes (Figure 5.18d, e). The as-deposited and irradiated stripes exhibit peaks in MO intensity at +20 Oe and −16 Oe, respectively. The peak shift discrepancy stems from a combination of different $\boldsymbol{H_d}$ in each type of stripe (unequal stripe widths for as-deposited and irradiated stripes) and a possible change in $\boldsymbol{H_{eb}}$ due to ion irradiation. Now, individual AMR responses can be fitted and normalized with respect to the volume encompassed by them (Figure 5.18f, g). Separate, individual AMR responses for both as-prepared and irradiated stripes have now been realized. Their individual AMR sensitivity curves ($\boldsymbol{dI/dH}$) can also be calculated (black curves in Figure 5.18f and g).

The overall local AMR response is the summation of the separated AMR responses (Figure 5.18h). For comparison the measured AMR curve is also displayed in Figure 5.18i. Similar to the measured AMR curve, the reconstructed response possesses two local AMR peaks at +18 Oe and −14 Oe. Reconstructing the AMR responses for each type of stripe individually clarifies the origin of the two peaks at $\pm\boldsymbol{H_{ext}}$ (Figure 5.18i). Dual AMR peak response originate from different exchange bias alignments of individual stripes (Figure 5.17d and h). Along the applied $\boldsymbol{H_{ext}}$ axis, they possess antiparallel $\boldsymbol{H_{eb}}$ components relative to each other (compare magnetization and $\boldsymbol{H_{ext}}$ alignments Figure 5.17d). However, unlike the measured response, the reconstructed peak amplitude are almost the same ($\mathrm{AMR_{recon}}$(+18 Oe) = 0.62 a.u. and $\mathrm{AMR_{recon}}$(−14 Oe) = 0.63 a.u) and the ratio of which (∼1) is noticeably different from the measured case (∼0.9). The discrepancies in terms of both the AMR peak positions and their relative amplitudes originates from imaging only a local, small area on the sample. Moreover for both stripes, the magnetization reversal processes through a combination of magnetic domain wall motion and magnetization rotation. Domain wall motion leads to divergence from linear AMR response.

Additional, exemplary measurements performed under different $\boldsymbol{H_{ext}}$ alignments are displayed in Figure 5.19. MO data after non-magnetic signal extraction, fitted and normalized curves, as well as the total local reconstructed and measured AMR data are displayed. Each row depict AMR data at distinct $\boldsymbol{H_{ext}}$ alignments, namely 90° with respect to the long axis of the stripes (Figure 5.19a, b, c), 45° (Figure 5.19d, e, f) and 135° (Figure 5.19g, h, i).

For $\boldsymbol{H_{ext}}$ applied perpendicular to the stripes (Figure 5.19a), the AMR response for either stripe varies largely linear with $\boldsymbol{H_{ext}}$ and since they both possess $\boldsymbol{H_{eb}}$ component along $+\boldsymbol{H_{ext}}$, both as-prepared and irradiated parts display a peak along $-\boldsymbol{H_{ext}}$ in their corresponding AMR curves. Peak shifts of −16 Oe and −18 Oe are resolved for as-prepared and irradiated stripes, respectively (Figure 5.19a and b).

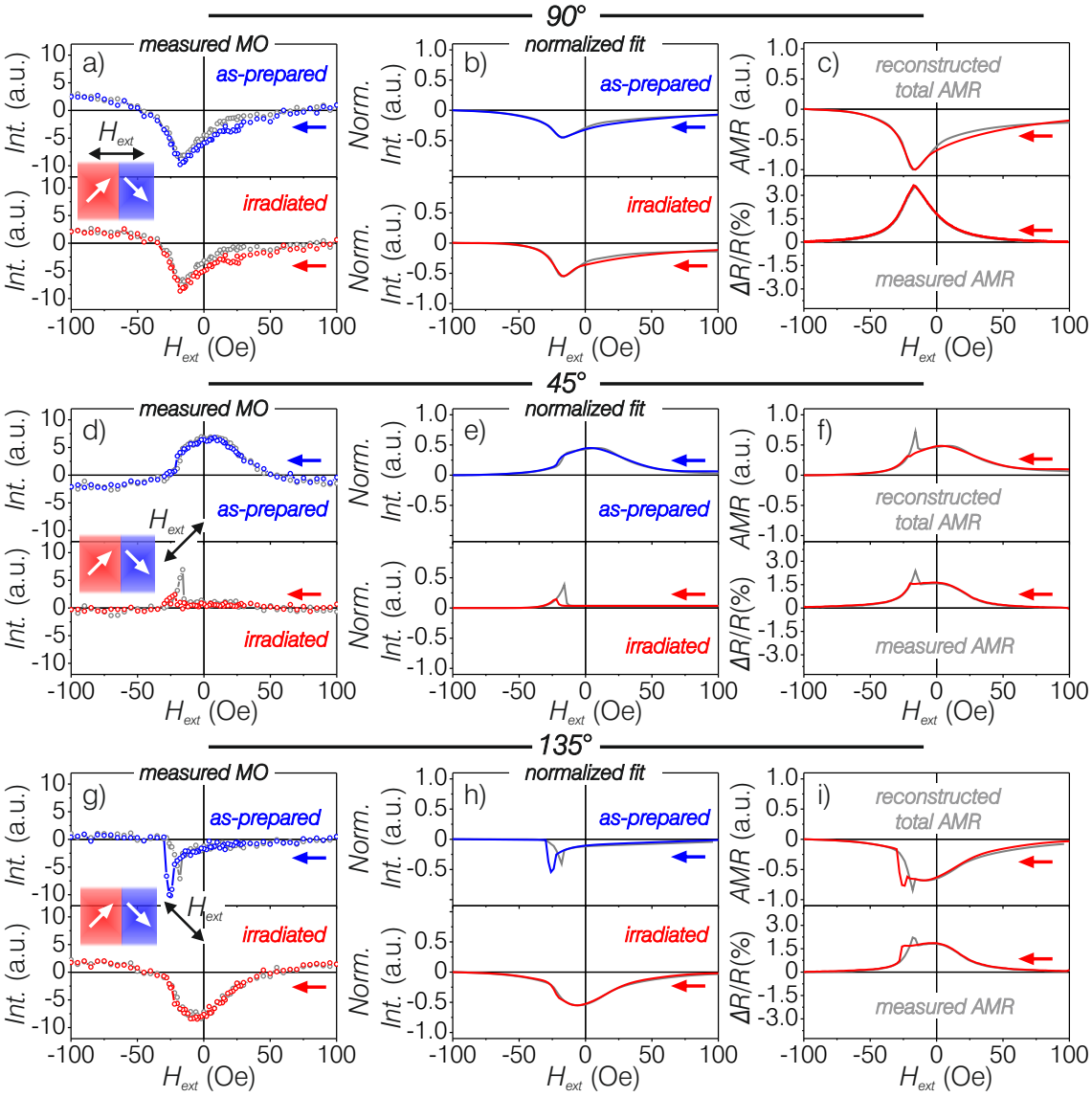

Figure 5.19: Data with $\boldsymbol{H_{ext}}$ along different directions are displayed. Individual MOVE responses from as-deposited and irradiated stripes (a, d, g) are displayed in the leftmost column, fits normalized according to individual stripe volumes (b, e, h) and reconstructed/ measured AMR curves (c, f, i) are presented in middle and right columns, respectively. The measurement direction (thus, also $\boldsymbol{H_{ext}}$ alignment) with respect to stripes' long axis are indicated in terms of degrees and also sketched in (a), (d), (g). (Sample: [Si/ SiO_2] 300 nm/ Ta 3 nm/ $Ni_{81}Fe_{19}$ 50 nm/ $Ir_{23}Mn_{77}$ 7 nm/ TaN 5 nm)

With their individual contribution calculated (Figure 5.19b), the total AMR response is reconstructed (Figure 5.19c). Dissimilar to the previous case with $\boldsymbol{H_{ext}}$ applied along the stripe length, only one global AMR peak is present (Figure 5.19c). At $\boldsymbol{H_{ext}}$ = -16 Oe, the contribution of both as-deposited and irradiated parts to the AMR response is almost maximal, resulting in reconstructed and measured AMR amplitudes of 1 a.u. and 3.6 %, respectively.

Other displayed data correspond to AMR responses with $\boldsymbol{H_{ext}}$ applied along one of the stripe's exchange bias direction and perpendicular to the other stripe. In the first case, $\boldsymbol{H_{ext}}$ is applied perpendicular to the as-prepared stripes, in this instance the AMR response of as-prepared regions is close to linear and almost symmetric (Figure 5.19d and e, as-prepared), indicating a coherent rotation of magnetization inside the as-deposited parts. Analyzing the irradiated parts of the hybrid magnetic structure, the AMR change is very limited with only two brief bumps along $-\boldsymbol{H_{ext}}$ direction as $\boldsymbol{H_{eb}}$ is compensated and activated (Figure 5.19d and e, irradiated). I.e. at the onset of $\boldsymbol{H_{eb}}$ compensation, as $\boldsymbol{H_{ext}}$ is decreased from +100 Oe (red curve), the AMR response first increases slightly but linearly with $\boldsymbol{H_{ext}}$, which points out towards coherent rotation of magnetization in this $\boldsymbol{H_{ext}}$ regime. After reaching a peak amplitude, with a small $\boldsymbol{H_{ext}}$ increase the AMR response suddenly drops to negligibly small values. $\boldsymbol{H_{eb}}$ is now compensated and the magnetization is aligned along $-\boldsymbol{H_{ext}}$ direction, the AMR response becomes zero. Similarly, for $\boldsymbol{H_{ext}}$ decreased from -100 Oe AMR response shows a slight increase as exchange bias is activated. However, the extent of the linear regime and the peak AMR amplitudes are not the same. This is an indication of commonly observed loop asymmetry in exchange biased polycrystalline films (i.e. polycrystalline $Ni_{81}Fe_{19}$ in our case) [59]. With the reconstructed and measured AMR responses at $\boldsymbol{H_{ext}}$ = 0 Oe as 0.48 a.u. and 1.63 %, respectively (Figure 5.19i). Both loops display a similar AMR behavior, such as the large bump at $\boldsymbol{H_{ext}}$= -16 Oe as $\boldsymbol{H_{ext}}$ is decreased from -100 Oe and the small bump for $\boldsymbol{H_{ext}}$ swept from +100 Oe is likewise less pronounced for both reconstructed and measured loops (Figure 5.19f, compare red and gray curves for reconstructed and measured AMR). In AMR operation, such sudden deviations from linearity do not add to the measured AMR signal since they are generally related to magnetic domain wall motion processes, which are commonly irreversible (e.g. as in the discussed case, the compensation and activation of exchange bias in the irradiated parts). Not only, this process is dependent on $\boldsymbol{H_{ext}}$ history, but for the discussed case due to $\boldsymbol{m^2}$ dependency of the AMR response, the irradiated parts do not add to the AMR response in sensor operation, AMR response is equivalent for $\pm\boldsymbol{m_i}$.

A similar instance but with $\boldsymbol{H_{ext}}$ aligned along the exchange bias direction of the as-prepared stripe, is displayed in Figure 5.19g-i. Now, the as-prepared stripe

response exhibits as expected a brief AMR increase along $-\boldsymbol{H_{ext}}$ direction, whereas the irradiated parts display an almost linear response (see corresponding responses in Figure 5.19g and h). The reconstructed curve likewise is in very good agreement with the measured AMR curve (Figure 5.19i). Both reconstructed and measured AMR curves display $\boldsymbol{H_{ext}}$ history dependent small bumps, which are more pronounced than the previously discussed case with $\boldsymbol{H_{ext}}$ applied 45° to the stripes (compare Figure 5.19i with Figure 5.19f). As indicated by the separated loops, they are linked to the magnetization response inside the as-prepared stripes. At $\boldsymbol{H_{ext}} = 0$ Oe, the resulting AMR amplitudes for the reconstructed and measured curves are 0.65 a.u. and 1.8 %, respectively.

In summary, visualization of $\boldsymbol{\lambda}$ response in state-of-the-art ME sensors and AMR response in hybrid magnetic films are demonstrated in an all MO manner through MOVE imaging. The acquired $\boldsymbol{\lambda}$(x, y), as well as AMR(x, y) maps directly expose the $\boldsymbol{m^2}$ response of the transpiring magnetic domain configurations. They furthermore allow reconstruction of local $\boldsymbol{\lambda}(\boldsymbol{H_{ext}})$ and AMR($\boldsymbol{H_{ext}}$) responses. They have been compared with their corresponding measured device responses. This way, differences in spatial contributions to the global device response are directly distinguished from one another. The overall device response is both separated from and linked to the occurring magnetization processes. Irreversible magnetic domain effects, which do not contribute to in-operando ME and AMR device responses, are identified.

6 Magnetization behavior in soft magnetic, model structures

In this chapter, magnetization responses of differently layered $Co_{40}Fe_{40}B_{20}$ (CoFeB) films to $\boldsymbol{H_{ext}}$ are reviewed. All model structures are sputter deposited on thermally oxidized [Si/ SiO_2] 300 μm substrates. During ferromagnetic and antiferromagnetic film deposition, an in-plane magnetic field $+\boldsymbol{H_{ext}}$ is applied, which is high enough to saturate the deposited ferromagnetic films and defines the magnetization induced magnetic anisotropy axis $\mathbf{K_u}$ and for the exchange biased films, the unidirectional magnetic anisotropy direction $\mathbf{K_{eb}}$.

First, data from full film magnetic structures are discussed. Later on, magnetization behavior of their structured counterparts are shown. The emphasis is given on hysteretic hard axis magnetization loops originating from magnetic domain formation and subsequent domain wall motion. The objective is to preserve a single domain magnetic state during magnetization reversal. The influence of demagnetizing field on magnetic domain formation is investigated.

6.1 Full film properties

The discussed full film structures possess in-plane dimensions of 1 cm x 2 cm. Magnetic films with total CoFeB film thicknesses of 80 nm and 160 nm are investigated. The effective magnetic anisotropy $\mathbf{K_{eff}}$ of all films lie in-plane along the long axis (sketch in Figure 6.1).

Ballistic local demagnetization factor variation along x-axis $\boldsymbol{N_x}$ [69] and the demagnetizing field $\boldsymbol{H_d^x}$, as well as full film dimensions with the applied coordinate system for the calculations are displayed in Figure 6.1. $\boldsymbol{H_d^x}$ is largely constant throughout the full film, drastically increasing at the very edges. The average $\mathbf{N_x}$ in the middle of the structures for 80 nm and 160 nm film thickness is $1.05{\cdot}10^{-6}$ and $2.1{\cdot}10^{-6}$, corresponding to $\mathbf{H_d^x}$ of 0.015 Oe and 0.03 Oe, respectively ($\mathbf{M_s}$ = 1.48 T [135]). Along the CoFeB film thickness $\mathbf{N_y} \approx 1$, thus the full films can be considered as extended films (not shown in Figure 6.1). As will be shown later, due to shape

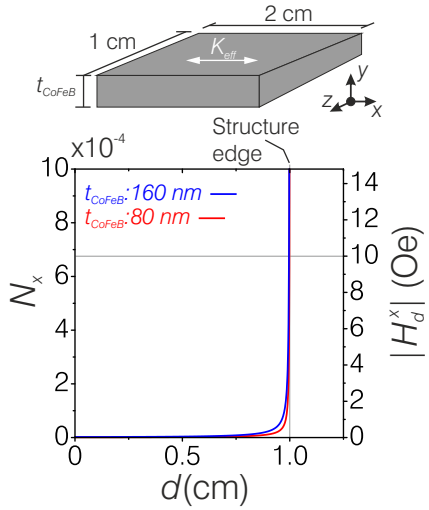

Figure 6.1: Calculated local demagnetizing field along x-axis for full film structures with 80 nm and 160 nm total CoFeB thicknesses are displayed. $\mathbf{H_d^x} = 10$ Oe is marked, which corresponds to the obtained $\boldsymbol{H_{eb}}$ for exchange biased structures. Due to curve symmetry at $\boldsymbol{d} = 0$ cm, half of the curve is shown. On top of the plot the in-plane dimensions are displayed.

anisotropy, the magnetization behavior of structured films can largely differ from full films. The intrinsic film properties such as $\mathbf{K_u}$ and $\mathbf{K_{eb}}$ can be obtained from the full films.

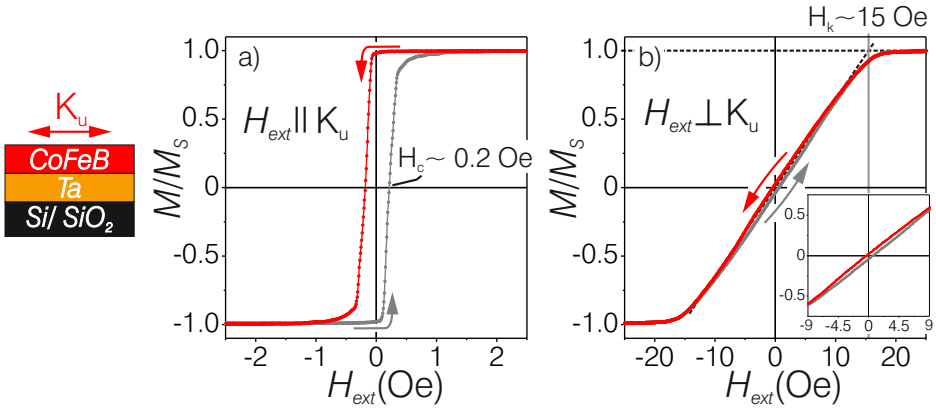

Figure 6.2: (a) easy and (b) hard axis magnetization loops for singlelayer CoFeB full film are displayed. Magnetic anisotropy field strength is marked in (b). Inset of (b) displays the same data in ±9 Oe. (In-plane dimensions: 1 cm x 2 cm) (Sample: [Si/ SiO_2] 300 μm/ Ta 5 nm/ CoFeB 160 nm/ TaN 5 nm)

The magnetization loops for the 160 nm thick unbiased CoFeB are displayed in Figure 6.2. The magnetization reversal measured along $\mathbf{K_u}$ ($\boldsymbol{H_{ext}} \| \mathbf{K_u}$) depicts a square shaped loop with a coercive field strength $\mathbf{H_c}$ of only 0.2 Oe (Figure 6.2a). Perpendicular to $\mathbf{K_u}$ ($\boldsymbol{H_{ext}} \perp \mathbf{K_u}$) magnetic anisotropy field $\mathbf{H_k}$ of 15 Oe is measured from the hard axis magnetization loop (Figure 6.2b), which corresponds to $\mathbf{K_u} = 888$ J/m^3 inside the CoFeB film. Furthermore, with the calculated magnetostatic energy coefficient $\mathbf{K_d}$ of $880 \cdot 10^3$ J/m^3, the quality factor $\mathbf{Q}$ for CoFeB is estimated to be 0.001, which indicates very soft magnetic properties for CoFeB ($\mathbf{Q} \ll 1$). The hard axis loop exhibits hysteretic magnetization response in the low $\boldsymbol{H_{ext}}$ regime (−9 Oe<$\boldsymbol{H_{ext}}$<+9 Oe) (see inset in Figure 6.2b). The non-linear, hysteretic magnetization response points out towards existance of magnetic domains

and a magnetization reversal by a combination of magnetic domain wall motion and coherent rotation of magnetization [36].

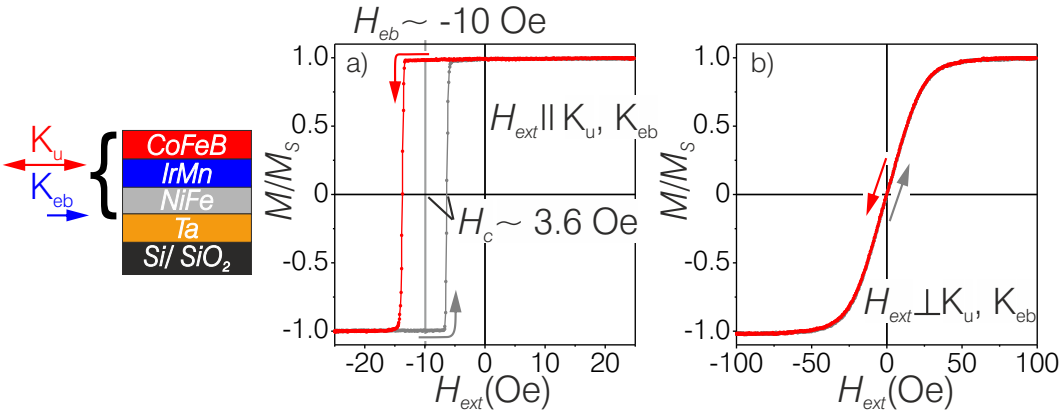

Figure 6.3: (a) easy and (b) hard axis magnetization loops for a singlelayer of exchange biased CoFeB are displayed. Resulting exchange bias field is marked in (a). (In-plane dimensions: 1 cm x 2 cm) (Sample: [Si/ SiO_2] 300 μm/ Ta 5 nm/ NiFe 2.5 nm/ IrMn 7 nm/ CoFeB 80 nm/ TaN 5 nm)

In order to obtain a coherent rotation of magnetization and thus, linearize the magnetization response, magnetic domain (and consequently domain wall) formation needs to be suppressed. This can, in example, be achieved by applying the exchange bias effect. Consequently, the demagnetizing field in the CoFeB film can be compensated internally and a single magnetic domain state can be obtained.

To facilitate the exchange bias, $Ir_{23}Mn_{77}$ (IrMn) is utilized as the antiferromagnetic material. A 3 nm Ta layer is deposited as a seed layer to grow 2.5 nm thick $Ni_{81}Fe_{19}$ (NiFe) with <111> texture and subsequently IrMn layer is epitaxially grown on the NiFe film. The NiFe layer provides the magnetization needed for exchange bias alignment. Finally, the 80 nm thick, amorphous CoFeB layer is deposited.

Figure 6.3 displays the magnetization loops of the exchange biased CoFeB film, obtained along the $\mathbf{K_{eb}}$, the axis of which also coincides with the induced $\mathbf{K_u}$ (Figure 6.3a; $\boldsymbol{H_{ext}}\| \mathbf{K_u}, \mathbf{K_{eb}}$) and perpendicular to it (Figure 6.3b; $\boldsymbol{H_{ext}}\perp \mathbf{K_u}, \mathbf{K_{eb}}$).

In Figure 6.3a, due to exchange coupling at the IrMn/ CoFeB interface, the easy axis loop is shifted to higher $\boldsymbol{H_{ext}}$ values. Independent of the magnetic field history, only one remanent magnetization state is present ($\mathbf{M(0\ Oe) \approx +M_s}$). The exchange bias field $\mathbf{H_{eb}}$ is approximately −10 Oe, which corresponds to an exchange coupling constant $\mathbf{J_{eb}}$ of 9.4×10^{-5} J/m^2 at the IrMn/ CoFeB interface (see equation (2.16)). Furthermore, $\mathbf{H_c}$ is increased to 3.6 Oe due to additional anisotropy contribution from the exchange bias (compare Figure 6.3a and 6.2a). Likewise, the magnetization loop measured perpendicular to the magnetic anisotropy axis depicts an increased saturation field (compare Figure 6.3b and 6.2b). Comparing the magnetic hysteresis

observed along the hard axis in the singlelayer CoFeB (Figure 6.2b) to the biased case (Figure 6.3b), the hysteresis has vanished possibly due to coherent rotation of magnetiztion in the biased CoFeB film. The magnetization response to $\boldsymbol{H_{ext}}$ is largely linearized, especially in the low $\boldsymbol{H_{ext}}$ regime.

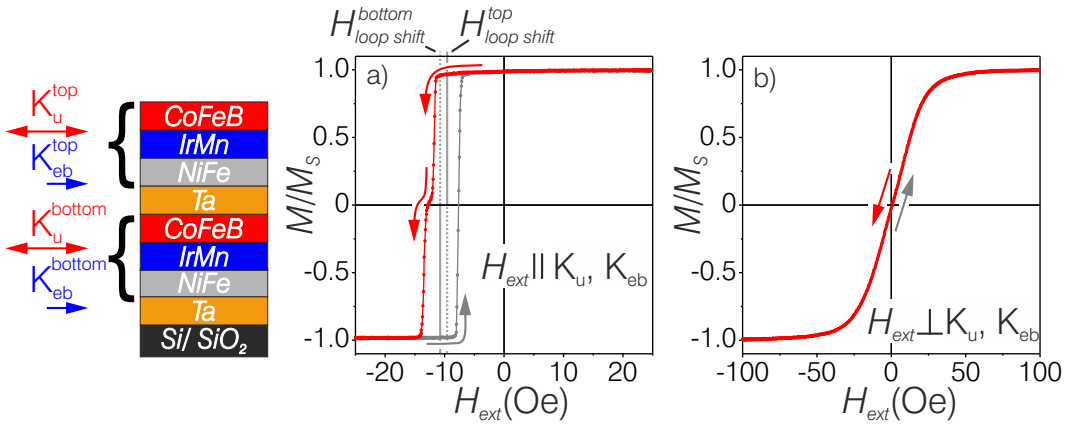

Figure 6.4: (a) easy and (b) hard axis magnetization loops for the CoFeB bilayer full film with parallel exchange bias are displayed. Resulting loop shifts $\boldsymbol{H_{loop\ shift}}$ are marked in (a). (In-plane dimensions: 1 cm x 2 cm) (Sample: [Si/ SiO_2] 300 μm/ Ta 5 nm/ NiFe 2.5 nm/ IrMn 7 nm/ CoFeB 80 nm/ Ta 3 nm/ NiFe 2.5 nm/ IrMn 7 nm/ CoFeB 80 nm/ TaN 5 nm)

Now, the idea is to upscale the total exchange biased CoFeB film thickness. Thus, the same magnetic film layer structure as in Figure 6.2 is sputter deposited two times with a 3 nm thick Ta layer separating them. The total CoFeB thickness, in this case, is 160 nm ($t_{top} = t_{bottom} = 80$ nm). The magnetic field during material deposition is applied along the same direction for all layers. Consequently, the obtained layer system is exchange biased along the same direction.

Figure 6.4 displays the obtained inductively measured magnetization loops. Similar to one layer of exchange biased CoFeB, the easy axis magnetization loop for both CoFeB layers is shifted to $-\boldsymbol{H_{ext}}$ (Figure 6.4a). Both layers are in single domain state at $\boldsymbol{H_{ext}} = 0$ Oe. $\boldsymbol{H_d}$ is effectively compensated by the induced $\boldsymbol{H_{eb}}$. However, a two step magnetization change occurs as $\boldsymbol{H_{ext}}$ is decreased from plus magnetic saturation $+\boldsymbol{H_{sat}}$. The first and second magnetization switch starts at $\boldsymbol{H_{ext,1}} = -11.4$ Oe and $\boldsymbol{H_{ext,2}} = -12.8$ Oe, respectively. As $\boldsymbol{H_{ext}}$ is decreased from $-\boldsymbol{H_{sat}}$, beginning at $\boldsymbol{H_{ext,3}} \approx -8$ Oe, $\boldsymbol{H_{eb}}$ is switched on for both layers.

MO imaging reveals that the top CoFeB layer switches first as $\boldsymbol{H_{ext}}$ is decreased from $+\boldsymbol{H_{sat}}$ (Figure 6.5a). With a small $\boldsymbol{H_{ext}}$ increase to -12 Oe (Figure 6.5b) the magnetization in both layers are aligned antiparallel with respect to each other. No sign of magnetic domain walls is detected. Further decrease of $\boldsymbol{H_{ext}}$ leads to magnetization switch at the bottom CoFeB layer (Figure 6.5c). Now decreasing $\boldsymbol{H_{ext}}$ from $-\boldsymbol{H_{sat}}$, around -8 Oe, the exchange bias in both layers are effectively compensated,

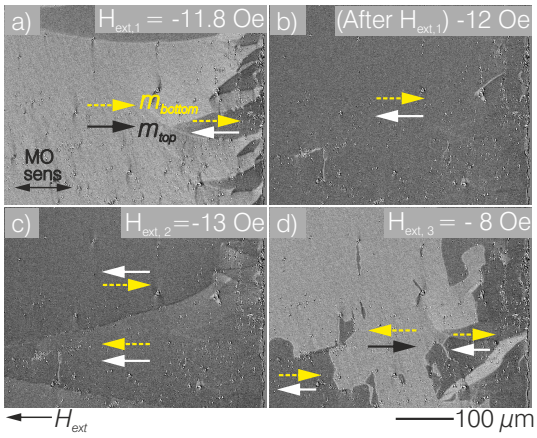

Figure 6.5: Some selected magnetic domain images from the sample in Figure 6.4 depicting the magnetic domain configuration on the top CoFeB layer of parallelly exchange biased CoFeB bilayer with $\boldsymbol{H_{ext}}$ applied against the exchange bias direction. Possible magnetization directions in the top and bottom CoFeB layers are sketched in the images.

meaning $\boldsymbol{H^{top}_{c,\,right}} = \boldsymbol{H^{bottom}_{c,\,right}} \approx -8$ Oe. Accordingly, the effective easy axis loop shifts for both layers are $\boldsymbol{H^{top}_{loop\ shift}} \approx -9.6$ Oe and $\boldsymbol{H^{bottom}_{loop\ shift}} \approx -10.65$ Oe. Deduced from singlelayer of exchange biased CoFeB, $\boldsymbol{H_{eb}} = -10$ Oe (Figure 6.3a), the effective loop shift in the parallel exchange biased CoFeB bilayer moves to $\boldsymbol{H^{top}_{loop\ shift}}=\boldsymbol{H^{SL}_{eb}}+0.4$ Oe and $\boldsymbol{H^{bottom}_{loop\ shift}}=\boldsymbol{H^{SL}_{eb}}-0.6$ Oe for the top and bottom CoFeB layer, respectively. The loop shift asymmetry in the bottom and top CoFeB layers can be attributed to a possible magnetostatic interaction through the Ta spacer between the bottom CoFeB layer and the thin NiFe film in the top stack (see sketch in Figure 6.4), which leads to a loop shift in the bottom CoFeB layer further in $-\boldsymbol{H_{ext}}$ direction by 0.65 Oe.

Although the effective loop shift are different for both layers, the magnetization loop measured perpendicular to $\boldsymbol{H_{eb}}$ (Figure 6.4b) depicts a non-hysteretic, mostly linear response.

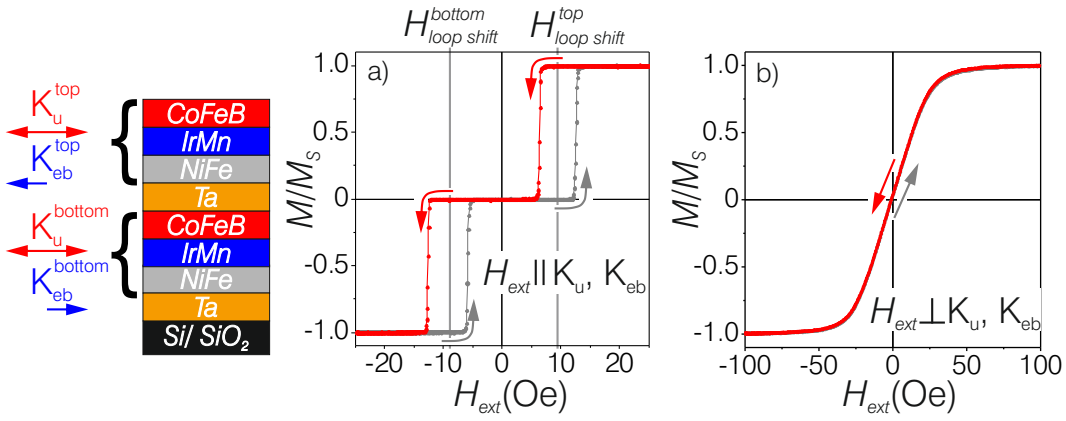

Figure 6.6: (a) easy and (b) hard axis magnetization loops for the CoFeB bilayer full film with antiparallel exchange bias are displayed. Resulting loop shifts $\boldsymbol{H_{loop\ shift}}$ are marked in (a). (In-plane dimensions: 1 cm x 2 cm) (Sample: [Si/ SiO_2] 300 μm/ Ta 5 nm/ NiFe 2.5 nm/ IrMn 7 nm/ CoFeB 80 nm/ Ta 3 nm/ NiFe 2.5 nm/ IrMn 7 nm/ CoFeB 80 nm/ TaN 5 nm)

Another way to obtain symmetric loop shift along the easy axis for a CoFeB bi-

layer structure is to use the magnetostatic interaction between the CoFeB layers. By retaining an antiparallel alignment of magnetization in top and bottom CoFeB layers the magnetic flux is closed internally inside the magnetic structure. As a result, the demagnetizing field is effectively compensated. The essential layer composition is the same as in parallelly biased CoFeB bilayer. However, in this case the antiparallel alignment of the exchange bias is achieved by applying $\boldsymbol{H_{ext}}$ during bottom layer's IrMn deposition along $+\boldsymbol{H_{dep}}$ and for the top layer IrMn along $-\boldsymbol{H_{dep}}$. The resulting magnetic structure is composed of CoFeB layers with the same $\mathbf{H_{eb}}$, but with different sign (Figure 6.6a).

Due to antiparallel alignment of exchange bias and symmetric magnetic material thickness in each stack, the net magnetization at magnetic remanance equals to zero. Since the layer thicknesses in both the parallelly and antiparallelly exchange biased films are identical, the magnetostatic interaction between the top NiFe and bottom CoFeB layers are the same (positive interaction constant). It is antiparallel with respect to the $\boldsymbol{H_{eb}}$ of the bottom CoFeB layer. This results in less effective loop shift in the magnetization loop for the bottom CoFeB layer. $\boldsymbol{H^{top}_{loop\ shift}}$ and $\boldsymbol{H^{bottom}_{loop\ shift}}$ are measured to be +9.4 Oe and −9.2 Oe, respectively. The top and bottom CoFeB layer's coercive field strength are $\boldsymbol{H_c^{top}} = 3.1$ Oe and $\boldsymbol{H_c^{bottom}} = 3.4$ Oe.

The hard axis magnetization reversal exhibits similar to previous biased films, little to no hysteresis (Figure 6.6b).

6.2 Magnetization behavior in structured films

The previous section exhibited the full film magnetic properties of differently layered CoFeB and here, systematic investigations performed on their structured counterparts are shown. The emphasis is given on locally changing demagnetizing field in structured CoFeB films and formation of magnetic domains. Calculated local demagnetization factor $\boldsymbol{N_x}$ and the corresponding demagnetizing field $\boldsymbol{H_d^x}$ for large (2 mm x 20 mm) and small (80 μm x 320 μm) structures with total CoFeB thicknesses of 80 nm and 160 nm are displayed in Figure 6.7a and b, respectively. $\mathbf{H_d^x = H_{eb}} = 10$ Oe is marked. For exchange biased structures, $\boldsymbol{H_d^x}$>10 Oe depicts the point, where exchange bias is not high enough to compensate the local demagnetizing field, which possibly results in magnetic domain formation.

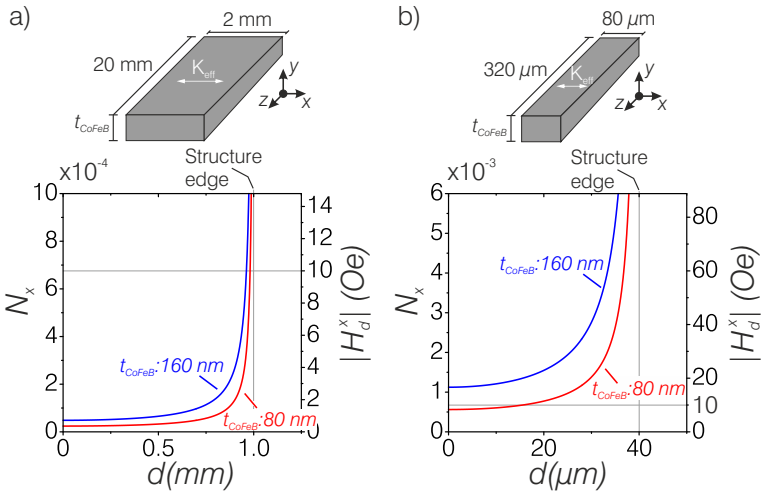

Figure 6.7: Calculated one dimensional local change in demagnetization factor $\boldsymbol{N_x}$ and field $\boldsymbol{H_d^x}$ along x-axis for two different CoFeB film thickness. (a) and (b) are for large (2 mm x 20 mm) and small (80 μm x 320 μm) structures. The axial symmetry allows for displaying half of the plots (from 0 to 1 mm for large structure and 0 to 40 μm for small structure). $\boldsymbol{H_d^x} = 10$ Oe is marked, which corresponds to $\mathbf{H_{eb}}$ for CoFeB 80 nm/ IrMn 7 nm (see Figure 6.3a).

6.2.1 Singlelayer $Co_{40}Fe_{40}B_{20}$ films

Inductively measured magnetization reversal along the long axis of a large structure, consisting of a singlelayer of CoFeB is shown in Figure 6.8. CoFeB film thickness is 160 nm. $\mathbf{K_u}$ axis coincides with the short axis of the structure. Unlike, the measured easy axis loop for its full film counterpart, the large structure's easy axis loop displays a non-square loop shape and saturates at higher $\boldsymbol{H_{ext}}$ (compare Figure 6.8a with Figure 6.2a). The magnetic response starts to divert from full film properties due to changing in-plane dimensions and the magnetic shape effects play

an important role. The measured $\mathbf{H_k}$ is similar to its full film counterpart, around 15 Oe (Figure 6.8b). The magnetization response is linear with $\boldsymbol{H_{ext}}$. A coherent rotation of magnetization can be considered. However, in-situ wide field magnetic domain observations display high amount of magnetic domain activity (Figure 6.9).

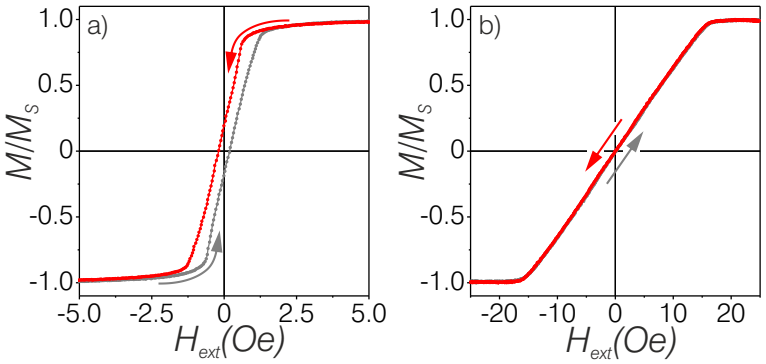

Figure 6.8: Inductively measured magnetization responses along the easy (a) and hard (b) axis of a large structure of singlelayer CoFeB film are displayed (In-plane dimensions: 2 mm x 20 mm). (Sample: [Si/ SiO_2] 300 μm/ Ta 5 nm/ CoFeB 160 nm/ TaN 5 nm)

Decreasing $\boldsymbol{H_{ext}}$ from magnetic saturation, the reversal takes place by nucleation of spike domains at the very edges of the film. They move into the material with decreasing $\boldsymbol{H_{ext}}$. When two spike domains from either side meet, a 180° wall is formed, which separate two neighboring magnetic domains with anti-parallel magnetization directions. A non-coherent, spatially varying magnetization reversal process takes place. Magnetic domain formation is dictated by domain wall motion, indicating a small angle between $\boldsymbol{H_{ext}}$ and the hard axis of magnetic anisotropy in the film. The domain wall alignment in the remanent magnetization state (Figure 6.9d) reveals a slight magnetic anisotropy alignment variation. Along the long axis of the structure, from the right edge to the left edge an angular difference of as high as 8° is measured between magnetic anisotropy axis to the intended axis (Figure 6.9d). Due to this inhomogeneous magnetic anisotropy distribution, with $\boldsymbol{H_{ext}}$ applied along the long axis of the structure, the magnetization reversal is performed by a combination of rotational and domain wall motion processes. In the inductive response measured along the hard axis (Figure 6.8b), the obtained loop is weighed spatially different. The most of the signal stems from the middle of the structure, where the $\mathbf{K_u}$ coincides almost entirely along the short axis of the structure (Figure 6.9d). Therefore, the corresponding inductive measurement displays a linear behavior.

For small structures, the hard axis magnetization response begins to diverge strongly from magnetic films with relatively large in-plane dimensions (compare Figures 6.2b and 6.8b with 6.10). Note that for the small structures the CoFeB film thickness is identical, only in-plane dimensions is different. Similarly, the $\boldsymbol{H_{ext}}$

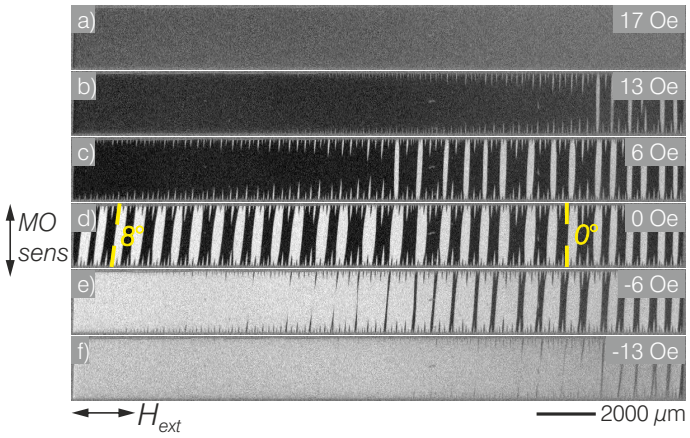

Figure 6.9: (a) Magnetization reversal along the long axis of a structured singlelayer CoFeB film. (b-h) displays the magnetic domain configurations with $\boldsymbol{H_{ext}}$ applied along the long axis of the structure (In-plane dimensions: 2 mm x 20 mm). (Sample: [Si/ SiO_2] 300 μm/ Ta 5 nm/ CoFeB 160 nm/ TaN 5 nm)

is applied along the long axis. Magneto-optically measured magnetization curve displays different magnetic susceptibilities depending on the $\boldsymbol{H_{ext}}$ history. Sudden magnetization jumps occur as $\boldsymbol{H_{ext}}$ is decreased from magnetic saturation, resulting in a hysteretic region in the magnetization loop. They do not only occur with decreasing $\boldsymbol{H_{ext}}$, also when $\boldsymbol{H_{ext}}$ is increased from the remanent state (Figure 6.10). In order to obtain a complete picture of the underlying magnetization processes, dual wavelength MOKE imaging is adopted.

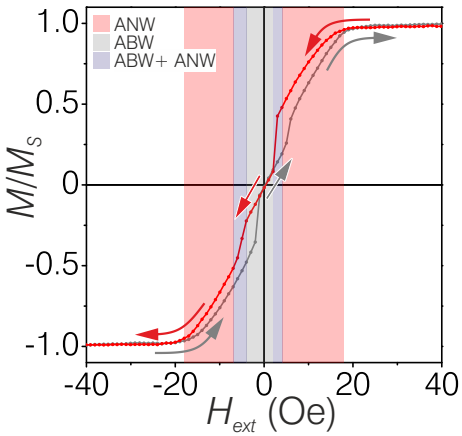

Figure 6.10: Magneto-optically measured magnetization loop along the hard axis of a small structure with singlelayer of CoFeB. $\boldsymbol{H_{ext}}$ ranges with asymmetric Néel (ANW) and Bloch walls (ABW) are marked (In-plane dimensions: 80 μm x 320 μm). (Sample: [Si/ SiO_2] 300 μm/ Ta 5 nm/ CoFeB 160 nm/ TaN 5 nm)

The upper rows in Figure 6.11 and 6.12 display magnetic domain configurations with vertical MOKE sensitivity parallel to the magnetic anisotropy (sensitive to $\boldsymbol{m_x}$), whereas the bottom rows show the same magnetic domain configuration imaged at horizontal MO sensitivity (sensitive to $\boldsymbol{m_y}$).

Decreasing $\boldsymbol{H_{ext}}$ from magnetic saturation, the formed magnetic domain configuration consist of magnetic domains separated by asymmetric Néel walls (ANWs) in the middle and closure domains at the sides (Figure 6.11b). Due to interacting ANW tails between adjacent walls, this domain configuration possesses low mag-

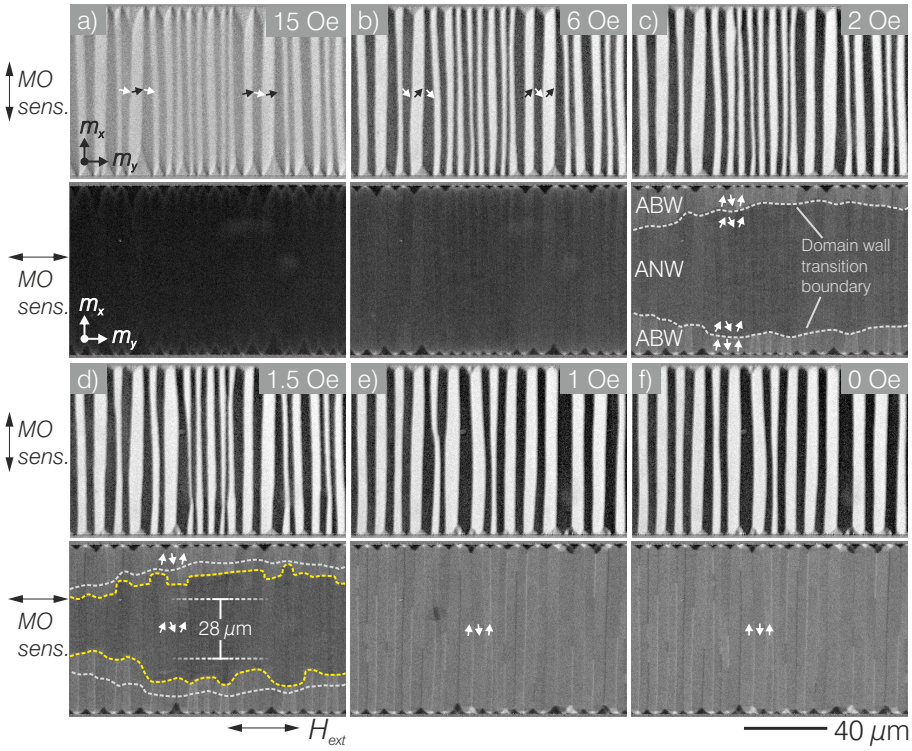

Figure 6.11: (a) Magnetization reversal along the long axis of a structured singlelayer CoFeB film. (b-h) displays the magnetic domain configurations with $\boldsymbol{H_{ext}}$ applied along the long axis of the structure (In-plane dimensions: 80 μm x 320 μm). (Sample: [Si/ SiO_2] 300 μm/ Ta 5 nm/ CoFeB 160 nm/ TaN 5 nm)

netic susceptibility and is defined as a blocked domain state. With decreasing $\boldsymbol{H_{ext}}$ (Figure 6.11c), the closure domains with net magnetization direction along applied field shrink. Additionally, at the same field range, magnetic domain wall boundaries form at the edges parallel to the long axis of the structure, which separate regions with ANWs (middle of the structure with dark MOKE contrast) from asymmetric Bloch walls (ABW) (edges of the structure with bright MOKE contrast). Decreasing $\boldsymbol{H_{ext}}$, the ANW region shrinks in size as the boundary moves into the middle of the structure with decreasing $\boldsymbol{H_{ext}}$ and subsequently ANW sections transition into ABWs (Figure 6.11d). The reason lies at locally changing $\boldsymbol{H_d^x}$ (Figure 6.7b, t_{CoFeB} = 160 nm). As a result, the magnetization response to $\boldsymbol{H_{ext}}$ varies spatially. The smallest ANW region before the magnetization drop is 28 μm in length along the short axis of the structure (Figure 6.11d). The average demagnetizing field in the middle is approximately $\mathbf{N_x^{middle}} \approx 0.001$. Therefore, the pronounced magnetization jump associated with the domain wall transition occurs suddenly in the middle of the structure. After the full domain wall transition (Figure 6.11e and f), the magnetic response becomes almost linear with $\boldsymbol{H_{ext}}$ (Figure 6.10). A coherent rotation of magnetization occurs throughout the magnetic structure.

The discussed sudden magnetization jumps are not only spotted with decreasing

$\boldsymbol{H_{ext}}$, but are also observed as $\boldsymbol{H_{ext}}$ is increased from the magnetic remanent state (Figure 6.10 and 6.12). At around 4 Oe, the linear magnetization response is interrupted with the domain wall transition from ABWs to ANWs. This is characterized by the relatively less pronounced magnetization jump at $\boldsymbol{H_{ext}} = -4$ Oe in Figure 6.10. Similarly, regions with different magnetic susceptibilities are formed and magnetization reversal proceeds with sudden regional magnetic domain transformations (Figure 6.12c).

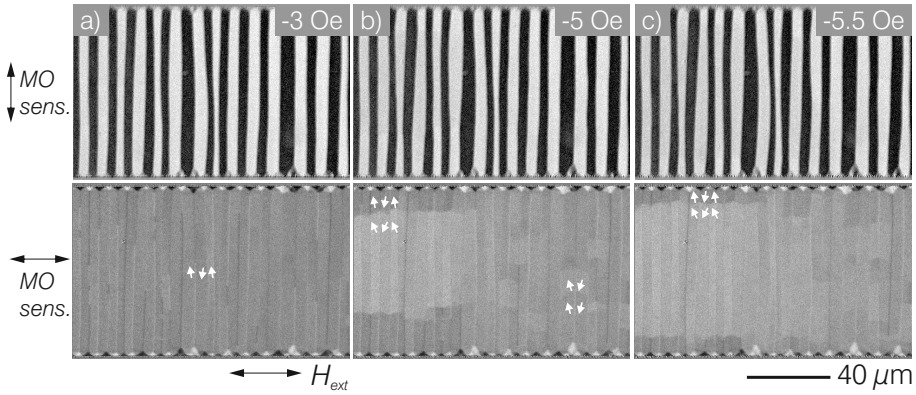

Figure 6.12: Magnetization reversal along the hard axis of magnetic anisotropy are displayed. MO sensitivity and direction of the applied magnetic field ($\boldsymbol{H_{ext}}$) are indicated (In-plane dimensions: 80 μm x 320 μm). (Sample: [Si/ SiO_2] 300 μm/ Ta 5 nm/ CoFeB 160 nm/ TaN 5 nm)

Figure 6.13a displays in high optical resolution, the magnetic domain configuration at $\boldsymbol{H_{ext}} = 1.5$ Oe. The wall angle separating two regions are defined by the angle of magnetization on either side of the wall. Analyzing the MOKE intensity in both regions (Figure 6.13b), magnetization alignments of 85° and 53° away from the saturated state are identified for ABW and ANW regions, respectively. The domain wall angle separating both regions is thus 70° (Figure 6.13b and c). Moreover, at limited sections along some of the domain walls, the magnetization alignment on either side are not identical (see the sketch in Figure 6.13c). Therefore, at these transition regions the wall structure is possibly a mixture of Bloch and Néel walls (ABW+ANW).

An important consequence of the non-coherent wall transformation is that the magnetization response varies likewise locally at $\boldsymbol{H_{ext}}$ values, where ANWs and ABWs coexist. Figure 6.10d displays the local magnetization responses at the very edge (red curve) and in the middle (blue curve) of the structure as the $\boldsymbol{H_{ext}}$ is swept from $+\boldsymbol{H_{sat}}$ to $-\boldsymbol{H_{sat}}$. Initially, both regions possess similar magnetic susceptibilities. At the edge region, a relatively stepwise magnetization change occurs, which is connected to the movement of the aforementioned domain wall boundary (Figure 6.11). With each $\boldsymbol{H_{ext}}$ decrement, the domain wall boundary moves into the middle. When it reaches the middle region, where the demagnetizing field is rela-

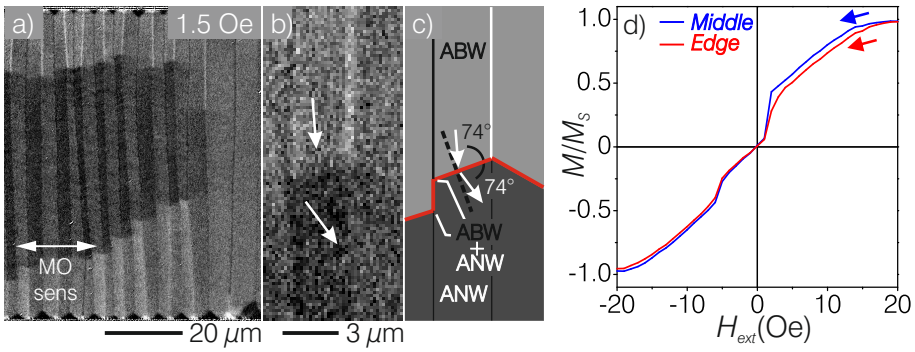

Figure 6.13: (a-b) High resolution MOKE image at $\boldsymbol{H_{ext}}$ = 1.5 Oe and (c) sketch depicting the magnetization distribution at the vicinity of domain wall transition boundary in Figure 6.11d. (d) shows the local magnetization response at the very top edge and in the middle of the sample. (Sample: [Si/ SiO_2] 300 μm/ Ta 5 nm/ CoFeB 160 nm/ TaN 5 nm)

tively homogeneous, the magnetization drops sharply with little decrease in $\boldsymbol{H_{ext}}$. At this point, both regions possess the same magnetic susceptibility and the magnetization response is homogeneous almost all over the sample until the ABW to ANW transition resumes. After a full magnetic domain transformation, both regions display an almost identical magnetization reversal behavior.

In summary, data displayed for large structures show inhomogeneous magnetic anisotropy distribution leading to spatially varying magnetization response. The reason for this can be due to some small thickness gradient present in the deposited material and also local variations in angle of material beam incidence during deposition adds noticeable modifications to local effective magnetic anisotropy [44, 136].

For structures in micrometer dimensions the adjusted in-plane $\boldsymbol{H_d}$ alters the transpiring magnetic domain configurations. Two distinct magnetic domain patterns with specific magnetic domain wall types are identified at different branches in the hard axis magnetization loops. The transformation between the two magnetic domain configurations are characterized by magnetization jumps. Furthermore, local $\boldsymbol{H_d}$ variations result in small regional magnetization changes.

6.2.2 Unbiased $Co_{40}Fe_{40}B_{20}$ bilayers

One way to compensate $\boldsymbol{H_d}$ and minimize magnetic domain formation is by laminating the magnetic structure with non-magnetic spacer layers. Here, two CoFeB films with symmetric layer thicknesses ($t_{CoFeB}^{top} = t_{CoFeB}^{bottom} = 80$ nm) are separated by a 5 nm thick Ta spacer layer. As a result, CoFeB interact magnetostaticly. Figure 6.14(a, b) display two examples of possible remanent magnetic domain configurations in a bilayer, where such magnetic domain configurations are unavailable to soft magnetic singlelayer films (Figure 6.14c).

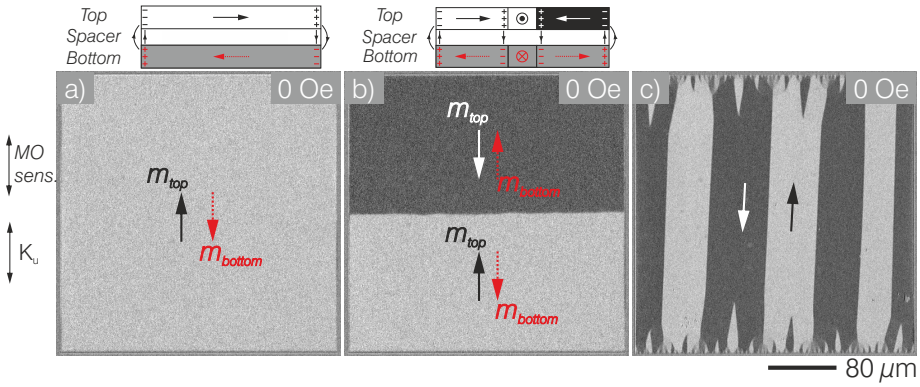

Figure 6.14: Easy axis remanent magnetic domain states for square shaped bilayer structure (a-b) and a singlelayer magnetic film (c). The total CoFeB film thickness is same for both samples (t^{total}_{CeFeB} = 160nm). Sketches on top of (a-b) indicate possible magnetization states observed from the cross-section. Full and dashed arrows indicate possible magnetization directions in top and bottom layers, respectively. (Samples: (a-b) [Si/ SiO_2] 300 μm/ Ta 5 nm/ CoFeB 80 nm/ Ta 5 nm/ CoFeB 80 nm/ TaN 5 nm and (c) [Si/ SiO_2] 300 μm/ Ta 5 nm/ CoFeB 160 nm/ TaN 5 nm)

In Figure 6.14a, the top CoFeB layer displays homogeneously bright MOKE contrast, indicating a single magnetic domain state for the top CoFeB layer. Likewise, optically invisible bottom CoFeB layer is in single domain state, whose magnetization direction is possibly antiparallel with respect to the top layer magnetization ($CoFeB_{bottom}\downarrow$/ Ta/ $CoFeB_{top}\uparrow$). Adjacent magnetic layers interact magnetostaticly through the Ta spacer. Thus, surface magnetic charges in each layer can be compensated at the neighboring CoFeB layer (see sketch in Figure 6.14a). The magnetic flux in both layers is closed through magnetostatic interactions. Consequently, closure domain structures at the edges and magnetic domains in the middle are effectively annihilated (compare Figure 6.14a and c).

Another consequence of lamination is displayed in Figure 6.14b, where a magnetic domain wall is formed, aligned perpendicular to $\mathbf{K_u}$. The wall separates head-to-head magnetized domains in the top CoFeB layer, whereas the magnetization in the bottom CoFeB layer is in tail-to-tail state (see sketched magnetization arrows in Figure 6.14b). Such a domain wall alignment is energetically unfavorable for single-layer films (Figure 6.14c). However, in laminated films, the inner magnetic domain wall structures are altered through interlayer magnetostatic interaction. A complete interlayer magnetic charge compensation occurs and thus the energy associated with Néel wall formation is reduced. Charge compensated superimposed Néel walls form, which can align under any in-plane angle [137].

For both cases (Figure 6.14a and b), the net magnetization in the bilayer equals to zero as the magnetization in every magnetic domain is compensated by another magnetic domain of reversed magnetization in the adjacent layer.

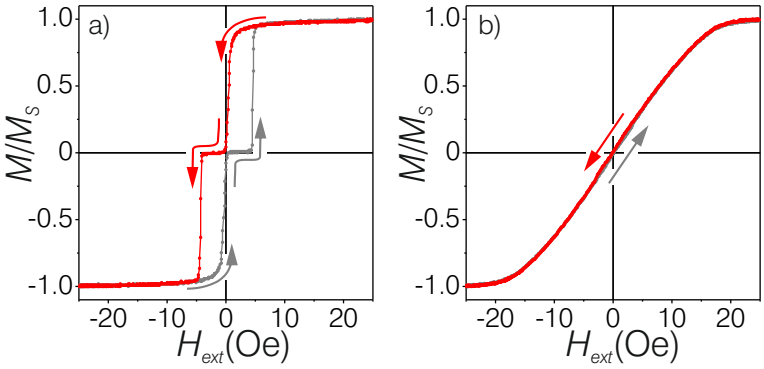

Figure 6.15: Magnetization loops measured inductively along the easy (a) and hard (b) axes of a structured (In-plane dimensions: 2 mm x 20 mm) CoFeB bilayer are displayed. (Sample: [Si/ SiO_2] 300 μm/ Ta 5 nm/ CoFeB 80 nm/ Ta 5 nm/ CoFeB 80 nm/ TaN 5 nm)

Figure 6.15 displays inductively measured magnetization loop of a laminated bilayer structure with in plane dimensions of 2 mm x 20mm. The total CoFeB layer thickness is kept the same as in singlelayer film, ($t_{FM}^{total} = 160$ nm). The easy axis loop measured along the short axis of the structure displays a two step magnetization reversal, when the field is swept from $+\boldsymbol{H_{sat}}$ to $-\boldsymbol{H_{sat}}$ and vice versa (Figure 6.15a). Due to magnetostatic interaction, the easy axis magnetization loop for both layers are shifted to higher $\boldsymbol{H_{ext}}$ but with opposite in sign with respect to each other. As a result, a near zero net magnetization state is obtained at remanence. The hard axis magnetization loop displays negligible hysteresis along the measurement direction (Figure 6.15b). The bilayer displays an almost linear magnetization response. Similar to the singlelayer film with identical in-plane dimensions, $\mathbf{H_k}$ is around 15 Oe (compare Figure 6.15b and 6.8b).

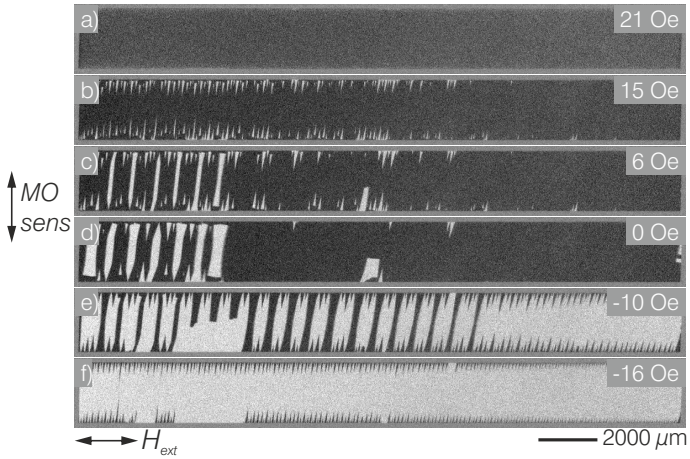

Figure 6.16: Selected MOKE images obtained with $\boldsymbol{H_{ext}}$ applied along the hard axis for a CoFeB bilayer (In-plane dimensions: 2 mm x 20 mm) (Sample: [Si/ SiO_2] 300 μm/ Ta 5 nm/ CoFeB 80 nm/ Ta 5 nm/ CoFeB 80 nm/ TaN 5 nm)

Large view MO imaging performed with $\boldsymbol{H_{ext}}$ applied along the hard axis of mag-

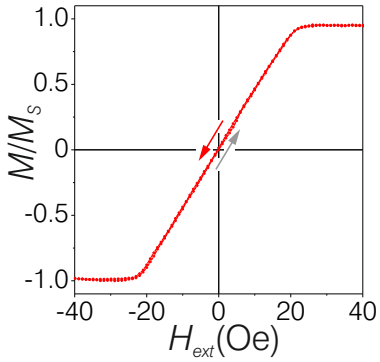

Figure 6.17: Magneto-optically measured magnetization loop along the long axis of an unbiased CoFeB bilayer (In-plane dimensions: 80 μm x 320 μm). (Sample: [Si/ SiO_2] 300 μm/ Ta 5 nm/ CoFeB 80 nm/ Ta 5 nm/ CoFeB 80 nm/ TaN 5 nm)

netic anisotropy exhibits high amount of magnetic domain activity (Figure 6.16). Decreasing $\boldsymbol{H_{ext}}$ from magnetic saturation, spike domains nucleate at the very edges of the film (Figure 6.16b). Further reduction in $\boldsymbol{H_{ext}}$ leads to expansion of the spiked further into the material and subsequent formation of 180° walls along the magnetic anisotropy axis (Figure 6.16c). At remanence, the top layer displays regions, where the alignment of magnetization on either side of the wall is head-to-head or tail-to-tail (Figure 6.16d). Increment of $\boldsymbol{H_{ext}}$ in the other direction, magnetic domains with collinear magnetization directions form in the middle. Similar to singlelayer CoFeB film, magnetic saturation is reached through subsequent annihilation of magnetic domains in the middle and following shrinkage of spike domains at the edges (Figure 6.16e, f).

For laminated films with smaller in-plane dimensions, the magnetic hysteresis is strongly reduced compared to their singlelayer counterparts (compare Figure 6.17 and 6.10). However, magnetic domain observations show that the magnetization reversal along the hard axis is not performed solely by coherent rotation of magnetization (Figure 6.18). The same magnetic domain configurations are imaged under dual-wavelength imaging conditions, the left and middle columns correspond to vertical (MO sens $\parallel \mathbf{K_u}$), horizontal (MO sens $\perp \mathbf{K_u}$) MOKE sensitivities, whereas the right column displays sketches of possible magnetization states in the bottom layer.

As $\boldsymbol{H_{ext}}$ is decreased from magnetic saturation, similar to the singlelayer film, two magnetic domain boundaries form parallel to the long axis of the magnetic structure, which separate two regions with different effective magnetic susceptibilities. At both vertical and horizontal MO sensitivities (Figure 6.18a), the MOKE contrast indicates that the magnetization is tilted away from the applied field direction. Locally high $\boldsymbol{H_d}$ at the edges result in formation of edge curling wall structures [138]. On the other hand, the middle region is in saturated state. As the $\boldsymbol{H_{ext}}$ is decreased, rectangular shaped magnetic domains start to nucleate in the middle (Figure 6.18b). The edge regions still possess homogeneously bright MO contrast. On the other hand, along the horizontal MO sensitivity, magnetic domain wall structures with bright MO contrast are revealed at the edges, where the same domain configuration

imaged in vertical MO sensitivity displays no change of magnetization on either side of these walls. They emerge from the bottom CoFeB layer. Compensating walls form in the top CoFeB layer through interlayer magnetostatic interactions to reduce the overall domain wall energy. In the middle, the top CoFeB layer possesses a zigzag magnetization distribution, whereas the bottom CoFeB layer displays regions with parallelly aligned magnetization separated by 0°compensated domain walls structures (see sketch in Figure 6.18b). As a consequence, the relative magnetization alignments in some regions for both CoFeB layers are parallel (Figure 6.18b, vertical MO sensitivity). Even in the middle of the magnetic structure, the magnetization inside the domains are not fully compensated by the adjacent CoFeB layer. As a result, regions with parallel magnetization alignment are annihilated abruptly with decreasing $\boldsymbol{H_{ext}}$ (compare Figure 6.18b and 6.18c) and at $\boldsymbol{H_{ext}} = 0$ Oe, the magnetization in both layers are aligned antiparallel with respect to each other (Figure 6.18d).

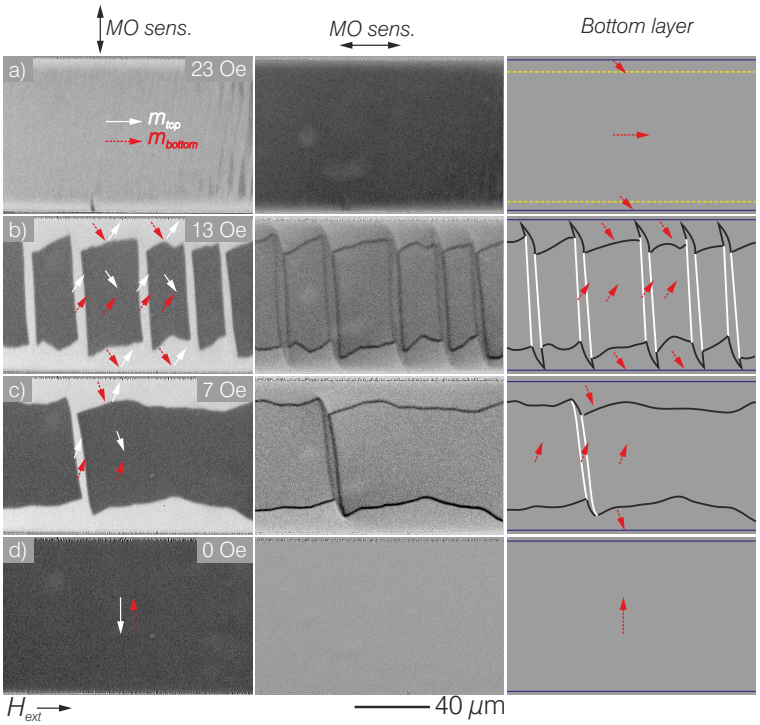

Figure 6.18: Magnetic domain response of a magnetostaticly interacting CoFeB bilayer structure with decreasing $\boldsymbol{H_{ext}}$ is displayed (a-d). Left and middle columns correspond to MO images of the same magnetic domain configurations obtained with vertical and horizontal MO sensitivities. In the right column, possible magnetization configurations in the optically invisible bottom layer are sketched. The black lines correspond to either superimposed or compensated Néel wall structures and the white lines are 0° compensating Néel wall structures stemming from the wall in the top CoFeB layer (In-plane dimensions: 80 μm x 320 μm). (Sample: [Si/ SiO_2] 300 μm/ Ta 5 nm/ CoFeB 80 nm/ Ta 5 nm/ CoFeB 80 nm/ TaN 5 nm)

Magnetic domain activity is not only observed as $\boldsymbol{H_{ext}}$ is swept down from mag-

netic saturation but also when a small $\boldsymbol{H_{ext}}$ is applied to the remanent magnetization state. Figure 6.19 depicts domain configurations (a-d) and the measured average magnetic domain wall profiles $\boldsymbol{d_{pro}}$ (e). The starting domain configuration consist of two 180° superimposed domain walls with $\boldsymbol{d_{pro}}$ = 5.8 μm (Figure 6.19a and e). Antiparallelly magnetized wall segments separated by Bloch lines are visible for both walls (Figure 6.19a). At $\boldsymbol{H_{ext}}$ = −4.8 Oe (along the dark MO contrast), the Bloch lines become darker in contrast, pointing out towards magnetic charging of the Bloch line segments (Figure 6.19b). Subsequently, the walls start to form extended tails and $\boldsymbol{d_{pro}}$ increases slightly to 6.6 μm.

Further $\boldsymbol{H_{ext}}$ increment to −5.5 Oe results in sudden reorganization of the left domain wall (Figure 6.19c). The resulting wall structure is a twin Néel wall, which displays double MO contrast (compare Figure 6.19b and c). The left and right side of the wall exhibits bright and dark contrast, respectively. The $\boldsymbol{d_{pro}}$ is now 6 μm (Figure 6.19e). The reason for the transition from superimposed to twin Néel wall structure lies in the inept compensation of magnetic charges along the walls in the superimposed wall state with increasing $\boldsymbol{H_{ext}}$. Therefore, the walls in the top and bottom CoFeB layer separate from each other and form compensating wall structures in the neighboring CoFeB layer [137]. The bright and dark wall contrasts observed in Figure 6.19c correspond compensated wall structures in bottom and top layer, respectively. At $\boldsymbol{H_{ext}}$ = −6 Oe, the domain wall profile remains to be almost the same $\boldsymbol{d_{pro}}$ = 6 μm. Meanwhile, the superimposed wall on the right (Figure 6.19a) also transitions to a twin Néel wall (Figure 6.19d).

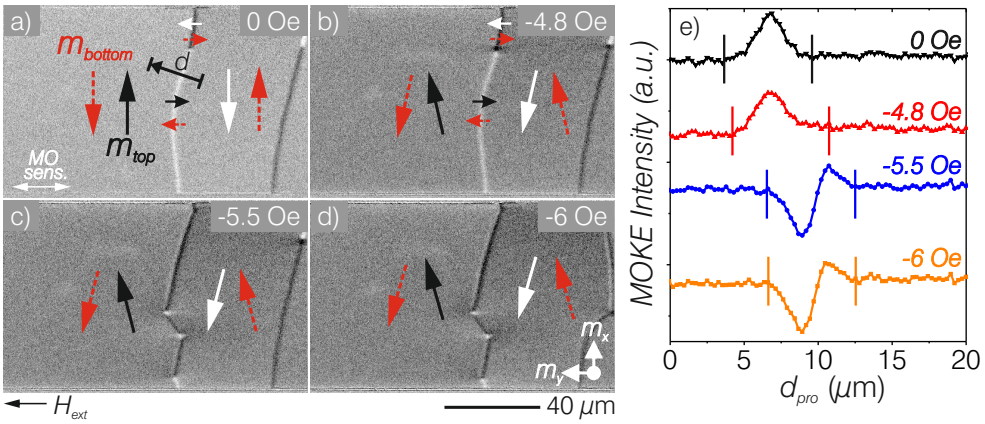

Figure 6.19: Some selected MO images displaying the magnetic domain response under small $\boldsymbol{H_{ext}}$ are shown (a-d). (e) exhibits the analyzed intensity perpendicular to the wall marked in (a) for all the selected domain images (In-plane dimensions: 80 μm x 320 μm). (Sample: [Si/ SiO_2] 300 μm/ Ta 5 nm/ CoFeB 80 nm/ Ta 5 nm/ CoFeB 80 nm/ TaN 5 nm)

In summary, the magnetostatic interactions in laminated magnetic layers lead to charge compensation between neighboring films. The magnetization induced mag-

netic anisotropy in such films are identical to their singlelayer counterparts. The hard axis magnetization loops generally depict reduced hysteresis and depending on $\boldsymbol{H_{ext}}$ history a single domain state can be obtained. On the other hand, especially prominent at high $\boldsymbol{H_{ext}}$ regime, subsequent magnetic domain formation and annihilation, as well as edge curling wall development at the edges lead to sudden magnetization changes. Even at small $\boldsymbol{H_{ext}}$ regime, where domain walls are present, local domain wall induced magnetization changes occur. Superimposed Néel walls transform to twin Néel walls due to uncompensated magnetic changes at the interface.

6.2.3 Exchange biased $Co_{40}Fe_{40}B_{20}$ films

Figure 6.20 displays the magnetization loops of a large sized (2 mm x 20 mm) singlelayer of exchange biased CoFeB film obtained along the structure's easy and hard axes. The easy axis magnetization loop (Figure 6.20a) shows a $\boldsymbol{H_{loop\ shift}}$ of −11.8 Oe and a $\boldsymbol{H_c}$ of 3.4 Oe. The difference in effective loop shift of −1.8 Oe compared to its full film counterpart of $\boldsymbol{H_{eb}^{full\ film}}$ = −10 Oe stems from the variation of $\boldsymbol{H_d}$. The hard axis loop (Figure 6.20b) exhibits a mostly a linear change.

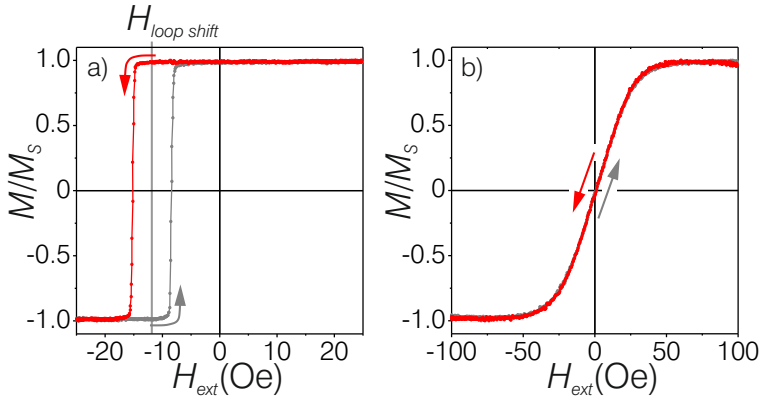

Figure 6.20: (a) easy and (b) hard axis magnetization loops for a structured, exchange biased CoFeB film are displayed. (In-plane dimensions: 2 mm x 20 mm). (Sample: [Si/ SiO_2] 300 μm/ Ta 5 nm/ NiFe 2.5 nm/ IrMn 7 nm/ CoFeB 80 nm/ TaN 5 nm)

The magneto-optically measured magnetization loops for the exchange biased film with smaller in plane dimensions are displayed in Figure 6.21. A $\boldsymbol{H_{loop\ shift}}$ = −9.2 Oe is measured from the magnetization loop obtained along the anisotropy axis (Figure 6.21a). The magnetization loop measured along the long axis shows noteworthy hysteresis (Figure 6.21b), which does not cross the origin indicating a small angular difference between $\boldsymbol{H_{ext}}$ and the effective hard axis in the material. The magnetic susceptibility is not the same for increasing and decreasing $\boldsymbol{H_{ext}}$, leading to non linear magnetization response with $\boldsymbol{H_{ext}}$.

Some selected magnetic domain images during long axis magnetization reversal are displayed in Figure 6.22. As $\boldsymbol{H_{ext}}$ is decreased from magnetic saturation, spike and closure domain structures nucleate at the very edges of the film (Figure 6.22a). The exchange bias is locally compensated at the edges of the film by the demagnetizing field $\boldsymbol{H_d}$ at this region and a multi magnetic domain state develops ($\boldsymbol{H_d^{edge}} > \boldsymbol{H}_{\mathrm{eb}}$). The middle region is in single domain state and the magnetization response is almost linear. Decreasing $\boldsymbol{H_{ext}}$ to 12 Oe (Figure 6.22b), closure domain structures with bright MO contrast form. Additionally, the spike domain alignment and volume start to change.

At $\boldsymbol{H_{ext}}$ = +5 Oe the edge region is in demagnetized state (Figure 6.22c). In-

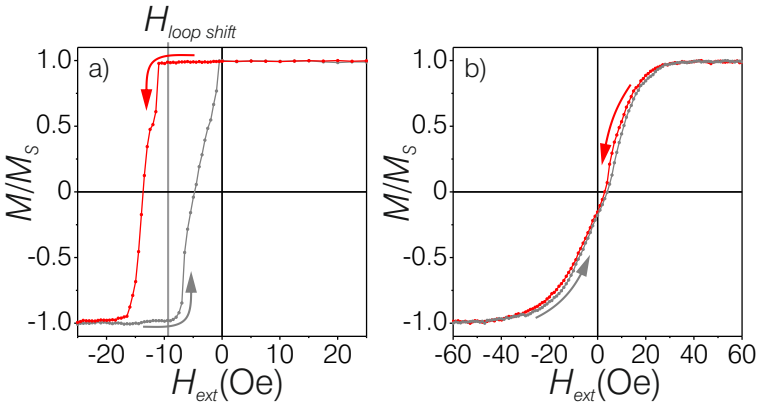

Figure 6.21: (a) easy and (b) hard axis magnetization loops for a structured, exchange biased CoFeB film are displayed (In-plane dimensions: 80 μm x 320 μm). (Sample: [Si/ SiO_2] 300 μm/ Ta 5 nm/ NiFe 2.5 nm/ IrMn 7 nm/ CoFeB 80 nm/ TaN 5 nm)

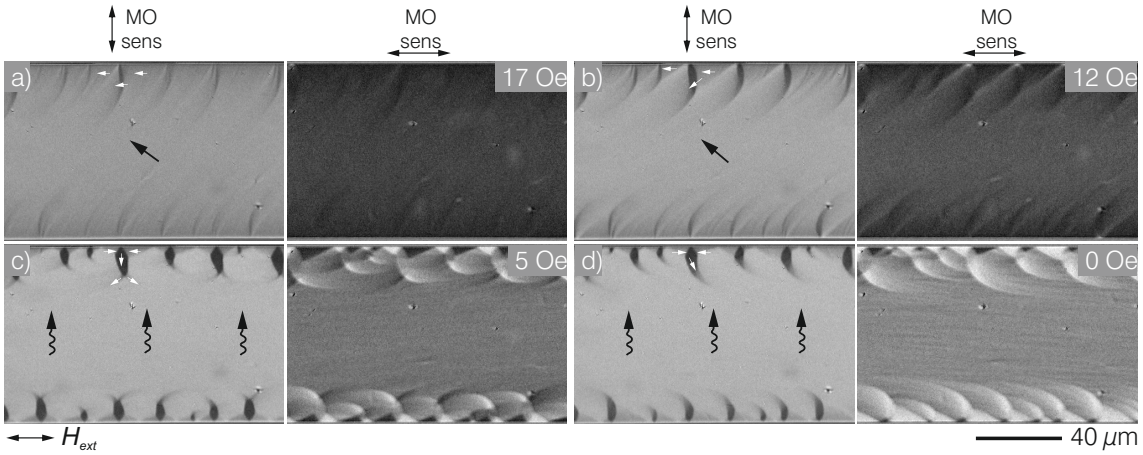

Figure 6.22: Some selected magnetic domain images obtained with two orthogonal MOKE sensitivities with $\boldsymbol{H_{ext}}$ applied perpendicular to the $\mathbf{K_{eb}}$ are displayed (In-plane dimensions: 80 μm x 320 μm). (Sample: [Si/ SiO_2] 300 μm/ Ta 5 nm/ NiFe 2.5 nm/ IrMn 7 nm/ CoFeB 80 nm/ TaN 5 nm)

terestingly, magnetization modulations are formed in the middle region, which is almost in single domain state. The formation of these ripple like structures results in decrement of the net magnetization. Similar magnetization modulations are well understood for polycrystalline magnetic materials. They are formed through small perturbations in magnetic anisotropy inside each grain causing small deviations from the material's effective magnetic anisotropy axis [59]. This grain texture is transferred further to the antiferromagnetic material deposited on top (i.e. IrMn in this case). However, for amorphous materials, where the material is anticipated to be homogeneous, such modulations are not to be expected. At $\boldsymbol{H_{ext}} = 0$ Oe (Figure 6.22d), the domain wall angle between the spike domains and the magnetization in the middle region, as well as the local analysis of the MO intensity exhibiting a tilting of magnatization inside the spike domains by 26.7° away from the intended magnetization axis, point out towards a local tilting of the unidirectional magnetic anisotropy at the edges. Moreover, the highest MO contrast observed for the modulations in the middle and the high bright closure domain volume at zero $\boldsymbol{H_{ext}}$ is in agreement with this observation. In the middle region, the exchange bias is oriented along the short axis of the structure, which is the intended axis. The formation of multi magnetic domain state results in locally varying magnetization response. At the edges spike and closure domain structures expand and shrink with $\boldsymbol{H_{ext}}$. As a consequence, magnetic hysteresis generates at magnetization loops measured along the effective hard axis of the structure (Figure 6.21b).

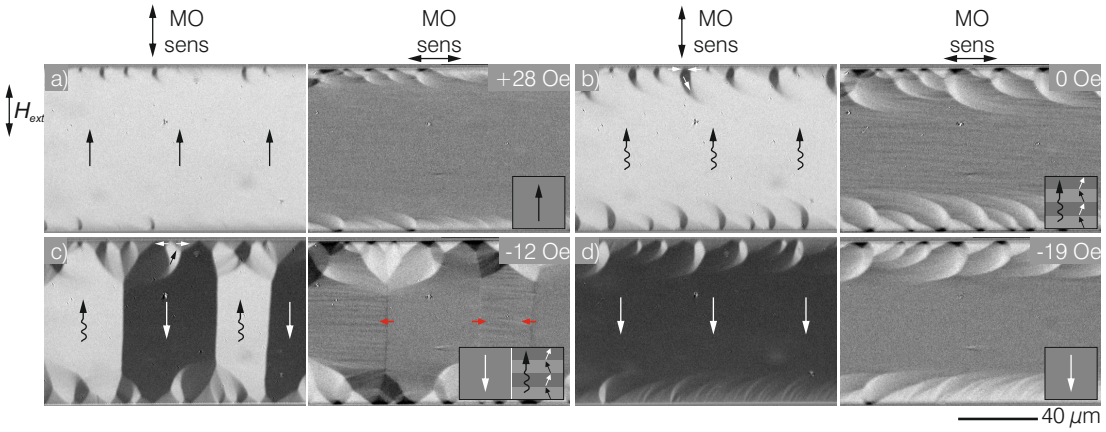

Figure 6.23: Some selected magnetic domain images obtained with two orthogonal MOKE sensitivities with $\boldsymbol{H_{ext}}$ applied along the $\mathbf{K_{eb}}$ (In-plane dimensions: 80 μm x 320 μm). (Sample: [Si/ SiO_2] 300 μm/ Ta 5 nm/ NiFe 2.5 nm/ IrMn 7 nm/ CoFeB 80 nm/ TaN 5 nm)

Possible indications to the origin of the observed magnetization modulations in low $\boldsymbol{H_{ext}}$ regime (e.g. Figure 6.22d) is acquired by applying $\boldsymbol{H_{ext}}$ along $\mathbf{K_{eb}}$ (Figure 6.23). At high enough $\boldsymbol{H_{ext}}$ applied parallel to $\mathbf{K_{eb}}$, the modulations in the middle region are effectively compensated (Figure 6.23a). Now, with $\boldsymbol{H_{ext}}$ increased

from the remanent magnetization state (Figure 6.23b) antiparallel with respect to induced $\mathbf{K_{eb}}$, around $\boldsymbol{H_{ext}}$ = -12 Oe, the exchange bias is compensated (compare Figure 6.21a, b to 6.23c). Magnetic domains form with magnetization antiparallel with respect to $\mathbf{K_{eb}}$ (Figure 6.23c). The magnetic film is in demagnetized state. With MO sensitivity aligned perpendicular, no domain modulations are observed inside the magnetic domains, where the exchange bias is compensated (see also sketch in Figure 6.23c). With increasing $\boldsymbol{H_{ext}}$, the exchange bias is fully compensated in the middle with no apparent modulations. Presumably, the domain texture of the thin NiFe layer used for setting the exchange bias is transfered to the IrMn and is further transmitted to the later deposited amorphous CoFeB film [59].

6.2.4 Exchange biased $Co_{40}Fe_{40}B_{20}$ bilayers

Parallel exchange bias: Figure 6.24 shows the magnetization loops measured inductively along easy (Figure 6.24a) and hard axis (Figure 6.24b) of a large structure consisting of a CoFeB bilayer, where each CoFeB layer is exchange biased individually. The essential layer structure and the deposition conditions are the same as the full film shown in Figure 6.4. The biasing direction is the same for both layers.

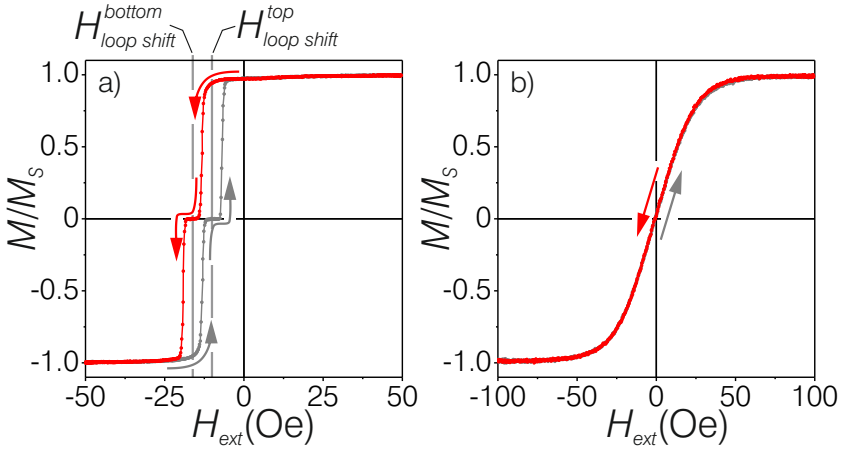

Figure 6.24: (a) easy and (b) hard axis magnetization loops for a structured, exchange biased CoFeB film are displayed. The induced exchange bias directions are parallel in both layers (In-plane dimensions: 2 mm x 20 mm). (Sample: [Si/ SiO_2] 300 μm/ Ta 5 nm/ NiFe 2.5 nm/ IrMn 7 nm/ CoFeB 80 nm/ Ta 3 nm/ NiFe 2.5 nm/ IrMn 7 nm/ CoFeB 80 nm/ TaN 5 nm)

Similar to data displayed in Figure 6.4a for its full film counterpart, the large structure shows a two step magnetization reversal behavior with $\boldsymbol{H_{ext}}$ applied along the exchange bias direction. As the $\boldsymbol{H_{ext}}$ is decreased from $+\boldsymbol{H_{sat}}$, starting from $\boldsymbol{H_{ext}}$ = -12.5 Oe first the top CoFeB layer switches its magnetization. Afterwards as the $\boldsymbol{H_{ext}}$ is further increased in the minus direction, beginning at $\boldsymbol{H_{ext}}$ = -18 Oe, the bottom layer magnetization switch occurs. Top and bottom layer loop shifts

are measured to be $\boldsymbol{H}^{top}_{loop\ shift}$ = -10 Oe and $\boldsymbol{H}^{bottom}_{loop\ shift}$ = -16.4 Oe, respectively. $\boldsymbol{H_c} \approx 3$ Oe is identical for both layers.

In Figure 6.25a-e, some selected magnetic domain images for the large structure obtained via large view microscope are displayed. $\boldsymbol{H_{ext}}$ is applied along the long axis of the structure ($\boldsymbol{H_{ext}} \perp \mathbf{K_u}, \mathbf{K_{eb}}$). Decreasing the $\boldsymbol{H_{ext}}$ from magnetic saturation (Figure 6.25a), the magnetization reversal is performed with rotation of magnetization. The magnetization changes almost linearly with $\boldsymbol{H_{ext}}$ (Figure 6.25a-e). At this magnification, no sign of magnetic domain formation is detected. However, high resolution domain observation (Figure 6.25f) exhibits nucleation of spike domain structures at the very edges. The exchange bias at the edges are compensated by the local $\boldsymbol{H_d}$.

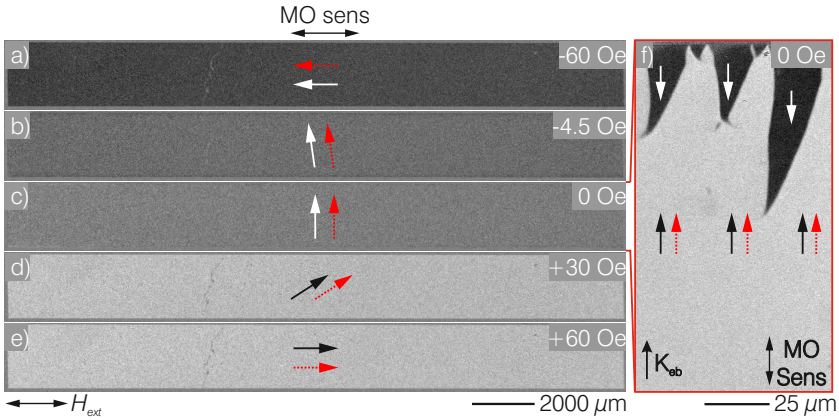

Figure 6.25: (a-e) Some selected magnetic domain images obtained with a large view microscope setup are shown. $\boldsymbol{H_{ext}}$ is applied along the long axis of the structure. (f) displays in high spatial resolution, the remanent magnetic domain state at the edge region. Magnetization directions are sketched (In-plane dimensions: 2 mm x 20 mm). (Sample: [Si/ SiO_2] 300 μm/ Ta 5 nm/ NiFe 2.5 nm/ IrMn 7 nm/ CoFeB 80 nm/ Ta 3 nm/ NiFe 2.5 nm/ IrMn 7 nm/ CoFeB 80 nm/ TaN 5 nm)

Magneto-optically measured magnetization loops along the short and long axes of a small structure are displayed in Figure 6.26a and b, respectively. The essential layer composition is same as in Figure 6.4 and 6.24. Note that the MO measurement is only sensitive to the top CoFeB layer. A two step magnetic reversal is observed as $\boldsymbol{H_{ext}}$ is decreased from $+\boldsymbol{H_{sat}}$. Around $\boldsymbol{H_{ext}}$ = +17 Oe, a sudden drop in magnetization occurs, which is followed by a second magnetization jump at $\boldsymbol{H_{ext}}$ = -3 Oe. For the top CoFeB layer only a small portion of the loop is shifted in the $-\boldsymbol{H_{ext}}$ direction, which is the induced $\boldsymbol{K_{eb}}$ direction. The magnetization loop measured along the long axis displays a pronounced hysteresis at low $\boldsymbol{H_{ext}}$ (Figure 6.26b). Both loops point out towards formation of magnetic domains in the top CoFeB layer.

Some selected magnetic domain images during the magnetization reversal for the small structure are shown in Figure 6.27. $\boldsymbol{H_{ext}}$ is applied along the long axis of the structure ($\boldsymbol{H_{ext}} \perp \mathbf{K_{eff}}$), which corresponds to the magnetization loop shown

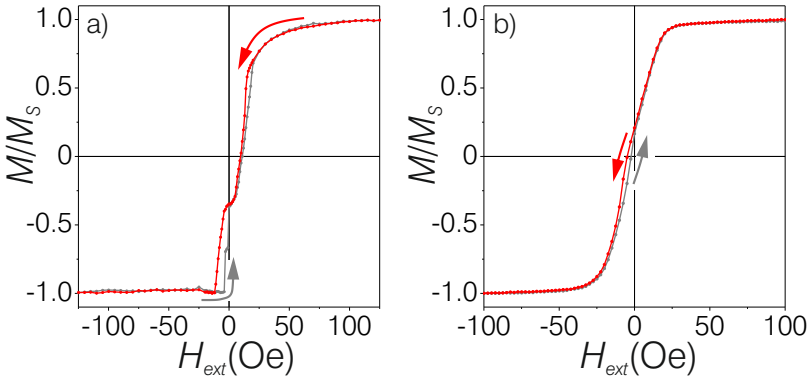

Figure 6.26: Magneto-optically measured easy (a) and hard (b) axis magnetization loops for an exchange biased CoFeB bilayer structure are displayed (In-plane dimensions: 80 μm x 320 μm). (Sample: [Si/ SiO_2] 300 μm/ Ta 5 nm/ NiFe 2.5 nm/ IrMn 7 nm/ CoFeB 80 nm/ Ta 3 nm/ NiFe 2.5 nm/ IrMn 7 nm/ CoFeB 80 nm/ TaN 5 nm)

in Figure 6.26b. With $\boldsymbol{H_{ext}}$ decreased from $\mathbf{-H_{sat}}$ (Figure 6.27a) magnetic domains nucleate throughout the structure (Figure 6.27b and c). Magnetic domain formation in the middle suggests that $\boldsymbol{H_d}$ exceeds the $\boldsymbol{H_{eb}}$ everywhere in the top CoFeB film. This is also supported by the calculated $\boldsymbol{H_d}$ shown in Figure 6.7. Moreover, similar to data shown for a singlelayer of biased CoFeB film (Figure 6.22 and 6.23), magnetic domains with magnetization direction aligned parallel to $\boldsymbol{K_{eb}}$ show ripple like magnetization modulations (Figure 6.27c). As previously discussed in the last section, most likely the texture originates from the polycrystalline NiFe layer. Furthermore, especially along the MO sensitivity axis aligned perpendicular to $\boldsymbol{K_{eb}}$ (MO sens $\perp$ $\boldsymbol{K_{eb}}$), a high amount of magnetization activity is revealed inside magnetic domain walls. Some domain walls show double contrast with Bloch lines separating them (Figure 6.27c). Variation of $\boldsymbol{H_{ext}}$ leads a change in the magnetization of the wall. As a result, the Bloch line moves along the wall (yellow circle in Figure 6.27c and d).

Until now no information on the magnetic domain state of the bottom CoFeB layer could be obtained. It can either be in single domain state or could as well possess the same magnetic domain configuration as the top CoFeB layer. Data on the magnetic domain configuration of the bottom CoFeB layer is obtained by applying $\boldsymbol{H_{ext}}$ along the short axis of the magnetic structure ($\boldsymbol{H_{ext}} \parallel \boldsymbol{K_{eff}}$) (Figure 6.28). Decreasing $\boldsymbol{H_{ext}}$ from $\boldsymbol{+H_{sat}}$, around +13 Oe magnetic domains form with antiparallel magnetization alignment with respect to $\boldsymbol{K_{eb}}$ (Figure 6.28a). They expand with decreasing $\boldsymbol{H_{ext}}$ and at remanent magnetization state, the top layer is multi domain state with net magnetization aligned antiparallel to the intended exchange bias direction (compare Figure 6.28b and 6.26a at $\boldsymbol{H_{ext}} = 0$ Oe). Now applying $\boldsymbol{H_{ext}}$ in the minus direction, at $\boldsymbol{H_{ext}} = -13$ Oe, the overall dark MO contrast indicates a

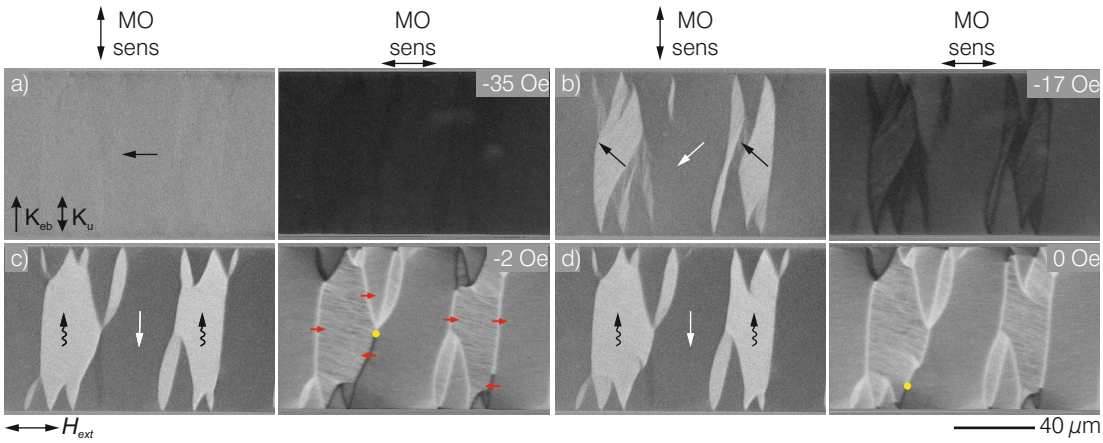

Figure 6.27: Some selected magnetic domain images obtained with two orthogonal MOKE sensitivities and $\boldsymbol{H_{ext}}$ applied along the long axis of the structure. Possible magnetization directions are sketched. Additionally, the position of a Bloch line is marked in c) and d) (In-plane dimensions: 80 μm x 320 μm). (Sample: [Si/ SiO_2] 300 μm/ Ta 5 nm/ NiFe 2.5 nm/ IrMn 7 nm/ CoFeB 80 nm/ Ta 3 nm/ NiFe 2.5 nm/ IrMn 7 nm/ CoFeB 80 nm/ TaN 5 nm)

complete compensation of the exchange bias in the top CoFeB layer. As of yet no magnetic domain information has been acquired from the bottom CoFeB layer. This indicates that the bottom CoFeB layer is magnetized homogeneously antiparallel with respect to the top CoFeB (Figure 6.28c). Further reducing $\boldsymbol{H_{ext}}$ to −26 Oe (Figure 6.28d), domain wall structures form at the top layer (check MO sens $\perp$ $\boldsymbol{K_{eb}}$). However, evidenced by the magnetic domain image obtained by MO sens $\parallel$ $\boldsymbol{K_{eb}}$ the top CoFeB layer is homogeneously magnetized (left image in Figure 6.28d). Both of which hint at a magnetization switch in the bottom CoFeB layer. Without application of $\boldsymbol{H_{ext}}$, the top and bottom CoFeB layers are in multi and single domain states, respectively. Both CoFeB stack involves a 2.5 nm thick NiFe film under IrMn layers. Similar to its full film counterpart, a magnetostatic interaction with positive coupling constant between the top NiFe and bottom CoFeB through the 3 nm thick Ta spacer serves as an additional bias to the bottom CoFeB layer. This clarifies both the origin of the two step magnetization switch in the overall stack, as well as why the bottom CoFeB layer remains to be in single domain state at remanence.

Antiparallel exchange bias: Inductively measured easy and hard axis magnetization loops for a large structure are displayed in Figure 6.29a and b, respectively. The $\boldsymbol{K_{eb}}$ of both CoFeB layers are aligned antiparallel with respect to each other. The essential layer structure and the deposition conditions are the same as for its full film counterpart displayed in Figure 6.6. Hence, the magnetization loop measured along the exchange bias directions exhibits two distinct magnetization branches shifted to higher $\boldsymbol{H_{ext}}$ values. Each of which are associated with magnetization reversal in

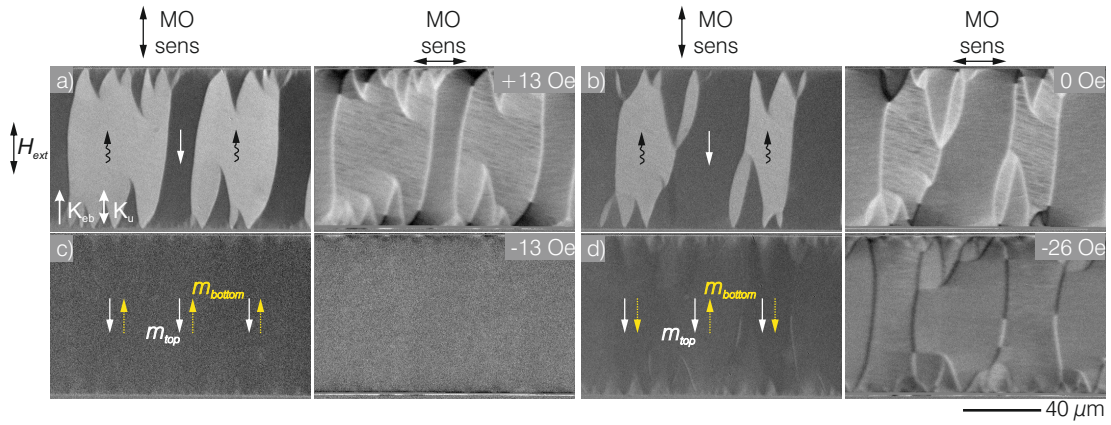

Figure 6.28: Some selected magnetic domain images obtained with two orthogonal MOKE sensitivities are shown. $\boldsymbol{H_{ext}}$ is applied along the short axis of the structure. Possible magnetization directions are sketched (In-plane dimensions: 80 μm x 320 μm). (Sample: [Si/ SiO_2] 300 μm/ Ta 5 nm/ NiFe 2.5 nm/ IrMn 7 nm/ CoFeB 80 nm/ Ta 3 nm/ NiFe 2.5 nm/ IrMn 7 nm/ CoFeB 80 nm/ TaN 5 nm)

bottom and top CoFeB layers (Figure 6.29a).

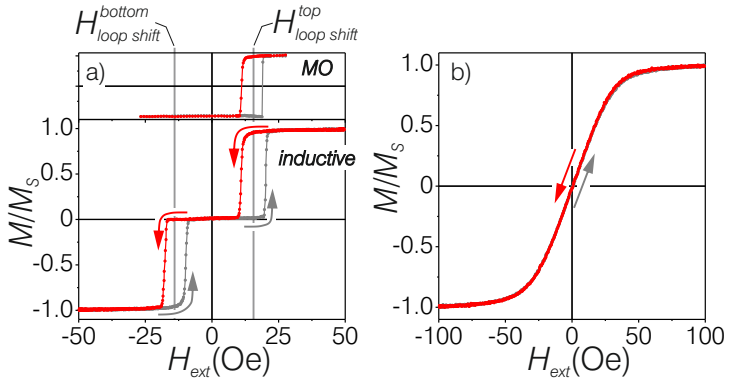

Figure 6.29: (a) easy ($\boldsymbol{H_{ext}} \parallel \mathbf{K_{eff}}$) and (b) hard ($\boldsymbol{H_{ext}} \perp \mathbf{K_{eff}}$) axis magnetization loops for a structured, exchange biased CoFeB film are exhibited. On top of (a), magnetooptically (MO) measured magnetization loop displays the top CoFeB magnetization reversal. The exchange bias in each CoFeB layer is antiparallel with respect to each other (In-plane dimensions: 2 mm x 20 mm). (Sample: [Si/ SiO_2] 300 μm/ Ta 5 nm/ NiFe 2.5 nm/ IrMn 7 nm/ CoFeB 80 nm/ Ta 3 nm/ NiFe 2.5 nm/ IrMn 7 nm/ CoFeB 80 nm/ TaN 5 nm)

The top $\boldsymbol{H^{top}_{loop\ shift}}$ and bottom $\boldsymbol{H^{bottom}_{loop\ shift}}$ CoFeB layer loop shifts are 15.5 Oe and −13.8 Oe, respectively (see magneto-optically measured magnetization loop for the top CoFeB loop shift in Figure 6.29a). $\mathbf{H_c}$ for top and bottom layers are 4.6 Oe and 3.9 Oe, respectively. Unlike the parallelly biased bilayer, the biasing direction and thus the magnetization in the top NiFe and bottom CoFeB layer are antiparallel with respect to each other. Since the essential layer structures are the same, the magnetostatic interaction is of the same sign (positive), which leads to an This leads to a decrease in the effective loop shift for the bottom CoFeB loop. As for

$\boldsymbol{H_{ext}}$ applied perpendicular to $\boldsymbol{K_{eff}}$, little to no hysteresis is observed (Figure 6.29b). The effective magnetic anisotropy $\boldsymbol{K_{eff}}$ is the same as the parallelly biased CoFeB bilayer.

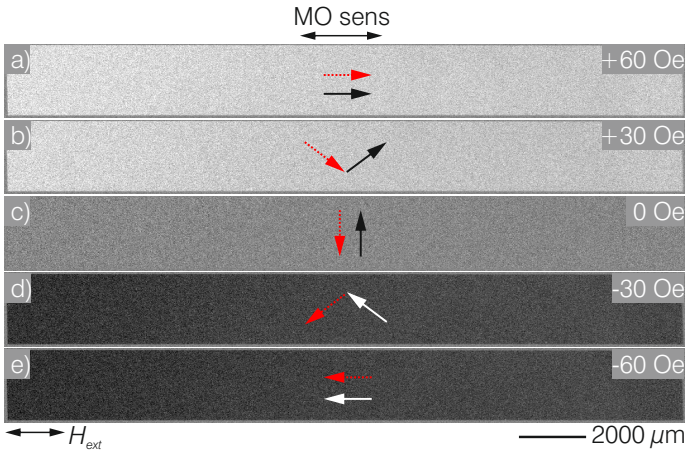

Figure 6.30: (a-e) Some selected magnetic domain images obtained with a large view microscope setup are displayed. $\boldsymbol{H_{ext}}$ is applied along the long axis of the structure. Possible magnetization directions are sketched (In-plane dimensions: 2 mm x 20 mm). (Sample: [Si/ SiO_2] 300 μm/ Ta 5 nm/ NiFe 2.5 nm/ IrMn 7 nm/ CoFeB 80 nm/ Ta 3 nm/ NiFe 2.5 nm/ IrMn 7 nm/ CoFeB 80 nm/ TaN 5 nm)

The large view magnetic domain observations performed with $\boldsymbol{H_{ext}}$ applied along the long axis of the large structure are shown in Figure 6.30. Independent of the magnetic field history along this $\boldsymbol{H_{ext}}$ axis, a coherent rotation of magnetization occurs in the top CoFeB layer. No magnetic domain formation is observed. Due to antiparallel alignment of magnetization inside the CoFeB layers, the $\boldsymbol{H_d}$ is effectively compensated.

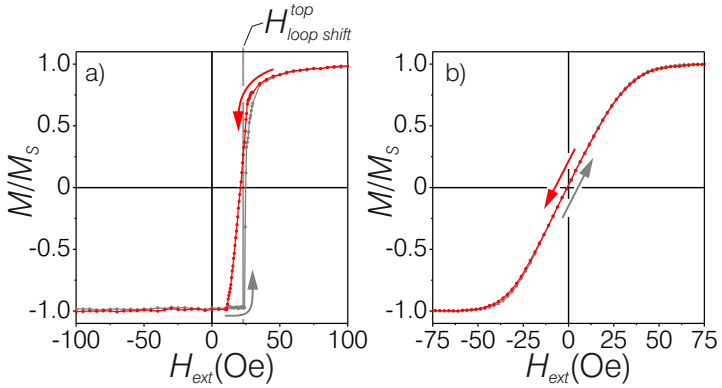

Figure 6.31: (a) easy and (b) hard axis magnetization loops for a structured, antiparallelly exchange biased CoFeB bilayer are displayed (In-plane dimensions: 2 mm x 20 mm). (Sample: [Si/ SiO_2] 300 μm/ Ta 5 nm/ NiFe 2.5 nm/ IrMn 7 nm/ CoFeB 80 nm/ Ta 3 nm/ NiFe 2.5 nm/ IrMn 7 nm/ CoFeB 80 nm/ TaN 5 nm)

A similar magnetic domain and reversal behavior is observed in small structure sizes. Magneto-optically measured magnetization loops for the small structure are

displayed in Figure 6.31. Possibly stemming from the magnetostatic interaction between the CoFeB layers, the top CoFeB loop shift $\boldsymbol{H}^{top}_{loop\ shift}$ is now 23 Oe (Figure 6.31a). The hard axis loop ($\boldsymbol{H_{ext}} \perp \boldsymbol{K_{eff}}$), depicts a magnetization reversal almost linearly with $\boldsymbol{H_{ext}}$ (Figure 6.31b).

Magnetic domain observations performed on the top CoFeB shows no sign of magnetic domain formation in the imaged area (Figure 6.32). The demagnetizing field is effectively compensated even at high $\boldsymbol{H_{ext}}$. Therefore, a mostly linear magnetization response due to coherent rotation of magnetization occurs (Figure 6.32a-f).

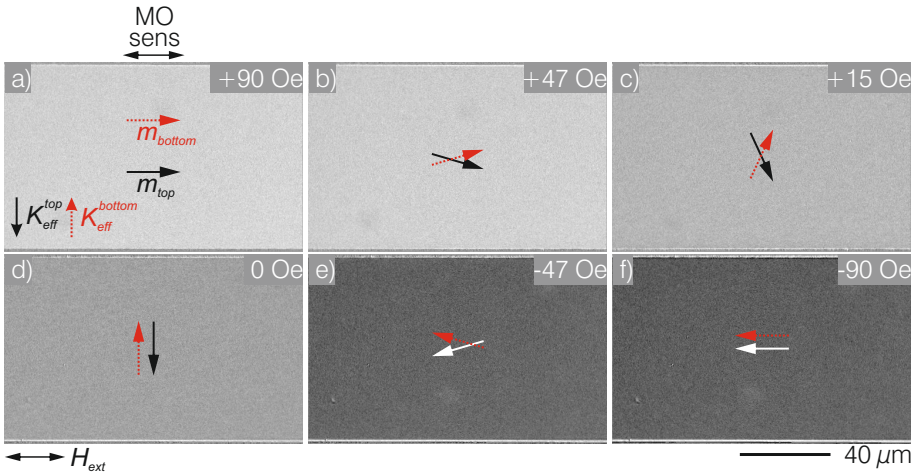

Figure 6.32: Some selected magnetic domain images with $\boldsymbol{H_{ext}}$ applied along the long axis of the structure are displayed. Possible magnetization directions are sketched for top and bottom CoFeB layers (In-plane dimensions: 80 μm x 320 μm). (Sample: [Si/ SiO_2] 300 μm/ Ta 5 nm/ NiFe 2.5 nm/ IrMn 7 nm/ CoFeB 80 nm/ Ta 3 nm/ NiFe 2.5 nm/ IrMn 7 nm/ CoFeB 80 nm/ TaN 5 nm)

In summary, the origin of the hysteresis observed in hard axis magnetization loops have been covered. Especially relevant from an application point of view, structures in micrometer in-plane dimensions display a noteworthy increase in in-plane $\boldsymbol{H_d}$. A multi magnetic domain state form with upscaling of the total CoFeB thickness. $\boldsymbol{H_d}$ begins to exceed the $\boldsymbol{H_{eb}}$ starting from the edges of the magnetic structures. As displayed for the parallelly exchange biased CoFeB bilayer (Figure 6.27), the concurrent process of nucleation and annihilation of magnetic domain and wall structures lead to $\boldsymbol{H_{ext}}$ induced magnetization hysteresis. Maintaining an antiparallel magnetization alignment in neighboring CoFeB layers, in our case by inducing antiparallelly aligned $\boldsymbol{K_{eb}}$ alternatingly, the total CoFeB thickness can be increased by keeping the total magnetic anisotropy the same (i.e. $\boldsymbol{K_u}$ and $\boldsymbol{K_{eb}}$). The single domain magnetic state is preserved at all times even for structures in micrometer dimensions (Figure 6.32) and a linear magnetization response to $\boldsymbol{H_{ext}}$ aligned perpendicular to the effective magnetic anisotropy $\boldsymbol{K_{eff}}$ is generated (Figure 6.31).

7 Summary and conclusions

This work dealt mainly with magnetic domain and domain wall transformations in soft magnetic, magnetostrictive materials and the extent of their influence on the device response in high sensitive, 2-2 ME sensors consisting of FeCoSiB and AlN. For this purpose, in combination with inductive magnetization and electrical ME response measurements, advanced MO microscopy techniques such as dual-wavelength imaging and high order MO effects like MOVE were employed.

Results beginning with Chapter 4 start with exploring the hysteretic hard axis magnetization response and stress induced magnetic domain effects in millimeter sized, unbiased FeCoSiB films and established the basis of several following chapters. The complementary data from the inductive measurements and MOKE imaging pinpointed an intertwined relationship between complex magnetic domain formation, inhomogeneous magnetic anisotropy distribution and the resulting unorthodox hysteretic magnetization reversal. Two distinct, $\boldsymbol{H_{ext}}$ dependent magnetic domain configurations with different magnetic susceptibilities were revealed, namely the blocked domain state and Landau-like, modulated (wide) domain state, as the origin of the hysteretic magnetization reversal. The developing domain wall type and density exclusive to each domain state were identified as the cause of the large magnetic susceptibility discrepancies. Furthermore, particularly interesting in terms of magnetic domain physics, the formation of domain modulations were covered. An overall non-uniform $\mathbf{K_u}$ distribution due to the presence of laterally varying tensile stress in the material was exposed. This was generated by the stress relaxation during introduction of $\mathbf{K_u}$ resulting in a local change of magnetic anisotropy sign at the very sides of the magnetic film. Concurrently, a zero magnetic anisotropy line was formed and in its vicinity, minimization of magnetoelastic energy became the driving force for magnetic domain formation leading to low angle magnetization modulations inside the domains.

Further into the chapter, the influence of FeCoSiB film topology on magnetic domain formation and magnetization response of differently layered FeCoSiB thin films deposited on Si/ SiO_2 and AlN surfaces was examined. The magnetization behavior of specimens deposited directly on Si/ SiO_2 substrates displayed very soft magnetic properties with well-defined $\mathbf{K_u}$ ($\mathbf{H_k}$ = 10 Oe and $\mathbf{H_c}$ = 0.5 Oe). How-

ever, the same FeCoSiB films deposited on AlN exhibited an inverted film behavior with an 80 times increase in $\mathbf{H_c}$ along both easy and hard axes. Magnetic domain observations uncovered substantial discrepancies in magnetization state, such as domain wall density and alignment. The surface profile of the underlying layers were transferred to the later deposited films and for rough surfaces, i.e. AlN, $\mathbf{K_s}$ begins to dominate over the $\mathbf{K_u}$. The results were particularly important for 2-2 composite ME sensors, where AlN is frequently integrated as the pizeoelectric phase. The displayed data suggested for ME sensors with AlN and the magnetostrictive material in direct contact (e.g. [23, 24]), a degradation in the overall sensor response due to occuring magnetic domain activity can be anticipated especially for low film thicknesses.

Chapter 5 delved into the transfer of the magnetization hysteresis to the sensor response by performing in-situ magnetic domain observations on a ME sensor in operation. Two distinct, $\boldsymbol{H_{ext}}$ dependent ME response branches related to the magnetization susceptibility of the existing magnetic domain state were identified. Moreover, complementary large view MO images revealed spatially varying magnetic domain response that is caused by a combination of $\mathbf{K_u}$ misalignment (i.e. 5° under the sensor electrodes) and demagnetization effects. Operating at a lower $\boldsymbol{H_{ext}}$ range ($\boldsymbol{H_{ext}} < \mathbf{H_k}$), outside the blocked domain state formation regime, the hysteretic sensor response vanished due to almost homogeneous magnetization response. However, the domain width data indicated substantial magnetic domain wall motion due to the mentioned inhomogeneous $\mathbf{K_u}$ distribution. For small $\boldsymbol{H_{ext}}$ excitations, the mentioned non-linear modifications are limited and mostly reversible but are very important for sensors operated via frequency modulation.

A side investigation focused on probing magnetic effects that are quadratic in magnetization direction (i.e. $\boldsymbol{\lambda}$ and AMR) via different MO effects and reconstruction of the device response. In the first part, local $\boldsymbol{m^2(x,\ y)}$ maps were derived from MOKE images. The obtained maps corresponded to the local $\boldsymbol{\lambda(x,\ y)}$ responses. Furthermore, such maps allowed reconstruction of local ME $\boldsymbol{d\lambda(H_{ext})/dH_{mea}}$ maps and response. The intensity in such maps revealed features like the maximum ME response and its local sign, also regions with zero contribution to the overall ME response. An almost twofold difference in ME response depending on the $\boldsymbol{H_{ext}}$ history was successfully reconstructed.

The second approach involved the rarely utilized MOVE as a means to probe the $\boldsymbol{m^2(x,\ y)}$ behavior firstly of in-operando unbiased and exchange biased ME sensors and followed by of a hybrid AMR element. MOVE presented an opportunity to directly acquire the local $\boldsymbol{\lambda(x,\ y)}$ maps through its shared quadratic magnetization symmetry with $\boldsymbol{\lambda}$ and AMR. The local intensity analysis of $\boldsymbol{\lambda(x,\ y)}$ maps showed spatially varying $\boldsymbol{\lambda}$ response for the unbiased sensor, whereas the biased sensor

displayed an almost linear $\boldsymbol{\lambda}$ change due to homogeneous magnetization response. The corresponding reconstructed $\boldsymbol{d\lambda(H_{ext})/dH_{mea}}$ curves could reproduce certain features like curve shape and relative response ratios, in well-agreement with the in-situ device responses. Discrepancies stemmed from the local MO probing of the $\boldsymbol{m^2}$ response, the information depth of the MO measurements and possible hysteretic processes occurring in the AlN. Finally, MOVE imaging was applied to a hybrid, stripe patterned magnetic film with zig-zag exchange bias orientation. Through MOVE imaging, local $\boldsymbol{m^2}$ response along different $\boldsymbol{H_{ext}}$ alignments of individual stripes were extracted and the total $\boldsymbol{m^2}$ response was reconstructed. They showed excellent agreement with complementary AMR measurements.

The acquisition of $\boldsymbol{m^2(x,\ y)}$ maps did not only reveal the $\boldsymbol{m^2}$ response of the transpiring magnetic domain configuration but also allowed separation of magnetic response from the device response and granted an opportunity to predict the device response in advance. Where applicable, MOVE imaging presents a promising prospect for investigating $\boldsymbol{m^2}$ behavior of magnetic materials.

Previous chapters linked the magnetic domain effects and their corresponding $\boldsymbol{\lambda}$ response to the ME response. The observed magnetization hysteresis showed the importance of magnetic domain control, which is further supported by noise level differences in LoD measurements obtained via direct measurement and frequency conversion techniques (e.g. [27]). Therefore, the focus in Chapter 6 was switched to demagnetization effects and magnetic domain control in differently layered and structured soft magnetic CoFeB films. It was shown for micrometer sized unbiased films that the magnetization response differs largely from their full film counterparts. Such that domain wall transition boundaries separating regions with ANWs and ABWs lead to local magnetization jumps accompanied by wall transitions. As a result, the magnetization response deviates from linearity.

The first approach to suppress domain wall formation was to institute a magnetostatically interacting bilayer structure. Consequently, a single domain state could be achieved and if present, the domain wall density was limited. On the other hand, the magnetic domain response at intermediate $\boldsymbol{H_{ext}}$ regime, as well as in the presence of magnetic domain walls displayed noteworthy domain wall formation, annihilation and movement (i.e. formation of edge curling walls and transitions into twin Néel walls). For envisioned integration of such a magnetic film structure to a ME sensor operated via frequency modulation, the discussed domain effects can be expected to transfer to the device response. Nonetheless, when layered correctly [138], such a multilayer structure can be advantageous in direct ME measurements over single layer films due to no additional anisotropy but low domain wall density.

The second approach involved employing exchange bias. It was shown for CoFeB film thicknesses as small as 80 nm that the induced $\boldsymbol{H_{eb}}$ was not enough to com-

pensate the demagnetizing field at the sides of the film. Now doubling the total CoFeB thickness but the $\boldsymbol{H_{eb}}$ sign and magnitude kept constant, the demagnetizing field exceeded $\boldsymbol{H_{eb}}$ even in the middle of the structure leading to a multi magnetic domain state throughout the structure. However, the effective bias in both CoFeB layers was interestingly not the same due to a small magnetostatic interaction between the top NiFe and bottom CoFeB films. As a result, the bottom CoFeB was in single domain state at remanent state. As a side observation, the magnetization along the $\boldsymbol{H_{eb}}$ direction was surprisingly modulated. This stems from the transfer of the domain texture of IrMn and possibly NiFe to the amorphous CoFeB film, resulting in reduced net magnetization and a complicated domain wall structure separating the modulated and non-modulated regions. It was shown that this complicated magnetic domain structure generated noteworthy magnetization hysteresis with $\boldsymbol{H_{ext}}$ applied along the effective hard axis of the magnetic films.

As final step, magnetostatic interactions between neighboring films and exchange bias were combined in order to eliminate the discussed magnetic domain effects. The antiparallelly aligned $\boldsymbol{H_{eb}}$ in neighboring CoFeB layers maintained the coherent rotation of magnetization with $\boldsymbol{H_{ext}}$ applied along the effective hard axis. Such magnetic anisotropy engineering allowed upscaling the total magnetic film thickness while impeding magnetic domain formation.

Overall, the ME response was found to be tightly linked to the occurring magnetic domain effects such that the commonly observed ME hysteresis originates predominantly from the magnetostrictive layer. Such stress and shape induced magnetic domain activity becomes more pronounced in small structure sizes. The next natural step for ME sensors would be, for example, to introduce antiparallel biasing as shown in Chapter 6, which will allow upscaling of the total magnetic film thickness and also bring the opportunity to require lower biasing, while maintaining a single magnetic domain state with $\boldsymbol{H_{ext}}$. The presented results are important for all magnetic field sensors with magnetic sensing layers, where magnetic domain control is necessary.

Appendices

Calculation of local demagnetizing field of rectangular prisms

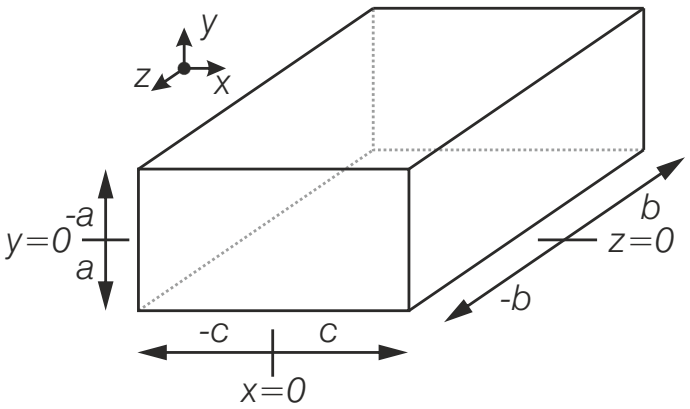

A1: Applied coordinate system for the calculation of demagnetizing factor along x-axis of the rectangular structure. The origin is in the center of the rectangular prism.

Averaged demagnetization factor in the middle: One dimensional averaged demagnetization factor in the middle part along x-axis for a rectangular prism can be calculated from (eq.A1) [69]. The applied coordinate system is given in **A1**.

$$\begin{aligned}\pi N_x = &\frac{c}{2a}\ln\left(\frac{\sqrt{4a^2+4b^2+c^2}+2b}{\sqrt{4a^2+4b^2+c^2}-2b}\times\frac{\sqrt{4b^2+c^2}-2b}{\sqrt{4b^2+c^2}+2b}\right)\\ &+\frac{c}{2b}\ln\left(\frac{\sqrt{4a^2+4b^2+c^2}+2a}{\sqrt{4a^2+4b^2+c^2}-2a}\times\frac{\sqrt{4a^2+c^2}-2a}{\sqrt{4a^2+c^2}+2a}\right)\\ &+\frac{c}{2ab}(\sqrt{4a^2+c^2}+\sqrt{4b^2+c^2}-\sqrt{4a^2+4b^2+c^2}-c)\\ &+2\arctan\left(\frac{4ab}{c\sqrt{4a^2+4b^2+c}}\right)\end{aligned} \qquad \text{(eq.A1)}$$

Non-averaged demagnetization factor along an axis One-dimensional local demagnetizing factor for a rectangular prism along x-axis can be calculated from (eq.A1) [70]. The applied coordinate is the same as the averaged case (**A1**).

$$\pi N_x(x) = \sum_{n=\pm 1} \left\{ \arctan\left(\frac{4ab}{(c+nx)F_1(a^2+b^2)}\right) + \frac{F_2(a)}{4b} + \frac{F_2(b)}{4a} + \frac{c+nx}{4ab}\left[F_1(a^2) + F_1(b^2) - F_1(a^2+b^2) - (c+nx)\right] \right\} \quad \text{(eq.A2)}$$

F_1 and F_2 are given in (eq.A3) and (eq.A4), respectively.

$$F_1(\xi) = \sqrt{4\xi + (c+nx)^2} \quad \text{(eq.A3)}$$

and

$$F_2(\eta) = (c+nx)\ln\left[\frac{F_1(a^2+b^2)+2\eta}{F_1(a^2+b^2)-2\eta}\frac{F_1(\eta^2)-2\eta}{F_1(\eta^2)+2\eta}\right] \quad \text{(eq.A4)}$$

Relating the ME response to magnetostriction and magnetic susceptibility

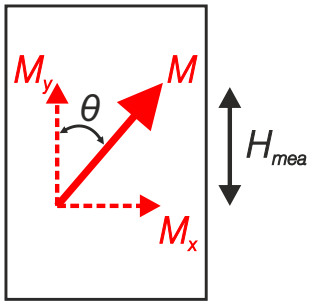

A2: Sketch depicting the magnetization components $\boldsymbol{M_x}$ and $\boldsymbol{M_y}$ of $\boldsymbol{M}$. $\boldsymbol{\theta}$ is the angle between $\boldsymbol{M_y}$ and $\boldsymbol{M}$. The measuring AC magnetic field $\boldsymbol{H_{mea}}$ and the DC external magnetic field $\boldsymbol{H_{ext}}$ are indicated.

The magnetic susceptibility $\boldsymbol{\chi}$ of magnetization $\boldsymbol{M}$ component $\boldsymbol{M_y}$ is expressed as (eq.A5).

$$\chi = \frac{dM_y}{dH_{mea}} \tag{eq.A5}$$

with $\boldsymbol{M_y} = \mathbf{M_s}\cos(\boldsymbol{\theta})$ (eq.A6) and further use of product rule for first-order derivation with respect to $\boldsymbol{\theta}$ (eq.A7), the equation becomes (eq.A8). $\mathbf{M_s}$ is the saturation magnetization of the material.

$$\chi = \frac{d(M_s\cos\theta)}{dH_{mea}} \tag{eq.A6}$$

$$\chi = M_s\frac{d(\cos\theta)}{d\theta}\frac{d\theta}{dH_{mea}} = -M_s\sin\theta\frac{d\theta}{dH_{mea}} \tag{eq.A7}$$

$$\frac{d\theta}{dH_{mea}} = \frac{-\chi}{M_s\sin\theta} \tag{eq.A8}$$

For 2-2 composite ME sensors, the ME response $\boldsymbol{\alpha_{ME}}$ is a product property of the constituent phases (eq.A9) [25, 90]. From magnetism point of view, $\boldsymbol{\alpha_{ME}}$ at an arbitrary $\boldsymbol{H_{ext}}$ scales with $\boldsymbol{d\lambda(H_{ext})/dH_{mea}}$ and by first-order derivation of (2.11), the $\boldsymbol{\alpha_{ME}}$ is approximated (eq.A10).

$$\alpha_{ME}(H_{ext}) = \frac{\partial E}{\partial H_{mea}} = \frac{\partial E}{\partial\sigma}\frac{\partial\sigma}{\partial\lambda}\frac{\partial\lambda}{\partial H_{mea}} \tag{eq.A9}$$

$$\alpha_{ME}(H_{ext}) \approx \frac{d\lambda(H_{ext})}{dH_{mea}} = \frac{d}{dH_{mea}}\left(\frac{3}{2}\lambda_s\left[\cos^2\theta - \frac{1}{3}\right]\right) = \frac{3}{2}\lambda_s\frac{d(\cos^2\theta)}{dH_{mea}} \tag{eq.A10}$$

Using the chain rule (eq.A11) and subsequent first-order derivation (eq.A12), an expression for the ME with respect to $\boldsymbol{\theta}$ is acquired.

$$\alpha_{ME}(H_{ext}) \approx \frac{d\lambda(H_{ext})}{dH_{mea}} = \frac{3}{2}\lambda_s \frac{d(\cos^2\theta)}{d\theta}\frac{d\theta}{dH_{mea}} \qquad \text{(eq.A11)}$$

$$\alpha_{ME}(H_{ext}) \approx \frac{d\lambda(H_{ext})}{dH_{mea}} = -3\lambda_s \sin\theta\cos\theta\frac{d\theta}{dH_{mea}} \qquad \text{(eq.A12)}$$

Now, (eq.A8) is inserted into (eq.A12).

$$\alpha_{ME}(H_{ext}) \approx \frac{d\lambda(H_{ext})}{dH_{mea}} = -3\lambda_s \sin\theta\cos\theta\left(\frac{-\chi}{M_s\sin\theta}\right) \qquad \text{(eq.A13)}$$

As a result, an expression for the ME response and respectively $\boldsymbol{d\lambda/dH_{mea}}$ at an arbitrary $\boldsymbol{H_{ext}}$ is obtained that is mainly dependent on $\boldsymbol{\lambda_s}$, $\boldsymbol{\chi}$ and $\boldsymbol{M_y}$ (eq.A14).

$$\alpha_{ME}(H_{ext}) \approx \frac{d\lambda(H_{ext})}{dH_{mea}} = \frac{3\lambda_s\chi}{M_s}\cos\theta = \frac{3\lambda_s\chi}{M_s^2}M_y \qquad \text{(eq.A14)}$$

References

[1] H. Neal Bertram. *Theory of Magnetic Recording*. Cambridge University Press, 1994. Cambridge Books Online.

[2] W.F. Witcraft, H. Wan, C.J. Yue, and T.K. Bratland. Method and apparatus for an integrated GPS receiver and electronic compassing sensor device. *US Patent 7,277,793*, 2007.

[3] D. Cohen. Magnetoencephalography: Detection of the brain's electrical activity with a superconducting magnetometer. *Science*, 175(4022):664–666, 1972.

[4] F. L. da Silva. EEG and MEG: Relevance to neuroscience. *Neuron*, 80(5):1112 – 1128, 2013.

[5] R. C. Jaklevic, John Lambe, A. H. Silver, and J. E. Mercereau. Quantum interference effects in Josephson tunneling. *Phys. Rev. Lett.*, 12:159–160, Feb 1964.

[6] D. Drung, C. Abmann, J. Beyer, A. Kirste, M. Peters, F. Ruede, and T. Schurig. Highly sensitive and easy-to-use SQUID sensors. *IEEE Transactions on Applied Superconductivity*, 17(2):699–704, 2007.

[7] F. Primdahl. The fluxgate magnetometer. *J. Phys. E: Sci. Instrum.*, 12:241–253, 1979.

[8] F. Yin, H. Lühr, J. Park, J. Rauberg, and I. Michaelis. Noise features of the CHAMP vector magnetometer in the 1–25 Hz frequency range. *Sensors and Actuators A: Physical*, 222:272–283, 2015.

[9] F. Jeffers. A measurement of signal-to-noise ratio versus trackwidth from 120 μm to 4 μm. *IEEE Transactions on Magnetics*, 23(5):2088–2090, 1987.

[10] P. Brown, T. Beek, C. Carr, H. O'Brien, E. Cupido, T. Oddy, and T. S. Horbury. Corrigendum: Magnetoresistive magnetometer for space science applications. *Measurement Science and Technology*, 23(059501), 2012.

[11] G. Binasch, P. Grünberg, F. Saurenbach, and W. Zinn. Enhanced magnetoresistance in layered magnetic structures with antiferromagnetic interlayer exchange. *Phys. Rev. B*, 39:4828–4830, 1989.

[12] S. S. P. Parkin, N. More, and K. P. Roche. Oscillations in exchange coupling and magnetoresistance in metallic superlattice structures: Co/Ru, Co/Cr, and Fe/Cr. *Phys. Rev. Lett.*, 64:2304–2307, 1990.

[13] S. M. Thompson. The discovery, development and future of GMR: The Nobel Prize 2007. *Journal of Physics D: Applied Physics*, 41(9):93001, 2008.

[14] M. Pannetier, C. Fermon, G. Le Goff, J. Simola, and E. Kerr. Femtotesla magnetic field measurement with magnetoresistive sensors. *Science*, 304(5677):1648–1650, 2004.

[15] M. Pannetier-Lecoeur, L. Parkkonen, N. Sergeeva-Chollet, H. Polovy, C. Fermon, and C. Fowley. Magnetocardiography with sensors based on giant magnetoresistance. *Applied Physics Letters*, 98(15):153705, 2011.

[16] S. Ikeda, J. Hayakawa, Y. Ashizawa, Y. M. Lee, K. Miura, H. Hasegawa, M. Tsunoda, F. Matsukura, and H. Ohno. Tunnel magnetoresistance of 604% at 300 K by suppression of Ta diffusion in CoFeB-MgO-CoFeB pseudo-spin-valves annealed at high temperature. *Applied Physics Letters*, 93(8):082508, 2008.

[17] S. Cardoso, D. C. Leitao, L. Gameiro, F. Cardoso, R. Ferreira, E. Paz, and P. P. Freitas. Magnetic tunnel junction sensors with pTesla sensitivity. *Microsystem Technologies*, 20(4-5):793–802, 2014.

[18] Manh-Huong Phan and Hua-Xin Peng. Giant magnetoimpedance materials: Fundamentals and applications. *Progress in Materials Science*, 53(2):323 – 420, 2008.

[19] L. V. Panina, K. Mohri, T. Uchiyama, M. Noda, and K. Bushida. Giant magneto-impedance in Co-rich amorphous wires and films. *IEEE Transactions on Magnetics*, 31(2):1249–1260, 1995.

[20] S. Gudoshnikov, N. Usov, A. Nozdrin, M. Ipatov, A. Zhukov, and V. Zhukova. Highly sensitive magnetometer based on the off-diagonal GMI effect in Co-rich glass-coated microwire. *physica status solidi (a)*, 211(5):980–985, 2014.

[21] M. Malatek, B. Dufay, S. Saez, and C. Dolabdjian. Improvement of the off-diagonal magnetoimpedance sensor white noise. *Sensors and Actuators A: Physical*, 204:20 – 24, 2013.

[22] H. Uppili and B. Daglen. Bi-directional giant magneto impedance sensor. *Advances in Materials Physics and Chemistry*, 3(5):249–254, 2013.

[23] H. Greve, E. Woltermann, H. Quenzer, B. Wagner, and E. Quandt. Giant magnetoelectric coefficients in $(Fe_{90}Co_{10})_{78}Si_{12}B_{10} - AlN$ thin film composites. *Applied Physics Letters*, 96(18), 2010.

[24] H. Greve, E. Woltermann, R. Jahns, S. Marauska, B. Wagner, R. Knöchel, M. Wuttig, and E. Quandt. Low damping resonant magnetoelectric sensors. *Applied Physics Letters*, 97(15), 2010.

[25] R. Jahns, H. Greve, E. Woltermann, E. Quandt, and R. H. Knochel. Noise performance of magnetometers with resonant thin-film magnetoelectric sensors. *IEEE Transactions on Instrumentation and Measurement*, 60(8):2995–3001, 2011.

[26] R. Jahns, H. Greve, E. Woltermann, E. Quandt, and R. Knöchel. Sensitivity enhancement of magnetoelectric sensors through frequency-conversion. *Sensors and Actuators A: Physical*, 183:16 – 21, 2012.

[27] V. Röbisch, E. Yarar, N. O. Urs, I. Teliban, R. Knöchel, J. McCord, E. Quandt, and D. Meyners. Exchange biased magnetoelectric composites for magnetic field sensor application by frequency conversion. *Journal of Applied Physics*, 117(17), 2015.

[28] S. Salzer, R. Jahns, A. Piorra, I. Teliban, J. Reermann, M. Höft, E. Quandt, and R. Knöchel. Tuning fork for noise suppression in magnetoelectric sensors. *Sensors and Actuators A: Physical*, 237:91 – 95, 2016.

[29] H. Bittel. Noise of ferromagnetic materials. *IEEE Transactions on Magnetics*, 5(3):359–365, 1969.

[30] M. H. Acuña. Space-based magnetometers. *Review of Scientific Instruments*, 73(11):3717, 2002.

[31] M. Kustov, R. Grechishkin, M. Gusev, O. Gasanov, and J. McCord. A novel scheme of thermographic microimaging using pyro-magneto-optical indicator films. *Advanced Materials*, 27(34):5017–5022, 2015.

[32] N.O. Urs, B. Mozooni, P. Mazalski, M. Kustov, P. Hayes, S. Deldar, E. Quandt, and J. McCord. Advanced magneto-optical microscopy: Imaging from picoseconds to centimeters - imaging spin waves and temperature distributions (invited). *AIP Advances*, 6(5):1, 2016.

[33] J.S.Y. Feng and D.A. Thompson. Permeability of narrow permalloy stripes. *IEEE Transaction on Magnetics*, 13(5):1521–1523, 1977.

[34] A. Aharoni and J. P. Jakubovics. Factors affecting domain wall mobility in thin ferromagnetic metal films. *Philosophical Magazine Part B*, 46(3):253–272, 1982.

[35] C. Tsang and S. K. Decker. The origin of Barkhausen noise in small permalloy magnetoresistive sensors. *Journal of Applied Physics*, 52(3):2465–2467, 1981.

[36] S. Middelhoek. Static reversal processes in thin Ni-Fe films. *IBM Journal of Research and Development*, 6(4):394–406, Oct 1962.

[37] C. Tsang. Magnetics of small magnetoresistive sensors (invited). *Journal of Applied Physics*, 55(6):2226–2231, 1984.

[38] S. W. Yuan and H. N. Bertram. Micromagnetics of small unshielded MR elements. *Journal of Applied Physics*, 73(10):6235–6237, 1993.

[39] K. Kuijk, W. van Gestel, and F. Gorter. The barber pole, a linear magnetoresistive head. *IEEE Transactions on Magnetics*, 11(5):1215–1217, 1975.

[40] B.B. Pant. Magnetoresistive magnetic sensor. *US Patent 4,847,584*, 1989.

[41] R.D. Hempstead, S. Krongelb, D.A. Nepela, D.A. Thompson, and E.P. Valstyn. Antiferromagnetic-ferromagnetic exchange bias films. *US Patent 4,103,315*, 1978.

[42] C.H. Tsang. Magnetoresistive read transducer having patterned longitudinal bias. *US Patent 4,663,685*, 1987.

[43] C. Kittel. Physical theory of ferromagnetic domains. *Rev. Mod. Phys.*, 21:541–583, Oct 1949.

[44] A. Hubert and R. Schäfer. *Magnetic domains: the analysis of magnetic microstructures*. Springer, 1998.

[45] N. A. Spaldin. *Magnetic materials*. Cambridge University Press, second edition, 2010.

[46] R. C. O'Handley. *Modern magnetic materials: Principles and Applications*. Wiley, 2000.

[47] S. Blügel. *Magnetische anisotropie und magnetostriktion (Theorie)*. Forschungszentrum Jülich, 1999.

[48] V. H. Guerrero and R. C. Wetherhold. Strain and stress calculation in bulk magnetostrictive materials and thin films. *Journal of Magnetism and Magnetic Materials*, 271(2–3):190 – 206, 2004.

[49] M. Fähnle and J. Furthmüller. The effect of external stress on the saturation magnetostriction constant of metallica glasses. *Phys. Stat. Sol. (A)*, 116(819):147–152, 1989.

[50] G. Herzer. Effect of external stresses on the saturation magnetostriction of amorphous Co-based alloys. *Blackpool conference proceedings*, pages 355–357, 1985.

[51] N. O. Urs, I. Teliban, A. Piorra, R. Knöchel, E. Quandt, and J. McCord. Origin of hysteretic magnetoelastic behavior in magnetoelectric 2-2 composites. *Applied Physics Letters*, 105(20), 2014.

[52] E. E. Fullerton, J. S. Jiang, M. Grimsditch, C. H. Sowers, and S. D. Bader. Exchange-spring behavior in epitaxial hard/soft magnetic bilayers. *Phys. Rev. B*, 58:12193–12200, 1998.

[53] W. H. Meiklejohn and C. P. Bean. New magnetic anisotropy. *Phys. Rev.*, 102:1413–1414, 1956.

[54] A.E. Berkowitz and Kentaro Takano. Exchange anisotropy — a review. *Journal of Magnetism and Magnetic Materials*, 200(1–3):552 – 570, 1999.

[55] R L Stamps. Mechanisms for exchange bias. *Journal of Physics D: Applied Physics*, 33(23):R247, 2000.

[56] P. J. van der Zaag, Y. Ijiri, J. A. Borchers, L. F. Feiner, R. M. Wolf, J. M. Gaines, R. W. Erwin, and M. A. Verheijen. Difference between blocking and néel temperatures in the exchange biased Fe_3O_4/CoO system. *Phys. Rev. Lett.*, 84:6102–6105, 2000.

[57] K. O'Grady, L.E. Fernandez-Outon, and G. Vallejo-Fernandez. A new paradigm for exchange bias in polycrystalline thin films. *Journal of Magnetism and Magnetic Materials*, 322(8):883 – 899, 2010.

[58] J. McCord, C. Hamann, R. Schäfer, L. Schultz, and R. Mattheis. Nonlinear exchange coupling and magnetic domain asymmetry in ferromagnetic/IrMn thin films. *Phys. Rev. B*, 78:094419, Sep 2008.

[59] J. McCord, R. Schäfer, R. Mattheis, and K.-U. Barholz. Kerr observations of asymmetric magnetization reversal processes in CoFe/IrMn bilayer systems. *Journal of Applied Physics*, 93(9):5491–5497, 2003.

[60] E. Lage, C. Kirchhof, V. Hrkac, L. Kienle, R. Jahns, R. Knöchel, E. Quandt, and D. Meyners. Exchange biasing of magnetoelectric composites. *Nature Materials*, 11(6):523–529, 2012.

[61] J. Nogués, D. Lederman, T. J. Moran, and I. K. Schuller. Positive exchange bias in FeF_2-Fe bilayers. *Phys. Rev. Lett.*, 76:4624–4627, 1996.

[62] D. Mauri, H. C. Siegmann, P. S. Bagus, and E. Kay. Simple model for thin ferromagnetic films exchange coupled to an antiferromagnetic substrate. *Journal of Applied Physics*, 62(7):3047–3049, 1987.

[63] C. Liu, C. Yu, H. Jiang, L. Shen, C. Alexander, and G. J. Mankey. Effect of interface roughness on the exchange bias for NiFe/FeMn. *Journal of Applied Physics*, 87(9):6644–6646, 2000.

[64] J. Hsu, A. Sun, and P. Sharma. Lateral grain size effect on exchange bias in polycrystalline NiFe/FeMn bilayer films. *Thin Solid Films*, 542:87 – 90, 2013.

[65] P. Savin, J. Guzmán, V. Lepalovskij, A. Svalov, G. Kurlyandskaya, A. Asenjo, V. Vas'kovskiy, and M. Vazquez. Exchange bias in sputtered FeNi/FeMn systems: Effect of short low-temperature heat treatments. *Journal of Magnetism and Magnetic Materials*, 402:49 – 54, 2016.

[66] V. Hrkac, E. Lage, G. Köppel, J. Strobel, J. McCord, E. Quandt, D. Meyners, and L. Kienle. Amorphous FeCoSiB for exchange bias coupled and decoupled magnetoelectric multilayer systems: Real-structure and magnetic properties. *Journal of Applied Physics*, 116(13), 2014.

[67] A. Buchter, R. Wölbing, M. Wyss, O. F. Kieler, T. Weimann, J. Kohlmann, A. B. Zorin, D. Rüffer, F. Matteini, G. Tütüncüoglu, F. Heimbach, A. Kleibert, A. Fontcuberta i Morral, D. Grundler, R. Kleiner, D. Koelle, and M. Poggio. Magnetization reversal of an individual exchange-biased Permalloy nanotube. *Phys. Rev. B*, 92:214432, 2015.

[68] A. Aharoni. Demagnetizing factors for rectangular ferromagnetic prisms. *J. Appl. Phys.*, 83(6):3432–3434, 1998.

[69] A. Aharoni, L. Pust, and M. Kief. Comparing theoretical demagnetizing factors with the observed saturation process in rectangular shields. *Journal of Applied Physics*, 87(9):6564–6566, 2000.

[70] A. Aharoni. "local" demagnetization in a rectangular ferromagnetic prism. *physica status solidi (b)*, 229(3):1413–1416, 2002.

[71] F. Bloch. Zur Theorie des Austauschproblems und der Remanenzerscheinung der Ferromagnetika. *Zeitschrift für Physik*, 74(5):295–335, 1932.

[72] D. C. Hothersall. Electron images of two-dimensional domain walls. *physica status solidi (b)*, 51(2):529–536, 1972.

[73] F. Bitter. Experiments on the nature of ferromagnetism. *Phys. Rev.*, 41:507–515, 1932.

[74] J. McCord and J. Westwood. Domain formation in Fe–N multilayers. *Journal of Applied Physics*, 87(9):6502–6504, 2000.

[75] A. Hubert. Domain wall structures in thin magnetic films. *IEEE Transactions on Magnetics*, 11(5):1285–1290, 1975.

[76] H. Riedel and A. Seeger. Micromagnetic treatment of Néel walls. *physica status solidi (b)*, 46(1):377–384, 1971.

[77] A. Hubert. Interaction of domain walls in thin magnetic films. *Czechoslovak Journal of Physics B*, 21(4-5):532–536, 1971.

[78] K. Ramstock, W. Hartung, and A. Hubert. The phase diagram of domain walls in narrow magnetic strips. *Phys. Stat. Sol. (A)*, 155(2):505, 1996.

[79] S. S. P. Parkin, M. Hayashi, and L. Thomas. Magnetic domain-wall racetrack memory. *Science*, 320(5873):190–194, 2008.

[80] E. Lage, N.O. Urs, S. Siddiqui, M. Baldo, J. McCord, and C. Ross. Depinning of domain walls by magnetic fields and current pulses in tapered nanowires with anti-notches. *IEEE Magnetics Letters*, PP(99):1–1, 2016.

[81] B.A. Lilley. Lxxi. energies and widths of domain boundaries in ferromagnetics. *The London, Edinburgh, and Dublin Philosophical Magazine and Journal of Science*, 41(319):792–813, 1950.

[82] M. J. Donahue and D. G. Porter. OOMMF user's guide. *National Institute of Standards and Technology*, 1999.

[83] G. Srinivasan, E. T. Rasmussen, J. Gallegos, and R. Srinivasan. Magnetoelectric bilayer and multilayer structures of magnetostrictive and piezoelectric oxides. *Phys. Rev. B*, 64:1–6, 2001.

[84] N.A. Hill. Why are there so few magnetic ferroelectrics? *J. Phys. Chem. B*, 104(29):6694–6709, 2000.

[85] R. Ramesh and N.A. Spaldin. Multiferroics: progress and prospects in thin films. *Nature Materials*, 6(1):21–29, 2007.

[86] D. Bensaid, N. Benkhettou, and A. Kourdassi. Structural and electronic properties of $BiXO_3$ (X=Mn, Fe, Cr). *Journal of Modern Physics*, 2(7):642–650, 2011.

[87] S. Marauska, R. Jahns, H. Greve, E. Quandt, R. Knöchel, and B. Wagner. MEMS magnetic field sensor based on magnetoelectric composites. *Journal of Micromechanics and Microengineering*, 22(6):065024, 2012.

[88] S. Marauska, R. Jahns, C. Kirchhof, M. Claus, E. Quandt, R. Knöchel, and B. Wagner. Highly sensitive wafer-level packaged MEMS magnetic field sensor based on magnetoelectric composites. *Sensors and Actuators A: Physical*, 189:321 – 327, 2013.

[89] A. Piorra, R. Jahns, I. Teliban, J. L. Gugat, M. Gerken, R. Knöchel, and E. Quandt. Magnetoelectric thin film composites with interdigital electrodes. *Applied Physics Letters*, 103(3), 2013.

[90] Ce-Wen Nan, M. I. Bichurin, S. Dong, D. Viehland, and G. Srinivasan. Multiferroic magnetoelectric composites: Historical perspective, status, and future directions. *Journal of Applied Physics*, 103(3), 2008.

[91] S. H. Bacon and B. B. Megdal. Hysteresis loop tracer with symmetric balance coil. *US Patent 6,538,432*, 2003.

[92] A. Gavrin and J. Unguris. SEMPA imaging of domain dynamics in amorphous metals. *Journal of Magnetism and Magnetic Materials*, 213(1–2):95 – 100, 2000.

[93] S. McVitie, D. McGrouther, S. McFadzean, D.A. MacLaren, K.J. O'Shea, and M.J. Benitez. Aberration corrected lorentz scanning transmission electron microscopy. *Ultramicroscopy*, 152:57 – 62, 2015.

[94] D. Zhang, J. M. Shaw, D. J. Smith, and M. R. McCartney. Domain structure and perpendicular magnetic anisotropy in CoFe/Pd multilayers using off-axis electron holography. *Journal of Magnetism and Magnetic Materials*, 388:16 – 21, 2015.

[95] J. McCord. Progress in magnetic domain observation by advanced magneto-optical microscopy. *Journal of Physics D: Applied Physics*, 48(33):333001, 2015.

[96] C. Hammond and J. Heath. Symmetrical ray diagrams of the optical pathways in light microscopes. *Microscopy and Analysis*, 20(5):5–8, 2006.

[97] B. Mozooni, T. von Hofe, and J. McCord. Picosecond wide-field magneto-optical imaging of magnetization dynamics of amorphous film elements. *Phys. Rev. B*, 90:054410, 2014.

[98] B. Mozooni and J. McCord. Direct observation of closure domain wall mediated spin waves. *Applied Physics Letters*, 107(4), 2015.

[99] Zeiss Axio Imager.Z2 Vario upright light microscope. `http://www.zeiss.com/microscopy/int/products/light-microscopes/axio-imager-vario-for-materials.html`. Accessed: 30.10.2016.

[100] UHP-LED for microscopy applications. `http://www.prizmatix.com/`. Accessed: 30.10.2016.

[101] Cairn research image splitter Optosplitter II. `https://www.cairn-research.co.uk/product/optosplit-ii/`. Accessed: 30.10.2016.

[102] Hamamatsu C10600-10B-H cooled CCD camera. `http://www.hamamatsu.com/jp/en/community/life_science_camera/product/search/C10600-10B`. Accessed: 30.10.2016.

[103] P. Bruno, Y. Suzuki, and C. Chappert. Magneto-optical Kerr effect in a paramagnetic overlayer on a ferromagnetic substrate: A spin-polarized quantum size effect. *Phys. Rev. B*, 53:9214–9220, 1996.

[104] J. Fassbender and J. McCord. Control of saturation magnetization, anisotropy, and damping due to Ni implantation in thin $Ni_{81}Fe_{19}$ layers. *Applied Physics Letters*, 88(25), 2006.

[105] T. Miyahara and M. Takahashi. The dependence of the longitudinal Kerr magneto-optic effect on saturation magnetization in Ni-Fe films. *Japanese Journal of Applied Physics*, 15(2):291, 1976.

[106] T. Sato, T. Simatsu, T. Miyahara, and T. Miyazaki. Magnetooptic effect of Fe-Ni,Ni-Co and Fe-Co binary alloy films. *IEEE Translation Journal on Magnetics in Japan*, 6(10):869–874, 1991.

[107] W. Rave, R. Schäfer, and A. Hubert. Quantitative observation of magnetic domains with the magneto-optical Kerr effect. *Journal of Magnetism and Magnetic Materials*, 65(1):7 – 14, 1987.

[108] P. Görnert, T. Aichele, A. Lorenz, R. Hergt, and J. Taubert. Liquid phase epitaxy (LPE) grown Bi, Ga, Al substituted iron garnets with huge Faraday rotation for magneto-optic applications. *physica status solidi (a)*, 201(7):1398–1402, 2004.

[109] M. Abes, C. T. Koops, S. B. Hrkac, J. McCord, N. O. Urs, N. Wolff, L. Kienle, W. J. Ren, L. Bouchenoire, B. M. Murphy, and O. M. Magnussen. Domain structure and reorientation in $CoFe_2O_4$. *Phys. Rev. B*, 93:195427, 2016.

[110] R. Mattheis and G. Quednau. Separation of the Voigt effect in longitudinal Kerr magnetometry. *Phys. Stat. Sol. (A)*, 172(2):r7–r8, 1999.

[111] R. Schäfer and A. Hubert. A new magnetooptic effect related to non-uniform magnetization on the surface of a ferromagnet. *Phys. Stat. Sol. (A)*, 118(1):271–288, 1990.

[112] D. Meyners, J. Puchalla, S. Dokupil, M. Lohndorf, and E. Quandt. Magnetoelectronical sensors for mechanical measurements. *ECS Transactions*, 3(25):223–233, 2007.

[113] C. Tsang and S. K. Decker. Study of domain formation in small permalloy magnetoresistive elements. *Journal of Applied Physics*, 53(3):2602–2604, 1982.

[114] S. Middelhoek. Domain walls in thin Ni–Fe films. *Journal of Applied Physics*, 34(4):1054–1059, 1963.

[115] J. McCord and J. Westwood. Domain optimization of sputtered permalloy shields for recording heads. *IEEE Transactions on Magnetics*, 37(4):1755–1757, 2001.

[116] J. McCord. Irregular domain patterns in structured magnetic thick films. *Journal of Applied Physics*, 95(11):6855–6857, 2004.

[117] M. Frommberger, S. Glasmachers, C. Schmutz, J. McCord, and E. Quandt. Microscopic magnetic and high-frequency properties of a stress sensor using FeCoBSi magnetostrictive thin films. *IEEE Transactions on Magnetics*, 41(10):3691–3693, 2005.

[118] N. Martin, J. McCord, A. Gerber, T. Strache, T. Gemming, I. Mönch, N. Farag, R. Schäfer, J. Fassbender, E. Quandt, and L. Schultz. Local stress engineering of magnetic anisotropy in soft magnetic thin films. *Applied Physics Letters*, 94(6), 2009.

[119] T. Crowther and M. Frongillo. Role of thin intermediate layers between polycrystalline copper and magnetic films. *Journal of Applied Physics*, 42(4):1431–1433, 1971.

[120] H. P. Murbach and H. Wilman. The origin of stress in metal layers condensed from the vapour in high vacuum. *Proceedings of the Physical Society. Section B*, 66(11):905, 1953.

[121] K. Y. Ahn and J. F. Freedman. The effects of metallic underlayers on properties of Permalloy films. *IEEE Transactions on Magnetics*, 3(2):157–162, 1967.

[122] B. I. Bertelsen. Silicon monoxide undercoating for improvement of magnetic film memory characteristics. *Journal of Applied Physics*, 33(6):2026–2030, 1962.

[123] J. Zhang and R. M. White. Topological coupling in magnetic multilayer films. *Journal of Applied Physics*, 79(8):5113–5115, 1996.

[124] J. Zhang and R. M. White. Topological coupling in spin valve type multilayers. *IEEE Transactions on Magnetics*, 32(5):4630–4635, 1996.

[125] U. B. Bala, M. C. Krantz, and M. Gerken. Electrode position optimization in magnetoelectric sensors based on magnetostrictive-piezoelectric bilayers on cantilever substrates. *IEEE Transactions on Ultrasonics, Ferroelectrics, and Frequency Control*, 61(3):392–398, 2014.

[126] D. Küppers, J. Kranz, and A. Hubert. Coercivity and domain structure of silicon-iron single crystals. *Journal of Applied Physics*, 39(2):608–609, 1968.

[127] B.L.S. Lima, F.L. Maximino, J.C. Santos, and A.D. Santos. Direct method for magnetostriction coefficient measurement based on atomic force microscope, illustrated by the example of Tb–Co film. *Journal of Magnetism and Magnetic Materials*, 395:336 – 339, 2015.

[128] E. Klokholm. The measurement of magnetostriction in ferromagnetic thin films. *IEEE Transactions on Magnetics*, 12(6):819–821, 1976.

[129] A. C. Tam and H. Schroeder. Precise measurements of a magnetostriction coefficient of a thin soft magnetic film deposited on a substrate. *Journal of Applied Physics*, 64(10):5422–5424, 1988.

[130] Hanju Lee, Shant Arakelyan, Barry Friedman, and Kiejin Lee. Temperature and microwave near field imaging by thermo-elastic optical indicator microscopy. *Scientific Reports*, 6(December):1–11, 2016.

[131] D. Markó, I. Soldatov, M. Tekielak, and R. Schäfer. Stray-field-induced faraday contributions in wide-field kerr microscopy and -magnetometry. *Journal of Magnetism and Magnetic Materials*, 396:9 – 15, 2015.

[132] J. McCord, L. Schultz, and J. Fassbender. Hybrid soft-magnetic lateral exchange spring films prepared by ion irradiation. *Advanced Materials*, 20(11):2090–2093, 2008.

[133] J. Trützschler, K. Sentosun, M. Langer, I. Mönch, R. Mattheis, J. Fassbender, and J. McCord. Optimization of magneto-resistive response of ion-irradiated exchange biased films through zigzag arrangement of magnetization. *Journal of Applied Physics*, 115(10):103901, 2014.

[134] J. Trützschler, K. Sentosun, B. Mozooni, R. Mattheis, and J. McCord. Magnetic domain wall gratings for magnetization reversal tuning and confined dynamic mode localization. *Scientific Reports*, 6, 2016.

[135] C. Hengst, M. Wolf, R. Schäfer, L. Schultz, and J. McCord. Acoustic-domain resonance mode in magnetic closure-domain structures: A probe for domain-shape characteristics and domain-wall transformations. *Phys. Rev. B*, 89:214412, 2014.

[136] J. Smit. *Magnetic properties of materials*. McGraw-Hill, 1971.

[137] I. Tomeš, H. Niedoba, M. Rührig, G. Wittmann, A. Hubert, H. O. Gupta, L. J. Heyderman, and I. B. Puchalska. Wall transitions and coupling of magnetization in NiFe/C/NiFe double films. *Phys. Stat. Sol. (A)*, 128(1):203–217, 1991.

[138] J. C. Slonczewski, B. Petek, and B. E. Argyle. Micromagnetics of laminated permalloy films. *IEEE Transactions on Magnetics*, 24(3):2045–2054, 1988.

Acknowledgments

First and foremost I would like to express my heartfelt gratitude to my supervisor Prof. Dr.-Ing. Jeffrey McCord for letting me be part of his group and pursue a scientific career in his group. He has introduced me to the fascinating, almost magical, world of magnetism and has been constantly supporting me on both professional and personal levels. All of which led me to understand and appreciate the informal expression for the doctoral supervisor in German, *der Doktorvater* (Doctor father).

I would also like to thank Prof. Dr.-Ing. Eckhard Quandt and his working group *Inorganic functional materials* for the close and engaging collaboration, in particular Dr.-Ing. André Piorra, Christine Kirchhof, Dr. rer. nat. Dirk Meyners, Patrick Hayes and Volker Röbisch.

Another thanks goes to my colleagues and friends in *Nanoscale magnetic materials - magnetic domains* (*nanomag*) with whom I have worked closely over the years, namely Babak Mozooni, Cai Müller, Ellen Riemer, Finn Klingbeil, Julia Trützschler, Matic Klug, Rasmus Bahne Holländer and Dr. rer. nat. Thomas von Hofe. Moreover, I am very grateful to my office colleagues Farzaneh Karimian, Umer Sajjad and Dr. Mikhail Kustov for the entertaining working hours and conversations. I am also grateful to Dr.-Ing. Enno Lage for his support over many years, first as he was pursuing his Ph.D. degree in Kiel, afterwards during his time as a postdoc in *Massachusetts Institute of Technology* and now during his time in the *nanomag* group. I have also had the chance to work with many bright master students to whom I am also thankful to. Furthermore, I am grateful to Cai, Enno, Finn, Matic and Rasmus for their invaluable inputs to my thesis.

Moreover, I would also like to thank all my colleagues in Collaborative Research Centre SFB 855 for the interdisciplinary and engaging work, especially Dr. Bridgett Murphy, Dr. Madjid Abes and Dr. Stjepan Hrkac from the department of Physics; Dr. Iulian Teliban, Prof. Dr. Reinhard Knöchel, Dr.-Ing Robert Jahns and Sebastian Salzer from the institute of electrical engineering.

I would also like to thank Matthias Burmeister, Berndt Neumann and the workshop staff for the extreme precision in manufacturing many of the experimental parts.

The funding for the Collaborative Research Centre SFB 855 “Magnetoelec-

tric Composite Materials-Biomagnetic Interfaces of the Future" and PAK 902 "Magnetostriktive Multilagen für magnetoelektrische Sensoren - Schichtaufbau und Domänen" from the German Science Foundation (DFG) are also highly acknowledged.

Lastly, I would also like to thank Dr.-Ing. Burak Erkartal, Emre Kızılkan, Juna, Kadir Şentosun, Dr. Mert Kurttepeli, Ruth Volk and my parents and sister for their friendship and being very supportive of me.